Solubility, redox and sorption behavior of plutonium in the presence of α-D-isosaccharinic acid and cement under reducing conditions

Zur Erlangung des akademischen Grades eines

DOKTORS DER NATURWISSENSCHAFTEN

(Dr. rer. nat.)

der KIT-Fakultät für Chemie und Biowissenschaften

des Karlsruher Instituts für Technologie (KIT)

genehmigte

DISSERTATION

von

Dipl. Chem. Agost Gyula Tasi

aus

Szeged, Ungarn

KIT-Dekan:	Prof. Dr. Reinhard Fischer
Referent:	Prof. Dr. Horst Geckeis
Korreferent:	Prof. Dr. Thorsten Schäfer

Tag der mündlichen Prüfung: 16.04.2018

Erklärung

Hiermit versichere ich, dass ich die vorliegende Arbeit selbständig verfasst und keine anderen als die angegebenen Quellen und Hilfsmittel verwendet habe. Darüber hinaus versichere ich, dass alle Stellen der Arbeit, die wörtlich oder sinngemäß aus anderen Quellen übernommen wurden, als solche kenntlich gemacht sind und die elektronische Version der Arbeit mit der schriftlichen übereinstimmt und dass die Arbeit in gleicher oder ähnlicher Form noch keiner Prüfungsbehörde vorgelegt wurde. Die Satzung des Karlsruher Instituts für Technologie (KIT) zur Sicherung guter wissenschaftlicher Praxis wurde in der jeweils gültigen Fassung beachtet. Zum Zeitpunkt der Einreichung der vorliegenden Arbeit wurden die hierin beschriebenen Studien bereits in ähnlicher Form von mir als federführendem Erstautor in internationalen, von Experten begutachteten Fachzeitschriften (Peer-Review) veröffentlicht und werden im Folgenden nicht weiter als solche ausgewiesen [1-3].

_____

Datum, Ort Unterschrift

Acknowledgments

Firstly, I would like to thank my scientific advisors Prof. Dr. Horst Geckeis and Dr. Marcus Altmaier for the interesting subject and for their guidance and continuous support throughout the study.

My honest and deepest gratitude is dedicated to my supervisors, Dr. Xavier Gaona and Dr. Thomas Rabung. I cannot be thankful enough for their precious helpfulness!

Besides my advisors, I would like to thank the members of Amphos 21 Consulting S.L.: Prof. Dr. Jordi Bruno, Dr. Mireia Grivé and Dr. Elisenda Colàs for establishing such an excellent project and providing professional endorsement during my work. The insightful comments and the sparkling scientific discussions we had on our joint meetings have helped me significantly in the improvement of a better understanding on the topic.

My sincere gratitude goes to Dr. Klas Källström for our fruitful discussions and to the Swedish Nuclear Fuel and Waste Management Co. for funding the project in which my doctoral study was embedded.

I am highly grateful for the support of Dr. Jörg Rothe and Dr. Kathy Dardenne in XAS data evaluations, who also happened to assist me with exceptional patience during the long beam times at the INE-Beamline.

Frank Geyer, Cornelia Walschburger and Annika Kaufmann are more than gratefully acknowledged for the (SF–)ICP–MS measurements. The outstanding support received from Julian Schepperle, Dr. Francesco Endrizzi, Dr. Vanessa Montoya and Dr. David Fellhauer is highly appreciated. Contributions of Dr. Robert Polly in theoretical calculations, the help of Dr. Christian Adam in the NMR analysis, Dr. Dieter Schild in XPS analysis, the exceptional support of Tanja Kisely in NPOC measurements, in addition to Dr. Nicolas Finck and Dr. Frank Heberling in XRD data collection and treatment are grandly acknowledged.

Many thanks goes to Dr. Andreas Bauer as well, for managing the controlled area of KIT-INE, where most of the experimental studies were performed.

My sincere thanks goes also to my “labmates”: Dr. Ivan Pidchenko, Dr. Michel Herm, Dr. Carl-Heinrich Graser, Dr. Ezgi Yalcintas, and Dr. Andreas Schnurr amongst many other fellow scientists at KIT–INE, for helping, sharing their excessive knowledge with me and for providing a cheerful atmosphere to make the *daily work*, in general, more “bearable”.

Last, but most importantly, I would like to thank my father, Dr. Gyula Tasi and my mother, Ildikó Dr. Tasiné Csúcs for continuously supporting me in my life and throughout my PhD period as well.

Abstract

Nuclear waste is planned to be embedded in deep underground facilities within suitable host rock formations. In the post-operational phase, ground water may intrude from the surrounding rock and saturate the repository. The present cementitious materials, used frequently for construction and waste conditioning purposes, will buffer the pH in the alkaline range ($10 \leq pH \leq 13.3$) over a very long time-scale, whereas strongly reducing conditions are expected to simultaneously evolve in the system due to the anaerobic corrosion processes of steel and related materials.

Plutonium in the waste inventory potentially contributes to the long–term radiological risk arising from the long half–life of ^{239}Pu ($t_{½}$ ^{239}Pu = $2.41 \cdot 10^4$ a). In reducing, aqueous environments, the formation of Pu(III) and Pu(IV) is foreseen. However, uncertainties in the available thermodynamic data lead to a rather ill–defined redox transition border, especially under alkaline to hyperalkaline pH conditions.

Large quantities of cellulosic materials may also be disposed of along with low- and intermediate-level nuclear waste (L/ILW). Under alkaline, Ca(II)-rich aqueous solutions, these materials are unstable and observed to decompose into smaller chained organic compounds. Alpha-D-isosaccharinic acid (HISA) is generated with a great yield and was previously identified as the most relevant ligand resulting from cellulose degradation. The strong affinity of ISA for the complexation with An(III) and An(IV) together with the often large inventory of cellulose and the lack of experimental studies on the system Cement-Pu-ISA were the main leading motivations in the development of this study.

A bottom-up, step-wise approach involving the investigation on four sub-systems was considered in the study of the ternary system Cement-Pu-ISA:

1) Firstly, the redox chemistry of Pu was investigated in the absence of ISA (and Ca(II)) under alkaline reducing conditions;
2) Then, the binary system Pu-ISA was studied (in the absence of Ca(II)) via systematic solubility experiments.
3) The binary system Pu-ISA was additionally assessed also in the presence of Ca(II), as expected for cementitious environments. The main aim of all solubility studies was to derive a comprehensive chemical and thermodynamic model on the Ca(II)-Pu(III/IV)-OH-ISA system valid under the boundary conditions of interest;

4) In the next step, sorption processes prevailing in the binary systems: Cement-Pu and Cement-ISA were assessed. Finally, the ternary system Cement-Pu-ISA was analyzed, and the knowledge gained in the previous sub-systems was adapted for the interpretation of this, most complex system.

All experiments were conducted under Ar atmosphere with strict control of redox conditions using hydroquinone (HQ, with pe + pH_m ~9.5), Sn(II) (with pe + pH_m ~1.5) or $Na_2S_2O_4$ (with pe + pH_m ~0.5) as buffering agents. The moderately reducing conditions imposed by the presence of HQ were considered as the reference case, with expected predominance of Pu(IV) in the aqueous and solid phases. The strongly reducing conditions defined by Sn(II) and $Na_2S_2O_4$ were taken as representative of the post-closure period in a geological disposal facility for L-/ILW. The solubility of an aged $^{242}Pu(IV)O_2$(ncr,hyd) solid phase was systematically investigated in alkaline reducing systems: (i) in the absence of ISA, (ii) in the presence of ISA and absence of Ca(II), and (iii) in the presence of ISA and Ca(II). The impact of ISA on the uptake of plutonium by cement was investigated using ordinary Portland cement (OPC, CEM I 42.5N BV/SR/LA, provided by the Swedish Nuclear Fuel and Waste Management Company, SKB). Experiments were performed with various solid-to-liquid ratios, Pu and ISA total concentrations. Special emphasis was given to investigate the impact of experimental preparation order and the reversibility of the sorption processes governing Pu concentrations in the system. The solubility and sorption experiments were complemented with characterizations via synchrotron-based techniques (*in–situ* XRD and Pu L_{III} edge XANES/EXAFS peformed at the INE–Beamline for Actinide Research at KARA synchrotron facility) and Density Functional Theory (DFT) calculations as well.

Topic 1: Solubility and redox behavior of plutonium under reducing, alkaline conditions

Solubility experiments in the absence of ISA resulted in very low total Pu concentrations in solution ($m(Pu)_{tot}$, as expressed in molal, $mol \cdot kg_w^{-1}$: m units) (~10^{-11} m) both for HQ and Sn(II) systems. EXAFS, *in–situ* XRD and XPS results confirmed that PuO_2(ncr,hyd) is the solid phase controlling the solubility in HQ systems. XANES indicated a significant contribution of Pu(III) (30 ± 5%) in the solid phases equilibrated in Sn(II) systems. Two hypothesis are proposed to explain these observations in Sn(II) systems: (i) the coexistence of PuO_2(ncr,hyd) and $Pu(OH)_3$(am) in the retrieved solid phases, or (ii) the presence of a homogenous oxygen-deficient, PuO_{2-x}(ncr,hyd) phase. These results provide a sound baseline for the interpretation of the solubility of Pu in the presence of ISA.

Topic 2: Plutonium solubility investigations in the presence of ISA (absence of Ca)

A pronounced increase of plutonium solubility by up to 2.5 log–units was observed in the presence of ISA (and absence of Ca(II)). In HQ systems, the slope analysis of solubility data in combination with solid phase characterization and DFT calculations resulted in the developement of a chemical model including the predominance of $Pu(OH)_3ISA_{-H}^{-}$ and $Pu(OH)_3ISA_{-2H}^{2-}$ complexes below and above $pH_m \approx 12$, respectively. The significantly higher $m(Pu)_{tot}$ measured in Sn(II) systems with $pH_m < 12$ indicated the formation of Pu(III)-ISA complexes under the given conditions. Above this pH_m, solubility data in HQ and Sn(II) systems were observed to be identical showing the prevalence of Pu(IV)-ISA complexes in both cases. A comprehensive thermodynamic model for the Pu(III/IV)-OH-ISA system was established using the Specific Ion interaction Theory (SIT) formalism and was proven to be valid for the wide-range variation of the applied pH_m, total ISA concentration ($m(ISA)_{tot}$) and activity of electron in solution (pe) experimental parameters. Differences identified with available literature data for Th(IV)-, U(IV)- and Np(IV)-ISA systems are discussed in terms of systematic trends along the actinide series. Although not included in the thermodynamic model derived, "Pu-ISA colloids" were found to importantly increase the solubility of Pu in the presence of ISA (and absence of Ca(II)) as detected directly in the supernatants of the experiments.

Topic 3: Plutonium solubility investigations in the presence of ISA and Ca

The presence of Ca(II) further enhanced the solubility of Pu(IV) in HQ–buffered systems (compared to Ca(II)–free, Pu-ISA system), indicating the formation of quaternary Ca(II)–Pu(IV)–OH–ISA aqueous complexes in solution. Chemical and thermodynamic models were derived for this system as well, based on the statistical analysis of solubility data and on results of solid phase characterizations, which included the formation of two quaternary complexes: $Ca(II)Pu(IV)(OH)_3ISA_{-H}^{+}$ and $Ca(IV)Pu(IV)(OH)_3ISA_{-2H}(aq)$, dominating below and above $pH_m \approx 11$, respectively. The proposed model slightly overestimates the experimentally measured solubility at $pH_m \geq 12.4$ and $m(ISA)_{tot} \geq 0.01$ m, likely due to the formation of a yet undefined Ca(II)-Pu(IV)-OH-ISA(s) solid phase. Data collected in Sn(II)–buffered systems do not support the formation of analogous Pu(III) quaternary complexes with Ca(II) ions. For the same reducing system with $pH_m > 11$, solubility data could be explained by the model derived for Ca(II)–Pu(IV)–OH–ISA in HQ systems. In contrast to the Ca(II)-free system, no evidence on the formation of "Pu-ISA

colloids" was found in the present case, pointing out the key role of Ca(II) in the destabilization of colloidal fractions. The obtained results provide key inputs to understand and quantitatively evaluate the solution chemistry (solubility, complexation) of Pu in the presence of ISA, under boundary conditions representative of reducing, cementitious systems.

Topic 4: Plutonium retention in the system Cement-Pu-ISA

Sorption studies performed under reducing conditions in the absence of ISA confirmed the strong uptake of Pu(IV) by the OPC solid phase (under conditions simulating cement degradation stage II). Distribution ratios (R_d) determined in present work were in good agreement with related data available in the literature for An(IV). For the uptake of ISA by cement under analogous conditions, a two-site Langmuir-isotherm was developed, which provided an empirical tool to evaluate the equilibrium concentration of ISA in solution at various S:L ratios.

Independent solubility experiments with PuO_2(ncr,hyd) using the porewater composition in equilibrium with cement were conducted at various ISA concentrations (in the absence of cement) to set upper concentration limits for Pu, to be considered in the interpretation of sorption experiments. These results further confirmed the validity of the thermodynamic model on the system Ca^{2+}–Pu^{4+}–OH^-–Cl^-–ISA^-–H_2O(l).derived in the course of the solubility studies of the present work.

Sorption experiments conducted in the presence of cement and ISA with the higher initially introduced total Pu concentration of $\log [Pu]_{in} \approx -5.5$ (as expressed in molar units) were observed to be solubility controlled, and thus, main conclusions on the uptake of Pu by cement were derived from sorption experiments with $\log [Pu]_{in} \approx -8.5$. Experimental results determined a relevant impact for the order of addition of components (Pu / ISA / cement) on sorption results (especially at $\log [ISA]_{tot} = -2$), with the sequence "(Pu + cement) + ISA" showing significantly higher $\log R_d$ values (≈ 1.5 log-units greater) than the other sequence: "(Pu + ISA) + cement".

Two different cases could be defined based upon experimental results obtained in the presence of cement and ISA with $\log [Pu]_{in} = -8.5$:

- *Case I* shows the strongest sorption and has been observed only in desorption experiments and sorption experiments following the sequence "(Cement + Pu) + ISA". Data in Case I represent lowest sorption reduction factors (F_{red}) and can be explained approximately by a simplified sorption model, which considers $\log R_{d,in}$ determined

experimentally in the absence of ISA, and assumes a decreased sorption caused only by formation of dissolved Ca(II)–Pu(IV)–OH–ISA complexes. Thermodynamic data derived in this PhD thesis are used to calculate the concentrations of the complexes Ca(II)–Pu(IV)–OH–ISA forming in solution.

- *Case II* results in systematically higher Pu aqueous concentrations in solution, and accordingly lower R_d and higher F_{red}. It corresponds to sorption experiments performed following the order "(Pu + ISA) + Cement". These observations are explained by a kinetic stabilization of aquatic Ca-Pu-ISA species or modification of the cement surface by the adsorbed ISA.

Although a solubility control may appear inconvenient in sorption experiments, note that Pu concentrations used in this study (log $[Pu]_{in} \approx -8.5$) were targeted to be in the range of those potentially expected in a repository for L/ILW [4]. Experiments with lower Pu concentrations (possibly using ^{238}Pu or ^{239}Pu) could help in providing a more insightful view on the sorption phenomena controlling Pu retention / mobility in cementitious systems.

This work demonstrates the significant impact of ISA on the retention of Pu by cement under reducing, alkaline conditions, but also reflects the high complexity of the ternary system cement-Pu-ISA. Although the results obtained in this PhD thesis represent a sound empirical basis to quantitatively assess the impact of ISA on the uptake of Pu by ISA, an unequivocal mechanistic understanding of the uptake process(es) is not yet possible.

The present PhD study was conducted in the framework of an international project by KIT–INE with Amphos 21 Consulting Agency (Spain). The project was funded by the Swedish Nuclear Fuel and Waste Management Company (SKB).

Table of Contents

List of Abbreviations and Symbols

$[\ i\ ]_{tot}$	Total concentration of species "*i*" in solution [mol·dm^{-3}]
β	Cumulative or overall stability constant
γ	Activity coefficient
ΔE	Energy shift [eV]
ε	Ion interaction coefficient [mol·kg^{-1}]
σ^2	EXAFS Debye-Waller factor
$\chi(k)$	EXAFS fine structure function
a	Activity
ACW	Artificial cement porewater
An	Actinide element(s)
ARTEMIS	Computer program for XAFS fitting
ATHENA	Computer program for XAFS analysis
BET	Brunauer–Emmett–Teller (surface area)
BGE	Background electrolyte
c	Concentration in molar units [mol·dm^{-3}]
CDP	Cellulose degradation product
CEM I	Portland-type cement
CEM V	Composite (slag and ash) cement
CE-SF-ICP-MS	Capillary electrophoresis hyphenated Sector Field-ICP-MS
CHES	2-(Cyclohexylamino)ethane-sulfonic acid
(–)COOH	Carboxylic acid functional group
C-S-H	Calcium-silicate-hydrates
DFT	Density functional theory
E_h	Standard electrode potential (vs. SHE)
EXAFS	Extended X-ray absorption fine structure
f, F	Mathematical objective functions
FEFF	Computer program for quantum-chemical calculations
FWHM	Full width at half maximum
g	standard gravity [9.80665 m·s^{-2}]
GLU	α-D-gluconate ion
HCP	Hardened cement paste
HDEHP	Di-(2-ethylhexyl)-phosphoric acid
HGLU	α-D-gluconic acid
HISA	α-D-isosaccharinic acid
$HISA_L$	α-D-isosaccharinate-1,4-lactone
HPLC	High performance liquid chromatography
HQ	Hydroquinone
IC	Ion chromatography
ICP-MS	Inductively coupled plasma-mass spectrometry
ICP-OES	Inductively coupled plasma–optical emission spectrometry
INE	Institute for Nuclear Waste Disposal
ISA	α-D-isosaccharinate ion
JCPDS	Joint Committee on Powder Diffraction Standards
K	Equilibrium constant / adsorption affinity constant [dm^3·mol^{-1}]
k	Wavenumber of photoelectron [Å^{-1}]
KARA	Karlsruhe Research Accelerator
KIT	Karlsruhe Institute of Technology
L-/ILW	Low- and intermediate-level nuclear waste

Ln	Lanthanide element(s)
LSC	Liquid scintillation counting
M	Metal element / molarity as unit [$mol \cdot dm^{-3}$]
m	Concentration in molal units [$mol \cdot kg_{water}^{-1}$]
$m(i)_{tot}$	Total concentration of species "*i*" in solution [$mol \cdot kg_{water}^{-1}$]
MWCO	Molecular-weight cut-off
n%	Normalized mol-percentage
N	Coordination number
NEA–TDB	Nuclear Energy Agency – Thermochemical Database
NIR	Near infrared
NIREX	Nuclear Industry Radioactive Waste Executive (UK)
NMR	Nuclear magnetic resonance
NPOC	Non-purgeable organic carbon-content
(–)OH	Hydroxyl functional group
OPC	Ordinary Portland cement
PDF	Powder diffraction file
pe	Negative decimal logarithm of electron activity in solution
PMBP	1-phenyl-3-methyl-4-benzoyl-pyrazol-5-one
PMMA	Poly-methyl-methacrylate
PP-PQC	Phree Plot – PhreeqC computer program packages
q	Adsorption capacity [$mol \cdot kg^{-1}$]
R^2	Coefficient of determination
R_{i-j}	neighboring atom (between *i* and *j*) distances
S_0^2	EXAFS amplitude reduction factor
SF-ICP-MS	Sector field-inductively coupled plasma-mass spectrometry
SHE	Standard hydrogen electrode
SIT	Specific ion interaction theory
SKB	Swedish Nuclear Fuel and Waste Management Company
S:L	Solid-to-liquid phase (weight-to-volume) ratio [$g \cdot dm^{-3}$]
TG-DSC	Thermogravimetric-differential scanning calorimetry
TIC	Total inorganic carbon-content
TOC	Total organic carbon-content
TRIS	2-Amino-2-(hydroxymethyl)propane-1,3-diol
UV-Vis	Ultraviolet-visible
V	Volume [dm^3]
w%	Normalized weight-percentage
WL	White line
XANES	X-ray absorption near edge structure
XAS	X-Ray absorption spectroscopy
XPS	X-ray photoelectron spectroscopy
XRD	X-ray diffraction

List of figures

List of Tables

1 Introduction

A widely accepted concept for the disposal of low- and intermediate-level nuclear waste (L-/ILW) is its emplacement in underground geological formations. L-/ILW is mostly generated during the operation of nuclear reactors, storage facilities and reprocessing plants. Sources of L-/ILW can be decommissioning and nuclear research activities as well as industrial and medical use of various radionuclides.

Prior to disposal, L-/ILW is often supercompacted in steel drums and steel containers for volume-reduction. In subsequent steps, the containers are filled in with cement (usually ordinary Portland cement, OPC) to encapsulate and immobilize the waste, and are placed into the engineered concrete vaults of a designated facility. Cementitious materials are favored not only for stabilization purposes, but also because they simultaneously act as physical and chemical barriers preventing the release of radionuclides. Besides several technical barriers, the geological barrier, *i.e.* the host rock itself provides additional isolation of the waste from the biosphere. The main geological formations considered for the construction of repositories for nuclear waste disposal are crystalline rock, clay rock and rock salt. A potential groundwater intrusion into the repository will interact with the cementitious materials and also with steel components and containers in the repository. As a result, pH of the groundwater media will be buffered in the alkaline to hyperalkaline range, whereas the anoxic corrosion of steel will impose strongly reducing conditions in the system [4].

Plutonium is a highly important actinide in the context of nuclear waste disposal, and can be also found with low inventory in L-/ILW. Plutonium contributes to the long-term risk of a repository as a result of the long half-life of ^{239}Pu ($t_{½} = 2.41 \cdot 10^4$ a). It can co-exist in up to four different oxidation states in solution and accordingly, the redox conditions defined by the repository environment have a strong impact on its solution chemistry, solubility and sorption behavior. Under the strongly reducing conditions set by the anoxic corrosion process of steel, Pu is foreseen to be present primarily as +IV, although the presence of Pu(III) cannot be disregarded, especially in weakly alkaline systems [5]. A relevant feature in the solution chemistry of Pu(IV) relates to its tendency to polymerize and form stable “colloids”. The colloidal species of Pu(IV) (denoted as $Pu(IV)_{coll}$) exhibit a wide-range of particle size (nanometers to microns) and have been called to play a key role in the redox properties of Pu in aqueous systems [6-8]. $Pu(IV)_{coll}$ species can also contribute to the overall solubility of Pu by an “apparent” increase up to several orders of magnitude, which was extensively discussed by Neck and co-workers [9].

Cellulose and cellulosic materials are disposed of in significant amounts along with L-/ILW. Under the porewater conditions defined by the degradation of cement (see Section 1.2), cellulosic materials are chemically unstable and degrade into certain smaller chained organic substances [10, 11]. These compounds are generally named as cellulosic degradation products (CDPs). Amongst CDPs, the most relevant ligand, alpha-D-isosaccharinic acid was identified to form very stable complexes with actinides (An) and lanthanides (Ln) [12, 13]. These species can enhance the solubility and reduce the sorption of An, and accordingly could contribute to the potential mobilization of An from the repository into the biosphere.

Within the analysis of the long-term performance of a nuclear waste repository, it is essential to assess the amount of radionuclides which could be mobilized from the facility. Main radionuclide retention mechanisms are related to radionuclide solubility equilibria (these are, in the case of Pu, strongly dependent upon prevailing redox conditions), and also to radionuclide sorption processes onto mineral phases present in the near- and far-field of a repository. Analysis is often done by means of geochemical computational tools, which allow the comprehensive modelling of specific scenarios, but in turn, highly depend on reliable thermodynamic data. With the aim of investigating plutonium retention under cementitious environment in the presence of ISA, all these aspects have been systematically studied in this work.

1.1 Aquatic chemistry of Pu – fundamentals and background

A fundamental knowledge of the aquatic chemistry of actinides is a necessary basis for numerous processes and research areas. Exemplary benefiting fields are the production of nuclear fuel from ores, reprocessing of spent nuclear fuel, development of a safe concept for the long-term disposal of radioactive wastes or understanding the behavior of actinides in the environment.

In the context of nuclear waste disposal, the knowledge on actinide solution chemistry represents a pillar element in the prediction of their potential migration from the repository into the biosphere [14]. To be able to describe the main retention processes, to identify pathways for their mobilization and to assess the kinetics of their related processes, an in-depth, qualitative and quantitative knowledge is required on the competing (geo-)chemical processes governing actinide concentrations in solution. As complexation and redox reactions control the distribution, speciation, and set the stabilities of actinide-bearing species, precipitation- and dissolution-reactions of their solid compounds define upper limit concentrations in solution. Physicochemical interactions of the dissolved species with mineral and rock surfaces or colloids will further affect their fate within the repository and in the environment as well.

Actinides represent thirteen elements with atomic numbers of 90 to 103, following actinium in the periodic table. Among the series, U, Pu, Np, Am and Cm arise as the most relevant actinide elements in the context of nuclear waste disposal. By interrupting the 6*d* transition metals, the electrons fill the 5*f* orbitals along the actinide row. In comparison with the 4*f* electrons of the lanthanide series, 5*f* electrons are more exposed, *i.e.* the corresponding valence orbitals have larger radial extensions (also in connection with the increased relativistic effects) [15]. Consequently, in contrast to the overall chemical homogeneity observed for the lanthanide series (where the increasing number of 4*f* electrons have a little influence on the nature of the chemical bonding), the chemical reactivity of the actinides is differing owing to their electronic configurations. The general trend is further disrupted by the closer energy states of the *f* and *d* electrons [16]. Hence, in the "early actinides", from Th to Am, the ground-state electronic configuration of most actinide atoms consists of one *d*-electron. In fact, for Th, the ground-state configuration is [Rn] $6d^2 7s^2$, indicating that the energy of the 6*d* orbital is actually lower than for the 5*f* orbital. Moving along the series with increasing atomic number, the orbital energies invert, 5*f* becomes lower in energy than 6*d* and this energy-gap further widens. The "early actinides" therefore, exhibit certain chemical features that are highly resembling to those of the d-transition metals. This transition-like behavior is reflected by the possibility of existence of their higher oxidations states, up to

+VII (or even +VIII, controversially discussed for Pu [17, 18]). As a sub-group, "early actinides" display more chemical variety than the "late actinides", where the $5f^n7s^2$ (n = 6 – 14) ground-state configuration becomes "again" stable, analogously to the standard configuration of the lanthanides with $4f^n6s^2$ (an exception is the case of Cm, which has [Rn] $5f^76d^17s^2$ ground-state configuration due to the half-filled *f* subshell and Lr where the f-shell is filled) [16]. All possible oxidation states of the "early actinides" are illustrated in Figure 1 (with rectangular symbols), together with their ground-state valence shell configurations.

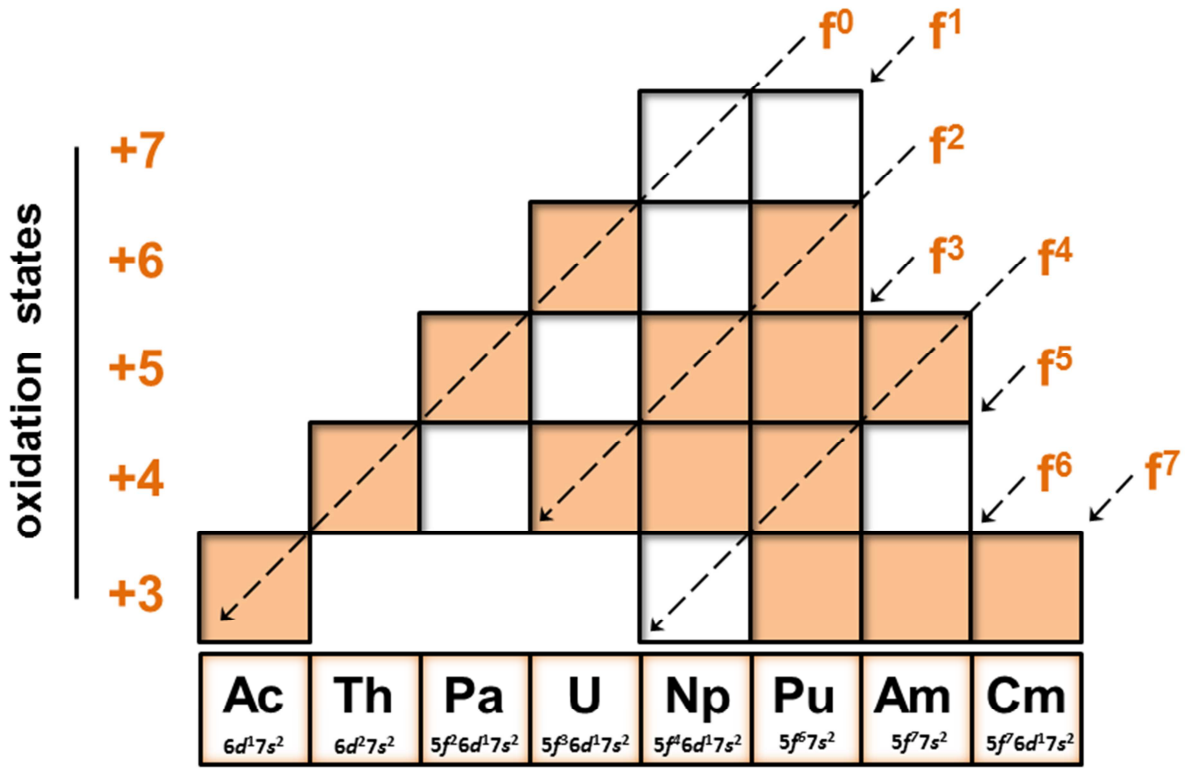

Figure 1. *Possible oxidation states (rectangular symbols) and ground-state valance shell configurations of the "early actinides". The most stable redox states under aqueous conditions are indicated by the filled symbols.*

1.1.1 Chemical behavior of Pu: historic aspects, challenges, aquatic systems

Plutonium has had a substantial impact on the modern history of mankind. Only 3 years after its first production and isolation in 1940 by a deuteron bombardment of ^{238}U in a cyclotron facility at the University of California, Berkeley, U.S., its first production reactor generating ^{239}Pu isotope was set up in Oak Ridge with the objective of constructing the first nuclear bomb [19]. ^{239}Pu is a fissile isotope with relatively high thermal neutron cross section. It

forms in nuclear reactors from ^{238}U, but it can be purposely added to the fresh nuclear fuel in the so-called mixed oxide fuels (MOX). Considering spent nuclear fuel and nuclear wastes in general, besides ^{239}Pu, the presence of other isotopes of Pu are also of high importance. These are ^{241}Pu and the fertile (to thermal neutrons), even-mass isotopes: ^{240}Pu, ^{242}Pu, generated through sequential neutron captures of ^{238}U.

Plutonium has the most complex chemical behavior amongst all metallic elements in the periodic table [20, 21]. Due to its electropositive nature, the Pu atom can easily loose its valance electrons to form positively charged cations. Provided its electronic configuration, five formal oxidations states are energetically stable under aqueous conditions: Pu(III), Pu(IV), Pu(V), Pu(VI), Pu(VII) [21]. Due to their close standard redox potentials, up to four of them (+III to +VI) can be simultaneously present in the same aqueous solution. This reflects a feature that makes Pu aquatic chemistry very complicated and outstandingly unique.

Under highly acidic conditions and in absence of other complexing ligands than water, tri- and tetravalent Pu exist in hydrated forms, *i.e.* as aquo ions. As a result of the high number of valence shell orbitals, coordination numbers for Pu^{3+} and Pu^{4+} aquo ions are 8, 9 and 10, depending mostly upon the ligand and the ionic strength of the media [21]. In case of the Pu(V) and Pu(VI) ions, the determinant trait is the actinyl structure, which can be traced back to the highly charged central Pu ions formally stripping oxo-anions from the water molecules to evolve into the energetically favorable, linear, trans-dioxo cation form. Pu(V) and Pu(VI) aquo ions as well as related complexes usually exhibit a pentagonal bipyramid coordinational structure, where the donor atoms (depending upon the ligand and the prevailing ionic strength, with a maximum number of 5) of the ligands bond in the equatorial plane of the cation core [21]. The substantial difference in structures between the Pu(III)/Pu(IV) and Pu(V)/Pu(VI) ion-couples is also reflected in the redox transition reactions and in their related parameter-dependence. Since the redox transformation between the "bold" aquo ions of Pu^{3+} and Pu^{4+} does not require any structural re-arrangement, the reaction is highly reversible and the rate is found to be independent upon the free proton concentration in solution [21, 22]. This is also valid for the Pu(V)/Pu(VI) couple, as the plutonyl structure is a permanent feature in both ends of the transition. On the other hand, the redox reaction between Pu^{4+} and PuO_2^{+} aquo ions is referred to as "irreversible", given that it involves the breakage / formation of the trans-dioxo structure and hence, it is also strongly dependent on the pH. The term "thermodynamical irreversibility", however mostly indicates that the reaction proceeds with much slower kinetics and often calls for a strong (electro-)chemical influence.

Pu aquo ions bear with high effective charge (Z_{eff}) density (low polarizability) and are considered as “hard”, class A acids according to Pearson’s “hard–soft acid–base”, HSAB theory. Consequent to the relatively tightly held valance electrons present in the Pu aqua ions, the metal–ligand interaction, “bonding” possesses a high degree of ionic character with a preferential tendency towards the complexation with “hard bases”, *i.e.* ligands with O– or N–donor atoms (and with F^-, Cl^- ions). The nature of the bonding strongly affects the stability of related complexes and it can be also correlated with the charge-to-ionic-radius ratio order within the Pu aquo ions [23], as follows:

$$Pu^{4+} > Pu^{3+} \approx PuO_2^{2+} > PuO_2^{+}.$$

The relative trend displayed before directly shows the order of many related overall stability constants of Pu ions with “hard bases”. The first hydrolysis constant is a typical demonstrative example of this kind: while Pu^{4+}(aq) ion forms the $Pu(OH)^{3+}$ species already above pH ~ 0, the first hydrolyzed species of Pu(V), PuO_2OH(aq) becomes predominant only above pH ~ 9.5. It is, however also worth mentioning, that partly due to the ionic character of the bonding, the step-wise formation constants can be further influenced by several factors such as steric or coulombic repulsion between the coordinating ligands.

As a consequence of the latter discussion, it can be clearly stated that the oxidation state of Pu determines its chemical behavior in solution. For instance, Pu(IV) and Pu(III) are (especially under alkaline aqueous conditions) relatively insoluble, whereas Pu(V) and Pu(VI) are in general, more soluble. The complexity of the aqueous speciation of Pu is further increased by the possible dis- and synproportionation reactions of the different ions and oxidation states.

A relevant feature of the aqueous chemistry of plutonium is the colloid formation reaction of Pu(IV). As Pu^{4+}(aq) undergoes hydrolysis, it readily forms even under acidic conditions, mononuclear hydroxo-complexes with the general formula of $Pu(OH)_n^{+(4-n)}$ with n = 1 – 4. At high alkalinity and / or at high total concentration of the metal, the hydrolysis is coupled with oligomerization reactions resulting in the generation of polynuclear clusters [8, 21, 24]. These clusters can exhibit hydroxo-bridged as well as oxo-bridged structures. The degree of poly-nuclearity depends upon several parameters, and can evolve into the production of colloidal suspensions with micron-sized particles [7]. The latter form resemble to the structure of hydrated Pu(IV)-dioxide, the most stable solid phase of Pu(IV) in aqueous solutions. Colloidal fractions of Pu(IV) are proven to play a relevant role in the redox reactions of Pu [6, 25]. However, the governing force leading to their formation and the thermodynamic aspects of their stability in solution are not yet fully understood or described [9]. Their presence is

definitely important as they can also contribute with an overall increase in Pu(IV) solubility by ≈ 2 log-units [5].

Pu(V) and Pu(VI) display an amphoteric behavior involving the formation of anionic hydroxo-species with stoichiometries $Pu(V)O_2(OH)_2^-$ or $Pu(VI)O_2(OH)_4^{2-}$, which increase the solubility of their solid phases under alkaline conditions [21]. In case of Pu(VI), it has also been shown that at higher Pu total concentrations, it is capable of forming a dimer, $(PuO_2)_2(OH)_2^{2+}$ and a trimer, $(PuO_2)_3(OH)_5^+$ as well, exhibiting μ–hydroxo–bridged, pseudo pentagonal bipyramid structures [26, 27]. Analogous polyatomic species have been also described for U(VI) and Np(VI).

Despite that the knowledge on the aquatic chemistry of Pu is considerably elaborate, there are many gaps to be filled and in some cases, the prevailing uncertainties may lead to the incorrect assessment of Pu solubility behavior and complexation phenomena. It is the aim of the thermodynamic database (TDB) project of the Nuclear Energy Agency (NEA) to provide the most up-to-date and precise compilation of the thermodynamic data for actinides and fission products. Partly based on the latest NEA-TDB update book on Pu [9], Table A1 and A2 of the Appendix summarize some fundamental thermodynamic properties of Pu aqueous species and compounds relevant in the context of the this PhD thesis. These thermodynamic data are used to calculate the Pourbaix diagram (pe *vs.* pH) of Pu, as shown in Figure 2. Pourbaix diagrams in general, display the "map" of possible stable (equilibrium) phases within an electrochemical system in an aqueous media, where the predominant species are separated by solid lines. These types of diagrams are useful tools in helping to understand the main tendencies regarding the relative stabilities of aqueous species and solid compounds. In Figure 2, the solid lines represent the calculation results on the system $Pu–Na^+–Cl^––OH–H_2O(l)$ for both, aqueous species and solid compounds of Pu (in this case, names of the dominant species and compounds are also shown), whilst the dashed lines are calculated by assuming the presence of only aqueous species in the system.

Figure 2 shows that the impact of hydroxide complexation, in other words hydrolysis: following the effective charge correlation, the predominance of Pu(IV) aqueous species is promoted with increasing pH under purely aqueous conditions. An interesting feature is represented by the differences in the predominance fields of the aqueous species of the different redox states. In this case, the aqueous species of Pu(III) (green), Pu(V) and Pu(VI) (red dashed lines) exhibit an extended in-solution stabilization, pointing out the possibility for the existence of reductive or oxidative dissolution equilibria for the PuO_2(am,hyd) solid phase over a wide-range of parameters (if provided a large inventory of Pu, *i.e.* in case of solubility

experiments). Accordingly, it is obvious as well, that without controlled redox conditions, different Pu oxidation states can contribute to the overall solubility and the speciation could instantly change, resulting in an incorrect assessment of solution equilibria.

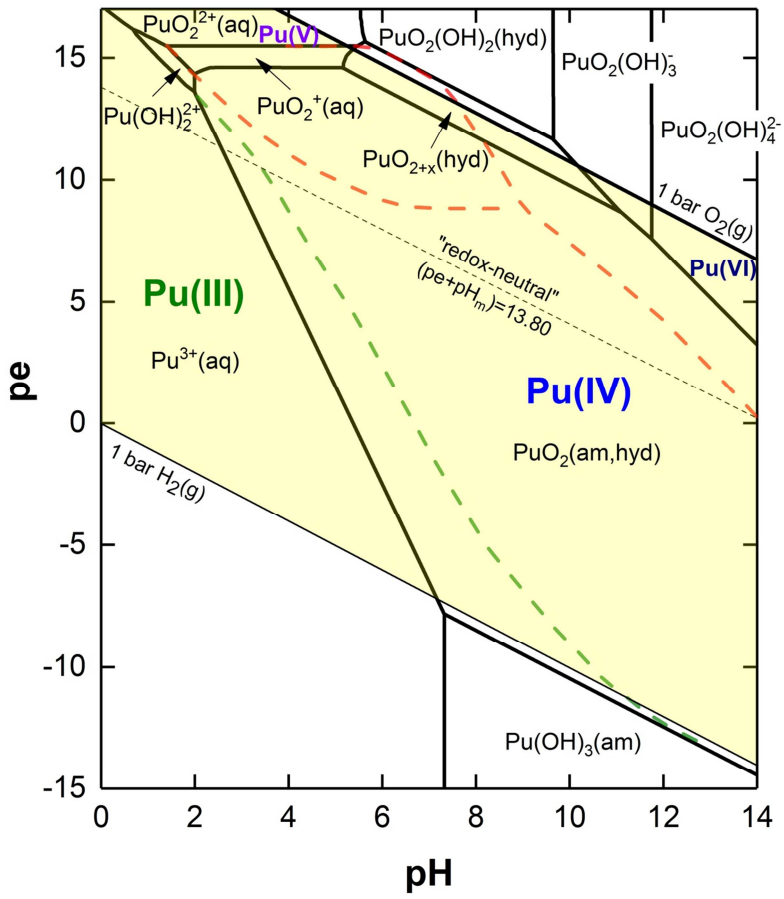

Figure 2. *Pourbaix diagram of Pu calculated for $m(Pu)_{tot} = 10^{-5}$ M and I = 0.10 M NaCl using thermodynamic and (SIT) activity models as described in the text. Solid lines designate the stability fields when both, aqueous species and solid compounds are included, whilst the dashed lines are indicating the calculation results when the presence of only aqueous species are taken into account. The stability borderlines of water at pe + pH_m = 20.77 and pe + pH_m = 0, the "redox-neutral" line at pe + pH_m = 13.8 are shown for comparison reasons.*

Compared to the analogous Pourbaix diagrams of other actinides, substantial differences can be identified with Pu [28]. For instance, in case of Am and Cm, the dominant oxidation state is mainly the +3, already depicting the "lanthanide-like" behavior in the series. U(III) is found to be unstable and rapidly oxidizes to U(VI) under most conditions, whilst U(V) also readily disproportionates to U(IV) and U(VI). On the other hand, the predominance field of Np(III) is located close to the lower border line of water stability field, and therefore its existence is

limited to strongly reducing, acidic conditions. For Pu, under alkaline conditions, the redox transitions: $Pu(IV)_{s/aq}$ / $Pu(III)_{s/aq}$ are found to be heavily impacted by the prevailing uncertainties associated to related thermodynamic data [9]. A comprehensive discussion on the experimental studies and results available in the literature regarding the given system is provided in Section 1.1.2.

The predominance fields displayed in Figure 2 of Pu aqueous species can be significantly affected by complexing ligands such as carbonate, which can be present in significant concentrations in natural waters or repository environments [28]. For instance, upon complexation with carbonate, the stability field of Pu(V) is largely increased compared to carbonate-free systems.

Based on the discussion above, it can be concluded that due to the close proximity of the stability fields for the various oxidation states of Pu (as aqueous species and solid compounds), in addition to the potential formation of $Pu(IV)_{coll}$ species (in the alkaline pH-range), the aquatic chemistry of Pu is highly complex and needs special experimental effort for characterization. While drawing chemical analogies with other actinides of same redox states could provide moderately accurate predictions for related overall stability constants, the redox behavior of Pu cannot be simulated by any element from the periodic table.

1.1.2 Solubility and redox equilibria of Pu under alkaline, reducing conditions

The number of experimental works studying the solubility and hydrolysis of Pu(III/IV), focusing specifically on reducing conditions is very limited [29] and are particularly lacking in the alkaline pH region below (pe + pH) = 4. As a consequence, relevant uncertainties are associated to the thermodynamic data on Pu(III) aqueous species and solid compounds forming in the alkaline to hyperalkaline pH-range, and conversely to the redox transition: Pu(IV) / Pu(III). The most relevant previous investigations on this system are discussed in the following paragraphs.

Felmy *et al.* [30] investigated the solubility of $Pu(OH)_3(s)$ within $6.5 \leq -\log[H^+] \leq 13$ in deionized water and two types of Waste Isolation Pilot Plant (WIPP) related brines. Redox conditions were buffered by the presence of Fe(0) powder. E_h values were only reported for the pH-range: $6.6 \leq -\log[H^+] \leq 8.1$, and confirmed the reducing conditions imposed by Fe(0) (pe + pH = 2 ± 1). Experimental solubility data at $-\log[H^+] \geq 9$ were below the detection limit of LSC (Liquid Scintillation Counting), and thus were disregarded in the thermodynamic interpretation by the authors. The experimentally measured total concentrations of Pu was

fully attributed to be only Pu^{3+}(aq) species, *i.e.* the unhydrolized aqua ion. Data at $pH_m \leq 9$ were used to derive $\log^*K°_{s,0}$ for the solubility reaction:

$$Pu(OH)_3(am) + 3\ H^+ \Leftrightarrow Pu^{3+} + 3\ H_2O(l) \quad (1)$$

The NEA-TDB review team accepted [31] the reported solubility product ($\log^*K°_{IIIs,0} = 15.8$), but assigned a very large uncertainty (± 1.5 log-units) to account for the large associated errors in the pH measurements (the latter values are provided in Table A1 and Table A2 of the Appendix). Apart from the experimental uncertainties, other relevant shortcomings appear in the study of Felmy and co-workers. For an example, the solubility limiting solid phase was not characterized but was only assumed to be predominantly $Pu(OH)_3$(s). As it was pointed out by Neck *et al.* [5], the oxidation of this solid phase to PuO_2(am,hyd) cannot be completely excluded under aqueous conditions. Since the recorded redox potentials were in the range of (pe + pH) = 2 ± 1, obviously above the stability line of $Pu(OH)_3$(s) at (pe + pH) = 0.4, the solid phase transformation is of particular interest in the context of their work. Nevertheless, the short equilibration time (24 days) within their investigation may prevent a significant solid phase transformation. On the other hand, their reported thermodynamic model and the basis of their fitting exercise was not consistent with the hydrolysis scheme currently selected in the NEA-TDB [9]. According to the valid model, calculations show that Pu^{3+}(aq) is dominating only at $-\log[H^+] \leq 6.5$ and under their given experimental conditions, $PuOH^{2+}$ species represent ~20% up to ~70% of the total Pu concentrations quantified. Consequently, the data evaluation procedure performed by Felmy *et al.* is impacted with a non-constant systematic error throughout the entire data series. These shortcomings are acknowledged with a large uncertainty assigned by the NEA-TDB group, and the work by Felmy and co-workers remains as the most reliable solubility study on $Pu(OH)_3$(s) published to date.

Nilsson *et al.* [32] studied the solubility of Pu within $3 \leq -\log[H^+] \leq 10$ in autoclaves with a H_2(g) pressure of 50 bar, in the presence of Pt wire. $Pu(OH)_3$(s) was expected to control the solubility of Pu under these strongly reducing conditions. The initially gained blue solid phase supported this hypothesis, but the change in color towards a greenish precipitate and the unexpectedly low detected Pu total concentrations indicated the formation of a $PuO_{2\pm x}$ solid phase and a solubility equilibrium governed by the reductive dissolution reaction, as expressed in Equation (2).

$$PuO_2(am,hyd) + 4\ H^+ + e^- \Leftrightarrow Pu^{3+}(aq) + 2\ H_2O(l) \quad (2)$$

This was also consistent with the mildly reducing redox potentials measured by the authors at the end of their experiments with (pe + pH) values of (8.5 ± 2).

In a recent combined solubility and spectroscopic study [33], Cho and co-workers determined the solubility product of freshly precipitated $Pu(OH)_3(am)$ phase and re-evaluated the first hydrolysis constant of Pu(III). A blue $Pu(OH)_3(am)$ precipitate was obtained by coulometric titration of a Pu(III) stock solution. The pH was varied between $3.10 \leq -\log [H^+] \leq 6.44$ (spectroscopic experiments) and $6.29 \leq -\log [H^+] \leq 8.42$ (solubility experiments). Plutonium was retained in the +III redox state electrochemically throughout the experiments. Solid phase characterization by XRD indicated the amorphous character of the solid phase used in the solubility experiments. Based on their UV-Vis measurements, the authors reported a greater value for the first hydrolysis constant of Pu(III) than the current selection in the NEA-TDB [9]. Although reporting solubility data mostly consistent with the previous solubility study by Felmy *et al.* [30], Cho and co-workers determined a significantly lower constant, $\log {}^*K°_{s,0}(Pu(OH)_3(am))$ as a result of a different hydrolysis scheme considered in their calculations. The results presented in Cho *et al.* [33], suggest that $Pu(OH)_3(am)$ is stable within the stability field of water, and converts to $PuO_2(am,hyd)$ only above (pe + pH) = (0.8 ± 0.5).

The reductive dissolution of $PuO_2(am,hyd)$ was more frequently investigated [29, 34-36]. This is probably due to the relatively large coexistent stability field for $PuO_2(am,hyd)$ and $Pu(III)_{aq}$. All these studies were performed within the pH-range 4–9, and provided an accurate control of the redox conditions by using hydroquinone ($C_6H_6O_2$), $Na_2S_2O_4$ or Fe(0) powder. As a result of this experimental effort and due to the well-defined (pe + pH) conditions in these studies, the thermodynamic data available for the redox equilibrium $Pu(IV)_s + e^- \Leftrightarrow Pu(III)_{aq}$ from mildly acidic to mildly alkaline pH conditions can be considered to be rather accurate. However, similar investigations under alkaline to hyperalkaline conditions are missing so far, reflecting the challenge that the stability field of Pu(III) aqueous species is expected to be smaller. Indeed, the hydrolysis of Pu(III) was only investigated under acidic to near-neutral pH conditions where the first hydrolysis species ($PuOH^{2+}$) forms [37-39] (for further details see the critical review provided in the recent NEA-TDB update book [9]). Thermodynamic data for higher hydrolysis species of Pu(III) are normally estimated based on data for Am(III) and Cm(III) [9].

Due to the relatively large coexistent stability field for $PuO_2(am,hyd)$ and $Pu(III)_{aq}$, the reductive dissolution of $PuO_2(am,hyd)$, expressed as in Equation (2) for the formation of the aqua ion, has been more extensively investigated ([29, 34, 36], among others). Within all

these reported studies, the conducted experiments focused on the acidic to slightly alkaline pH-range ($4 \leq -\log [H^+] \leq 9$), coupled with an accurate control of the redox conditions by using either hydroquinone, $Na_2S_2O_4$ or Fe powder. As a result of the experimental effort, well-defined (pe + pH) conditions are present in all cases. Hence, the thermodynamic data available for the redox equilibrium (2) of the reductive dissolution of PuO_2(am,hyd) is considered to be sufficiently accurate, bearing with a low associated uncertainty as well.

Both the solubility of Pu(III) and the reductive dissolution of Pu(IV) were comprehensively discussed by Neck and co-workers [5]. The authors concluded, based upon the published experimental evidences, with special focus on available (pe + pH) measurements, that in the latest NEA-TDB review work [9] a satisfactory explanation of the experimental observations, together with the thermodynamic data selection is provided. Neck and co-workers also highlighted the relevant role of Pu(IV) colloids in the solubility and redox chemistry of Pu under near-neutral to alkaline pH conditions.

In a recent, extensive study by D. Fellhauer [40], redox equilibria of Pu(IV)s / Pu(III)aq was evaluated over a broad range of (pe + pH) conditions, within $3.3 \leq -\log[H^+] \leq 7.8$ and by using a large variety of redox buffers (hydroquinone, $FeCl_2$ / $FeCl_3$, $Na_2S_2O_4$, $Fe(CN)_6^{4-}$ / $Fe(CN)_6^{3-}$ and AH_2QDS / AQDS). The author concluded that the abovementioned redox equilibrium can be properly described with the available thermodynamic data. However, based on the solubility and solid phase characterization data collected for one of the most reducing samples at $-\log[H^+] = 6.6$, Fellhauer outlined that the solubility of $Pu(OH)_3$(s) reported in Felmy *et al.* [30] might be overestimated but still lies within the larger uncertainty range assigned by the NEA-TDB review team [9].

Besides solubility studies, numerous experimental investigations [40-47], among others, are focusing on the redox chemistry of Pu in two-phase ternary systems, most commonly involving the interaction with various iron-containing solid phases (particularly magnetite, Fe_3O_4(cr)). These experiments are mainly performed under acidic to weakly alkaline pH conditions.

Kirsch *et al.* [43] reported a qualitative agreement between thermodynamic calculations and experimentally measured Pu redox distribution in magnetite, mackinawite and chukanovite systems with $6 \leq -\log[H^+] \leq 8$, based on a combination of XAFS and wet-chemistry measurements (pH, pe and $[Pu]_{tot}$). In the magnetite system the formation and predominance of a very stable Pu(III) surface complex was observed, whereas PuO_2(am,hyd) prevailed in the presence of mackinawite and chukanovite.

In the work of González-Siso *et al.* [47], the stabilization of Pu(III) was supported in magnetite systems under strongly alkaline ($-\log[H^+] = 12.8$) and highly reducing conditions imposed by the addition of Sn(II) (pe + pH = 2 ± 1). Despite the fact that the presence of Fe(II)–Fe(III) surface is certainly playing a decisive role in the reduction of Pu in the given systems, this observation opens the possibility of the stabilization of Pu(III) under hyperalkaline, reducing conditions, relevant in certain repository concepts.

1.1.2.1 Thermodynamic background

In case of assuming the presence of $Pu(OH)_3(s)$ as a solubility controlling solid phase under reducing, alkaline conditions in the absence of any complexing ligand besides water or hydroxide-ion, the corresponding equation, governing the activity of free $Pu^{3+}(aq)$ at the reference state is expressed as in Equation (3).

$$\log {}^*K^\circ_{\mathrm{IIIs},0} = \log a_{Pu^{3+}(aq)} + p a_{H^+} = (15.8 \pm 1.5) \quad (3)$$

The given constant, $\log {}^*K^\circ_{\mathrm{IIIs},0}$ is the solubility product of $Pu(OH)_3(s)$ at zero ionic strength, according to Equation (1), originally reported by Felmy and co-workers [30] but recognized with an increased uncertainty by the latest NEA-TDB update book [9]. The determinative redox conditions, *i.e.* (pe + pH) values, that are defining the solid phase transformation of $Pu(III)_s \leftrightarrow Pu(IV)_s$, in Equation (8) can be calculated by the combination of Equations (3), (5), (7) through the related chemical reactions (1), (4), (6), according to the thermodynamic data from NEA-TDB [9]:

$$PuO_2(am,hyd) + 4\ H^+ \Leftrightarrow Pu^{4+}(aq) + 2\ H_2O(l) \quad (4)$$

$$\log {}^*K^\circ_{\mathrm{IVs},0} = \log a_{Pu^{4+}(aq)} + 4\ p a_{H^+} = -(2.33 \pm 0.52) \quad (5)$$

$$Pu^{3+}(aq) \Leftrightarrow Pu^{4+}(aq) + e^- \quad (6)$$

$$\log {}^*K^\circ_{\mathrm{IIIaq/IVaq}} = \log a_{Pu^{4+}(aq)} + \log a_{Pu^{3+}(aq)} - pe = -(17.69 \pm 0.04) \quad (7)$$

$$Pu(OH)_3(am) \Leftrightarrow PuO_2(am,hyd) + H_2O(l) + H^+ + e^- \quad (8)$$

$$\log {}^*K^\circ_{\mathrm{IVs/IIIs}} = \log a_w - (pe + p a_{H^+}) =$$

$$= \log {}^*K^\circ_{\mathrm{IIIs},0} + \log {}^*K^\circ_{\mathrm{IIIaq/IVaq}} - \log {}^*K^\circ_{\mathrm{IVs},0} = (0.4 \pm 1.6) \quad (9)$$

Consequently, the $Pu(OH)_3(s)$ is expected to be thermodynamically stable only below the lower border line of the stability field of water: (pe + pH) = 0.0, *i.e.* under strongly reducing conditions, where (pe + pH) ≤ –(0.4 ± 1.6) applies. Hence, $Pu(OH)_3(s)$ is often considered as a metastable solid phase in aqueous systems [5]. Nevertheless, taken into account the large associated uncertainty, originating from the propagation of the reported value for $\log {}^*K°_{IIIs,0}$ [9], a final conclusion cannot be drawn regarding the stability of this phase under aqueous conditions.

If the solubility of Pu under reducing, alkaline conditions is controlled by $PuO_2(am,hyd)$, the following dissolution equilibrium reaction (10) and redox equilibria (12), (14), (16) in the aqueous and mixed phases with corresponding stability constants (11), (13), (15) and (17) can be defined in the view of the thermodynamic selection from [9]:

$$PuO_2(am,hyd) + 2\ H_2O(l) \Leftrightarrow Pu(OH)_4(aq) \quad (10)$$

$$\log {}^*K°_{IVs,4} = \log a_{Pu(OH)_4(aq)} = -(10.8 \pm 0.7) \quad (11)$$

$$Pu(OH)_4(aq) + 3\ H^+ + e^- \Leftrightarrow Pu(OH)^{2+} + 3\ H_2O(l) \quad (12)$$

$$\log {}^*K°_{IVaq/IIIaq,1} = \log a_{Pu(OH)^{2+}} + 3 \log a_w - \log a_{Pu(OH)_4(aq)} + 3\ pa_{H^+} + pe = (19.3 \pm 0.6) \quad (13)$$

$$Pu(OH)_4(aq) + 2\ H^+ + e^- \Leftrightarrow Pu(OH)_2{}^+ + 2\ H_2O(l) \quad (14)$$

$$\log {}^*K°_{IVaq/IIIaq,2} = \log a_{Pu(OH)_2{}^+} + 2 \log a_w - \log a_{Pu(OH)_4(aq)} + 2\ pa_{H^+} + pe = (11.1 \pm 0.9) \quad (15)$$

$$Pu(OH)_4(aq) + H^+ + e^- \Leftrightarrow Pu(OH)_3(aq) + H_2O(l) \quad (16)$$

$$\log {}^*K°_{IVaq/IIIaq,3} = \log a_{Pu(OH)_3(aq)} + \log a_w - \log a_{Pu(OH)_4(aq)} + pa_{H^+} + pe = (0.0 \pm 0.7) \quad (17)$$

In the only presence of water or hydroxide-ion as complexing ligands, in alkaline systems, the concentration of Pu(IV) is controlled by the formation of Pu(IV)-hydroxo-complexes, expressed through Equation (3) using the the related formation constants: $\beta°_{IV,n} = [Pu(IV)(OH)_n{}^{4-n}]\cdot[Pu^{4+}(aq)]^{-1}\ [OH^-]^{-n}$. In dilute, basic solutions with ~$7.5 \leq -\log[H^+]$, where the activity of the 1,4 hydrolized species: $\gamma_{Pu(OH)_4(aq)}$ is approximately equal to 1, the predominating Pu(IV)–bearing aqueous species is $Pu(OH)_4(aq)$, thus for the total concentration of Pu(IV), the value of the related constant (11) provides a relatively good estimate in log–units over a wide pH–range. In cases, when the aqueous media has a sufficiently strong reducing influence, the total Pu concentration, *i.e.* the solubility of Pu can

be further enhanced by the formation of $Pu(III)_{aq}$ species through Equations (12), (14) and (16). In Equations (13), (15) and (17), the calculations involve the use of the corresponding cumulative constants for the second and the third hydrolysis of Pu(III) ($\beta°_{III,n}$) adapted from analogous data of Am(III) [9]. Consequently, the solubility of Pu through the reductive dissolution of PuO_2(am,hyd), as expressed in Equation (2) is affected by relevant uncertainties under alkaline to hyperalkaline conditions, where $Pu(OH)_2^+$ and $Pu(OH)_3$(aq) complexes are the prevailing Pu(III) aqueous species (already from ~7.0 ≤ –log[H^+]).

As it is indicated in the discussion above, the significant uncertainties associated to log $*K°_{IVs/IIIs}$, log $*K°_{IVaq/IIIaq,2}$ and log $*K°_{IVaq/IIIaq,3}$ hinder the correct assessment of Pu chemistry under alkaline, reducing conditions. Furthermore, the propagation of these errors will affect the evaluation / prediction of the impact of any complexing ligand on the solubility of Pu.

1.2 Cement systems: chemical composition and degradation path-ways

Generally, the cementitious materials used to immobilize radioactive waste are composed of significant amounts of Portland-type cement [48]. Portland cements normally comprise four main clinker components: 50 – 70 w% alite (tricalciumsilicate: Ca_3SiO_5), 20 – 30 w% belite (dicalciumsilicate: β–Ca_2SiO_4), 5 – 10 w% aluminates (mainly as tricalcium aluminate: $Ca_3Al_2O_6$), 5 – 12 w% ferrite (calcium aluminoferrite: $Ca_2(Fe_2O_3Al_2O_3)_5$ and ~ 2% gypsum (calcium sulfate: $CaSO_4$). An important aspect in the characteristics of the ordinary Portland cement is the chemical balance, which is typically differing from those of other cement types. As the initial Ca:Si ratio is relatively high, at about ~ 2.5, not all Ca content can be combined into the calcium silicate hydrate (C-S-H) or aluminoferrite hydrate and sulfoaluminate phases during the hydration process. This feature enacts the excess of Ca to form a relevant fraction of portlandite, $Ca(OH)_2$(s) within the system. Thus, the two main co-existing phases in the hydrated OPC are the amorphous C-S-H phases and the crystalline $Ca(OH)_2$(cr). Minor phases are usually Ettringite (aluminoferrite trisulfate, Aft), monosulfate (aluminoferrite monosulfate, Afm), hydrogarnet and hydrotalcite. Although all these solid phases provide potential sorption surfaces for radionuclides dissolved in the pore fluids, C-S-H phases are considered to be the most important amongst them. The large surface area of C-S-H phases (for instance: 148 m^2/g at Ca:Si ratio of ~1.7, provided by Tits *et al.* [49]), together with its high sorption affinity results in high surface densities of sorption sites ($mol·m^{-2}$ or as "number of sites·nm^{-2}") and consequently for hydrated OPC pastes, large sorption capacity is expected for radionuclides and other contaminants.

The interacton of OPC with (intruding) water will result in the degradation of the material and corresponding chemical buffering of the porewater composition. The latter is a key feature in the development of the main parameters governing the chemical equilibria of the radionuclides within the near-field of a disposal facility. In the distinct states of the OPC degradation process, pH and the concentrations of various metal ions in solution will exhibit a wide range of levels controlled by different solid phases [50-53].

In general, three main degradation stages can be defined for cement. In the degradation stage I, the pore fluid of hardened OPC will feature hyperalkaline pH conditions (13 < pH) and a chemical composition that is dominated by alkali metal ions (Na^+, K^+). At this initial stage, Ca(II) total concentration in the pore solution is relatively low (~ 10^{-3} M) due to the limited solubility of portlandite at high pH. After the quantitative removal of the alkali ions, the degradation stage II is reached, where both, the pH and the Ca(II) ion concentration of the porewater will be controlled by the solubility equilibria of portlandite, leading to pH = constant = ~ 12.5 and $[Ca^{2+}]_{tot}$ = constant = 0.020 M. Stage III virtually starts when portlandite is completely removed from the system. In this stage, pH and also Ca(II) ion concentration are controlled by the incongruent dissolution processes of C-S-H phases. Depending on the Ca:Si ratio of the these phases, pH of the porewater will be set in the range of 12.5 – 10, whilst $[Ca^{2+}]_{tot}$ will be subsequently decreased to the millimolar level. At the end of this period, with the disappearance of the C-S-H phases from the system, pH will be fixed at ~10 [50]. After the latter stage of the cement degradation process, as the main constituents of the hydrated cement phases are already removed, pH and Ca(II) ion concentration of the pore fluid will be controlled by the remaining aggregate minerals (mainly by calcite, $CaCO_3$(cr)) and also by the initial conditions of the intruding water. The resulting pH is further decreased below pH = 9, whilst Ca(II) concentration in solution is buffered within the 10^{-3} – 10^{-4} M range. (In some review studies [50], this period, with pH < 9, is often referred to as stage IV.)

1.3 α-D-isosaccharinic acid: generation, complexation, stability, sorption

In Ca(II)-rich alkaline solutions, the main degradation product of cellulose was found to be the isosaccharinic acid with an approximate total yield of 80 % [10, 11, 54, 55] and with the equal proportions of the alpha(α)- and beta(β)-diastereomer forms [56] (see additional information on the structure of these diastereomers in Section 1.4). Previous investigations attributed stronger complexing capabilities towards metal ions to alpha-D-isosaccharinate compared to the beta-form. The latter observation was based on the phenomena that the

observed stability of the beta-isosaccharinate–Eu(III) complex was determined to be two orders of magnitude lower than the analogous species with the alpha–form. Furthermore the influence of a mixture of cellulose degradation products and the pure alpha-D-isosaccharinic acid on the sorption of Eu(III) (onto feldspar resin at pH_c = 13.3) was detected to be identical [57].

Important to mention that for hemicellulose (expected to be present in wood-related conglomerates), the alkali degradation process results in the substantial generation of xyloisosaccharinic acid (a sugarcarboxylic acid, structurally related to isosaccharinic acid) as it was pointed out by [58]. In a recent comprehensive work [59], solubility studies attributed high complexing capabilities for the deprotonated form of xyloisosaccharinic acid towards Th(IV) and Eu(III) under alkaline conditions. Randall *et al.* concluded that since the ligand is not present at high enough concentrations within the various synthetically produced leachates, the effect of CDPs on radionuclide behavior can be represented by assuming alpha-D-isosaccharinic acid as the only dominant complexing ligand in all investigated systems. Furthermore, in contrast to their solubility results, xyloisosaccharinic acid was shown to have only a minor impact on the sorption of radionuclides onto NIREX Reference Vault Backfill (NRVB) material, haematite and kaolinite. Then again, alpha-D-isosaccharinate depicted in all cases a significant effect as it decreased the distribution ratios by a factor of 10^3 for Eu(III) and Th(IV) across the range of investigated conditions.

Owing to its stronger complexing properties (and its high abundance in CDPs), the alpha-D-isosaccharinic acid ($C_6H_{12}O_6$, hereafter denoted as HISA, or in the deprotonated form, alpha-D-isosaccharinate denoted as ISA) is of great relevance because of its potential capability for radionuclide mobilization [11, 57, 60, 61]. In a recent study [62], applying the kinetic model proposed by [10], the degree of cellulose degradation was estimated over time. The original model, based on a 12-year-long degradation experiment of 4 different cellulosic material under artificial cement porewater conditions was extrapolated to repository conditions and timescales (> 5000 years), using the reported reaction rate constants. Calculations show, that the cellulose content of Tela tissue and paper will be completely degraded (~99%) after 5000 years, whilst in the case of cotton, the simulation indicated a lower degradation rate, suggesting its virtual completion only after 25’000 years. Concentrations of alpha-D-isosaccharinic acid were also estimated [62], with and without considering the sorption of the ligand onto the available hydrated cement. In most of the relevant waste packages, the mass of produced HISA exceeds the amount that can be removed by the available hydrated cement, suggesting that sorption processes do not play a decisive role in controlling the concentrations

of the free ligand in solution. Upper limit calculations show that after 1000 years of cellulose degradation, in the pore and void volume inside the majority of the waste packages, the concentrations of alpha-D-isosaccharinic acid reaches the solubility limit of $Ca(ISA)_2(s)$ ($2 \cdot 10^{-2}$ M) during the degradation stage II of cement. Even considering further sorption processes of isosaccharinate in the different compartments/caissons, the dissolved concentrations are only reduced to a maximum of $1.2 \cdot 10^{-2}$ M (including both, alpha- and beta-forms). Further details on the behavior of ISA under cementitious environment are discussed in Section 1.3.2.

Taking into account its high affinity towards metal ions, together with its potential concentrations present, alpha-D-isosaccharinic acid is of fundamental importance to assess the long-term radionuclide release into the near field of a geological disposal facility for L-/ILW. Another important aspect is the presence of Ca^{2+} in cement porewater, which could give a rise to the possibility of enhanced radionuclide-ISA complex stability through the formation of Ca(II)-containing ternary (or quaternary) complexes [12].

In general, the stability of the metal ion-ISA complexes (*i.e.* the formation constants) is closely correlated to the effective charge (Z_{eff}) of the cation. Accordingly, the sequence An(IV) (Z_{eff} = +4) > An(VI) (Z_{eff} = +3.2) > An(III) (Z_{eff} = +3) > An(V) (Z_{eff} = +2.3) is expected for the complex formation constants of complexes between ISA and actinides of redox state +III to +VI. A detailed summary is provided in Section 1.3.3 on the main experimental studies available in the literature regarding complexation of ISA with actinides and lanthanides in the absence and presence of Ca(II) ions. Due to the expected predominance of Pu(IV) and Pu(III) in the experimental conditions investigated in this study, focus has been given to studies dealing with (Ca(II)–)An(IV)– and An(III)/Ln(III)–ISA systems.

1.3.1 Structure and complexation with calcium(II): the Ca(II)–OH–ISA system

Isosaccharinic acid (2-(hydroxymethyl)-3-Deoxy-D-pentoic acid) has 2 diastereomers: the *erythro*-form: alpha-D-isosaccharinic acid (2S,4S) (see Figure 3) and the *threo*-form: beta-D-isosaccharinic acid (2R,4S). As it belongs to the polyhydroxycarboxylic acids (like alpha-D-gluconic acid: HGLU), isosaccharinic acid has also a carboxyl group but only four aliphatic hydroxyl groups on the rest of the carbon-chain (HGLU has 5, see Figure 3 for details).

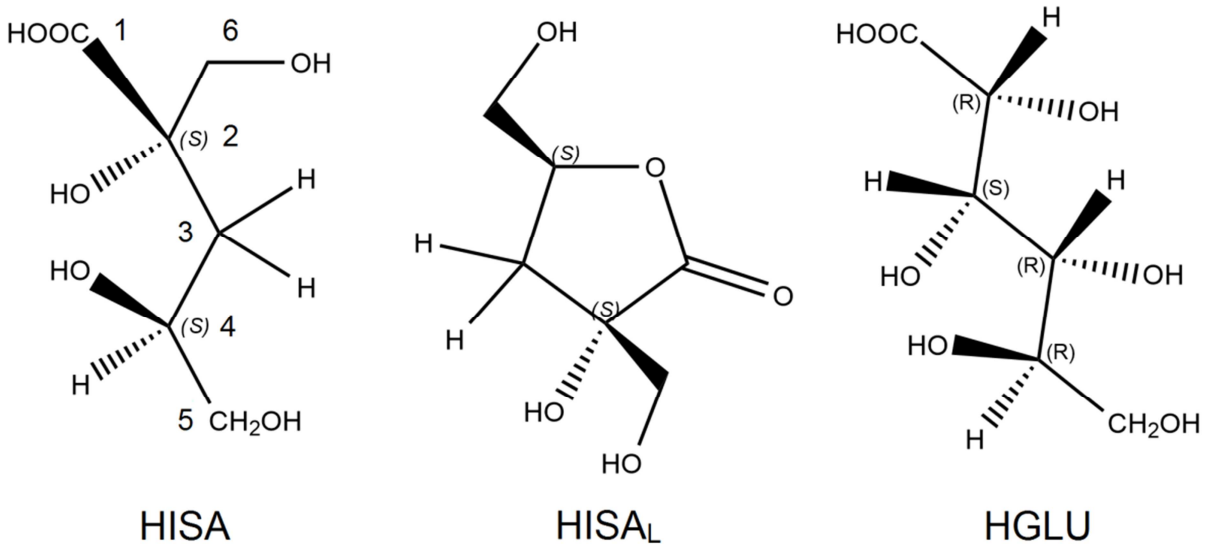

Figure 3. *Schematic structures (with the designation of carbon-atom numbers and related absolute configurations) of α-D-isosaccharinic acid (HISA), α-D-isosaccharinate-1,4-lactone ($HISA_L$) and α-D-gluconic acid (HGLU).*

Both HISA and HGLU could form complexes with metal ions, through the coordination of the deprotonated carboxyl group (in acidic solutions) or, in a bidentate mode, through both the carboxylate and the hydroxyl group(s), when the media is more alkaline and/or the metal ion has a sufficiently large positive charge. The main solution parameters which can exert an impact on the free concentration of the ligand in cementitious environment are the pH and the free Ca(II) ion concentration. As it was indicated before, the alpha-form of the isosaccharinic acid exhibits stronger complexing capabilities towards metal ions than the beta-form [57]. Hence, the acid-base properties and the complexation reactions with Ca(II) are only discussed for the alpha-form (HISA). The considered stability constants at the reference state are listed in Table 1.

In the absence of complexing metal ions, within the acidic pH-range, there are two types of reactions which affect the speciation of the free ligand itself: a, the lactonization reaction of the original acid (HISA), resulting in the α-D-isosaccharinate-1,4-lactone (denoted as $HISA_L$ on Figure 3) and b, the deprotonation reaction of the carboxylic group of HISA. The two processes are overlapping in the function of pH, making the pure protonation, as an intrinsic constant, hard to be determined individually. Hummel *et al.* pointed out [63], that the protonation constants, obtained by any methodology other than nuclear magnetic resonance spectroscopy (NMR) are composite values. These constants, due to the incorrect calculation of the mass balance of the ligand are always higher than the “real”, intrinsic values.

Considering the discrepancies within the reported values of the lactonization constant of HISA, the review of [63] selected an average, composite protonation constant for HISA with an enlarged uncertainty to cover the range of expectation (see Table 1). The equilibrium constant for the lactonization reaction of HISA was taken from a very recent reevaluation of the available constants, provided in [64]. As in the case of HGLU, under extremely alkaline conditions, further deprotonation(s) of the alcoholic hydroxyl group(s) is/are also possible. Based upon potentiometric titrations, an estimation for the second deprotonation constant (as a conditional value, listed in Table 1) was provided by [65]. The analogous value for GLU is considerably higher (approximately by one logarithmic unit), which can be traced back to the structural differences between the two ligands: due to the vicinity of another hydroxyl group (on the third C-atom, that is lacking in the case of ISA) the resulting alcoholate functional group is gaining further stability through H-bonding in the case of GLU. However, the deprotonation of alcohol groups in HISA and HGLU can also take place at lower pH values, in the process of complex formation with strong Lewis acids such as actinides [66, 67].

In view of the current study, it must be kept in mind that small variations of the listed values for the acid-base properties of HISA have no effect on the assessment of the ligand on any solubility data, conducted under alkaline (to hyperalkaline) pH conditions ($8 < pH_c < 13$), given that the existing aqueous species of the free ligand itself is the deprotonated form (ISA) alone.

The complex formation reactions between Ca(II) and ISA have been investigated through the solubility equilibrium of $Ca(ISA)_2(s)$ in several publications [68-74]. The comprehensive work of Hummel *et al.* [63] summarizes all the undertaken studies (except the most recent one [74]) and provides a reevaluation of the available experimental data [63]. The thermodynamic interpretation concluded by Hummel and co-workers, originally suggested by [70] can explain all the observed tendencies and the behavior of the system within the available experimental data sets. Consequently, the given model, presented by [63] is being favored for the Ca(II)-ISA-OH system (also applied in [12]) and it has been directly adapted in the course of data evaluation within the framework of the current study.

In summary, the Ca(II)-ISA-OH system in the pH-range from 1 to 13, can be described with the following chemical processes: 1. dissolution equilibria of $Ca(ISA)_2(s)$, 2. deprotonation and lactonization reactions of HISA (limited to the acidic pH-range), 3. the pH-independent ($6 < pH < 12$), weak complexation of Ca(II) with ISA (with 1 to 1 ratio), 4. formation of the $Ca(OH)^+$ species 5. formation of the deprotonated Ca(II)-ISA complex species with the formula of $Ca(ISA_{-H})^0(aq)$, present under higher alkalinity and furthermore: 5. the solubility

equilibrium of $Ca(OH)_2(s)$, expected to precipitate only in the hyperalkaline pH-range. The collection of thermodynamic constants (at the reference state), corresponding to the abovementioned equilibria are listed in Table 1. It is of interest that in more recent studies [64, 74], the equilibrium constants for the deprotonation, lactonization of ISA and the stability of its complexes with Ca(II) has been re-evaluated / re-measured and found to be in an excellent agreement with the recommended values provided in [63].

Table 1. *Adapted thermodynamic model for the Ca(II)-OH-ISA system.*

Equilibrium	***log K°(I →0; 298.15K)***	***Reference***
$HISA(aq) \leftrightarrow HISA_L(aq) + H_2O$	(0.49 ± 0.09)	[64]
$H^+ + ISA^- \leftrightarrow HISA(aq)$	(4.0 ± 0.5)	[63]
$H^+ + ISA_{-H}^- \leftrightarrow ISA^-$	14.31 (at I ~ 2 M)	[65]
$Ca^{2+} + 2\ ISA^- \leftrightarrow Ca(ISA)_2(s)$	(6.4 ± 0.2)	[63]
$Ca^{2+} + ISA^- \leftrightarrow Ca(ISA)^+$	(1.7 ± 0.3)	[63]
$Ca^{2+} + ISA^- \leftrightarrow Ca(ISA_{-H})^0(aq) + H^+$	–(10.4 ± 0.5)	[63]
$Ca^{2+} + OH^- \leftrightarrow Ca(OH)^+$	1.22	[75]
$Ca^{2+} + 2OH^- \leftrightarrow Ca(OH)_2(s)$	–5.19	[75]

1.3.2 The fate of ISA in cementitious environment: stability and Cement-ISA system

The key processes governing the effective, free concentration of ISA ($[ISA]_{free}$) in pore fluids in a cementitious environment are as follows: i, in-solution reactions (speciation-changes through deprotonation, complexation with metal ions, etc.), ii, degradation processes (chemical or microbial) and iii, heterogeneous equilibria (with hydrated cement phases: chemi- and/or physisorption of the ligand onto the available sorbing sites or precipitation of the ligand in the form of $Ca(ISA)_2(s)$).

Several studies have reported the chemical stability of Ca- and Na-salts of both α- and β-ISA up to 125°C [76, 77]. Two independent research groups identified the possible degradation of ISA in aqueous solutions under oxidizing conditions, also at low temperatures (25 °C) [78, 79].

Greenfield and co-workers investigated [78] the degradation of ISA saturated $Ca(OH)_2$ solutions flushed with O_2, N_2 or air at T = 25 and 80°C. After 10 months of equilibration time, only a small fraction of the ISA was degraded at T = 25°C in the systems purged with O_2 and air. In the same oxidizing conditions but at T = 80°C, the degradation occurred to a larger degree. Anaerobic conditions resulted in no significant loss of ISA from the systems, neither

at 25°C nor at 80°C. These results highlight the relevant role of oxygen in the process of ISA degradation.

In the comprehensive study by Glaus *et al.* [79], the key role of O_2 in the fast decomposition reaction of ISA in aqueous media was again underlined. In the absence of oxygen, minor loss of ISA was also detected by the conversion into smaller chain organic acids (glycolic, formic and lactic acid) in solutions with pH > 12. Through individual batch experiments, the transformations of 1 μmol of ISA per gram of solid $Ca(OH)_2(s)$ or OPC powder were observed in the heterogeneous systems under anaerobic conditions up to 542 days of equilibration time. The observed loss of ISA from the anaerobic experiments (at 28 and 90 °C as well) were not fully understood and attributed to a potential surface-related decomposition reaction, taking place independently of the applied solid phase. Nonetheless, when the total concentration of ligand exceeded the 1 μmol limit, ISA was shown to be apparently stable for even longer observations times.

No experimental studies on the degradation of ISA under reducing alkaline conditions are available in the literature. In contrast to the processes driving degradation of ISA under oxidizing conditions, the reducing conditions of interest in the present work may promote the reduction of the –COOH or –OH functional groups of ISA.

Another aspect for potential loss of ISA is its biological degradation in solution. Although the effect of microbial activities on the stability of ISA (especially under conditions expected in the near-field of a cementitious deep geological disposal facility) have been recently in the focus of related research-fields [80-83], discussions of these studies are out of the scope of the present work. Even so, it is worth mentioning that due to the high alkalinity of pore fluids, strong microbial degradation of ISA may not be expected under repository-relevant conditions, as in some specific cases above pH = 11, significant loss of biomass was witnessed from the system, indicating the instability of these microorganisms under hyperalkaline conditions [80]. Any degradation process of ISA under the anticipated boundary conditions and timeframe investigated within the present work (resulting in the loss of ISA from the system) has not been considered.

The uptake of ISA by hardened cement pastes under conditions related to the early stages of cement degradation was studied by a PSI research group [57, 84]. The average size-distribution fraction of 100 – 400 μm was used of the crushed and sieved cement (CEM I, 52.5 N HTS), which was then let in contact with filtered artificial cement porewater (ACW, with an equilibrium composition of 110.5 mM Na^+, 176 mM K^+, 1.75 mM Ca^{2+} and a pH of 13.3) under controlled N_2 atmosphere in the presence of ISA (with varying total

concentrations of the ligand: 10^{-5} M < $[ISA]_{tot}$ < 0.3 M). Solid-to-liquid ratios (S:L ratio) in the range of 25 to 500 gdm^{-3} were applied for the individual batch experiments (t_{eq} = 1 day – 9 months). The amount of ISA sorbed on the cement phases, $[ISA]_{sorbed}$ ($mol \cdot kg^{-1}$) was calculated using the initial concentration $[ISA]_{tot}$ (often referred to as $[ISA]_{in}$) (M) and the equilibrium concentration $[ISA]_{eq}$ (M) of the ligand (remaining in the liquid phase), by Equation (18).

$$[ISA]_{sorbed} = ([ISA]_{tot} - [ISA]_{eq}) \cdot V_L \cdot (\text{porewater, } dm^3) \cdot m(\text{cement, kg})^{-1}. \quad (18)$$

The maximum relative error was found to be ~20%, following the uncertainty of the detection of $[ISA]_{eq}$. An important feature of the sorption process was the evolution of ISA concentration in solution with equilibration time, in most cases the authors experienced a fast decrease in $[ISA]_{liq}$, usually reaching equilibrium within 1 day.

Van Loon *et al.* fit a two-site Langmuir isotherm to their experimental sorption data, expressed as in Equation (19) for ISA sorption onto hardened cement pastes (HCP):

$$[ISA]_{sorbed} = K_1 \cdot q_1 \cdot [ISA]_{eq} \cdot (1 + K_1 \cdot [ISA]_{eq})^{-1} + K_2 \cdot q_2 \cdot [ISA]_{eq} \cdot (1 + K_2 \cdot [ISA]_{eq})^{-1}, \quad (19)$$

where q_1 and q_2 represent the sorption capacities for the two hypothetical sorption sites available on the hydrated cement phases (in $mol \cdot kg^{-1}$) and K_1 and K_2 parameters are the related adsorption affinity constants (in $dm^3 \cdot mol^{-1}$). The optimized best-fit values of the parameters for the two sites were as follows:

$q_1 = (0.10 \pm 0.01)$ $mol \cdot kg^{-1}$, $K_1 = (1730 \pm 385)$ $dm^3 mol^{-1}$ and
$q_2 = (0.17 \pm 0.02)$ $mol \cdot kg^{-1}$, $K_2 = (12 \pm 4)$ $dm^3 mol^{-1}$. (20)

The total sorption capacity derived by the authors [57, 84] for the used cement with regard to ISA ($q_1 + q_2$) = 0.27 $molkg^{-1}$ was found to be in close agreement with the estimate of 0.32 $molkg^{-1}$, provided in the work of Bradbury and Sarott [85]. The Freundlich isotherm was not able to properly explain sorption data.

Despite the lack of an exact chemical explanation for the sorption reaction, Van Loon *et al.* proposed, based on the fast nature of the process, the existence of strong specific interactions between ISA and the surface sites (of the C-S-H phases). This specific interaction was then believed to be the reason why the ligand bearing with one negative charge can overcome the

electrostatic repulsion against the negatively charged surface, allowing it to sorb on the surface of the hydrated solid phase.

The latter argumentation was later debated by the work of Pointeau *et al.* [86, 87]. Prior to the investigations with ISA, the authors also assessed the evolution of the surface potential of hydrated cement pastes (CEM I and CEM-V) and the chemical composition of cement porewaters as a function of the cement degradation [88]. In the latter study, Pointeau *et al.* demonstrated through zeta potential (ζ) measurements in cement suspensions that two isoelectric points exist in the function of the HCP leaching process: 1. for pH 13.3 to pH 12.65 (fresh HCP states) zeta potential increases from −17 to +20 mV and decreases from 20 to −8 mV for pH 12.65 to 11 (degraded HCP states). Applying the diffuse double-layer theory (DLM) with surface complexation model (SCM) [89] for the present C-S-H phases, the authors developed a model, providing a good prediction of the surface potential evolution for both HCP. According to their model, the surface charge is controlled by the deprotonation of surface silanol- and silanidol-groups (>SO−) and by the surface complexation of calcium (>SOCa+), causing a positive charge-balance. On the other hand, the calcium concentration was controlled by portlandite or calcium silicate hydrate (C-S-H) solubility equilibria.

Under similar experimental conditions but at different S:L ratios using the CEM-I type hydrated cement paste suspensions, sorption studies were also performed by Pointeau *et al.* in the presence of various anionic ($^{36}Cl^-$, $^{125}I^-$, $^{14}CO_3^{2-}$, $^{75}SeO_3^{2-}$) radionuclides and organic ligands (ISA and EDTA) [86, 87]. The cement phases were equilibrated with porewater leachates corresponding to 12 different states (pH conditions ranged from 11.5 to 13.3) of the cement degradation process.

Concerning the experiments with organic ligands, the authors concluded that the sorption process of ISA (and EDTA) was fast, usually reaching equilibrium within 3 days. The behavior of the ISA uptake was found to be correlated to the evolution of Ca(II) concentration in solution (and to the zeta potential as well): increased sorption was determined with decreasing pH from 13.2 to 12.5 (R_d = 4 to 100 cm^3g^{-1}, respectively), following the degradation stages of the cement system, then the R_d values suffered gradual decrease (till R_d = 25 cm^3g^{-1}) by the further decrease of pH condition till 11.8 in the pore fluids.

Based on the fast nature of the process, Pointeau *et al.* modelled the sorption of ISA onto HCP as an adsorption reaction applying the DLM with SCM [89] theories together with the surface equilibria previously proposed for the chemical modeling of the C-S-H phases. Speciation calculations for ISA in solution were performed by applying the corresponding data set for the system Ca(II)-ISA-OH summarized in the work of Hummel *et al.* [63].

The representation of the experimentally determined R_d values were found to be probable only with the assumption of the mixed surface complexation equilibria, where Equation (22) depicts the best fit values of the formation constant corresponding to the chemical reaction (21).

$$>SiOH + Ca^{2+} + ISA^{-} \leftrightarrow >SiOCaISA + H^{+} \quad (21)$$

$$\log K° = -7.5 \quad (22)$$

In this respect, uptake of ISA by HCP was interpreted as a mixed surface complexation reaction rather than being a selective chemisorption process via specific sorption sites as originally reported by the PSI team.

It has to be emphasized, that the R_d values corresponding to ISA sorption onto HCP taken from the work of Pointeau *et al.* [87] are highly differing from those which can be calculated using the Langmuir isotherm reported by the PSI team [57, 84]. Applying identical experimental conditions as in the study of Pointeau *et al.* [87], where at pH = 13.2 R_d = ~4 $cm^3 \cdot g^{-1}$ was predicted for $[ISA]_{tot} = 8.5\ 10^{-3}$ M at relatively low applied S:L ratio (unreported, but presumably 1 gdm^{-3} as in their previous work), the two-site model of the Langmuir isotherm (obtained at pH = 13.3) results in the significantly higher value of R_d = ~66 $cm^3 \cdot g^{-1}$. Experimental details, such as for instance: differences in the characteristics of the cement phases applied between the two studies (specific surface areas were not reported) or differences in the investigated experimental conditions could explain this large discrepancy. In the work of Pointeau *et al.* a relatively small S:L ratio (1 $g \cdot dm^{-3}$) was applied for all investigations, whilst the investigations by the PSI team were carried out at larger S:L ratios (25 to 500 $g \cdot dm^{-3}$). Consequently, the applicability of the two-site Langmuir isotherm for different conditions can be criticized, although the predictions within the investigated parameter-range are in excellent agreement with the experimental data points collected. On the other hand side, the comprehensive surface complexation model provided by Pointeau *et al.* is based on multiple parameters obtained partly from previous experimental studies (ζ, $[Ca]_{tot}$ *vs.* pH) and some are extracted from averaged structural properties of C-S-H phases or simply just assumed. Though the latter given model provides a proper explanation for the chemical behavior and tendency for ISA uptake by HCP with regard to the evolution of pH (and $[Ca]_{tot}$) in the leached porewater fluids, it is inapplicable under significantly differing experimental conditions than those of the original study.

The conclusion drawn from the discussions above is that the only relevant process, capable of reducing the free concentration of ISA in cement porewater solutions is the potential sorption of the ligand on hydrated cement phases (if the total concentration of the ligand is below its solubility limits). In this aspect, for a specific sorption study involving the use of ISA and a metal ion (M), it appears to be necessary to assess the free ligand concentration in solution as an addition to the study targeting the ternary system cement–M–ISA.

1.3.3 Review of previous experimental studies on the complexation behavior of ISA with tri- and tetravalent actinides

This section summarizes the main experimental studies available in the literature on the complexation of ISA with actinides and lanthanides. For all these systems, the NEA-TDB review on the complexes of U, Np, Pu, Am, Tc, Se, Ni and Zr with selected organic ligands [63] is taken as the most authoritative reference.

One of the open questions affecting the complexation of ISA with actinides (and with metal cations in general) is the possible role of the alcohol groups of ISA on the chelation of the metal cation. Although the pK_a of the α–OH group of ISA has been estimated [65] to be ≈ 14.3 (see Table 1 in Section 1.3.1), the enhanced acidity of this alcohol group caused by the complexation with a metal cation is expected to result in the deprotonation of the α– (and even β–) alcohol group under significantly less alkaline conditions. Hence, the protons released in the complex formation under alkaline conditions can be assigned to both hydrolysis of the metal cation and deprotonation of alcoholic groups:

$$M^{n+} + x\ H_2O(l) + ISA^- \Leftrightarrow M(OH)_xISA^{n-x} + x\ H^+ \quad (23)$$

$$M^{n+} + y\ H_2O(l) + ISA^- \Leftrightarrow M(OH)_y(ISA_{-zH})^{n-z-y} + (y + z)\ H^+ \quad (24)$$

where $x = (y + z)$ and $ISA_{-zH}^{-(1+z)}$ corresponds to an ISA ligand with the deprotonated carboxylic and with z as the number of alcohol groups. The choice of one or the other complexation mode has no implications in the mass-action laws and, therefore they do not affect the calculated equilibrium constants either. For the sake of simplicity and consistency with previous studies and reviews [12, 90], the first option (H^+ released assigned to hydrolysis of metal cation) is initially favored in the course of the present work (if no further knowledge available). This must not be taken as an indication of the correct stoichiometries of prevailing chemical processes.

1.3.3.1 Pu(IV)–ISA

The number of studies directly assessing the interaction between Pu(IV) and ISA under alkaline conditions is limited [78, 91-93]. These studies were conducted in the framework of the NIREX Safety Assessment Research Programme (NSARP). The derived models are mostly based on solubility experiments, conducted from oversaturation state in the presence of ISA, except in [92], where the reduction effect of ISA on the sorption of Pu(IV) was determined on a specific, NIREX Reference Vault Backfill (NRVB) material.

Solubility experiments were performed under nitrogen atmosphere in the absence of a redox controlling reductant at I = 0.01 M (NaCl). The starting Pu solid phases were freshly precipitated from a Pu(IV) stock solution in the form of $Pu(OH)_4$(am) and were directly added to ISA-containing matrix solutions with pH_c = 12 – 12.5. Redox potentials were not measured experimentally, and the E_h values were only assumed to be in the range of 0 to +100 mV, due to the applied inert atmosphere. As it was pointed out by Neck *et al.* [5, 6] even under a well-controlled inert Ar-atmosphere, traces of oxygen can be scavenged by the $Pu(IV)O_2$(am,hyd) solid phase, resulting in the mixed valent PuO_{2+x}(s,hyd) phase, that may be simultaneously in equilibrium with Pu(IV)(aq) and Pu(V)(aq), given the kinetically hindered redox reaction between Pu^{4+} and PuO_2^+. Due to these experimental shortcomings and the lack of solid phase characterization throughout the reported studies, the redox state of Pu in the precipitated solid phases and in the aqueous phases remains unclear. Furthermore, since no information on the applied phase separation method is given within the studies, the presence of polynuclear Pu(IV)-bearing colloids cannot be ruled out. A reevaluation of the data conducted in [12] showed that the observed Pu total concentrations are clearly falling in the concentration range of Pu(IV) colloidal species as reported by [5], indicating the presence of a $Pu(OH)_4$(col,hyd) solid phase with a comparatively high solubility. According to these observations, solubility data at pH_c = 12 reported in [91] and [78] were then recalculated, proposing the formation of $Pu(OH)_4(ISA)^-$ and $Pu(OH)_4(ISA)_2^{-2}$ complex species in the range of 10^{-6} to 10^{-2} M ISA total concentrations at pH_c = 12. The derived $\log^*\beta°$ values are also shown in Table 2 (extrapolated to infinite dilution, by using SIT formula), along with the other formation constants of further to-be-discussed complex species. The large uncertainty (± 1.6) assigned in [12] accounts for these experimental shortcomings. The stoichiometry of the species, however remains undefined as the speciation model originally proposed by the authors was not supported by other type of experiments (*e.g.* series of solubility experiments with Pu in the function of pH_c at a constant ISA total concentration).

Sorption experiments of Pu(IV) onto NRVB material were carried out by [92] under N_2 atmosphere and hyperalkaline conditions, in the presence of 0.01 M ISA. Assessment of the redox state of Pu is again missing from the study and furthermore, the individual sorption of the ligand onto the used material was also neglected. Using the derived speciation model from the solubility data and the corresponding formation constants of the Pu(IV)–ISA–OH system, the reproduction of the observed sorption reduction factor was achieved in [12]. The good agreement between the calculated and the experimentally determined values of the defined constant served as an additional confirmation on the speciation and the stability constants of Pu(IV)-ISA species, resulting from the reevaluation procedure.

1.3.3.2 Np(IV)–ISA

Rai and co-workers published the only available experimental work on the Np(IV)-ISA system [72, 94, 95]. The basis of the derived comprehensive chemical model were series of independent undersaturation solubility experiments with NpO_2(am) in the presence of ISA at different ionic strengths, conducted either at a constant pH_c (approximately 5 and 12) with the variation of the ISA total concentration (10^{-4} – 0.1 M) or at a fixed ISA total concentration (0.0016 and 0.008 M) with different pH_c (~2 – 14). Reducing conditions were attained using $Na_2S_2O_4$ (0.01 M) as buffering chemical. The oxidation state of Np in solution was also monitored for all the samples using a liquid-liquid extraction method, involving thenoyltrifluoroacetone (TTA) under acidic conditions. The reducing conditions maintained by the presence of sodium-dithionate were confirmed by the detected Np(IV) content, representing the 70 to 98 percentage of the total Np in solution. As a consequence, regardless of the lack of solid phase characterization methods, the predominance of Np(IV) redox state both in aqueous and solid phase is most probably a valid case. Uncertainty of the data can also originate to a certain extent from the preparation method of the NaISA stock solution, used for the solubility batch experiments. The initially dissolved $Ca(ISA)_2$(s) was claimed to be dissolved quantitatively via addition of 2 M NaOH solution and the gained $Ca(OH)_2$(s) was then removed by centrifugation. The supernatant, containing NaISA, together with the portion of unreacted NaOH in solution was used for the subsequent preparations. In this context, considering the solubility of $Ca(OH)_2$(s) in concentrated NaOH solutions, ranging from 0.7 to 0.5 mM in 1.0 M and 2.0 M NaOH solutions [96], the remaining quantity of $Ca(OH)^+$ together with $Ca(ISA)^+$ and $Ca(ISA_{-H})^0$ complex species in the separated supernatant may have resulted in non-negligible concentrations of available Ca (especially with increasing ISA

total content) throughout the conducted experiments. In this respect, depending upon the original $Ca(ISA)_2(s)$ to added NaOH quantity ratio, the yielding total Ca(II) to ISA concentration could vary significantly, which can eventually lead to the formation of possible ternary species involving Np^{4+}, ISA and Ca^{2+}, providing additional enhancement to the solubility of $NpO_2(am)$. Given, that no data were reported on the Ca(II)-content of the used NaISA stock solution of interest, the total concentrations of Ca(II) are unquantifiable in the corresponding study [72]. According to a former data in [94], the author detected less than 0.002 M Ca(II)-content in the prepared 0.05 M NaISA stock solution, which gives a hint towards the possible presence of relevant Ca(II) concentrations in the majority of the batch solubility experiments.

Applying the Pitzer model to account for the ionic strength corrections, Rai and co-workers conducted a comprehensive fitting of all the gained solubility data. The thermodynamic model suggested the presence of 4 Np(IV)-ISA complex species, dominating under different boundary conditions:

- Under acidic conditions: $Np(OH)_3(ISA)^0(aq)$ and $Np(OH)_3(ISA)_2^-$
- Under alkaline conditions: $Np(OH)_4(ISA)^-$ and $Np(OH)_4(ISA)_2^{2-}$

At higher ISA concentrations ($\geq$ 0.10 M) the complex species with Np(IV):ISA ratio of 1:2 prevail. Despite of the systematic relevant differences between the calculated and the experimentally measured solubility values of Np at the majority of applied ionic strengths, the proposed model describes the observed tendencies in the data and provides an overall good prediction of the influence of ISA in a wide range of total ISA concentrations and pH_c conditions on $NpO_2(am)$ solubility. Stability constants, originally provided by Rai *et al.* for the complex species, forming under alkaline conditions were recalculated (and extrapolated to infinite dilution, using SIT formalism) by Gaona and co-workers [12] (see table 2), applying the updated thermodynamic database of NEA-TDB for Np(IV) aqueous species and solid compounds [9].

1.3.3.3 U(IV)–ISA

The influence of ISA on the solubility of $UO_2.2H_2O$ has only been investigated in two studies [92, 97]. Relevant experimental shortcomings were identified in [92] by [12] such as the lack

of solid phase characterization and the absence of redox controlling agents, therefore the aforementioned work was disregarded from the reevaluation process.

The undersaturation solubility experiments with $UO_2 \cdot 2H_2O$(am), reported in [97] were performed in the presence of Fe powder and $Na_2S_2O_4$ as redox-buffering agents at different pH_c values from acidic (3.25 and 6.21) to alkaline conditions (13.5) with the variation of the total concentration of ISA and GLU (either at 0.04 M or 0.06M). The author concluded that the dominating species in the conditions of the experiment was $U(OH)_4ISA^-$ (or rather $U(ISA_{-4H})^-$). Considering the mathematically questionable interpretation of the data and the lack of solubility enhancement of ISA at pH_c = 3.51, along with a wrong chemical model (the deprotonation and the lactonization reaction of ISA was not included and inconsistent speciation scheme for U(IV) was used), the derived stability constants are not reliable. Gaona and co-workers however undertook a reevaluation of the experimental data of Warwick *et al.*, by assuming the analogy with other An(IV)ISA systems the author proposed the formation of the $U(OH)_4(ISA)^-$ and $U(OH)_4(ISA)_2^{2-}$ complex species. On one hand, the stability constant of the $U(OH)_4(ISA)^-$ species was estimated via Linear Free-Energy Relationships with other tetravalent actinides and on the other, the stability constant of the $U(OH)_4(ISA)_2^{2-}$ complex species was calculated upon a single experimental point. Both constants (listed in table 2) were extrapolated to zero ionic strength via the SIT formula. Provided, that the speciation scheme of U^{4+} in the presence of ISA is ill-defined and the reevaluation by [12] is based on a pure hypothesis, the information on the U(IV)-ISA system is insatisfactory.

1.3.3.4 Th(IV)–ISA

The available thermodynamic data on the Th(IV)-ISA binary system are either originating from solubility [59, 92, 95, 98], sorption [71, 99, 100] or liquid-liquid extraction studies [101, 102].

The extensive solubility study, performed by Rai and co-workers was aimed to assess the influence of ISA on the solubility of $Th(OH)_4$(am) solid phase with series of independent undersaturation solubility batch experiments. Within the different series, conditions were set either to a constant pH_c (~6 or 12), while the total ISA concentration was varied ($2 \cdot 10^{-4}$ – 0.2 M) or at fixed $[ISA]_{tot}$ (0.008 or 0.08 M) the pH_c was ranging from ~4.5 to 12 (at I = 0.1 M, $NaClO_4$). In case of systems with higher ISA total concentrations (0.08 M) steady state $[Th(IV)]_{tot}$ concentrations were reached already within 15 days, whereas in the experiment set

at low ISA concentration (0.008 M), where the pH_c condition was varied equilibrium was only reached within 55 days.

In order to develop a reliable model for Th(IV)-ISA complexes, several combinations of monomeric, multi-ligand and mixed-hydroxo-ISA species were used by Rai and co-workers to represent their experimental data. The initial set of species and corresponding stability constants were determined through the thermodynamic analyses of the series of ThO_2(am,hyd) solubility data at fixed ISA total concentrations in the function of pH_c. In a later step, the model was tested to predict the experimental Th(IV) solubility data as the function of ISA total concentrations under constant pH_c conditions. The speciation scheme, that provided the best fit for the entire data set included the complex species: $Th(OH)ISA^{2+}$, $Th(OH)_3(ISA)_2^{2-}$ and $Th(OH)_4(ISA)_2^{2-}$ with the stability constants (at reference state), listed in Table 2 (only for the species forming under alkaline conditions: $Th(OH)_3(ISA)_2^{2-}$ and $Th(OH)_4(ISA)_2^{2-}$). For ionic strength corrections, Rai *et al.* used the SIT model with certain estimates of ion interaction parameters for the newly formed species. Independent solubility data for the Th(IV)-ISA system, provided by [92], gained under similar conditions but only with the variation of the total ISA concentration ($2 \cdot 10^{-4}$ – 0.2 M) at pH_c = 12 were also in close agreement with the experimental results of [98].

In the formerly discussed comprehensive study of [59], oversaturation solubility experiments with ThO_2(am) in the presence of various synthetically produced CDPs (and $Ca(OH)_2$(s)) under alkaline conditions were performed. Despite the extensive work involving ISA, the authors did not assess the higher obtained Th solubility of the freshly precipitated solid phase and furthermore the questionable interpretation of the results, using an internally determined solubility product for ThO_2(am) led to the systematic overestimation of the stability of the suggested Th(IV)-ISA species. Regardless of the experimental shortcomings and the problems with the interpretation of the solubility data, the study verified the predominance of the previously reported complex, $Th(OH)_4(ISA)_2^{2-}$, at pH_c = 9 and 12 as well in a wide range of applied total ISA concentrations, underlining the model proposed by [98].

Liquid-liquid extraction studies by [101, 102], reported the formation of three Th(IV)-ISA complexes ($Th(ISA)_n^{4-n}$, with n = 1, 2 and 3), using 0.025 M acetylacetone in toluene as an extracting agent from equilibrated solutions (with < $5 \cdot 10^{-5}$ M total ^{234}Th(IV) concentrations) at pH_c = 8.3 and I = 1.0 M ($NaClO_4$) and at three different temperatures (15 °C, 25 °C, 35°C). Considering the applied alkaline pH_c conditions, achieved via the slow titrations of the ISA-free solutions with 1.0 M NaOH solution and the relatively high initial total concentrations of Th(IV), the formation of $Th(OH)_4$(am) as a colloidal precipitate can be reasonable in many of

the performed experiments. Nonetheless, the authors did not document any experimental effort to account for the formation of such species throughout their investigations. As it was pointed out by [98], the most serious limitation of the study is the data interpretation itself. The authors evaluated their results, assuming the formation of $Th(ISA)_n^{4-n}$ species, by neglecting the hydrolysis of Th(IV), which then led to the large overestimations of the corresponding stability constants. As a consequence, the representation of the solubility data of ThO_2(am,hyd) in the function of $[ISA]_{tot}$ or pH_c with the model proposed by [101, 102] results in large deviations by several orders of magnitude from the data, presented in [98] or [92]. The reevaluation of the liquid-liquid extraction data, carried out by [98], through the calculations of the distribution factors for Th(IV) showed, that the proposed speciation model, along with the determined stability constants not only describes their data, but it also provides an equally good representation of the extraction results within the given uncertainties.

Vercammen and co-workers [71, 99, 100] investigated the sorption of the Th(IV) onto different materials (feldspar, polyallomer, BioRad resin) in the presence of ISA (10^{-8} – 10^{-2} M), at pH_c = 10.7 – 13.3 (at I = 0.3 M). (Similar experiments in the presence of Ca were also conducted within the abovementioned studies, those are discussed separately in Section 1.3.4.2.2.) The authors, based on the slope analyses of their sorption data ($logR_d$ *vs.* $log[ISA]_{tot}$), proposed the formation of only one complex in their experiments with the formula $Th(OH)_4(ISA)^-$. Due to the lack of data at $[ISA]_{tot} > 10^{-3}$ M, formation of higher ISA complexes cannot be confirmed. Gaona *et al.* pointed out, that the thermodynamic model, published by Vercammen and co-workers [100], gives a systematic overestimation on the effect of ISA on $Th(OH)_4$(am) solubility at pH_c = 12 [12]. An unequivocal explanation for the observed inconsistency could not be assigned. However, with regard to the relatively low applied total concentrations of Th(IV) (in the range of $1.2 – 1.6 \cdot 10^{-13}$ M) and the possibility of the inefficient separation of the solid-liquid phases, together with the allowed rapid equilibration times (3 days), sorption data can be affected by relevant uncertainties. Further discussion and comparison of the findings, obtained by solubility and sorption studies on the Th(IV)-ISA system is out of the scope of the current work.

1.3.3.5 Ca(II)–Th(IV)–ISA

The available thermodynamic data on An(IV)-ISA-Ca(II) ternary systems are limited to the case of Th(IV) and are based mostly on sorption experiments [100, 103-105], whilst only a single work [59] reported solubility results on the system.

Vercammen and co-workers [100] investigated the sorption of ^{234}Th(IV) onto different materials (feldspar, polyallomer, BioRad) in the presence of ISA (10^{-8} – 10^{-2} M) and Ca(II) ions ($7\cdot10^{-4}$ – $1.8\cdot10^{-3}$ M) in the pH-range of 10.7 – 13.3 (at I = 0.3 M, $NaClO_4$). The authors reported the formation of the notably stable quaternary complex $CaTh(OH)_4(ISA)_2(aq)$. The equilibrium constant determined in their study [100] was later re-calculated in [12] consistently with a more recent thermodynamic data for Th(IV) hydrolysis equilibria reported in the work of Altmaier and co-workers [106].

Tits, Wieland and co-workers [103, 105] investigated the sorption of ^{228}Th(IV) onto calcite and hardened cement paste in the presence of ISA and α-D-gluconate (GLU). Experiments were conducted with artificial cement porewater (pH = 13.3; $[Ca]_{tot}$ ~$1.6\cdot10^{-3}$ M). Special care was taken to avoid the formation of colloidal species, and the possible sorption of ISA/GLU onto the solid phases was thoroughly evaluated. Due to constant pH and $[Ca]_{tot}$ used in their experiments, the authors could not evaluate the stoichiometry of the Th(IV)–ISA complex forming, but assumed the predominance of the complex $CaTh(OH)_4(ISA)_2(aq)$ as previously proposed by Vercammen *et al.* [100]. (As a sidenote: Tits, Wieland and co-workers proposed the formation of an analogous, quaternary complex with GLU.) One of the main inconsistencies with the model reported [105] on the Ca(II)-Th(IV)-OH-ISA system is in connection with the comparison of the prevailing species in solution with the initial assumptions and the experimental parameters applied. Under the conditions investigated (pH = 13.3, 10^{-6} M < $[ISA]_{tot}$ < 10^{-3} and $[Ca]_{tot} = 1.6\cdot10^{-3}$ M), the authors evaluated their Th(IV) sorption data by disregarding the formation of the $Th(IV)(OH)_4ISA^-$ species previously reported by Vercammen *et al.* [100]. Using the combination of the thermodynamic constants (based on all the sorption studies performed by the PSI team) the dominating species under the conditions of interest is predicted to be indeed, the Th(IV)-OH-ISA species. In this context, the thermodynamic model and data reported by Tits *et al.* [105] are affected by relevant uncertainties.

Randall and co-workers [59] performed solubility experiments with $ThO_2(am)$ in the presence of ISA and porewater at pH ≈ 9 and 12 previously equilibrated with $Ca(OH)_2(s)$. Unfortunately, the authors did not report $[Ca]_{tot}$ after the corresponding equilibration with $Ca(OH)_2(s)$, and thus this parameter remains ill-defined in the evaluation of their results. Slope analysis of their solubility data indicated the formation of a complex with Th(IV):ISA ratio of 1:2. The calculation of the solubility of $ThO_2(am)$ using the equilibrium constant reported in the work of Vercammen *et al.* [100] for the complex $CaTh(OH)_4(ISA)_2(aq)$ resulted in a large overestimation of the experimental observations. It is also unclear which

Ca(II) total concentrations were used in the given study for such calculations [59]. In a similar context but using GLU instead of ISA, Colàs [107] reported a similar impact of GLU in the solubility of Th(IV) in the absence and presence of Ca(II), thus challenging the detection of quaternary Ca(II)–Th(IV)–GLU complexes previously reported in the study of Tits and co-workers [105]. For the stability constant of the Ca(II)–Th(IV)–GLU species, Colàs [107] derived an upper limit value which is in good agreement with independently determined value of Tits *et al.* [105], as later recalculated by Gaona *et al.* [12]. However, analogous investigations with ISA are missing from the work of Colàs *et al.*

The possible formation of quaternary complexes Ca(II)–An(IV)–ISA has relevant implications in the context of L/ILW disposal, where large amounts of ISA (through cellulose degradation) and Ca(II) (through cement materials) are expected. Thermodynamic calculations using data on the quaternary complex $CaTh(OH)_4(ISA)_2(aq)$ reported by Vercammen and/or Tits, Wieland and co-workers [100, 103-105] result in a significant enhancement of the solubility of Th(IV) in cementitious environments. The possible formation of analogous complexes with other An(IV) is thus expected to have important implications in the source term of key radionuclides such as Pu. However, the sparse experimental data available, and the controversial results reported by different studies, represent a call to cautiousness. Further experimental studies are needed before making any definitive claim on the relevance of such, analogous quaternary complexes involving other tetravalent actinide ions.

1.3.3.6 Ca(II)–An(III)/Ln(III)–ISA systems

The interaction of trivalent actinides and lanthanides with ISA was investigated in a number of experimental studies [57, 59, 100, 103, 105, 108].

Analogously to the studies with Th(IV), the PSI team performed sorption experiments with different solid materials (feldspar, polyallomer, BioRad resins and calcite) to evaluate the interaction of ISA with $^{152}Eu(III)$ and $^{241}Am(III)$ under alkaline to hyperalkaline pH conditions, both in the absence and presence of Ca [57, 100, 103, 105]. Although the chemical model for Eu(III) under alkaline conditions and absence of ISA was different in [57],[100] (predominance of $Eu(OH)_4^-$) and in [105] (predominance of $Eu(OH)_3(aq)$), experimental sorption data for Eu(III) in all these studies were in moderate agreement and indicated the predominance in solution of the complex $Eu(OH)_3ISA^-$. Tits and co-workers conducted analogous sorption experiments with Am(III). Experiments were only conducted at pH = 13.3, and thus the authors assumed the formation of a complex with the same stoichiometry as

for Eu(III), $Am(OH)_3ISA^-$. Due to the poorer statistics of the results compared to those with Eu(III), the reported equilibrium constants was considered to be only a first estimate. Equilibrium constants reported in [105] for the formation of the complexes $Eu(OH)_3ISA^-$ and $Am(OH)_3ISA^-$ are summarized in Table 2.

The possible formation of ternary Ca(II)–An(III)/Ln(III)–ISA complexes under alkaline to hyperalkaline pH conditions ($10.7 \leq pH \leq 13.3$) was also evaluated in [100] and [105] considering $1.8 \cdot 10^{-3}$ M $\leq$ [Ca] $\leq 1.0 \cdot 10^{-2}$ M. Within these boundary conditions, the authors found no experimental evidence on the participation of Ca(II) in the complex formation of ISA with Eu(III) or Am(III).

Zhernosekov and co-workers determined the step-wise equilibrium constants for the formation of $Tb(III)(L)_x$ complexes at pH = 7.0 (L = glycolate, GLU or ISA) using an electromigration technique [108]. Experiments were performed in 0.10 M $NaClO_4$ with $1.0 \cdot 10^{-6}$ M $\leq$ [ISA] $\leq 1.0 \cdot 10^{-2}$ M. The authors (correctly) assumed that unhydrolyzed Tb^{3+} prevailed at this pH, and proposed the formation of the complexes $TbISA^{2+}$, $Tb(ISA)_2^+$ and $Tb(ISA)_3(aq)$ based on the fit of the measured ion mobility. Only three experimental points were collected within 10^{-3} M $\leq$ [ISA] $\leq 10^{-2}$ M, although the thermodynamic model derived indicates the predominance of Tb(III)–ISA complexes stricktly above [ISA] = 10^{-3} M. This suggests a strong overparametrization of the fit by [108], and thus the reported thermodynamic model is disregarded in this work.

Randall and co-workers conducted oversaturation solubility experiments with Eu(III) under alkaline to hyperalkaline pH conditions in the presence of ISA and Ca(II) [59]. Preliminary solubility experiments at pH = 12 in the absence of ISA resulted in log [Eu(III)] between –4.5 and –7, clearly indicating the predominance of colloidal Eu(III). The tendency of Ln(III) to form colloids when approaching solubility from oversaturation conditions is well-known. Addition of ISA (10^{-4}–10^{-2} M) to the system resulted in a slight increase of the solubility at the highest ISA concentration. However, because of the large dispersion of the acquired data (both in absence and presence of ISA) and the expected predominance of Eu(III) colloidal species in solution, any quantitative interpretation of this study is disregarded in the present work.

Table 2. *Speciation scheme and corresponding equilibrium constants, according to Equation (23), reported by various authors for Ln(III)/An(III)/An(IV)-ISA complexes, forming under alkaline conditions (see text for more details).*

Species	***log*β° (I → 0, 298.15K)***					
	Pu(IV)	***Np(IV)***	***U(IV)***	***Th(IV)***	***Eu(III)***	***Am(III)***
$M(OH)_3(ISA)^-$					$-(20.9 \pm 0.2)^{i,}$	$-(21.4 \pm 1.0)^{i,}$
$M(OH)_4(ISA)^-$	$-(3.8 \pm 1.6)^{a,b,}$	$(4.06 \pm 0.62)^{a,c,}$	$-(6.8 \pm 0.9)^{a,d,}$	$-13.20^{e,}$ $-(11.5 \pm 1.5)^{a,f,}$		
$M(OH)_4(ISA)_2^{2-}$	$(0.4 \pm 1.1)^{a,b,}$	$-(2.20 \pm 0.62)^{a,c,}$	$-(4.9 \pm 1.0)^{a,d,}$	$-10.40^{e,}$ $-(11.2 \pm 1.5)^{a,g,}$		
$CaM(OH)_4(ISA)_2(aq)$				$-(4.0 \pm 0.4)^{a,f,h,i,}$		

a, revaluated in [12]; b, [78, 91]; c, [72]; d, [97]; e, [107]; f, [100]; g, [95]; h, [103]; i, [105]

1.3.4 Literature overview of experimental studies on cement-An(IV)(-ISA) systems

This section is intended to give an overview of available literature data on the system cement-Pu(IV)(-ISA) system. A special emphasis is given to the experimental details of the discussed studies in order to gain useful insights in the development of the experimental program in this PhD thesis.

Data available on the binary system cement-An(IV) are shortly discussed in Section 1.3.4.1, including recommended distribution ratios. Concerning the ternary system, the so far available literature work is found to be scarce, except for the case of Th(IV). The only study reported on the cement-Pu(IV)-ISA system is separately discussed in Section 1.3.4.2.1. More attention was dedicated to discuss the sorption reduction effect of ISA on Th(IV) uptake by hydrated cement phases. The available literature data on the system are summarized in Section 1.3.4.2.2.

1.3.4.1 Cement–An(IV) system

Tetravalent actinides are in general strongly sorbed by hydrated cement phases. The most important interacting cementitious solid phase, responsible for the uptake of An(IV) is the amorphous C-S-H phase [13, 50, 109]. Quantitatively, the sorption process is expressed, through the detection of the loss of radionuclide from the solution in terms of (solid-to-liquid) distribution ratios (R_d in dm^3kg^{-1} or in m^3kg^{-1}), as in Equation (25). R_d values depict the partitioning of the nuclide between the cement porewater and the cementitious material:

$$R_d = [An(IV)]_{sorb} / [An(IV)]_{eq} \quad , \qquad (25)$$

where the $[An(IV)]_{sorb}$ is the molar amount of the sorbed actinide ion per unit mass of cement and $[An(IV)]_{eq}$ is the equilibrium concentration of An(IV) in the porewater in molar units. Although the majority of the published sorption studies on cement-An(IV) systems do not report any specific information on the mechanism of the process, the fast kinetics together with the reversibility of the sorption reaction (as it is suggested for Th(IV) [110]) could be potential indications for the control by surface equilibria.

In the context of cement-An(IV) sorption studies, the following equilibria have influence on the experimentally measured R_d values:

1. Precipitation processes (precipitation or surface precipitation as a separate, pure solid phase and co-precipitation with other metal ions)
2. Solid-solution formation (lattice incorporation or diffusion into a present solid phase)
3. Adsorption onto available surfaces (physisorption, chemisorption)

If precipitation and solid-solution formation can be excluded via experimental findings, distribution ratio is equal to the distribution coefficient, K_d, which in this case represents purely the adsorption equilibrium between the solid and liquid phases in the system. The evolution of the sorption process is also proven to be relevant to the net effect of the hydrated cement phases, since subsequent to a fast adsorption process onto the surface sites, partly through solid phase re-crystallization processes, metal cations can also be taken up into the structure of the C-S-H phases. Recent studies revealed clear evidences for the uptake of trivalent (Eu^{3+}) [111] and tetravalent (Np^{4+}) [112] actinides by structural incorporation into the C-S-H phases.

The uptake of plutonium by HCP is influenced by the degradation stage of the cement (and the chemical conditions prevailing within the porewater) and also by the oxidation state/s of Pu. Under the boundary conditions of interest in this PhD thesis, Pu(IV) is expected to be the predominating state of Pu with minor contributions of Pu(III). Concerning the high alkalinity in porewater solutions, given that the solubility of Pu under the anticipated conditions is very low ($\log [Pu]_{tot} \sim -10.83$), the exclusion and the assessment of the potential $Pu(OH)_4(am)$ phase precipitation in the course of sorption studies is a critical experimental point.

The available literature data on the cement-Pu(IV) system is very limited. A closer inspection of these studies reveals that either of them has applied redox-buffering agents within the executed experiments, thus, the contribution of other redox states of Pu to the quantified distribution ratios cannot be fully ruled out.

For the sake of consistency, considering the different review works on cement-An(IV) sorption studies provided in the literature [13, 50, 85, 109, 113], the most recent, comprehensive work of Ochs *et al.* [50], together with the references therein has been taken as the reference study.

Ochs and co-workers critically reviewed the available sorption data for Pu in the presence of different cementitious materials (crushed concrete, CEM I, CEM V-type HCP, OCP, C-S-H

phases, Nirex reference vault backfill material: NRVB, Ettringite and other minor crystalline phases) with regard to the different states of cement degradation (I to III). The authors also took into account crucial experimental details such as the potential appearance of precipitation, colloid formation, application of different filtration methods, prevailing redox conditions, etc. In their work, selected, averaged R_d values for Pu(IV) sorption on cement phases at degradation stages I to III are also provided, which are found to be in good agreement with the estimates of previous reviews [13, 109]. The most relevant aspects concerning the cement-Pu(IV) system discussed by Ochs *et al.* are as follows:

1. Stage I: The similar sorption behavior for Pu(IV) in analogy with Th(IV) across the entire pH-range of interest (pH ~ 8 – 13.5) was not supported by the summarized data, where the reported R_d values [114, 115] corresponding to Pu(IV) uptake by HCP at state I (pH ~ 13.5 – 12.6) were systematically lower than for state II and III. Hence, the Ochs and co-workers selected a conservative R_d value of $5 \cdot 10^3$ dm^3kg^{-1} for this stage of cement degradation.
2. For stages II and III, based on the analysis of the available sorption data, one single R_d value was assigned. This unified value is in line with the constant aqueous speciation of Pu(IV) within the pH-range (pH ~12.6 – 9), provided also that for other tetravalent actinides the same tendency was observed. Nevertheless, in view of the high scatter within the literature data, an uncertainty of 1.5 orders of magnitude was associated to the best estimate value of $3 \cdot 10^4$ dm^3kg^{-1} in the work of Ochs *et al.* [50].

In contrast to the above listed values, Wieland *et al.* provided a higher value with $R_d = 10^5$ dm^3kg^{-1} for An(IV) uptake by HCP for all the three stages of the degradation process, based on the analogy with the Th(IV) system [13].

It can be considered as clear experimental evidence that Pu(IV) sorption onto hydrated cement phases is the strongest at Stages II and III of the cement degradation process. However, in view of all the available experimental data, the R_d values typically detected in the range of pH = 12 – 12.6 particularly show a huge variation. The values at pH ~12.6 determined by Bayliss *et al.* for Pu(IV) sorption on cement with different compositions and NRVB material [116, 117], were found to be strongly influenced by the applied phase separation methods: derived R_d values increased when a filtration step was also performed and a further, large increase (from 10^3 to $7 \cdot 10^4$ dm^3kg^{-1} on NRVB) was identified when the pore size of the used filter was decreased from 5 μm to 30’000 *Da* MWCO [116]. In comparison, significantly

higher R_d values ($3 \cdot 10^5$ dm^3kg^{-1}) were obtained by Aggarwal *et al.* for Pu(IV) sorption on OPC blends and C-S-H phases in the pH-range of 12.2 – 12.6 [118]. The authors also concluded that the sorption of Pu(IV) on HCP is mainly due to the sorption on C-S-H phases. In accordance with the values of Aggarwal *et al.*, Pointeau and co-workers also reported a stronger uptake of Pu(IV) by hydrated CEM I-type cement pastes for a broad pH-range (10 – 12) [119]. In spite of this, as the phase separation method is not indicated in their work and the applied S:L ratios were also low (0.5 gdm^{-3}), reliability of their determined distribution ratios (laying within the $R_d = 10^4 – 10^6$ dm^3kg^{-1} range, ~ $8 \cdot 10^4$ dm^3kg^{-1} at pH = 12.4) is questionable.

Sorption of Pu (and Am) onto a series of repository, backfill and geological relevant materials (including OPC based concrete and mortar) was studied in the context of the Rokkasho-Mura site by Baston *et al.* [120]. The authors performed additional experiments to investigate the impact of organic ligands (ISA among them) on the system (see Section 1.3.4.2.1 for related discussions on the ternary system). Batch experiments were prepared at S:L = 20 or 200 gdm^{-3} using the crushed and sieved material (< 250 μm) with porewater solutions (generated by pre-equilibrating the concrete or mortar powders with synthetic groundwater, resulting in pH = 12.2 with $[Ca]_{tot}$ = 2 mM or pH = 12.4 with $[Ca]_{tot}$ = 8 mM, respectively). Solutions were spiked with a stock solution of ^{236}Pu to reach a total Pu concentration of $(5 \pm 1) \cdot 10^{-12}$ M. Initial redox state of Pu was not reported by the authors (presumably +4 was dominating), and just as in all other studies, no buffering agents were applied and the valence state of Pu was not assessed either. Prior to quantification (method not indicated) a centrifugation and a filtration step was also performed (through a 0.45 μm and in some cases through a 30'000 Da MWCO filter as well). Reported R_d values for cement and concrete at 20 gdm^{-3} S:L ratio for both pH conditions were significantly higher ($1.4 – 6.4 \cdot 10^6$ dm^3kg^{-1}) than the results of previously published studies. Sorption processes were interpreted using an equilibrium diffuse layer model in combination with a surface complexation model. In the absence of Pu, at high pH values and Ca(II) concentrations, the authors assumed the formation of three calcified silanol surface-species on the C-S-H phases. The related parameters were fitted during the modelling exercise. Surface equilibria for Pu was adapted from a former, unpublished work by the same authors. It was based on the experimentally measured E_h values in the system (as the experiments were performed under non-reducing conditions) and assumed the generation of a mixed Ca(II)-Pu(V)-surface complex, forming between the $Pu(V)O_2(OH)_2^-$ species and the positively charged, calcified silanol groups, as expressed in Equation (26).

$$>SiOH + 2\ Ca^{2+} + Pu^{4+} + 6\ H_2O \leftrightarrow >Si(OCa)_2OHPuO_2(OH)_2 + e^- + 9\ H^+ \quad (26)$$

The surface density of available sites were adjusted to give a good representation of data obtained in concrete and mortar equilibrated systems at 200 gdm^{-3} S:L ratios. Calculated R_d values ($3.8 \cdot 10^6$ dm^3kg^{-1} at pH = 12.2 and $6.9 \cdot 10^6$ dm^3kg^{-1} at pH = 12.4) were found to be in relatively good agreement with the experimental data. Nonetheless, the assumptions considered in the modelling exercise were not supported by any experimental characterization results and the in-solution oxidation of Pu(IV) with the subsequent surface complexation involving the $Pu(V)O_2(OH)_2^-$ species could not be explained either. Thus, the basis of the comprehensive modelling attempt and its justification cannot be taken as reliable. Since redox potentials were not assessed systematically during the sorption experiments with Pu, the expectedly faster and stronger sorption of Pu(IV) onto the available C-S-H phases could have possibly taken place rather than sorption of Pu(V) with its lower effective charge. On the other hand, the nature of the uptake process (assumed to be a rapidly reversible surface sorption) was not underlined either by any experimental evidence. This is again strongly questionable in the context of the available mechanism for Np^{4+} sorption onto C-S-H phases, where irreversible sorption was stated? [112]. Considering the lack of experimental details, data provided by Baston *et al.* can only be taken as orientative estimates.

Figure 4 shows an overview on recommended R_d values for Pu(IV) (An(IV)) sorption onto various cementitious materials as function of the cement degradation stages. In view of all available data, the value of approximately 10^5 dm^3kg^{-1} reported by Wieland et al. [13, 113] for stage II seems to represent a realistic average.

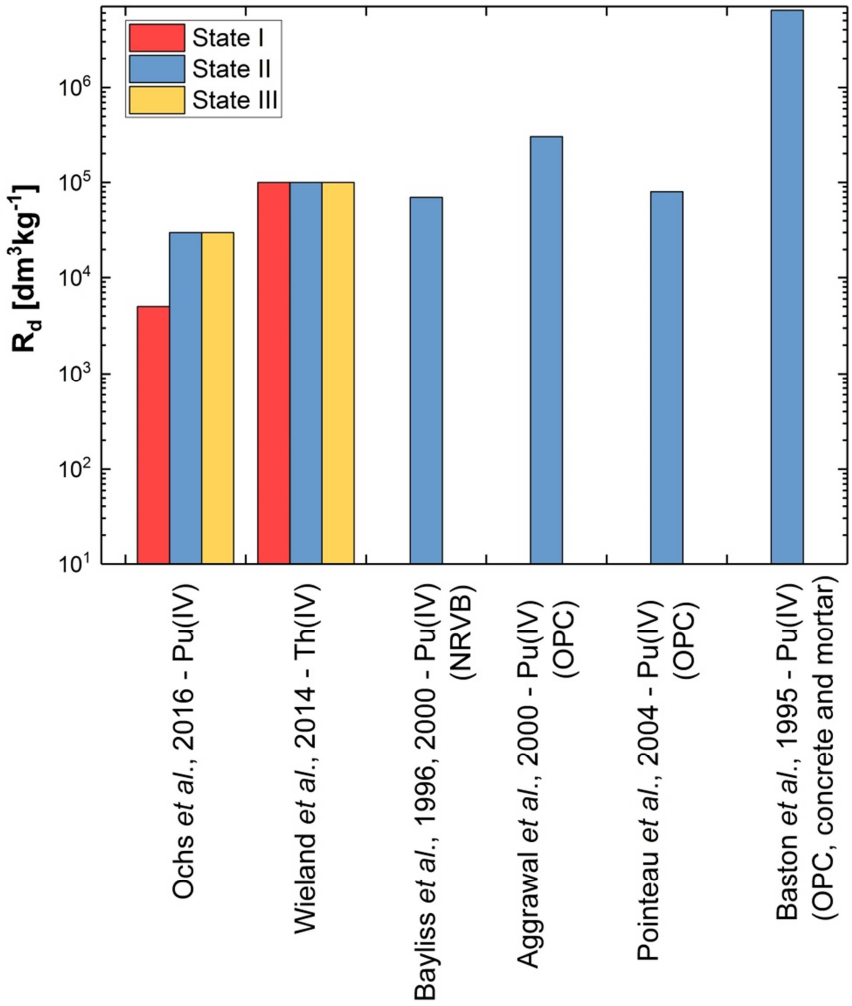

Figure 4. *Reported data on distribution ratios for Pu(IV)/Th(IV) uptake by various hydrated cement phases with regard to the state of the cement degradation process.*

1.3.4.2 Cement–An(IV)–ISA systems

Complexing ligands in general could cause several processes that will influence positively or negatively the (ad)sorption of radionuclides onto hydrated cement phases. These processes can occur separately, but (likely) also simultaneously:

1. Complex formation in the aqueous phase
2. Formation of mixed ligand-radionuclide-surface complexes
3. Non-competitive adsorption of the ligand onto available surface sites
4. Competitive adsorption of the ligand onto available surface sites
5. Surface precipitation of the ligand onto the available solid-liquid interfaces
6. Precipitate formation of the ligand with the radionuclide

Concerning the above raised points and the currently available literature data, the impact of ISA on radionuclide uptake by cementitious materials is mostly limited to complex formation with cationic radionuclides in the aqueous phase (causing reduction in the associated R_d values). As for anionic species, Pointeau *et al.* demonstrated that the adsorption of ISA onto C-S-H phases is a competing reaction to the adsorption of SeO_3^{2-} in cement paste suspensions. This implies that the adsorption processes of the two negatively charged species take place on the same type of surface sites on the C-S-H phases.

Literature data on the Cement-An(IV)-ISA systems are almost completely constrained to studies dealing with Th(IV) (see Section 1.3.4.2.2 for the discussion of these data). The only work involving other tetravalent actinide than Th(IV) (with Pu) was published by Baston and co-workers [120].

1.3.4.2.1 Cement–Pu(IV)–ISA system

Prior to their investigations with ISA, Baston *et al.* assessed the sorption of Pu(IV) onto the crushed and sieved (OCP based) hydrated concrete and mortar powders at highly alkaline pH and various S:L ratios [120]. (for further details see Section 1.3.4.1) Under analogous conditions, Baston *et al.* also conducted identical sorption experiments in the presence of ISA with a total ligand concentration of $2 \cdot 10^{-3}$ M to study the effect of the ligand on the uptake of Pu by different materials. Detected R_d values on concrete (quantified after performing centrifugation and filtration steps) were found to be significantly decreased by the ligand, to the level of R_d = 68 – 190 dm^3kg^{-1} under highly alkaline conditions with pH ~ 12.4. These results indicate a large sorption reduction factor (F_{red}), as expressed in Equation (27) for ISA with an approximate value of ~ $2 \cdot 10^4$ (at 20 gdm^{-3} and $[ISA]_{tot} = 2 \cdot 10^{-3}$ M) on Pu(IV) uptake by the hydrated concrete powder:

$$F_{red} = R_{d,in} / R_{d,ISA} \quad , \qquad (27)$$

where $R_{d,in}$ is the determined distribution ratio for Pu in the absence of ISA and $R_{d,ISA}$ is the value collected under identical conditions with the presence of ISA in porewater (at $[ISA]_{tot} = 2 \cdot 10^{-3}$ M).

Data interpretation was attempted using of the formerly established DLM with SCM models (validated in the absence of ISA), involving an additional complexation equilibrium for Pu(V) interaction with ISA in solution, as expressed in Equation (28):

$$Pu^{4+} + ISA^{-} + 2\ H_2O \leftrightarrow Pu(V)O_2ISA_{-2H}^{2-} + 6\ H^{+} + e^{-} \quad (28)$$

The overall stability constant related to Equation (28) was fitted during the modeling exercise of the sorption data. Calculated R_d values were in good agreement with the experimentally determined ones. Just as in the absence of ISA, redox potentials in the solution were not measured and the redox state of Pu was not characterized either at any stage of the sorption experiments with the ligand. In this respect, possible contributions of Pu(IV)-ISA species to the quantified total Pu-contents in solution cannot be excluded (and should even be expected). Hence, the reliability of the established surface complexation model and its applicability under any conditions other than the investigated ones is highly uncertain. Regardless of the latter observation, Baston *et al.* demonstrated the strong sorption reduction capabilities of ISA towards Pu, providing experimentally determined R_d values and sorption reduction factors for the ligand under highly alkaline conditions in the presence of (OPC based) crushed concrete material.

Important to note that the derived F_{red} values for ISA at the applied $[ISA]_{tot} = 2 \cdot 10^{-3}$ M concentrations are close to the sorption reduction factors reported by Bradbury *et al.* ($F_{red} = 2 \cdot 10^{4}$ at $[ISA]_{tot} = 10^{-3}$ M) calculated using the model for the Pu(IV)-OH-ISA system provided by Moreton and Greenfield *et al.* [91-93], under reducing conditions related to the state II of cement degradation process [85]. This points out the possible predominance of $Pu(IV)_{aq/sorb}$ species throughout the experiments performed by Baston *et al.* and again strongly questions the reliability of the established model involving the presence of $Pu(V)_{aq/sorb}$ species.

1.3.4.2.2 Cement–Th(IV)–ISA system

One of the first studies on the cement-Th(IV)-ISA system was reported by Holgersson *et al.* [121]. Within their work, the authors investigated the impact of ISA (in pure form and also within cellulose degradation leachates) on Cs(I), Ni(II), Pm(III) and Th(IV) sorption onto and diffusion into hydrated cement pastes. A synthetic fresh concrete porewater was prepared by dissolving NaOH, KOH in Milli-Q water and saturated with portlandite to set the Ca(II) total concentration in solution at a constant level ($4 \cdot 10^{-5}$ M). Sorption batch experiments were prepared (under N_2 atmosphere) using a crushed and sieved ordinary Portland cement powder (with the average size fraction of d = 63 – 125 μm) at a constant S:L ratio of 50 gdm^{-3}. A pre-equilibration time of 3 months were allowed for the cement pastes with the synthetic

cement porewater before the supernatants were replaced with identical porewater solutions containing the radionuclides and the organic additives. The total concentrations of ISA in the porewater solutions were $3 \cdot 10^{-3}$ M at pH = 13.40, $5 \cdot 10^{-3}$ M at pH = 13.42 and $2.7 \cdot 10^{-2}$ M at pH = 12.67, all with a final $[Ca(II)]_{tot}$ value below 10^{-5} M. Samplings were systematically performed up to a contact time of 3 months. Quantification of total radionuclide concentration in solution was assessed by liquid scintillation counting (phase separation method not reported). R_d values for Th(IV) uptake by HCP in the absence of ISA were found to be high (below the level of the detection limit, denoting $R_d > 10^3$ dm^3kg^{-1}). ISA appeared to have a significant effect on Th(IV) sorption onto HCP: Th(IV) total concentrations in solution with $[ISA]_{tot} = 2.7 \cdot 10^{-2}$ M remained high throughout the entire sampling period, showing a constantly reduced R_d value ($R_d = 10 – 20$ dm^3kg^{-1}, F_{red} ~100) for the uptake by the hydrated cement pastes.

The uptake of Th(IV) by HCP and various C-S-H phases in the presence of ISA at pH = 13.3 (corresponding to state I of HCP degradation process, using the APW as discussed previously in Section 1.3.4.1) was reported in multiple studies by the PSI team [13, 57, 61, 104]. Before conducting the uptake studies with Th(IV), Wieland *et al.* also assessed the stability of HCP in the presence of ISA, to determine the dissolution of Ca-bearing hydrated cementitious phases with regard to the total ligand concentration in solution [104]. For sorption experiments with HCP, the average size-distribution fraction d < 70 μm (Brunauer–Emmett–Teller surface area using N_2 gas: N_2-BET surface area = 46 ± 4 m^2g^{-1}) was applied at S:L ratios of 0.1 and 5 gdm^{-3} from the crushed and sieved cement solid phase (CEM I, 52.5 N HTS) and was let in contact with the filtered ACW, at pH = 13.3, I = 0.3 M (under controlled N_2 atmosphere) in the presence of ISA with 10^{-5} M < $[ISA]_{tot}$ < 0.3 M. Analogous sorption experiments with synthetic C-S-H phases were also conducted by Wieland *et al.*, investigating the effect of Ca:Si ratio on the uptake of Th(IV) [13]. These phases were also used in the course of experiments with ISA at 0.1, 1 and 10 gdm^{-3} S:L ratios. The stability tests with ISA and HCP were conducted at a slightly higher S:L ratio of 12.5 gdm^{-3}.

In order to avoid precipitation of ThO_2(am,hyd), Th(IV) was introduced to the sample at a low initial total concentration (in the range of $10^{-11} – 10^{-8}$ M). Up to 1 month of equilibration time was allowed for all experiments. Quantification of Na, K, Ca, Al, Si and S total concentrations was performed by ICP-OES, whilst for assessing the ^{228}Th(IV) total concentrations, gamma counting and LSC was applied after a phase separation via ultracentrifugation (at 95’000 *g* for 1 hour). Special care was taken during the quantification

of Th(IV)-content to account for the amount of the radiotracer sorbed on the walls of the storage vials.

Wieland *et al.* showed [104] that the effect of ISA on the chemical composition of the porewater (concerning $[Ca(II)]_{tot}$ and pH) in contact with the OPC paste can be modelled by assuming portlandite solubility equilibrium together with the formation of Ca(II)-ISA-OH species in solution (for $[ISA]_{tot} = 10^{-5}$ M – 10^{-2} M, $[Ca]_{tot}$ was ranging from $1.6 \cdot 10^{-3}$ to $2.8 \cdot 10^{-3}$ M). Based on a chosen limit of weight reduction for the HCP (Δ_{max} = 5 w/w%), the authors set the maximum "allowed" total ISA concentrations (to be applied for the sorption experiments) at 10^{-3} M with a S:L ratio of 0.1 gdm^{-1} and at $5 \cdot 10^{-2}$ M with a S:L ratio of 5 gdm^{-1}.

Sorption data collected in the HCP systems were indistinguishable from those of the experiments conducted with synthetic C-S-H phases, depicting the key role of C-S-H phases in the uptake process of tetravalent actinides.

Th(IV) total concentrations in solutions were remarkably enhanced when 10^{-4} M < $[ISA]_{tot}$ was present in porewater. Thus, a "no effect concentration" of 10^{-4} M was assigned to ISA under conditions related to state I and II of the cement degradation process with regard to An(IV) uptake by HCP [13, 122]. Although Ca(II) total concentrations and pH conditions were different within the two studies, R_d values obtained by Holgersson *et al.* (especially for 2.7 10^{-2} M $[ISA]_{tot}$, pH = 12.67, $[Ca(II)]_{tot} < 10^{-5}$ M and S:L ratio = 50 gdm^{-3}) were in good agreement with the sorption data of Wieland *et al.* [121]. However, the fading impact of ISA on Th(IV) sorption with increasing equilibration time at lower total concentration of the ligand ($3 \cdot 10^{-3}$ M at pH = 13.40, $5 \cdot 10^{-3}$ M at pH = 13.42) cannot fit in the overall trend observed by Wieland and co-workers. The higher limit of detection for the measurement of $[Th(IV)]_{tot}$ performed by Holgersson *et al.* using LSC could serve as a reasonable explanation. Under the given conditions, R_d values higher than 10^3 dm^3kg^{-1} were not quantifiable in their experiments and according to the dispersion of the data set reported by Wieland *et al.*, these values are predicted to lie in the range of $0.5 – 50 \cdot 10^3$ dm^3kg^{-1}, which is then matching with the data of Holgersson *et al.*

Wieland and co-workers, observed a rather fast kinetics for the process, *i.e.* $[Th(IV)]_{tot}$ in solution usually reached steady state value within 2 days, which hinted towards that the sorption reaction mainly involves surface equilibria. As a consequence, it was concluded that the uptake of Th(IV) and its complexation with ISA and Ca(II) in solution are counteracting reactions. Assuming the $CaTh(OH)_4(ISA)_2(aq)$ complex as the only predominating species in solution, adapted from elsewhere [100, 103], the authors reproduced the reduction effect of

ISA on Th(IV) sorption in a semi-empirical way using a simplified sorption model, as expressed in Equation (29) [13, 104].

$$\log R_d = \log R_{d,in} \cdot - \log (1 + \beta'_{1,2,1} \cdot [Ca^{2+}] \cdot [ISA^-]^2 \cdot A^{-1} \cdot [H+]^{-4}) \quad , \tag{29}$$

where $R_{d,in}$ is the initial distribution ratio, describing Th(IV) uptake by HCP in the absence of ISA, $\beta'_{1,2,1}\cdot$ is the related stability constant of the solution species under the given condition (adapted from [103]) and the *A* term (denoted as the "side-reaction coefficient") accounts for the hydrolysis of Th(IV) as shown in Equation (30):

$$A = 1 + \beta'_{1,4} \cdot [OH^-]^4 \quad , \tag{30}$$

where $\beta'_{1,4}$ is the hydrolysis stability constant for the formation of the $Th(OH)_4(aq)$ species at the certain ionic strength. Considering the prevailing high pH condition in solution, deviation between the value of *A* and the free $[Th^{4+}]$ concentration is negligibly small.

The presented simplified model in the form of Equation (29) is based on a representative $R_{d,in}$ value and allows to quantify the reduction effect of the ligand on Th(IV) uptake by HCP, through the formation of solution species with high stability. Within their presented model, Wieland *et al.* did not implement the separate sorption of ISA onto the hydrated cementitious phases (which decreases significantly ISA equilibrium concentrations in solution at low $[ISA]_{tot}$ applied) and furthermore, the formation of Ca(II)-OH-ISA and the binary (Th(IV)-ISA) complex species were also neglected, *i.e.* $[ISA^-]$ was set equal to $[ISA]_{tot}$ (which again causes high deviations with regard to the existing free concentrations of $Ca^{2+}(aq)$ and ISA^- ions).

Collected Th(IV) sorption data with ISA and HCP was able to be successfully modelled by Equation (29), only when the initial $R_{d,in}$ was set to $6 \cdot 10^6$ dm^3kg^{-1} (as supported by uptake measurements carried out at a S:L ratio of 0.01 gdm^{-3}). Conversely, using $R_{d,in}$ with a value of $3.5\ 10^5$ dm^3kg^{-1}, quantified in the ISA-free systems at S:L ratio = 0.10 gdm^{-3}, the sorption reduction effect of ISA was overestimated by one order of magnitude with increasing $[ISA]_{tot}$ in solution. As the sorption studies on Th(IV) uptake by C-S-H phases also suggested the lower $R_{d,in}$ value to be used within the model, the authors described such deviations by a potential surface complexation reaction. The reaction supposedly involves Th(IV) and ISA, additionally delimiting the dissolution of Th(IV) [104].

Felipe-Sotelo and co-workers also studied the effect of ISA (within generated cellulose degradation products) on Th(IV) uptake by NRVB material and also separately by its individual components: OPC, limestone and hydrated lime [123]. Porewater was generated by equilibrating the powdered NRVB material with deionized water at S:L ratio = 20 gdm^{-3} for 8 days. Ca(II) total concentration was determined to be $(8.7 \pm 0.1)\cdot 10^{-3}$ M and pH = 12.8 – 12.9. Cellulose degradation leachate was prepared by mixing deionized water with cut-up Kimwipe tissues and powdered NRVB material in a stainless steel canister and put as closed in a heating-oven for 30 days at 80 °C. The amount of ISA within the CDPs were quantified to be $1.5\cdot 10^{-3}$ M. The yielding leachate had a similar final chemical composition as the porewater itself: pH = 12.7 – 12.8 and $[Ca]_{tot} = (8.6 \pm 0.2)\cdot 10^{-3}$ M.

Sorption experiments were performed at a S:L ratio of ~ 2.4 gdm^{-3} by mixing the porewater or the CDP leachate with crushed and sieved (average size fraction of d = 250 – 500 μm, N_2-BET surface area = (17.07 ± 0.12) m^2g^{-1}) NRVB material which was followed by the addition of the radionuclide ($Th(NO_3)_4$). An equilibration time of 8 days was allowed for all sorption experiments. Total concentrations of Th(IV) were quantified by ICP-MS after a filtration step (0.22 μm membrane).

As the individual sorption data of CDP leachates with the NRVB material did not show any distinct trend, the authors did not account for the loss of ISA in the subsequent experiments. Th(IV) sorption data showed significant retention in the presence of OPC and NRVB material as well with $R_d \sim 6\cdot 10^6$ dm^3kg^{-1} and $4\cdot 10^6$ dm^3kg^{-1}, respectively. However, observations revealed that the main sorbing solid phase within NRVB is the OPC and the other constituents: limestone flour and hydrated lime simply dilute the effect of the latter phase, causing a slightly lower uptake for Th(IV). CDPs appeared to have only a small impact on Th(IV) sorption onto OPC and NRVB material with newly detected R_d values of 1.9 – $3.7\cdot 10^6$ dm^3kg^{-1}. These determined distribution ratios (depicting a sorption reduction effect of $F_{red} \sim 2$) at the given $[ISA]_{tot} = 1.5\cdot 10^{-3}$ M for Th(IV) uptake by OPC are found to be significantly differing from the values previously reported at $[ISA]_{tot} = 10^{-3}$ M with $R_d \sim 10^3$ dm^3kg^{-1} ($F_{red} \sim 100$) [104] and also from the data provided by Holgersson *et al.* at $[ISA]_{tot} = 2.7\cdot 10^{-3}$ M with $R_d \sim 20$ dm^3kg^{-1} (F_{red} ~100, not well-defined) [121]. An unambiguous explanation for the observed discrepancies was not provided by Felipe-Sotelo and co-workers.

In the general context of studies on cement-An(IV)-ISA systems, dealing with radionuclides strongly sorbing onto HCP with simultaneously occurring stable complex formation reaction(s) in solution, it can be concluded that the experimental window for the assessment of such a system is rather narrow [13]. It is found to be limited by many constraints, such as:

1. Maximum quantifiable $R_{d,in}$ in the absence of the ligand. This is influenced by the maximum total initial concentration of the radionuclide to be introduced into the system (hereafter denoted as $[An(IV)]_{in}$) as well as by the performed phase separation method coupled with the detection limits of applied analytical techniques.
2. Optimum total ligand concentration and S:L ratio to be applied, without affecting the composition of HCP and still maintaining the free concentration of the ligand at a considerably high level (*i.e.* sorption of the ligand onto HCP shall not be too extensive or it has to be accounted for under identical conditions as in the ternary system)
3. Solubility of the An(IV) under the given conditions. This sets the theoretical maximum value of $[An(IV)]_{in}$ in order to assess R_d values which are purely related to sorption (reduction) processes. (It is also important that below saturation level, surface precipitation can be still witnessed.)
4. Allowed equilibration time. Whilst the sorption processes of tetravalent actinides onto HCP are kinetically fast reactions, complexing ligands tend to prohibit and slow down this reaction.

The final interpretation of sorption data collected for Cement-An(IV)-ISA systems, as shown by the literature data on the Th(IV) uptake studies, strongly relies on the solution speciation scheme applied for the Ca(II)-An(IV)-OH-ISA system as well as it is also highly dependent on the correct assessment of the binary sorption equilibria with regard to the Cement-An(IV) and Cement-ISA systems.

1.4 Definition of Objectives

This study aims at providing a fundamental and quantitative description of the system cement-Pu-ISA under conditions relevant in the context of nuclear waste disposal. Performed experiments were either solubility- or sorption-type of investigations. The study is conceptualized following a bottom-up approach, starting with a redox study on Pu, building-up with the binary system Pu-ISA (in absence and presence of Ca(II)), and concluding with the ternary system Cement-Pu-ISA, where the lessons learnt in steps I and II are implemented (and strictly necessary) in the interpretation of the results:

1. **Solubility and redox behavior of plutonium in alkaline, reducing aquatic systems** (Chapter 3.1)**:**

   This part of the study aims at reducing uncertainties affecting the redox chemistry and solubility of Pu under reducing, alkaline conditions. A special emphasis is given to the characterization and assessment of Pu redox states in aqueous phases as well as within the solubility controlling solid phases. As a very important milestone of this part of the PhD, this solubility study intends to set the proper baseline for the interpretation of later solubility experiments in the presence of ISA.

2. **Solubility, speciation and redox chemistry of Pu in the presence of ISA under reducing, alkaline conditions** (Chapter 3.2)**:**

   The solubility of Pu in the presence of ISA was investigated under reducing, alkaline conditions in a comprehensive approach including the systematic variation of pH_m and ISA concentration. In combination with extensive solid phase characterization and DFT calculations, this study aimed at providing realistic Pu solubility upper limits in the presence of ISA under repository-relevant conditions and, further, to derive chemical and thermodynamic models for the system Pu^{3+}–Pu^{4+}–Na^{+}–ISA^{-}–Cl^{-}–OH^{-}–H_2O(l). Because of the direct implications in this solubility study, but also considering its relevance in the context of waste disposal, the stability of ISA in alkaline, reducing solutions was evaluated using different techniques within a timeframe of 2 years.

3. **Solubility, speciation and redox chemistry of Pu in the presence of ISA and Ca(II) under reducing, alkaline conditions** (Chapter 3.3)**:**

   Building-on the solubility study targeted in the previous chapter, this study aimed at evaluating the impact of ISA on the solubility of Pu in the presence of Ca(II), *i.e.* under

conditions representative of cementitious systems. One of the main motivations is the possible formation of quaternary complexes Ca(II)–Pu(IV)–OH–ISA, which may importantly enhance the solubility of Pu and that have been controversially discussed in the literature for the analogue system with Th(IV). The final goal is the development of chemical and thermodynamic models for the system derive chemical and thermodynamic models for the system Pu^{3+}–Pu^{4+}–Na^{+}–Ca^{2+}–ISA^{-}–Cl^{-}–OH^{-}–H_2O(l), which can be implemented in thermodynamic databases (TDB) and geochemical calculations within boundary conditions of relevance in the context of nuclear waste disposal (and in particular in the framework of cementitious systems).

4. **Uptake of Pu by cement in the presence of ISA (and Ca(II)) under reducing, alkaline conditions** (Chapter 3.4)**:**

   This study focused on the conditions simulating Stage II of the cement degradation process. Investigations were conducted in a step-wise approach: firstly targeting the binary systems Cement-Pu and Cement-ISA, and finally the ternary system Cement-Pu-ISA. Initial experiments on the Cement-Pu system were assigned to set the baseline for the uptake of Pu by the ordinary Portland cement phase. Sorption of ISA onto the cement was assessed separately with the aim of quantifying the concentration of ligand remaining in solution.

   Aside from the sorption experiments, the formerly derived thermodynamic model on the Ca-Pu-OH-ISA system was also tested by a newly conducted solubility experiment series in order to verify its validity range concerning the parameters related to Stage II of the cement degradation process.

   The evaluation and modelling of the Cement-Pu-ISA system benefitted from the quantitative descriptions and models set for the binary systems as well as from the thermodynamic model on the Ca-Pu-OH-ISA resulting from the comprehensive solubility study. A special emphasis was put on the reversibility of the observed sorption processes and also on the redox speciation of Pu prevailing in various systems. The final aim is to provide experimentally determined R_d values and accordingly calculated sorption reduction factors (F_{red}) representing the effect of ISA on the uptake of Pu by cement. Due to the complexity of the system investigated, this study targets the development of a semi-empirical model describing the sorption of Pu in the presence of ISA under reducing conditions simulating stage II of the cement degradation process.

2 Experimental

Experiments involving plutonium were performed in specialized α-laboratories within the controlled area of KIT–INE. All experiments were prepared, stored and executed in controlled gloveboxes at T = (22 ± 2) °C under Ar-atmosphere with O_2 concentration below 2 ppm, except otherwise indicated.

2.1 Chemicals

All solutions were prepared with ultra–pure water purified with a Milli–Q apparatus (Millipore, 18.2 MΩ, 22 ± 2 °C) and purged for several hours with Ar before use. The Milli–Q water used for the preparation of ISA stock solution was further boiled for several hours with simultaneous purging by Ar gas. $C_8H_{17}NO_3S$ (CHES; p.a.), diethyl–ether ($C_4H_{10}O$, p.a.), NaCl (p.a.), NaOH (Tritrisol), KOH (p.a.), HCl (Tritrisol), $Na_2S_2O_4$ (> 87%), hydroquinone (p.a.), Propan-2-ol (> 99.9 %, for spectroscopy ®Uvasol) xylene (isomeric mixture, p.a.) and toluene (p.a.) were obtained from Merck. $C_4H_{11}NO_3$–$C_4H_{11}NO_3$·HCl (TRIS–TRIS·HCl; p.a.) and $SnCl_2$ (p.a.) were purchased from Sigma–Aldrich. 1-phenyl-3-methyl-4-benzoyl-pyrazol-5-one (PMBP) and Di-(2-ethylhexyl)-phosphoric acid (HDEHP) were obtained from Fluka (purum). Carbonate impurities in fresh 1.0 M NaOH (Titrisol) were quantified as $(3 \pm 1)\cdot10^{-5}$ M using a Shimadzu TOC5000 equipment. $Ca(ISA)_2$(s) [$CaC_{12}H_{22}O_{12}$] was purchased from Alfa Aesar. NaISA(s) was generated by an ion exchange method from commercial $Ca(ISA)_2$(s) using an ion exchange resin (Chelex® 100, Na-form, Sigma Aldrich, analytical grade purity) and diethyl-ether ($C_4H_{10}O$, ACS reagent grade, VWR BDH Prolabo®). A detailed description of the synthesis, purification and characterization of NaISA(s) is provided in the Appendix (Section 5.2). The resulting NaISA stock solution applied throughout the present work as well was characterized as (0.16 ± 0.02) M NaISA at pH_m = 8.9 with an excess of 0.18 M NaCl.

The isotopic composition of Pu stock solution and solid phases applied in this study was 99.4 wt. % ^{242}Pu, 0.58 wt. % ^{239}Pu, 0.005 wt. % ^{238}Pu and 0.005 wt. % ^{241}Pu. The use of the long-lived ^{242}Pu isotope ($t_{½}$ = $3.75\cdot10^5$ a) avoids redox processes induced by radiolysis effects.

Hydrated cement paste rods were obtained from the Swedish Nuclear Fuel and Waste Management Company (SKB). The specimens were casted from a mixture of Swedish structural Portland cement for civil engineering (CEM I 42.5N BV/SR/LA) and deionized water at a water-to-cement weight ratio of 0.5. Chemical composition of the cement as provided by the manufacturer is listed in Table 3.

Table 3. *Chemical characteristics of Swedish CEM I 42.5N BV/SR/LA*

Chemical formulation	***CaO***	***SiO_2***	***Al_2O_3***	***Fe_2O_3***	***MgO***	***Na_2O***	***K_2O***	***SO_3***	***'Cl'***
w%	64	22.2	3.6	4.4	0.94	0.07	0.72	2.2	0.01

2.2 Measurements of pH and E_h

Combination pH–electrodes (type Orion Ross, Thermo Scientific), freshly calibrated against standard pH buffers (pH = 3 – 13, Merck) were used to determine the total free concentration of proton in molar ($pH_c = -\log [H^+]$) or molal units ($pH_m = -\log m_{H^+}$). In aqueous solutions of ionic strength $I_m \geq 0.1$ mol·kg^{-1}, the measured pH value (pH_{exp}) is an operational, apparent value related to m_{H^+} ($[H^+]$) by $pH_m = pH_{exp} + A_m$ ($pH_c = pH_{exp} + A_c$), where A_m (A_c) is an empirical parameter including the activity coefficient of the proton (γ_{H^+}) and the liquid junction potential of the electrode for a given background electrolyte and ionic strength (and temperature, pressure). The empirical A_m (A_c) values for NaCl were taken from the literature [124]. In NaCl–NaOH solutions with $m_{OH^-} > 0.03$ m, the H^+ concentration was calculated from the given m_{OH^-} and the conditional ion product of water (K'_w) at the ionic medium concentration used in the experiments. The latter was calculated from the standard state constant ($K°_w$) extrapolated by the SIT approach using the parameters from NEA-TDB compilations [9]). In general, experimental pH values related to solubility studies are provided in molal units as pH_m, whilst in the course of the sorption part, these are displayed in molar units, denoted as pH_c.

The redox potential was determined with combined Pt or Au and Ag/AgCl reference electrodes (Metrohm). The measured potentials were converted to E_h (*versus* standard hydrogen electrode: SHE) by correcting for the potential of the Ag/AgCl inner-reference electrode with 3 m KCl and T = 22 °C (+207 mV). E_h values were finally transformed to the negative logarithm of electron activity, $pe = -\log a_{e^-}$ according to Equation (31):

$$E_h = -RT \ln(10) F^{-1} \log a_{e^-} \quad , \tag{31}$$

where R is the ideal gas constant (8.31446 J·mol^{-1}·K^{-1}), F is the Faraday constant (96485.33 C·mol^{-1}) and a_{e^-} is the activity of the electron. E_h values of the solutions were collected following the protocol described by Altmaier *et al.* [125], which involved approximately 15

minutes of equilibration time. Sufficiently stable E_h readings were obtained in HQ− and in many of the Sn(II)-containing samples, when the absolute drift of the electrode was observed to be < 0.5 mV/min after the indicated time. The uncertainty of E_h values collected within 15 mins of equilibration time ranged between ± 15 and ± 30 mV (calculated as 2σ of repeated E_h readings). E_h measurements in Sn(II)-buffered systems with pH_m < 11 normally required longer equilibration times. This is mostly due to the sparingly soluble Sn(II)-oxides and -oxy-hydroxides forming in these conditions[126] (SnO(cr), or $Sn_6O_8H_4$(s) / $Sn_6O_4(OH)_4$(s)), and the accordingly low Sn(II) total concentration in solution. For these critical samples, E_h values were collected repeatedly with increasing equilibration times (15 minutes, 1, 2 and 6 hours). Longer equilibration times resulted in significantly lower absolute drift of the redox potential (< 0.08 mV/min), leading also to clearly lower numerical deviations in the measured values (± 10 to ± 16 mV, calculated as 2σ of repeated E_h readings, see Table 7 in Section 3.1.2.1). This was considered to be a satisfactory compromise between the accuracy of the E_h readings and the time-frame of the solubility experiments.

2.3 Pu solubility experiments

The solid phase, PuO_2(am,hyd) used throughout the entire study was originally prepared at KIT–INE facilities in 2006 and stored to date under controlled Ar-atmosphere. The plutonium used for the preparation of the solid phase consists of an isotopic composition of 99.4 wt. % ^{242}Pu, 0.58 wt. % ^{239}Pu, 0.005 wt. % ^{238}Pu and 0.005 wt. % ^{241}Pu. The original solution was purified from the daughter nuclides and characterized by α–, γ–spectrometry and inductively coupled-mass spectrometry (ICP–MS). The resulting Pu stock solution (in 1.0 M $HClO_4$, containing a mixture of different oxidation states) was quantitatively reduced on a platinum cathode at $E_{cathode}$ = – 0.2 V to Pu(III) followed by a partial oxidation to Pu(IV) at E_{anode} = + 0.8 V. UV-Visible / Near Infrared (UV–Vis/NIR) spectroscopy revealed a ratio for Pu^{4+}:Pu^{3+} of approx. 3:1 in the final solution. Slow addition of 0.10 M NaOH yielded a dark green precipitate of Pu(IV)-hydrous-oxide, which was washed several times with water and stored in 0.1 M NaCl for two weeks. The precipitate was then distributed to 6 samples, 0.1 M NaCl solutions with $3 \leq pH \leq 6$. After the initialization of the experiments, the samples have been regularly monitored for pH, E_h values and Pu concentrations after 10 kD ultrafiltration (pore size ≈ 2 nm) (Nanosep ®, Pall Life Sciences). The very last sampling of this series was conducted in the context of the current study and corresponds to an equilibration time of 2886 days (7.9 years). For the determination of the redox state distribution of Pu in selected samples of the latter series, a certain liquid-liquid extraction method [5] and capillary

electrophoresis hyphenated (CE-) sector-field-ICP-MS technique was applied (see Section 2.5.2 and 2.5.3, respectively).

2.3.1 Experiments under alkaline, reducing conditions

Two series of batch experiments were prepared differing in the redox conditions, which were either buffered by 2 mM hydroquinone or Sn(II). The former defines mildly reducing conditions (pe + pH_m ~ 9.5) where Pu(IV) is the only oxidation state of Pu in the system. Whilst, in the case of applying Sn(II), redox potentials were adjusted close to the border of water reduction (pe + pH_m ~ 2) [127, 128]. Owing to the large uncertainties in thermodynamic data available for Pu aqueous species and compounds forming in these alkaline and very reducing conditions, both $Pu(III)_{s/aq}$ and $Pu(IV)_{s/aq}$ might be stable (relevant) in the samples buffered with Sn(II).

Ionic strength was maintained constant in all the samples with 0.1 M NaCl–NaOH solutions. In both series (hydroquinone and Sn(II), pH_m values of the matrix solutions were adjusted between 8 and 13. Systems at pH_m = 8 and 9 were buffered with 20 mM of TRIS and CHES, respectively. Whenever necessary, pH_m was further adjusted with HCl and NaOH solutions of same ionic strength. After achieving constant readings of pH_m and E_h values (within the related given uncertainties), PuO_2(am,hyd) solid phase was added to the system.

The aged Pu solid phase (~8 years) at pH_m = 5.93 was newly characterized for this study using powder X-ray diffraction (XRD), X-ray Photoelectron Spectroscopy (XPS) and X-ray absorption near edge spectroscopy (XANES) (see Section 2.6). Approximately 0.2 mg of this solid phase were added to each of the batches. A larger amount (ca. 1 mg) was added to four selected samples with pH_m = 9 and 12 (of both hydroquinone and Sn(II) systems) aiming at a later solid phase characterization.

Subsequently to the introduction of the Pu solid phases, pH_m, E_h and $m(Pu)_{tot}$ of all the samples were regularly monitored. (Characterization procedures performed to quantify Pu total concentrations in the aqueous phase are detailed in Section 2.5.) After reaching equilibrium conditions (constant pH_m, E_h and $m(Pu)_{tot}$, with an allowed equilibration time of 150 d), selected solid phases from the solubility series in hydroquinone and Sn(II) were characterized by XPS, XAFS and *in-situ* XRD as described in Section 2.6.

2.3.2 Experiments in the presence of ISA: Pu–ISA system

The system Pu–ISA was investigated in four experimental series with a total of 34 independent batch samples. Redox conditions were set by using 2 mM of either HQ (with pe + pH_m ~ 9) or Sn(II) (with pe + pH_m ~ 1).

In the presence of each redox buffering agent, two series of solubility experiment were prepared:

a. pH_m was varied from 8 to 12.9, and $[ISA]_{tot}$ = constant = 10^{-3} M. For the HQ system, an additional series with $[ISA]_{tot}$ = 0.01 M was prepared.
b. pH_m = constant = 12, and $[ISA]_{tot}$ was varied from 10^{-5} to 0.10 M.

Solutions with pH_m = 8 and 9 were buffered with 20 mM of TRIS and CHES, respectively. The ionic strength of the solutions was kept constant at 0.10 M NaCl, except for the sample with the highest ISA concentration (0.10 M), where the individual ionic strength of the NaISA stock solution set the overall ionic strength to a slightly higher value, I = 0.23 M. Whenever necessary and before the addition of the Pu solid phase, the pH_m values of the matrix solutions were adjusted with HCl and NaOH solutions of same ionic strength. After achieving constant readings of the pH_m and E_h values, approximately 0.25 mg of the initial, $Pu(IV)O_2$(am,hyd) solid phase were added to the each individual batch sample. A larger amount (1.5 – 2.5 mg) was inserted into six samples with pH_m = 9 and 12 ([ISA] = 10^{-3} M) and with [ISA] = 0.10 M (pH_m = 12) (for both, HQ- and Sn(II)-buffered systems), aiming at a later solid phase characterization. After the addition of the solid phase, pH_m, E_h and $[Pu]_{tot}$ were regularly monitored for 90 days. (Characterization procedures performed to quantify Pu total concentrations in the aqueous phase are detailed in Section 2.5.) Equilibrium conditions (constant pH_m, E_h and $[Pu]_{tot}$ values) were attained within 30 days of contact time.

As a separate investigation, complementing the solubility study, stability of ISA under alkaline, reducing aqueous conditions was also tested (details can be found in the Appendix, Section 6.3). All results unequivocally underlined the stability of the ligand and its prevalence in the free form within the boundary conditions applied. Hence, trends (such as speciation changes and complexation reactions) later to be observed can be clearly assigned to the the ISA^- species itself, as the original structure and the concentration of the free ligand as well are proved to remain the same throughout the experimental series.

2.3.3 Experiments in the presence of ISA and Ca(II): Ca–Pu–ISA system

The system Ca–Pu–ISA was investigated in six experimental series of independent undersaturation solubility batch samples (with total volumes of 25 mL). Redox conditions were set by using 2 mM of either HQ or Sn(II). Solutions with pH_c = 8 and 9 were buffered with 20 mM of TRIS and CHES, respectively. The ionic strength of the solutions was kept constant at 0.10 M with NaCl.

In the presence of each redox buffering agent, three series of solubility experiment were prepared:

a. pH was varied from 8 to 12.4, $[ISA]_{tot}$ = constant = 10^{-3} M and $[Ca]_{tot}$ = constant = 0.01 M.
b. $[ISA]_{tot}$ was varied from 10^{-5} to 0.01 M, pH = constant = 12 and $[Ca]_{tot}$ = constant = 0.01 M.
c. $[Ca]_{tot}$ was varied from $3\cdot10^{-4}$ to $2\cdot10^{-2}$ M, pH = constant = 12 and $[ISA]_{tot}$ = constant = 10^{-3} M.

Before the addition of the Pu-bearing solid phase, pH_m values of the matrix solutions were adjusted with HCl and NaOH solutions of same ionic strength until attaining constant pH_m and E_h readings. The concentration ranges considered for Ca(II) and ISA was based upon preliminary thermodynamic calculations, with the aim of maintaining constant ionic strength (I = 0.10 M NaCl–NaOH–NaISA–$CaCl_2$) within the series and to avoid the unwanted precipitation of $Ca(ISA)_2$(s) and/or $Ca(OH)_2$(s) phases. Although the saturation indices of both solid phases in the conditions of experiments were calculated to be negative, aliquots of the supernatants (of selected systems with high Ca– or ISA–contents) were further analyzed for $[Ca]_{tot}$ (ICP–MS) and $[ISA]_{tot}$ (NPOC) after two weeks of equilibration time prior to the initialization of the Pu solubility experiments. In all cases, $[Ca]_{tot}$ and $[ISA]_{tot}$ were found to be identical to the initial values, thus confirming the absence of any precipitation phenomena.

After achieving constant readings of pH_m and E_h, approximately 0.25 mg of the initial, $Pu(IV)O_2$(am,hyd) solid phase was added to each individual batch sample. With the aim of a comprehensive solid phase characterization, larger amounts (1.5 – 2.5 mg) were introduced to selected samples with pH = 9 and 12 (for both, HQ- and Sn(II)-buffered systems). The structural properties and solubility behavior (in the absence of ISA and Ca in solution) of the initially used material are published elsewhere [1]. After the addition of the Pu solid phase, experimental parameters pH_m, E_h and $m(Pu)_{tot}$ of each sample were regularly monitored for 90

days (characterization procedures performed to quantify Pu total concentrations in the aqueous phase are detailed in Section 2.5). Equilibrium conditions (constant pH_m, E_h and $m(Pu)_{tot}$ values) were normally attained within 30 days of contact time.

2.4 Sorption experiments

The aqueous supernatants of all sorption experiments were prepared by using synthetic porewater. The solution, simulating Stage II of the cement degradation process, was generated by mixing the cement powder (d_{av} < 100 μm) and Milli-Q water after removing the alkali content of the cement with a pre-washing step. Experimental details on the preparation and characterization of the porewater are discussed in Section 2.4.1. This leachate was then later used (avoiding further dilution to the highest possible extent) in combination with the original, dry cement powder (at various S:L ratios) for the preparation of all batch sorption experiments involving Pu and/or ISA.

In order to assess the free ligand concentration, before performing investigations on the ternary Cement-Pu(IV)-ISA system, separate batch sorption experiments on the Cement-ISA system were carried out. Aliquots of the formerly characterized ISA-stock solution (see Appendix and reference [2] for more details) were added to porewater solutions and the ISA-containing porewater was mixed with the dry, cement powder at different S:L ratios and total concentrations of ISA (see Section 2.4.3 for further details).

The series of performed sorption experiments involving ^{242}Pu can be separated into three different cases:

a. binary, “Cement–Pu system” experiments,
b. ternary, “Cement–Pu–ISA system” experiments and
c. “Complementary experiments”.

The source of Pu was a Pu(VI) stock solution. The consideration of introducing Pu in its hexavalent state to all sorption experiments was set to avoid oversaturation conditions for Pu(IV) which may lead to the formation of colloidal species. The stock was prepared by acidic dissolution of a $Na_2Pu_2O_7{\cdot}xH_2O$(am) solid phase (~5 mg) synthetized and characterized formerly in-house at KIT-INE as reported elsewhere [129]. Details on the preparation of the stock solution are discussed in Section 2.4.4. Very small aliquots of the diluted stock solution (10 – 50 μL) were introduced to the matrix solutions with or without ISA and the hydrated cement pastes.

Two series of experiments were conducted for the binary system cement-Pu: “screening experiments” and “redox experiments”. The initial, screening sorption experiments (Section 2.4.5) were conducted only in the presence of HQ as redox-buffering agent. These batch experiments aimed at assessing the kinetics of the sorption processes and the analytical detection limit of Pu in the system with regard to added initial Pu total concentrations ($[Pu]_{in}$) and to the S:L ratios to be applied for later investigations.

The more extensive experiments on the binary, cement-Pu system, denoted as the “redox experiments” involved the use of three redox-buffers in solution: HQ, Sn(II) and $Na_2S_2O_4$. Experimental description on this system is also detailed in Section 2.4.5. These experiments served also for comparison purposes with regard to the HQ-buffered case, where $Pu(IV)_{aq/s}$ is expected to dominate speciation of Pu. Furthermore, in the course of this investigation, at two fixed S:L ratios and $[Pu]_{in}$ concentrations, the uptake of Pu(III/IV) by the hydrated OPC phase was evaluated to set general R_d values applicable to the specific conditions of the present study (in the absence of ISA, denoted as $R_{d,in}$).

Series of sorption batch experiments on the ternary system Cement-Pu-ISA were conducted at various S:L ratios and at two total ligand concentrations $[ISA]_{tot} = 10^{-3}$ M and 10^{-2} M in the presence of the previously used redox buffers with two different orders of preparation. Related experimental details are listed in Section 2.4.6. These investigations were aimed to assess the impact of ISA on the uptake of Pu by the OPC pastes.

Preparation details on the complementary experiments are discussed in Section 2.4.7. In the course of these investigations, desorption experiments and undersaturation solubility experiments coupled with sorption experiments were conducted. Desorption experiments were performed with selected samples of the HQ-buffered, well-equilibrated initial screening experiments by replacing the supernatant solutions with ISA-containing porewater solutions. These experiments were intended to test the reversibility of the ternary system in the sense of evaluating the potential incorporation processes of Pu(IV) into the hydrated phases of the cement pastes with extended allowed equilibration times and its impact on the sorption reduction capabilities of ISA.

As a complementary experiment, undersaturation solubility experiments were also prepared by introducing the previously well-characterized initial, PuO_2(am,hyd) solid phase (see Section 2.3.1 and reference [1] for details) into the porewater solutions with ISA at different total concentrations of the ligand. After reaching equilibrium conditions, the validity of the formerly established thermodynamic, solubility model on the Ca(II)-Pu(IV)-OH-ISA system was examined upon the collected data. The later separated supernatants of these solutions

were applied in the course of additional sorption experiments as well. These solutions were mixed at different S.L ratios with fresh cement powder, aiming at strictly investigating sorption excluding the possibility of precipitation of a Pu(IV) solid phase.

In the course of all sorption experiments with Pu, a systematic sampling method was followed. Related experimental details on the undertaken procedures are discussed in Section 2.5.

2.4.1 Initial cement powder

The first step in the powdering process of the received cement specimens was a manual crushing. Further reduction of the particle size was achieved by the use of an agate-ball (m = 0.50 kg, diameter of 70 mm) mill (®pulverisette 0, Fritsch Gmbh) under ambient conditions. Different particle-size fractions were gained through a continuous-flow, vibrational sieving mill (®pulverisette 0, Fritsch Gmbh) equipped with stainless steel sifters. The fraction with an average particle diameter-size of d_{av} < 100 μm was used for all sorption experiments performed (hereafter it is generally denoted as the initial cement powder) and for the generation of the leached porewater solution as well (simulating stage II of the cement degradation process, for further details see Section 2.4.2). The resulting powder was analyzed by means of different solid and (after acidic digestion) liquid phase characterization methods, namely: X-ray powder diffraction (XRD), X-ray photoelectron spectroscopy (XPS), thermogravimetric analysis coupled with differential scanning calorimetry (TG-DSC), inductively coupled plasma–optical emission spectrometry and –mass spectrometry (ICP–OES and ICP–MS). Experimental details on the application of these methods are given in Section 2.5. As the later data evaluation did not involve the use of thermodynamic parameters related to the present cementitious phases within the hydrated pastes, the performed solid phase characterization campaign was limited to the qualitative identification / detection of the major phases (focusing mainly on Portlandite).

2.4.2 Cement porewater

For the synthesis of the cement porewater solution, simulating Stage II of the cement degradation process, Milli-Q water (1.8 dm^3) was combined with the powdered cement solid phase at 25 gdm^{-3} S:L ratio. The solution was systematically analyzed (after a centrifugation step at 4’020 *g* for 15 mins) for the prevailing pH condition and the quantity of the major (Na, K, Ca, Mg) and minor (Al, Ti, V, Cr, Mn, Fe, Co, Ni, Cu, Rb, Ba, Pt) component-concentrations by ICP-OES and ICP-MS techniques. Equilibrium conditions, *i.e.* steady major

metal ion concentrations and constant pH values were observed to be reached within 1 week of contact time.

This initial leachate, after one month of allowed contact-time, was separated via sedimentation from the HCP and replaced with fresh Milli-Q water to gain the final porewater solution.

For the generation of sorption experiments, various amounts of the newly gained porewater were firstly separated from the main stock and centrifuged (at 4'020 *g* for 15 mins) for the removal of unwanted cement particles. The resulting clear supernatant solutions were serving as the porewater (liquid phase) in the course of all sorption experiments performed. The pH value of this solution was frequently measured and it was also analyzed for the minor and major elemental components in solution as well as for TOC/TIC contents. A small quantity (~0.1 g) of the cement phase in equilibrium with the porewater was taken in a suspension and separated by centrifugation (at 4'020 *g* for 15 mins) after ~10 months of equilibration time (after the preparation of the sorption experiments). Hydration stoppage was achieved with propan-2-ol and the dried powder was characterized by means of XRD, XPS and TG-DSC methods (see Section 2.6 for details).

2.4.3 Cement–ISA system

The uptake of ISA by the OPC paste used in this study was investigated in two series of independent batch experiments (with V_{liquid} = 5 cm^3 and 11 batches in total). In one case, at a constant S:L ratio of 4 gdm^{-3}, $[ISA]_{tot}$ = 10^{-2}, 10^{-3}, 10^{-4}, 10^{-5} M were set and in the other, at fixed $[ISA]_{tot}$ = 10^{-3} M, S:L ratios of 2, 4, 8, 15, 20 and 50 gdm^{-3} were applied. Furthermore, to assess the organic carbon content leaching from the HCP (originating from the presence of various additives in the material), an analogous series of experiments with identically set S:L ratios was also prepared in the absence of ISA.

The pH conditions were systematically monitored for all samples. After 7 days and 14 days of allowed contact time for the ISA-containing experiments, aliquots of the supernatant solutions subsequent to a centrifugation step performed (at 4'020 g for 15 mins) were pipetted in diluted HNO_3 solutions (2 w/w%) and were analyzed for non-purgeable organic carbon-content (NPOC) by the use of the previously applied Shimadzu TOC5000 instrument. To assess the proper background organic carbon content (related to impurities within the HCP), bigger volumes were analogously separated from the experiments without ISA and measured for NPOC.

As the main condition of interest for the Cement-Pu-ISA system was at 2 gdm^{-3} S:L ratio, the sample with $[ISA]_{tot}$ = 0.01 M concentration was characterized (at t_{eq} = 14 days) more extensively to ensure the retainment of Portlandite in the system at high ISA total concentrations. The supernatant was also analyzed for major (Na, K, Ca, Mg) and minor (Al, Ti, V, Cr, Mn, Fe, Co, Ni, Cu, Rb, Ba, Pt) component-concentrations by ICP-OES and ICP-MS techniques and furthermore the treated cement solid phase was retrieved by centrifugation (hydration stoppage was achieved by the use of propan-2-ol) and characterized with XRD, XPS and TG-DSC techniques as described in Section 2.6.

2.4.4 Pu(VI) stock solution

The source of Pu was an acidic stock solution of Pu(VI) prepared by the dissolution of an electrochemically synthetized $Na_2Pu_2O_7{\cdot}xH_2O$(am) solid phase. (Details on the exact preparation procedure and the characterization results of the latter solid phase are reported elsewhere [129].) A small quantity of this solid phase was compacted and separated from the supernatant solution (0.005 M NaClO in approx. 1.5 M NaOH) via four centrifugation steps at (4'020 *g* for 15 mins). The paste was washed with a NaOH solution of pH_c = 11 (300 μL) to remove the hypochlorite-content of the remaining supernatant. After an additional separation by centrifugation (at 4'020 *g* for 15 mins), 1.50 cm^3 of 0.01 M HCl solution was added to the solid phase and it was further titrated with 1.00 M HCl solution until complete dissolution (total volume required: 110 μL). In order to maintain the strongly acidic conditions within the stock (pH_c = 0.72 – 1.2), 180 μL of the 1.00 M HCl were added to the solution. The resulting stock solution was characterized and further monitored by means of spectrophotometric measurements, in the wavelength range of λ = 200–1020 nm using a UV-Vis-NIR spectrophotometer (Carl Zeiss AG, MSC-500 system, double-beam instrument). Measurement of the sample (in PMMA cuvettes with 1 cm light-path length, Brand Gmbh & Co.) within the glove-box under protective Ar-atmosphere was enabled by an optical fiber and a mobile sample-holder (Harrick, FiberMate™). Data collection was performed in a single-beam mode, with 0.1 nm data interval at a scan-rate of 50 $nmmin^{-1}$ and a slit-width of 0.5 nm. Baseline correction was executed using the spectra of a Pu-free reference solution with identical ionic strength and acidity. Recorded spectra were not used for quantification purposes, but only served as a qualitative identification of prevailing redox states of Pu in the stock solution before and after the preparation of the sorption experiments (t_{eq} = "0 d" and 1.2 years, respectively). Final total Pu concentration of the stock solution after dilution with 2 % HNO_3 solution was quantified by ICP-MS and LSC methods, as described in Section 2.5. Details on

the preparation and characterization results of the main stock solution is provided in the Appendix (section 6.4). The Pu(VI) stock solution was diluted for further use and aliquots of the less concentrated stock solutions were introduced to batch sorption experiments to reach an approximate total initial Pu concentration of ~10^{-6} or ~10^{-9} M.

2.4.5 Cement–Pu system

Experiments on the binary cement-Pu system can be separated into two series: "screening experiments" and "redox experiments".

Screening experiments

In the course of the screening experiments (11 individual batches with total aqueous phase volume: V_{tot} = 10 cm^3), the weighted cement powder was added to the porewater containing HQ in solution (with 2 mM total concentration applied) at varying S:L ratios of ~0.1 gdm^{-3} – 4 gdm^{-3}. Prior to the introduction of Pu, samples were let to equilibrate for 2 days and pH_c, E_h values in the centrifuged supernatants were collected. Very small volumes (10 – 20 μL) of the diluted Pu stock solutions were pipetted into these systems, aiming at log $[Pu]_{in}$ ~ -6 or -9.

After the addition of Pu, the values of pH_c, E_h and total Pu concentrations in the aqueous phase, $[Pu]_{aq}$, were monitored for 3 months. $[Pu]_{aq}$ was measured after centrifugation at 4'020 *g* for 15 mins, either as clear supernatant solution or after sub-sequent phase separation (ultrafiltration or ultracentrifugation). Characterization procedures performed to quantify Pu total concentrations in the aqueous phase are detailed in Section 2.5.

Well-equilibrated solid phases of selected samples were separated (by centrifugation at 4'020 g for 15 mins) at t_{eq} = 167 d and applied as pastes in the course of desorption experiments with ISA to test the reversibility of the uptake process. Details on the preparation of these batch experiments are given in Section 2.4.7.

Redox experiments

In the second set of experiments (12 batches, with V_{tot} = 10 cm^3), the cement powder was mixed with porewater solutions at two S:L ratios = ~0.1 gdm^{-3} or ~2 gdm^{-3} in the presence of HQ or Sn(II) or $Na_2S_2O_4$ in solution (with 2 mM total concentrations). In all cases, 2 days of pre-equilibration time was allowed for the systems, before Pu was inserted as small aliquots of the stock solutions to reach log $[Pu]_{in}$ = -6 or -9 under each reducing conditions.

After the addition of Pu, pH_c, E_h values in the clear solutions and $[Pu]_{aq}$ concentrations were collected in the time-frame of ~4 months (characterization procedures performed to quantify Pu total concentrations in the aqueous phase are detailed in Section 2.5.)

To assess the prevailing redox state and the potential precipitation of Pu in selected systems (S:L ratio = 2 gdm^{-3}, log $[Pu]_{in}$ = -6, t_{eq} = 132 d) the cement pastes were retrieved by centrifugation (at 4'020 *g* for 15 mins) and analyzed *in-situ* by Pu L_{III}-edge XANES measurements (for Sn(II)- and HQ-buffered systems). A fraction of dry solid (without hydration stoppage) was also characterized by XPS (only for the HQ-buffered sample).

2.4.6 Cement–Pu–ISA system

Experiments on the ternary, Cement-Pu-ISA system are classified in three different series as a function of the applied solid-to-liquid ratios: 1. *"0.2 gdm^{-3} S:L"* series; 2. *"2 gdm^{-3} S:L"* series and 3. *"0.2 – 50 gdm^{-3} S:L"* series.

All batch experiments were set up following two orders of preparation (see Figure 5 for clarification): (i), the hydrated cement phase was let in equilibrium with the introduced Pu and redox buffer in the porewater solution (for t_{eq} = 2 d) and then the ISA was added to this system as pipetted from a stock solution or (ii), Pu and ISA were allowed to equilibrate in the porewater solution (together with the redox buffer) for 2 days and then the given, weighted amount of fresh cement powder was added to this solution to reach the aimed S:L ratio. The sorption experiments conducted using the former order of preparation are hereafter referred to as the "(Pu + Cement) + ISA" experiments, whilst in the latter case, "(Pu + ISA) + Cement" order is used to denote the differences in the applied preparation order.

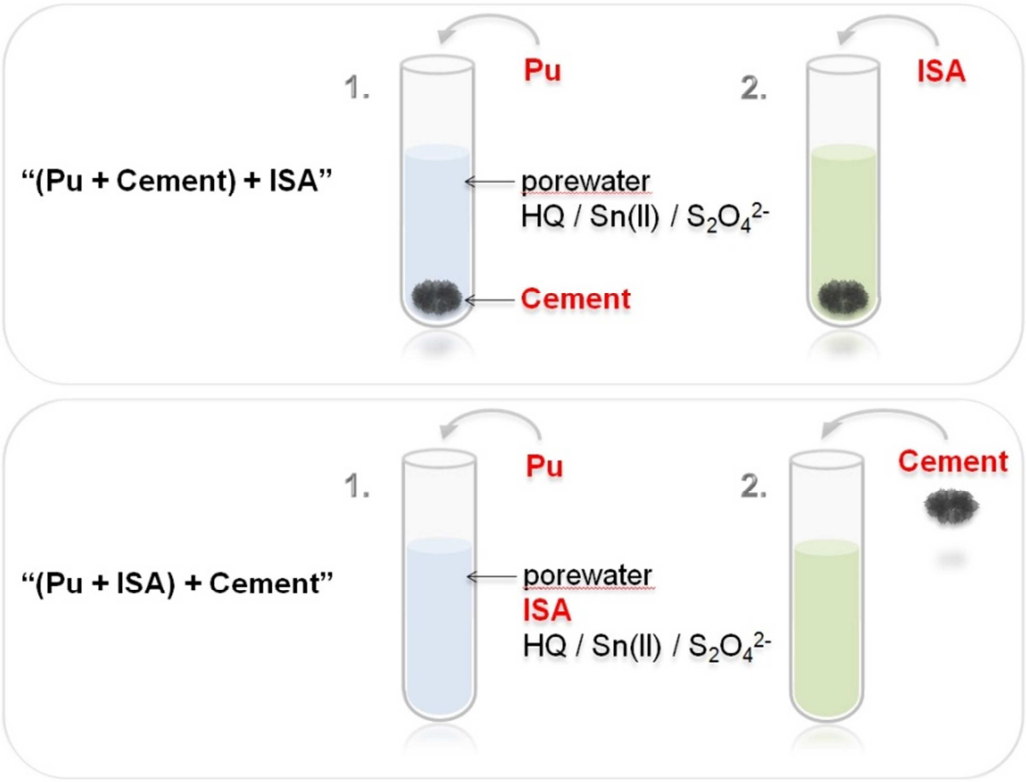

Figure 5. *Illustration for the order of addition followed in the course of sorption experiments on Cement-Pu-ISA system: "(Pu + Cement) + ISA" or "(Pu + ISA) + Cement".*

0.2 gdm^{-3} S:L series

Across the *0.2 gdm^{-3} S:L* series of experiments (24 in total), a constant value with 0.2 gdm^{-3} was applied as S:L ratio with regard to the weighted cement powder and the volume of the used porewater solution (with V_{tot} = 10 cm^3). ISA was added by pipetting from the corresponding stock solution to reach either $[ISA]_{tot} = 10^{-2}$ or 10^{-3} M in the porewater matrix solution. At each ligand total concentration, samples were conducted with all the three different previously used redox-buffers (HQ or Sn(II) or $Na_2S_2O_4$ in solution at 2 mM total concentrations). Before introducing Pu into the system, pH_c and E_h values in the matrix solutions were measured to ensure that the reducing conditions are maintained and constant.

Aliquots of Pu stock solutions were added aiming at a log $[Pu]_{in}$ = -6 or -9. After the introduction of Pu to the samples, they were let to equilibrate for 2 days (in both experimental preparation order) and then the aimed sorption experiments were initialized by introducing the third part into the system (either the ISA, pipetted from the stock solution or the weighted fresh cement powder), as discussed above.

After the initialization of the sorption experiments, pH_c, E_h values in the clear solutions and $[Pu]_{aq}$ concentrations were collected in the time-frame of ~4 months (characterization

procedures performed to quantify Pu total concentrations in the aqueous phase are detailed in Section 2.5).

The redox state of Pu in selected samples of this series (S:L ratio = 0.2 gdm^{-3}, log $[Pu]_{in}$ = -6, t_{eq} = 130 d) was further investigated by means of Pu L_{III}-edge XANES measurements. For this purpose the cement pastes were compacted by a centrifugation step (at 4'020 *g* for 15 mins) and analyzed as *in-situ* by Pu L_{III}-edge XANES measurements (for Sn(II)- and HQ-buffered systems) and as dried powders (without hydration stoppage) by XPS method (only for the HQ-buffered sample).

2 gdm^{-3} S:L series

The *2 gdm^{-3} S:L* series of batch experiments (18 samples in total) were conducted similarly as the *0.2 gdm^{-3} S:L* series, except for a few differing experimental parameters. In the present series the applied S:L ratio was increased to 2 gdm^{-3}, and only two redox-buffers were investigated (HQ or $Na_2S_2O_4$, (2 mM in each case). Total ligand concentrations were $[ISA]_{tot} = 10^{-2}$ or 10^{-3} M. Before the insertion of Pu, pH_c and E_h values were collected within the matrix solutions. Initial total plutonium concentrations were set to log $[Pu]_{in}$ = -6 or -9, just as previously.

Further experimental details as the order of preparation and the sampling procedure are also identical to those of the former, *0.2 gdm^{-3} S:L* series. Allowed equilibration time was t_{eq} = ~4 months in the course of this series as well.

0.2 – 50 gdm^{-3} S:L series

Within the *0.2 – 50 gdm^{-3} S:L* experimental series (12 samples in total), at a constant total ligand concentration of $[ISA]_{tot} = 10^{-2}$ M in the matrix solutions with V_{tot} = 5 cm^3, the applied S:L ratio was modified between the batches to reach the values of 4, 5, 8, 10, 20 and 50 gdm^{-3}. Only HQ was used as the redox-buffering agent. Prior to the initialization of the experiments applying the two different preparation order, pH_c and E_h values of the porewater solutions were collected to determine the prevailing redox conditions. Initial total Pu concentration was set to log $[Pu]_{in}$ = -6 in all cases.

Further related experimental details on the preparation and on the sampling procedure followed in the present experiments are identical to those of the previously discussed two cases (*0.2 and 2 gdm^{-3} S:L* series).

2.4.7 Complementary experiments

The complementary experiments consisted of two series: i. “undersaturation solubility coupled sorption” experiments, and ii. “desorption experiments”.

Undersaturation solubility coupled sorption experiments

The sorption experiment series denoted as “*Undersaturation solubility coupled sorption*” consisted of two main steps.

Firstly, a series of HQ-buffered (2 mM), cement porewater matrix solutions (a total number of 11, each with V_{tot} = 10 cm^3) were prepared with $[ISA]_{tot}$ ranging from 10^{-5} M to 10^{-2} M. The formerly well-characterized PuO_2(ncr) solid phase was introduced in the matrices, identically as in the course of the solubility studies [1, 2]. After 54 days of allowed contact time (equilibrium conditions with regard to collected pH_c, E_h values and $[Pu]_{aq}$ were attained at t_{eq} of 2 - 3 weeks), a centrifugation step was performed (at 4’020 g for 15 mins) and 5 cm^3 of the supernatant solutions (saturated with PuO_2(cr)) were pipetted onto different amounts of the weighted fresh, initial cement powder. The conducted sorption experiments were aimed to reach either a constant S:L ratio of 4 gdm^{-3} where $[ISA]_{tot}$ was applied at 10^{-5}, 10^{-4}, 10^{-3} or 10^{-2} M concentrations (4 samples) or to maintain at a constant level of $[ISA]_{tot}$ = 10^{-3} M concentration, varying S:L ratios with 0.2, 2, 4, 8, 15, 20, 50 gdm^{-3} values (7 samples).

After the insertion of the cement phases, pH_c, E_h values in the clear solutions and $[Pu]_{aq}$ concentrations were collected in the time-frame of 1 months (characterization procedures performed to quantify Pu total concentrations in the aqueous phase are detailed in Section 2.5).

Desorption experiments

Desorption experiments were conducted using the well-equilibrated solid phases separated from the supernatant solutions of selected samples from the *screening experiments* (see Section 2.4.5). The solid phases were retrieved by centrifugation (at 4’020 g for 15 mins) at t_{eq} = 167 d from 6 individual batches with S:L ratios of 0.2 – 2.5 gdm^{-3} and log $[Pu]_{in}$ = -6 or -9 and applied as pastes within the present experimental series. After phase separation, the previous supernatants were immediately replaced with HQ-buffered (2 mM), ISA-containing porewater solutions at $[ISA]_{tot}$ = 10^{-3} M or 10^{-2} M, whilst keeping the original container.

After the initialization of the experiments, pH_c, E_h values in the clear solutions and $[Pu]_{aq}$ concentrations were collected in the time-frame of 4 months (characterization procedures performed to quantify Pu total concentrations in the aqueous phase are detailed in Section 2.5).

2.5 Characterization of aqueous phases

The quantification of total Pu concentrations in the aqueous phase of the Pu solubility and sorption experiments was performed in a well-defined, systematic procedure.

Exclusively for the sorption experiments, samples (as stored in 10 mL Sarstedt vials) were firstly centrifuged at 4'020 *g* for 15 mins, in order to gain better separation between the aqueous and solid phases present. In the course of the solubility experiments, the samples were let standing for 1 day, avoiding any mechanical influence to facilitate the sedimentation process. In each case, aliquots of 100 – 350 μL were carefully taken from the clear supernatants, avoiding any external mechanical influence (causing the potential resuspension of Pu-solid phases or cement particles) and either transferred to vial with a 10 kDa filter (pore size ≈ 2–3 nm, Nanosep ®, Pall Life Sciences) or directly acidified with 2% HNO_3 solution. Note that the measurements conducted on the supernatants aimed at evaluating the possible presence of Pu(IV) intrinsic colloids in the system. Phase separation was achieved at 4'020 g (15 mins) on the given 10 kDa filter and the resulting solutions were immediately acidified (using 2% HNO_3 solution). For selected samples, phase separation was (also) performed using a bigger volume of the supernatant solution (3 – 4 cm^3) by ultracentrifugation (Beckman XL-90, rotor type 90Ti) at 90'000 rpm (694'000 *g*) in welded vials for one hour. In each case, the acidic solutions were analyzed for the aqueous total concentration of Pu using liquid scintillation counting (LSC, see Section 2.5.1), standard inductively coupled plasma mass spectrometry (ICP–MS) or sector field inductively coupled plasma mass spectrometry (SF–ICP–MS). The detection limits (DL) of the latter two techniques for Pu in the conditions of the present study are ~$10^{-10.5}$ M (ICP–MS) and ~10^{-13} M (SF–ICP–MS).

The quantified plutonium concentrations in molar units (M) (and potentially other concentrations evaluated in this study as well) were often converted to the molal scale (m, $mol \cdot kg_w^{-1}$) using the conversion factors reported for NaCl solutions in the NEA-TDB [9]. Total concentrations of Pu collected in the course of the solubility studies are referred to as $m(Pu)_{tot}$ (in molal units), whilst values related to sorption experiments are denoted as $[Pu]_{aq}$ (in molar units, given the ill-defined ionic strength).

2.5.1 Liquid Scintillation Counting of ^{242}Pu

Liquid Scintillation Counting (LSC) was used for the quantification of $[Pu]_{tot}$ in those samples with higher concentration of plutonium in solution (> ~10^{-9} M). The isotopic composition of Pu stock solution and solid phases used in this study includes α-(^{242}Pu, ^{239}Pu, ^{238}Pu) and β-

(^{241}Pu) emitters (see Section 2.1), as well as traces of the α-emitter ^{241}Am resulting from the decay of ^{241}Pu ($t_{1/2}$ = 14.35 a). Due to the very close energy of the α-peaks of ^{242}Pu, ^{239}Pu, ^{238}Pu and ^{241}Am and the uncertainty associated to the contribution of ^{241}Am to the total counts, the concentration of Pu in solution was quantified using the signal of the low-energetic β-emitter ^{241}Pu.

Aliquots of the untreated supernatant (including potential colloidal fraction) and of the 10 kD ultrafiltered sample were acidified with 2% HNO_3 and mixed with 10 mL of LSC cocktail (Ultima Gold XR, Perkin Elmer). LSC measurements were performed on a low-level LSC equipment type Quantulus 1220 (LKB WallacOy, Turku, Finnland, currently PerkinElmer) for 30 minutes. Standard addition with 50 µL of a well-defined Pu stock solution ($4.36 \cdot 10^{-7}$ M or $3.18 \cdot 10^{-7}$ M) with the same isotopic composition was used to overcome the effect of the matrix solution on the counting efficiency of ^{241}Pu of unknown samples.

The detection limit of the LSC technique in the conditions of this study is about ~$10^{-9.2}$ M, clearly above the expected solubility of PuO_2(am,hyd) under alkaline pH conditions. Thus, the quantification of Pu concentration in most of the samples was performed using ICP–MS and SF–ICP–MS techniques with the variation of different phase separation methods (see Section above).

2.5.2 Liquid-liquid extraction

The oxidation state of Pu in the aqueous phase was determined for selected samples using a liquid-liquid extraction method described in [5]. The method is a combination of previously reported approaches [130-134], and allows the quantification of Pu(III), Pu(IV), Pu(V), Pu(VI) and colloidal Pu(IV) with an uncertainty of 20% (for the Pu concentration-range evaluated in this study). Owing to the slower redox transformation kinetics of $Pu^{n+} \leftrightarrow PuO_2^{z+}$ reaction, the method itself is proven to be more reliable for the relative quantification of Pu redox states in groups, as follows: (Pu(III) + Pu(IV)) and (Pu(V) + Pu(VI)).

The extraction was performed after 10 kD ultrafiltration for those samples with $m(Pu)_{tot} \geq 10^{-7}$ m (acidic series, pH_m = 3.76, 3.86). The used extractants were PMBP dissolved in xylene and HDEHP dissolved in toluene for the separation of Pu(IV) and (Pu(IV) + Pu(VI)), respectively. The combination of both extraction steps with an additional oxidation step (using $K_2Cr_2O_7$) of Pu(III) to Pu(IV) and Pu(V) to Pu(VI) reveals the complete redox state distribution of Pu in the aqueous phase (see Table 4 for details).

Table 4. *Distribution of Pu oxidation states in the organic and aqueous phases according to the extraction method used in this work (see text for more details).*

Method	Oxidation State Distribution	
	Organic Phase	**Aqueous phase**
PMBP extraction at pH = 0	Pu(IV)	Pu(III), (IV)coll*, (V), (VI)
PMBP extraction at pH = 0, with $K_2Cr_2O_7$	Pu(III), (IV)	Pu(IV)coll*, (V), (VI)
HDEHP extraction at pH = 0	Pu(IV), (VI)	Pu(III), (IV)coll*, (V)
HDEHP extraction at pH = 0, with $K_2Cr_2O_7$	Pu(III), (IV), (V), (VI)	Pu(IV)coll*

*Pu(IV)coll refers to the colloidal species of Pu(IV)

After the separation of the aqueous and organic phases, both aliquots were added to 10 mL of LSC cocktail and the Pu concentration was determined by LSC. The same extraction procedure was carried out with MilliQ water to correct for the contribution of changes in the background electrolyte solutions within the LSC measurements. This is especially important due to the presence of organic solvents and colored reagents that can eventually lead to quenching effects.

2.5.3 CE-SF-ICP-MS

For the validation of the liquid-liquid extraction method and for the analysis of further selected samples (supernatant solutions or after 10kD ultrafiltration), the oxidation state distribution of Pu was also investigated by capillary electrophoresis hyphenated sector-field-ICP-MS technique (CE-SF-ICP-MS). All separations were carried out using a commercial Beckman Coulter P/ACE MDQ capillary electrophoresis system. Conventional fused-silica 75 µm internal diameter capillary with 73 cm length was used for separation. Prior to application, the capillaries were conditioned for several hours by rinsing with 0.1 M HCl (Merck, Suprapur), 0.1 M NaOH (Merck, Titripur), Milli-Q water and with the background electrolyte: 1.00 M acetic acid (BGE). During the separation, the temperature of the capillary was kept constant, at 15 °C by the use of a surrounding liquid cooling agent within the

instrument. Under the given experimental conditions, the temperature gradient across the capillary's cross section was estimated to be 0.7 °C. The hyphenation of the CE to the SF-ICP-MS (Thermo Element XR) instrument was achieved via using a Mira Mist CE nebulizer (Burgener Research, Mississauga, ON, Canada).

The capillary was washed with the BGE for 5 min at 20 psi before each measurement. Separations were performed with +30 kV applied potential at a constant pressure of 0.4 psi and accomplished within 20 min. The rinsing sequence after each separation was 5 min (1 min 0.1 M HCl, 1 min 0.1 M NaOH, 3 min BGE). The sample injections (with volumes of appr. 2.3 nL) were achieved hydrodynamically at 2 psi for 10 seconds. In order to exclude redox phenomena induced by oxygen, the CE apparatus was placed in a N_2 glovebox with O_2 < 5 ppm. A more detailed description of the installation and the implementation of the performed measurements is given in [135].

2.6 Characterization of solid phases

For selected cases, solid phases retrieved from various experiments were analyzed by means of complementary characterization techniques as listed in this section.

In the case of solubility experiments, the Pu(IV) hydrous oxides were first compacted by centrifugation at 4'020 g for 15 minutes, then retrieved from the samples and washed four times with ethanol under Ar-atmosphere in order to remove the traces of background electrolyte (NaCl). The resulting solid was re-suspended with 25 µL ethanol and used further for analysis. (for *in-situ* XRD and Pu L_{III}-edge measurements, the pre-treatment was not applied, see related section for further details.)

The initial cement powder as well as equilibrated cement solid phases were characterized by means of various techniques listed below. For selected, equilibrated samples (only in the absence of Pu) the cement solid phases (with m_{cement} = 0.08 – 0.5 g) were treated with propan-2-ol (20 cm^3) to stop the hydration process. The retrieved paste after a centrifugation step (at 4'020 *g* for 15 min) was soaked in the organic phase for 20 minutes, then the suspension was filtered through a PTFE membrane with 5 µm pore size (Millipore) using a vacuum pump (Becker). In order to obtain the well-dried powder for analysis, it was additionally placed in a heating oven for 20 minutes at 40 °C and, if necessary, the samples were further stored in sealed vials under Ar atmosphere.

2.6.1 Quantitative and semi-quantitative chemical analysis

Quantification of the minor (transition metal-content) and major elemental components (Ca, Si, Al, Na, Mg, S, Fe) were performed for the initial cement powder to validate the retainment of the chemical composition as provided by the manufacturer after the powdering and sieving procedure. For this purpose, 200 mg of the cement powder were dispersed in 1500 mg of melted KOH. The molten mixture was then let cool down and was dissolved in 30 cm^3 of concentrated HCl solution. The clear solution was then filled up to 250 cm^3 with Milli-Q water. The dissolved contents of Ca, Si, Al, Na, Mg, S, Fe were quantified by ICP–OES (Optima 8300 DV, Perkin Elmer), whilst the concentration of minor components were determined by ICP–MS (X-Series II, Thermo Scientific) in a semi-quant mode (up to 60 elements included in the scan). The accuracy of the scanning-type, semi-quantitative characterization is approximately ± 50%. As KOH was involved the preparation of the cement material for the characterization, the method did not allow the quantification of K in the original sample.

2.6.2 Standard X-ray powder diffraction

For standard XRD analysis of Pu-hydrous-oxides, ~0.5 mg of the pre-treated solid phase was placed on a single crystal silicon waver and dried up at room temperature under Ar atmosphere. In case of hydrated cement samples, approximately 50 mg of the dried cement powder (initial powder, or pre-treated equilibrated phases) were placed on the waver. XRD measurements were performed using a D8 Advance diffractometer (Bruker AXS) equipped with a Cu radiation tube (Cu K-α, λ = 0.15418 nm, current: 25 mA, voltage: 40 kV), Ni filter and a Sol–X detector. For Pu-hydrous-oxide samples, the XRD pattern was recorded in the range of $5 \leq 2\,\Theta \leq 80°$ with a step size of 0.015° and a counting time of 6 seconds per step. For cement solid phases, the measurement was executed with 15 rpm horizontal spin-rate in the range of $2 \leq 2\Theta \leq 98°$ with a step size of 0.01° and a counting time of 15 seconds per step. Data processing was performed using the Bruker AXS Diffrac^{Plus} EVA software (Bruker AXS, Germany, version 3.1). The resulting diffractograms were compared to the XRD patterns of the possible relevant solid phases available in the JCPDS database [136]. Rietveld refinement of selected diffractograms was performed with the Bruker Diffrac^{Plus} TOPAS software package (Bruker AXS, Germany, version 4.2).

2.6.3 X-ray photoelectron spectroscopy

Selected solid phases (pre-treated equilibrated, hydrated cement solid phases or pre-treated Pu-hydrous-oxides) for XPS analyses were prepared (in concentrated suspensions) onto an indium foil and mounted on a sample holder under anoxic conditions (Ar atmosphere). XPS measurements were performed using a PHI 5000 VersaProbe II (ULVAC-PHI Inc.) system equipped with a scanning microprobe X-ray source (monochromatic Al Kα (1486.7 eV) X-rays) in combination with an electron flood gun and a floating ion gun generating low energy electrons (1 eV) and low energy argon ions (6 eV) for charge compensation at isolating samples (dual beam technique), respectively. Survey scans were recorded with an X-ray source power of 31 W and pass energy of 187.85 eV. Narrow scans of the elemental lines were recorded at 23.5 eV pass energy of the analyzer which yields an energy resolution of 0.69 eV full width at half maximum (FWHM) on the Ag $3d_{5/2}$ elemental line of pure silver. Calibration of the binding energy scale of the spectrometer was performed using well-established binding energies of elemental lines of pure metals (monochromatic Al K_α: Cu $2p_{3/2}$ at 932.62 eV, Au $4f_{7/2}$ at 83.96 eV) [137]. C 1s of hydrocarbon at 284.8 eV is used as charge reference. Error of binding energies of elemental lines is estimated to be ± 0.2 eV. Data analysis was performed using ULVAC-PHI MultiPak program, version 9.6.0.

2.6.4 Thermogravimetric analysis, differential scanning calorimetry

TG-DSC was performed with a STA409 (Netzsch Gerätebau GmbH) on 20 – 50 mg of the (treated or untreated) dry cement powder samples, applying a heating rate of 10 °C/min from 25 to 1200 °C under N_2 atmosphere. The crucibles are made of Al_2O_3 (corundum) and the sample holder is a type S Pt 10% / Pt-Rh. The high temperature Pt oven can be operated in the range of RT to 1500°C.

2.6.5 Brunauer–Emmett–Teller surface area measurements

The specific surface area of the initial cement powder was measured by means of the Brunauer–Emmett–Teller method. The used instrument was a Quantachrome Autosorb Automated Gas Sorption System with N_2(g) adsorbate. Analysis was performed on ~0.5 g of the freshly grinded, well-homogenized powder for 70 mins at an outgas temperature of 105 °C applying a multi-point method.

2.6.6 *In-situ* XRD and Pu L_{III}-edge XANES measurements

XAFS (X-ray Absorption Fine Structure) spectra and Laue-type diffractograms were recorded on various, selected samples as *in-situ* under the protective, supernatant solutions at the INE–Beamline for Actinide Research at KARA, KIT Campus Nord [138]. The KARA storage ring was operated at 2.5 GeV electron energy with a mean electron current of 120 mA.

The tunable monochromatic beam was delivered by a double crystal monochromator (DCM), equipped with a pair of Ge(422) crystals (2d = 2.310 Å). Possible higher harmonic radiation was suppressed by detuning the parallel alignment of the crystals to obtain 70% of photon flux peak intensity at the rocking curve maximum.

All samples for XAFS and (synchrotron-based) *in-situ* XRD measurements were prepared in 400 µL polyethylene vials. A suspension containing ≈ 1 mg (for pure Pu-hydrous-oxides) or ≈10 – 20 mg of material (for equilibrated, hydrated cement pastes, without any pre-treatment) were transferred to the vial and centrifuged for 10 min at 4'020 *g*. For Pu-hydrous-oxide samples (when *in-situ* XRD measurements were also performed), the vials were heat sealed in a plastic bag (polyethylene). All samples were mounted in a gas-tight cell inside the Ar-glovebox and transported to the INE-Beamline. During the XAFS measurements, Ar was continuously flushed through the cell to ensure the presence of an inert atmosphere. Data collection was performed at T = (22 ± 2) °C.

XANES spectra of the Pu L_{III}-edge (E ($2p_{3/2}$) Pu(0): 18,057 eV) were recorded in fluorescence yield detection mode using a 5-pixel low energy Ge solid-state fluorescence detector (Canberra-Packard Ultra-LEGe, Olen, Belgium) and an Ar-filled ionization chamber at ambient pressure to record the incident beam intensity. 8–10 scans were collected for each Pu sample. The spectra were calibrated against the first inflection point in the K-edge spectrum of a Zr metal foil (E (1s) Zr(0): 17,998 eV) and averaged to reduce statistical noise. XANES and EXAFS data reduction were performed with the ATHENA program package [139], following standard procedures for edge jump normalization and EXAFS χ(k) extraction. E_0, the origin for calculating the EXAFS χ(k)-function, was fixed at the 'white line' (WL) peak maximum in the XAFS spectra at ≈ 18,068 eV. The Pu L_{III}-edge XANES spectra obtained in this work were compared with Pu(III) and Pu(IV) reference spectra collected at the INE-Beamline under the same experimental conditions and data analysis procedure [1, 7, 140].

EXAFS data analysis was based on standard least squares fit techniques using the UWXAFS program package [141] (The procedure was executed by Dr. Jörg Rothe). Metric parameters (*i.e.*, neighboring atom distances R_i, EXAFS Debye-Waller factors σ^2_i, coordination numbers N_i for the different coordination shells i) were determined using the feffit code (v2.98).

Backscattering amplitude and phase shift functions for single scattering paths in a 45-atom PuO_2 cluster with fluorite structure were obtained from FEFF8.2 calculations [142]. All fit operations were performed in R-space over the individual radial distance ranges given in Table 3. The amplitude reduction factor: S_0^2 was fixed at 1.0.

After completing the XAFS data accumulations, for selected, purely Pu-hydrous-oxide samples, the sealed vials in the double-containment were individually taken out of the Ar-flushed sample cell, and the *in-situ* diffractograms were collected as well. The double containment (vial and an outer plastic bag) in addition to the redox buffers in the protecting solution (hydroquinone and Sn(II)) underneath the Ar atmosphere are considered to be sufficient to avoid any redox transformation of the bulk material within the timeframe of the XRD measurements (approximately 5-10 minutes).

The 2D XRD patterns were recorded in Laue transmission geometry using radiation sensitive high efficiency storage phosphor screens (V×H: 125mm × 252mm) with a high dynamic range (MultiSensitive Phosphor Screen, PerkinElmer, Germany). The screen was mounted perpendicular to the incident beam (E = 17.0 keV, λ_{exc} = 0.7 Å, size (V×H) 200µm × 500µm) at a distance of 20 cm from the sample. An indium metal disk, mounted on the tip of a plastic rod was used as central beam-stop. The irradiated phosphor screen was scanned by a laser based read-out system (Cyclone Plus Phosphor Imager, PerkinElmer LAS, Rodgau-Jügesheim, Germany), transforming the diffracted 2D X-ray intensity into a high resolution digitized image (600 dpi) with quantitative data as an image file (OptiQuant™ software).

The collected frames were transformed into one-dimensional diffraction patterns by using the XRDUA software package [143]. The images were corrected for dark-current, spatial distortion and detector pixel response. The XRD pattern of an Y_2O_3 powder sample was used as reference for calibration [144]. After correcting and calibrating the images, azimuthal integration was performed and the resulting diffractograms were normalized for the incident beam intensity. The background subtraction was achieved with a cubic spline polynomial fitting of the baseline.

The set-up available at the INE–Beamline for the *in-situ* XRD characterization of active samples is a unique, non-invasive tool for the investigation of redox-sensitive solid phases.

2.7 Evaluation and modelling methods of solubility data

After deriving the corresponding chemical models, experimental solubility data sets were evaluated using the Solver tool of Microsoft Excel, and with the PhreePot – PhreeqC (PP-PQC) program packages (version 3.3.5, svn 10806) [145-147]. For ionic strength

corrections, the Specific Ion-interaction Theory (SIT) [148] adopted within the NEA-TDB project was used. The ion-interaction parameters ($\varepsilon_{i,j}$) of the newly formed complex species were estimated based on the charge correlation approach described in [149]. Worth noticing, that due to the relatively low ionic strength in all the experiments (I = 0.10 m NaCl), the main contribution to the activity corrections results from the Debye–Hückel term rather than the ion-interaction parameters. Hence, the use of estimated $\varepsilon_{i,j}$ values has a limited impact on the calculated values of $\log K°$. Although simultaneously maximum two parameters were optimized, the reproducibility of the resulting values were further tested by the systematic variation of the initial input values. To gain further confidence on the obtained results the corresponding objective functions were minimized by the use of both, gradient-based (modified Levenberg-Marquardt, [150]) and non-gradient-based (SIMPLEX, [151]) methods.

2.8 Theoretical methods

The structures of the Pu(IV)–OH–ISA and Pu(III)–OH–ISA complexes were investigated by R. Polly of KIT-INE via density functional theory (DFT) calculations [152, 153]. DFT calculations were performed using TURBOMOLE (version 7.0, 2015) [154-160] with the BP86 functional [161] and the def2-SVP basis set [160] on C, O and H. The use of 5f-in core pseudo potentials (PP) for Pu(III) [162] and Pu(IV) [163] allowed to circumvent several problems arising with DFT calculations involving actinides: (i) difficulties due to open shells can be avoided, (ii) multi reference effects do not occur and (iii) the number of electrons and thus the computer time is greatly reduced. This leads to a theoretical task suited for DFT, and avoids complex and computational very demanding multi reference ab initio methods.

For a more realistic description of the Pu(III/IV)–OH–ISA systems investigated, several water molecules saturating the alcohol groups of the ISA and the Pu ion were considered in the calculations. A second step in the calculations included the aqueous media approximated with the conductor-like screening model (COSMO) [164, 165]. Considering the first water shell explicitly and dealing with the additional solvation effects by means of COSMO provides a realistic model to investigate species in aqueous solution.

3 Results and discussion

This section is divided into two main parts with the aim of discussing the results of the performed: solubility studies (Section 3.1) and sorption investigations (Section 3.2).

3.1 Plutonium solubility studies

Results of solubility studies can be separated into three main chapters, where redox and solubility behavior of Pu were investigated under alkaline, reducing conditions: in the absence of ISA and Ca(II) (Section 3.1.1), in the presence of ISA and absence of Ca(II) (Section 3.1.2), and finally in the presence of ISA and Ca(II) as well (Section 3.1.3).

3.1.1 Pu solubility and redox behavior under alkaline, reducing conditions

3.1.1.1 Characterization of the starting PuO_2(am,hyd) solid phase

This section summarizes the results of the characterization by XRD, XANES and XPS of the PuO_2(am,hyd) solid phase used as starting material in all the solubility experiments under alkaline to hyperalkaline pH conditions. After preparation (cf. Section 2.3.1), PuO_2(am,hyd) was aged for ~ 8 years in a 0.1 M NaCl solution with pH_m ~ 6. The relatively long pre-equilibration time of the solid ensures that solubility experiments are not impacted by short-term alterations of the solid phase, *e.g.* by changes in crystallinity, and consequently, also in solubility.

The XRD pattern of the starting material perfectly matches the diffractogram of PuO_2(cr), corresponding to the PDF 41–1170 in the JCPDS database [136] (Figure 9 in Section 3.1.1.4). The widths of the diffraction peaks are consistent with a nanocrystalline structure of the solid phase. Rietveld refinement (on Fm-3m space group) of the collected pattern revealed the mean value for the crystal domain size of (4 ± 1) nm and an average cell parameter of (5.405 ± 0.005) Å (R_p = 12.18 %, R_{wp} = 15.53 %). The latter is in good agreement with the reference value reported by [166] and [167] (5.396 Å). Since the oxygen deficiency results in unit-cell expansion, the slight difference is probably due to a minor substoichiometry ($PuO_{1.98}$) in the investigated solid phase [167]. In the subsequent parts of the study this solid phase is referred to as the “starting material”.

The white line energy position in the Pu L_{III} XANES spectrum of the starting material is in excellent agreement with the Pu(IV) reference spectrum reported in Brendebach *et al.* [140] (Figure 10 in Section 3.1.1.4). Differences in amplitude observed between both spectra are

related to the state of Pu in the sample (solid in the present work, aqueous in the reference [140]), as previously discussed in Rothe *et al.* [168]. The EXAFS fit parameters obtained for this sample (*cf.* Table 5) are in good agreement with those obtained for $Pu(IV)(OH)_4(am)$* precipitate in reference [169] (*i.e.*, 4.3 (4.0) oxygen atoms at R_{Pu-O} = 2.33 (2.32) Å and 2.3 (2.4) plutonium atoms at R_{Pu-Pu} = 3.84 (3.87) Å). The apparently low coordination numbers for both next neighbor shells reflect the strongly distorted Pu coordination in these materials with different Pu to $–O^{2–}$, $–OH_2$, $–OH^–$ distances and a high density of voids and dislocations, while this phase is still sufficiently ordered to exhibit a regular Pu-Pu second next neighbor interaction. Note that the fit significantly worsens when fixing the first shell coordination number to 8 (*cf.* Table 6 and the discussion in Section 3.1.1.4).

The X-ray photoelectron spectrum of the starting material is also in accordance with the findings of XRD and XANES measurements. Pu 4f photoemission peak exhibit a spin–orbit doublet for the Pu $4f_{7/2}$ peak at about 426.2 eV, in line with previously reported values [170-172]. A satellite is observed at approximately 6.9 eV higher binding energy than the Pu 4f main line. The difference in energy between the main line and the satellite is in agreement with data previously reported [170] for PuO_2(cr).

All experimental evidences collected for the starting material (XRD, XANES, EXAFS, XPS) are consistent with the predominance of PuO_2(ncr,hyd). This solid phase is therefore established as the anchor point in the interpretation of the solubility data obtained under alkaline to hyperalkaline pH conditions. It has to be clarified however, that thermodynamic data selected for Pu(IV) hydrous oxide generally quotes PuO_2(am,hyd) (see [9] and [5]). Calculations involving the latter solid phase are indicated consistently with the original publication / thermodynamic selections.

3.1.1.2 pH and E_h measurements

The experimentally measured pH_m and E_h (converted into pe) values of all the evaluated samples are shown in the Pourbaix diagram of Pu in Figure 6. Thermodynamic solubility and hydrolysis constants for plutonium reported in [5] were taken for the calculations. SIT ion interaction parameters estimated in [173] were used to account for ionic strength corrections of Pu(IV), whereas ε(i,j) values reported in [174] for Am(III) and Nd(III) were taken for the

* The notation $Pu(IV)(OH)_4(am)$ corresponds to a freshly precipitated Pu(IV) amorphous phase. Both $Pu(IV)(OH)_4(am)$ and $Pu(IV)O_2(am,hyd)$ are considered in the NEA-TDB reviews for amorphous, hydrous Pu(IV) oxides. The latter is nevertheless preferred, and has been also adopted in the present work.

corrections of Pu(III) aqueous species. ε(i,j) values reported in [175] for Np(VI) were taken for the SIT corrections of the analogous Pu species.

Experimentally measured pH_m and E_h values for redox unbuffered samples (prepared previously to this study, see Section 2.3.1) under acidic conditions (symbols ● and ○ in Figure 6) scatter around the redox neutral line at pe + pH_m = 13.8, where hypothetical partial pressures of $\log(2*P(O_2(g))) = \log P(H_2(g)) = -27.6$ are calculated for the reaction of $H_2O(l) \leftrightarrow H_2(g) + 0.5\ O_2(g)$, with $\log K° = -41.55$. These measured E_h values are considered less reliable due to the low concentration of plutonium in solution (below 10^{-5} M, see also Figure 7), which is considered to control the redox potential in the absence of other redox couples in the system.

Pu solubility samples in the presence of HQ and Sn(II) prepared within the current study showed stable readings of pH_m (± 0.05) and E_h values (± 30 – 50 mV, depending upon pH-region) within the time frame (~ 9 months) of the solubility experiment (symbols are ■ for HQ- and ▲ for Sn(II)-systems in Figure 6). HQ sets moderately reducing conditions with pe + pH_m = (9.5 ± 1), which clearly fall within the stability field of Pu(IV)s and $Pu(IV)_{aq}$. This system serves as the reference, $Pu(IV)_{s/aq}$-case for further points of the investigation. Tin(II) is well-known to be a strong reducing agent which buffers the redox condition of the system, with pe + pH_m = (2 ± 1), very close to the border line of water reduction [40, 127, 176]. Under these conditions, currently available thermodynamic data predict the predominance of Pu(IV) both in the aqueous and solid phases above pH_m = 9. Below this pH_m, the predominance of Pu(III) aqueous species (with the consequent increase in the solubility of PuO_2(am,hyd), according to Equation (2)) could be expected (see Figure 6). As discussed in Section 1.1.1, associated uncertainties to the available thermodynamic data are affecting the prediction of redox processes prevailing under these conditions, overall leading to an ill-defined Pu(IV) / Pu(III) redox border, especially for pH_m > 9 systems.

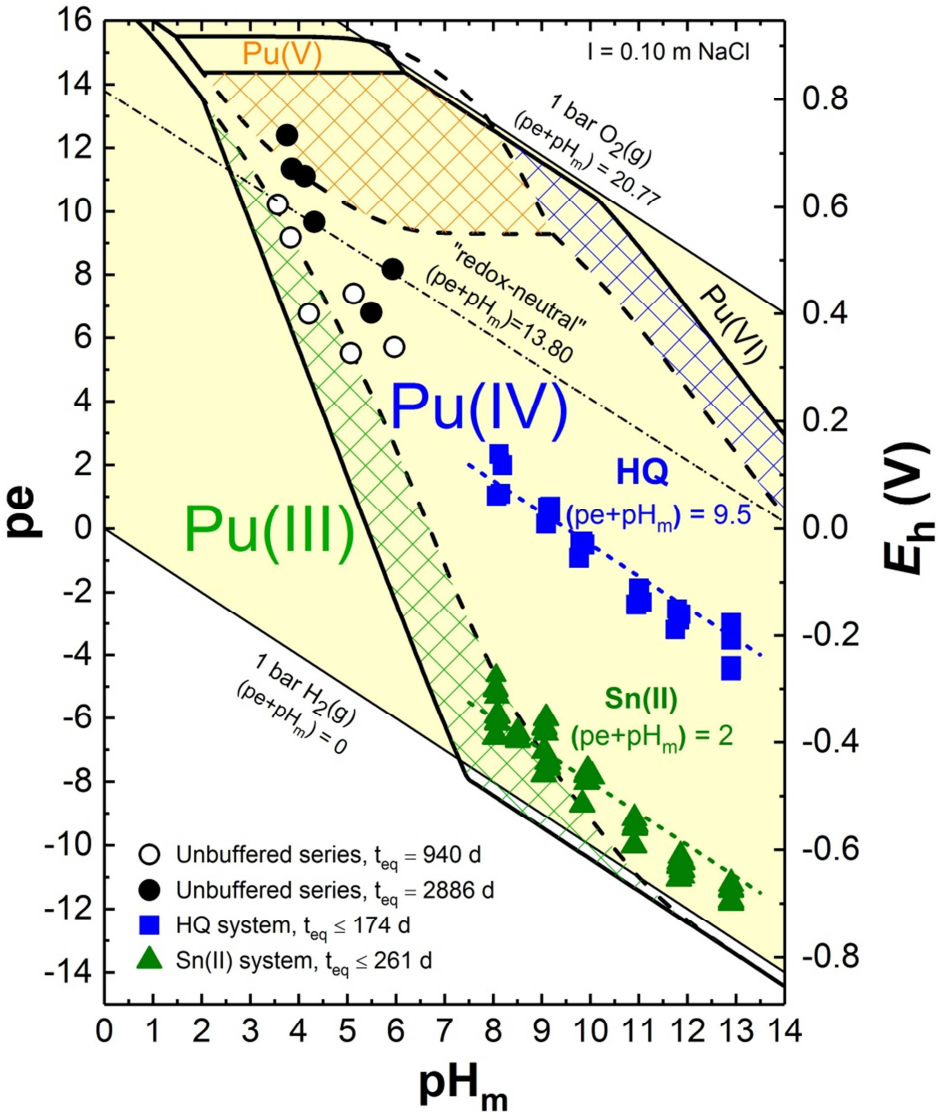

Figure 6. *Pourbaix diagram of Pu calculated for $m(Pu)_{tot} = 10^{-5}$ M and I = 0.1 M NaCl using thermodynamic and (SIT) activity models as described in the text. pH_m and E_h values experimentally determined for Pu(IV) solubility experiments in the absence of redox buffers (○: 940 days, ●: 2886 days), and in the presence of HQ (■) and Sn(II) (▲). The stability borderlines of water at pe + pH_m = 20.77 and pe + pH_m = 0, the "redox-neutral" line at (pe + pH_m) = 13.8 and the lines at (pe + pH_m) = 2 and 9.5 are shown for comparison reasons.*

3.1.1.3 Solubility measurements

Total concentrations of plutonium in equilibrium with PuO_2(ncr,hyd) in the absence and presence of redox buffers (hydroquinone, Sn(II)) are shown in Figure 7. The figure also shows the thermodynamically calculated solubility of PuO_2(ncr,hyd) in equilibrium with

$Pu(IV)_{aq}$ species and for ($pe + pH_m$) = 2 (Sn(II) system, both Pu(IV) and Pu(III) aqueous species contributing to solubility). Although not expected according to the Pourbaix diagram of Pu in Figure 6, Figure 7 includes also the thermodynamically calculated solubility of $Pu(OH)_3$(am) in equilibrium with $Pu(III)_{aq}$ species.

Acidic pH region, unbuffered systems

The two sets of experimentally measured solubility data (in Figure 7) of PuO_2(ncr,hyd) at the acidic $3.8 \leq pH_m \leq 6$ region with equilibration time of 940 (○) and 2886 (●) days are showing consistent values, indicating that thermodynamic equilibrium has been reached. Note that only the latter data collection (corresponding to t_{eq} = 2886 days) was undertaken within the context of this work.

The total concentration of Pu in this system is higher (more than 2 orders of magnitude) than thermodynamic calculations conducted for the equilibrium of PuO_2(am,hyd) ↔ Pu(IV)aq, using the thermodynamic data selection in [9] (see black solid line in Figure 7). On the other hand, Pu concentrations measured in these samples are clearly below the solubility of PuO_{2+x}(s,hyd) reported in [177]. Since the average crystal domain size: d = (4 ± 1) nm, determined by Rietveld analysis of the collected solid from sample with pH_m = 5.93, agrees well with the particle size distribution of PuO_2(am,hyd) [6], the observed discrepancy in Pu total concentrations cannot be caused by the differences in the degree of crystallinity of the presently used, aged solid phase. Hence, the only explanation remaining for the higher observed solubility of Pu within the unbuffered systems is the contribution of different redox states of Pu in solution, through oxidative or reductive dissolution and consequent redox reactions of the given aqueous species.

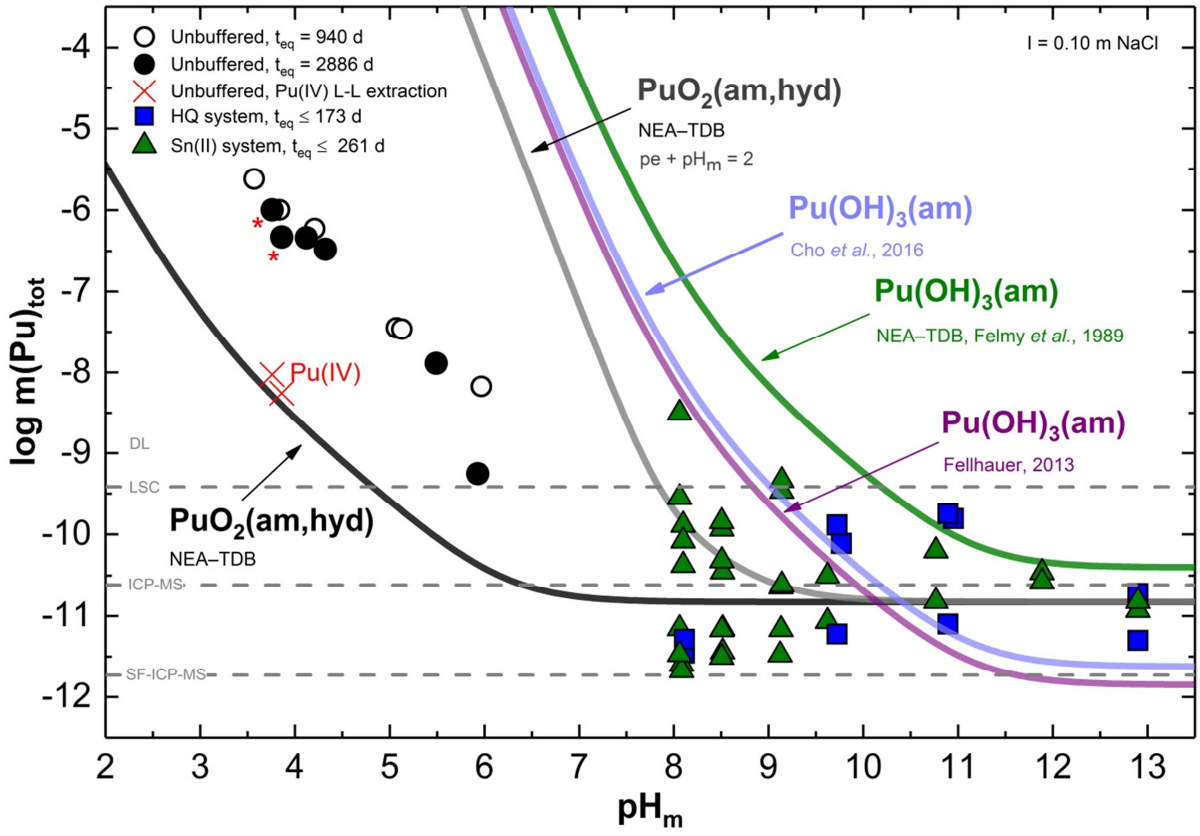

Figure 7. *Plutonium total concentration in solution at I = 0.10 m NaCl in equilibrium with PuO_2(ncr,hyd) for redox unbuffered (○: 940 days, ●: 2886 days) and redox buffered systems (■: hydroquinone; ▲:Sn(II)). Red crosses (X) show the concentration of $Pu(IV)_{aq}$ for selected unbuffered systems (*) as quantified by liquid-liquid extraction. Solid lines correspond to the thermodynamically calculated solubility of PuO_2(am,hyd) in equilibrium with $Pu(IV)_{aq}$ (black line) and for (pe + pH_m) = 2 (grey line, predominance of $Pu(III)_{aq}$ at $pH_m \leq 9$). Green, purple and light blue lines show the solubility lines of $Pu(OH)_3$(am) as calculated with log $^*K°_{IIIs,0}$ values selected in the NEA-TDB [9] and reported in Fellhauer's work [40] and in Cho et al. [33], respectively. Horizontal dashed lines indicate the lowest limits of Pu quantification in solution for LSC, ICP–MS and SF–ICP–MS techniques, respectively.*

To assess the possible contribution of other redox states of Pu to the total Pu solubility under acidic conditions, liquid-liquid extraction and CE-ICP-MS measurements were performed with the two most concentrated redox-unbuffered samples at pH_m = 3.76 and 3.86. Both redox speciation analysis showed the predominance of $Pu(V)_{aq}$ (~98 % of the total Pu concentration) in the investigated solutions after 10kD ultrafiltration. Figure 8 shows the electropherogram of the supernatant of the unbuffered sample with pH_m = 3.76. The first intense response at ~470 s retention time, peak (1) with an electrophoretic mobility of $1.6 \cdot 10^{-4}$

$cm^2V^{-1}s^{-1}$ corresponds to the presence of $Pu(V)_{aq}$ while the second signal, peak (2) at ~600 s with $1.2 \cdot 10^{-4}$ $cm^2V^{-1}s^{-1}$ electrophoretic mobility, followed by a tailing at t > 600 s indicates contributions from Pu(IV) aqueous monomeric and polynuclear, colloidal species [135]. In addition, liquid-liquid extraction of the given ultra-filtrated solutions quantified relevant contribution of Pu(VI) species (log $m(Pu)_{tot}$ = –7.3 and –7.9, respectively) and showed clearly lower, but non-negligible $Pu(IV)_{aq}$ concentrations as well (in Figure 8: log $m(Pu)_{tot}$ = –8.0 and –8.3, respectively). The presence of Pu(V) and (to less extent) Pu(VI) in the aqueous phase is thus responsible for the observed increase in Pu solubility, and reflects the complexity of the redox chemistry of Pu. This is especially true in acidic conditions, where Pu(III), Pu(IV), Pu(V) and Pu(VI) have their own predominance field within a very narrow pe-range (see Figure 6).

The determination of $m(Pu(IV))_{tot}$ by liquid-liquid extraction allows the direct assessment of the equilibrium PuO_2(ncr,hyd) ↔ Pu(IV)aq, independently of the contributions by Pu(V) and Pu(VI). Although, the depicted $m(Pu(IV))_{tot}$ values in Figure 7 show already an excellent agreement with thermodynamic calculations for this equilibrium reaction, the results of the liquid-liquid extraction have been used in combination with the hydrolysis scheme and corresponding thermodynamic constants reported in [9] to slightly adjust the $\log^*K°_{IVs,0}$ of the solid phase PuO_2(ncr,hyd) used in the present study (see Section 3.1.1.7).

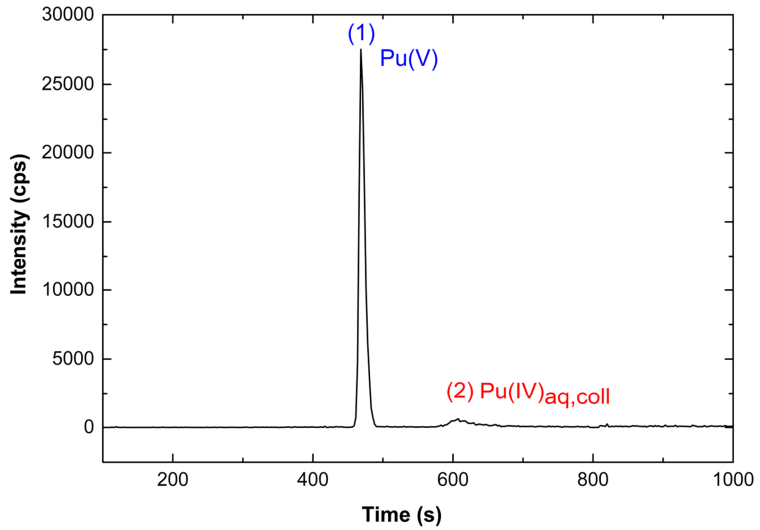

Figure 8. *Electropherogram of supernatant solution of unbuffered Pu solubility experiment with* pH_m *= 3.76. Peak (1) corresponds to* $Pu(V)_{aq}$*, peak (2) indicates* $Pu(IV)_{aq,coll}$ *species, with characteristic tailing at t > 600 s.*

Alkaline to hyperalkaline pH region, under reducing conditions

In the alkaline pH region, total concentration of Pu in equilibrium with PuO_2(ncr,hyd) measured by LSC after 10 kD ultrafiltration remains mostly below or close to the detection limit of the technique ($10^{-9.2}$ m) for both, the hydroquinone and the Sn(II) system. Therefore, these data were considered to be excluded from the corresponding figures. Pu solubility data quantified by ICP–MS and SF–ICP–MS after ultracentrifugation are shown in Figure 7 for hydroquinone (■) and Sn(II) (▲) systems (equilibration time: $t_{eq} \leq 173$ days and $t_{eq} \leq 261$ days, respectively). Above $pH_m > 9$, very low concentrations of Pu ($10^{-9.9}$ m $\leq m(Pu)_{tot} \leq 10^{-11.4}$ m) are measured for both redox systems, consistently with the solubility control by PuO_2(am,hyd) in equilibrium with $Pu(IV)(OH)_4^0$ species. In systems with $pH_m \leq 9$, under the redox-influence of hydroquinone again low solubility is determined, whereas in the case of Sn(II) systems, discrepant values are obtained.

In spite of the dispersion in the measured log $m(Pu)_{tot}$ (~1.5 log-units) caused by the very low concentration of Pu and the predominance of neutral species in solution, data collected for the hydroquinone system are in perfect agreement with the solubility expected for PuO_2(am,hyd) in equilibrium with Pu(IV) aqueous species (black solid line in Figure 4). This observation also underlines thermodynamic expectations, originating from the experimentally measured ($pe + pH_m$) values, that are in the case of the hydroquinone series plotting in the stability field of $Pu(IV)_{aq/s}$.

A more complex picture arises in the case of Sn(II) systems, where both the reductive dissolution of PuO_2(am,hyd) (grey line in Figure 7) and the solubility equilibrium $Pu(OH)_3(am) \Leftrightarrow Pu(III)_{aq}$ (green [9, 30], purple [40] and light blue [33] lines in Figure 4) would explain the experimental observations obtained in this study. A more detailed discussion in combination with the results obtained by *in-situ* XRD, XANES, EXAFS and XPS is provided in Section 3.1.1.8.

For selected supernatant solutions of the Sn(II)-buffered system, CE-ICP-MS measurements were also performed. In all cases, due to the very low total Pu concentrations the resulting electropherogram showed an indistinct picture of the redox speciation of Pu (not shown). The only visible feature was an unusually elongated tailing of the electrophoretic peak of Pu(IV) aqueous species at t > 600 s, characteristic to the formation of Pu(IV) colloidal species with a partial sorption onto the wall of the capillary. Since the expected concentrations of the hydrolyzed species of Pu(IV) (or eventually Pu(III)) is in the range of $10^{-8.5}$ to 10^{-11} m for the given samples, the detection of the different redox states of Pu is highly influenced by the minor changes in the media. The stabilization of a redox state in the investigated system is

directly depending on the total Pu in solution to available Sn(II) hydrolyzed species concentration ratio, which is in the case of the separation by CE might be affected by the eluent (1.0 M acetic acid), due to the formation of highly stable Sn(II)-acetate complexes [178]. This has possibly led to changes in the redox condition of the analyte solution and thus facilitated the oxidative alteration of the low Pu content by traces of oxygen in the system (under N_2 atmosphere with O_2 content < 5 ppm). As a consequence, CE-ICP-MS method could not provide relevant input on the redox speciation of the buffered samples.

3.1.1.4 Solid phase characterization

XRD

Figure 9 shows the *in-situ* XRD patterns of the solid phases controlling the solubility of Pu in hydroquinone and Sn(II) systems at pH_m = 9 and 12 (t_{eq} = 146 days), collected at the INE-Beamline as described in Section 2.6.2. The figure also shows the diffractogram of the empty double containment used in the synchrotron-based measurements, as well as the XRD patterns of the starting material collected with a conventional diffractometer.

Highly resolved diffractograms are obtained for all samples investigated at the INE-Beamline. A perfect match with PuO_2(cr) patterns previously reported [166] is obtained for the solid phases equilibrated in hydroquinone solutions, thus confirming that the initial nanocrystalline PuO_2(ncr,hyd) remains stable and controls the solubility of Pu in these systems. Although showing a weaker signal, a very good agreement with PuO_2(cr) patterns is also obtained for the solid phase recovered from the Sn(II) system at pH_m = 12. Besides the pattern of PuO_2(cr), a number of additional reflections are observed in the Sn(II) system at pH_m = 9. The latter show moderate agreement with the diffractogram of $Sn_6O_4(OH)_4$(s) (PDF 14-0140) and SnO(s) (PDF 13-0111), which are the expected [126] solid phases controlling the solubility of Sn(II) at this pH_m. At pH_m = 12, Sn(II) is completely dissolved due to the formation of anionic hydrolysis species, in good agreement with the lack of reflexes corresponding to Sn(II)-containing phases in the Sn(II) buffered system at this pH_m.

These results confirm the presence of PuO_2(ncr,hyd) in both hydroquinone and Sn(II) systems. Note, however that both cubic Pu_2O_3(cr) (PDF 06328) and PuO_{2-x}(cr) (PDF 41-1171) share similar reflections with PuO_2(cr), and thus cannot be ruled out from the findings gained by XRD.

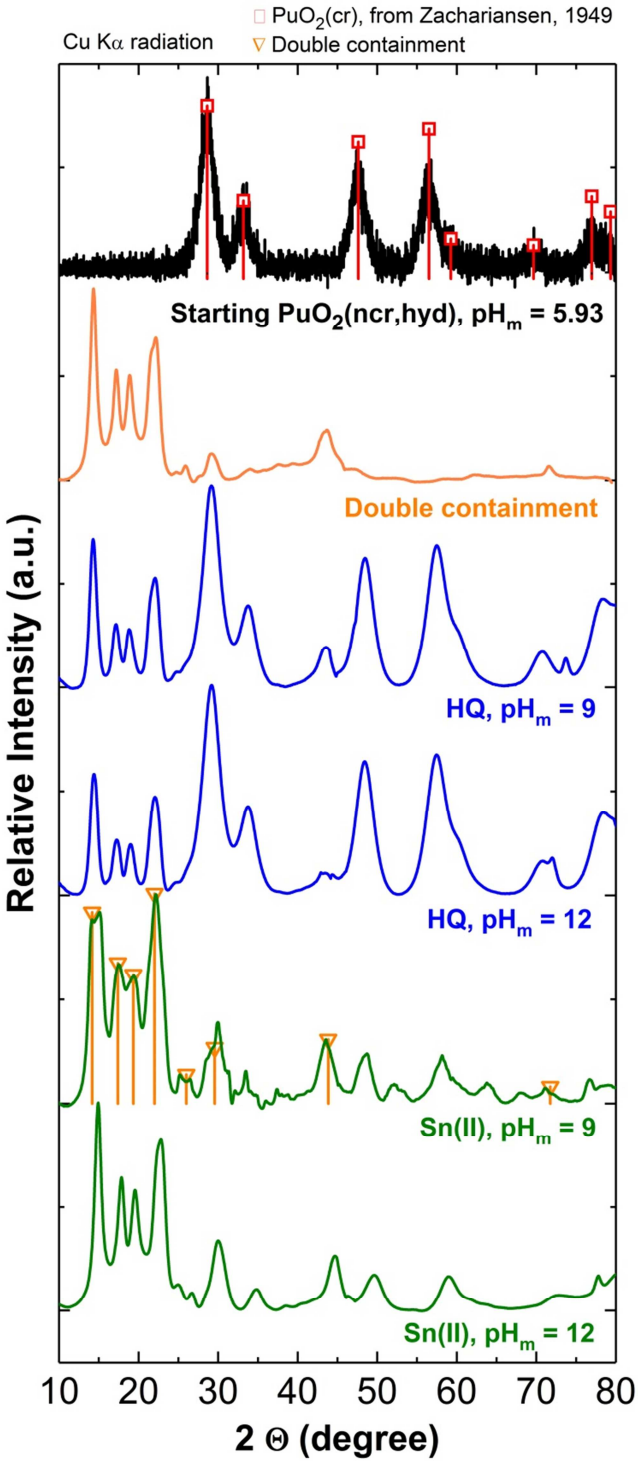

Figure 9. *Powder diffractogram of the starting PuO_2(ncr,hyd) phase collected with a conventional spectrometer (top), and in-situ XRD patterns collected at the INE–Beamline for the empty double containment and Pu solid phases recovered from solubility experiments at pH_m = 9 and 12 in hydroquinone and Sn(II) systems (t_{eq} = 146 days). Squares indicate peak positions and relative intensities reported [166] for PuO_2(cr). Triangles correspond to peak positions and relative intensities of the double containment used for in-situ XRD measurements.*

XPS

XPS spectra of solid phases recovered from the hydroquinone and Sn(II) systems after an equilibration time of 126 days indicate the predominance of PuO_2(ncr,hyd) in all cases, confirming that the structure of the starting material is retained. However, the spectra collected in Sn(II) systems with $pH_m \leq 11$ exhibit poor quality, likely due to the significant presence of Sn(II)–containing phases and consequently lower Pu atomic concentration on the surface of the evaluated samples.

The identification of minor contributions of other Pu redox states (e. g. +III) can also be hindered by the relatively broad range of Full Width at Half-Maximum (FWHM) observed for the Pu $4f_{7/2}$ elemental lines (2.27 eV ≤ FWHM ≤ 2.87 eV). Variations in the FWHM are likely to be related to structural disorder characteristics of amorphous phases, but also to inhomogeneous surface charging due to the presence of salts such as NaCl or Sn(II) oxy-hydroxides.

XANES

Pu L_{III}–edge XANES spectra collected for the solid phases controlling the solubility of Pu in hydroquinone and Sn(II) systems at pH_m = 9 and 12 are shown in Figure 10. The figure includes also the XANES spectra of the starting material, as well as the reference spectra reported in Brendebach *et al.* [140] for aqueous Pu(III) and Pu(IV) species in acidic conditions.

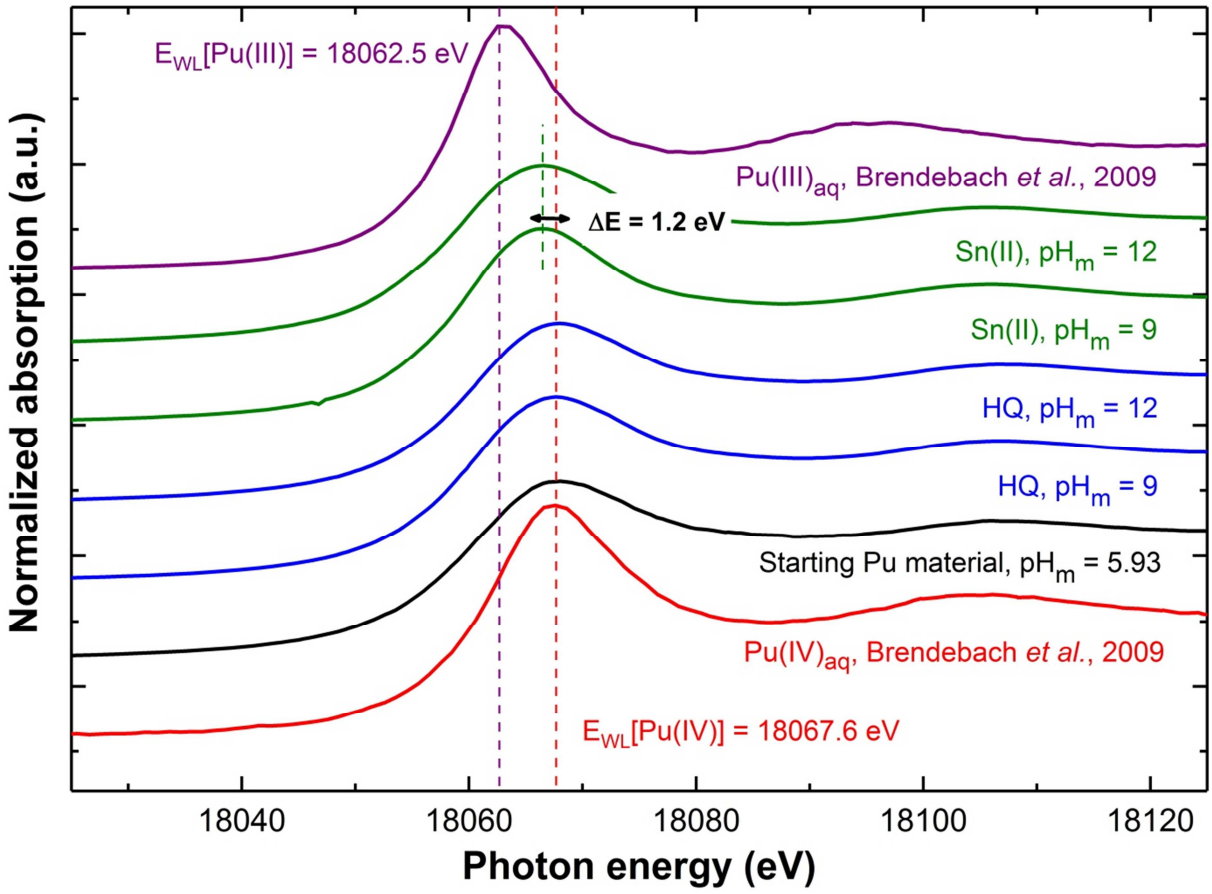

Figure 10. *Pu L_{III}–edge XANES spectra of solid phases recovered from HQ (blue line) and Sn(II) systems (green line) at pH_m = 9 and 12 (t_{eq} = 146 days). The spectra of the starting material (black) used in this study and the given references for the aqueous species of Pu(III) (purple line, position of WL = 18062.5 eV) and Pu(IV) (red line, position of WL = 18067.6 eV) reported in Brendebach et al. [140] are shown for comparison.*

The edge energies of the XANES spectra (listed in Table 2) collected for Pu solid phases in hydroquinone systems are in excellent agreement with the Pu(IV) reference spectrum [140]. Furthermore, these spectra perfectly match the XANES spectrum collected for the starting material, and clearly show the existence of a PuO_2 fluorite-like structure in the analyzed solid. The shift in the white line position to lower energy (≈ 1.2 eV, Figure 10) observed for Pu solid phases in Sn(II) systems is beyond the typical energy calibration error margin (≈ 0.5 eV), and unequivocally confirms a significant contribution of Pu(III). The reproduction of these spectra as a linear combination of Pu(III) and Pu(IV) reference spectra indicates an average Pu(III) content of (30 ± 5) %, both at pH_m = 9 and 12. Since the predominance of Pu(IV) was confirmed in the starting material, this observation indicates the reduction of the initial Pu(IV) and further stabilization of Pu(III) under these (pe + pH_m) conditions. It has to

be emphasized that a beam induced reduction in the Sn(II)-buffered samples is ruled out accounting for the confirmed predominance of Pu(IV) in the hydroquinone samples, which were measured under exactly the same experimental conditions. Two hypotheses are considered to explain the presence of Pu(III) in the solid phases controlling the solubility of Pu in Sn(II) systems: (i) the coexistence of PuO_2(ncr,hyd) and $Pu(OH)_3$(am), or (ii) the formation of a sub-stoichiometric PuO_{2-x}(s) phase. Both options are discussed in the following sections in connection with EXAFS and solubility data.

Table 5. *Pu L_{III}–edge inflection points and white-line positions of the XANES spectra in Figure 10: starting material used in the present study, solid phases recovered from the hydroquinone and Sn(II) systems at pH_m = 9 and 12 (t_{eq} = 146 days) and $Pu(III)_{aq}$ and $Pu(IV)_{aq}$ references [140].*

Sample	***First inflection point*‡ [eV]***	***White line (WL)* [eV]***
PuO_2(ncr,hyd), starting material	18060.3	18068.3
HQ, pH_m = 9	18060.9	18067.9
HQ, pH_m = 12	18060.7	18068.1
Sn(II), pH_m = 9	18059.9	18066.6
Sn(II), pH_m = 12	18059.3	18066.7
$Pu(III)_{aq}$ (HCl, pH = 0) [140]	18059.9	18062.5
$Pu(IV)_{aq}$ (HCl, pH = 3) [140]	18062.4	18067.6
$Pu(IV)(OH)_4$(am) (sample H) [169]	18060.5	18068.4

* Energy calibration relative to first infection point of Zr K-edge XANES assigned to 17998 eV (E 1s) Calibration error (due to DCM motor encoder step uncertainty): ± 0.5 eV

‡ Note that the position of the first inflection point is affected also by the Pu aggregation state (*i.e.*, aqua ion vs. colloidal oxy-hydroxide species or solid precipitates.

EXAFS

The Fourier-Transformed (FT) representation of the k^2-weighted EXAFS data depicted in Figure 11 for hydroquinone and Sn(II) systems (left panel: FT magnitude, imaginary part and fit results in R-space, right panel: raw data, Fourier-filtered data and fit results in k-space) corresponds to a radial pair distribution function uncorrected for photoelectron phase-shifts of

the central and neighboring atoms. Two coordination shells are discernible for all samples investigated in the present work: the first one around 1.75 Å (R−Δ), which typically reflects Pu bonding to bridging oxygen atoms and to oxygen from terminal water and hydroxide units. These different oxygen neighbors, if simultaneously present in a compound, exhibit a spread of bond distances generally leading to large Debye–Waller factors or requiring inclusion of an asymmetry parameter (3rd cumulant) in the fit - or even a second oxygen neighbor shell (*cf., e.g.* to Rothe *et al.* [169]). The second shell around 3.6 Å (R−Δ) reflects backscattering from second next Pu neighbors in the solid precipitates. All metric parameters evaluated are listed in Table 3. The fit results obtained for both Pu phases equilibrated in hydroquinone systems are almost identical and very similar to those obtained for the untreated starting material discussed in Section 3.1. The apparent disagreement between the PuO_2 fluorite-type structure observed in the XRD patterns and the reduced O and Pu coordination numbers in the Pu L_{III} EXAFS fits is actually in line with previous results obtained for Pu oxy/hydroxide phases or amorphous colloids: a rather rigid –Pu–O–Pu– 'backbone' or fluorite structure type lattice gives rise to the clear XRD signature, while the local order around individual Pu centers can be significantly distorted - leading to strongly reduced coordination numbers (fluorite-type PuO_2: R_{Pu-O} = 2.32 Å, N_O = 8; R_{Pu-Pu} = 3.81 Å, N_{Pu} = 12) due to destructive interference of the backscattered photoelectron waves. This discrepancy merely reflects the different sensitivity of EXAFS as a short range structural probe for order/disorder phenomena in solid materials compared to XRD, where the latter is prone to be blind to local deviations from a long range ordered structure. Interestingly, Pu samples equilibrated in Sn(II) systems (at both pH_m values) exhibit a significant and consistent shrinking of both Pu-O and Pu-Pu distances by about 0.04–0.05 Å compared to the two hydroquinone samples (fit errors are estimated to 0.01 Å for R_{Pu-O} and 0.02 Å for R_{Pu-Pu}).

The impact of the possible coexistence of PuO_2(ncr,hyd) and $Pu(OH)_3$(am) on the average Pu-O distances (measured by EXAFS) in the Pu solid phases equilibrated in Sn(II) systems is unclear. Virtually no information is available on the structure of the amorphous phase $Pu(OH)_3$(am), which should be probably better defined as $PuO_x(OH)_{3-2x}{\cdot}yH_2O$(am). Pu(III)–OH bonds are expectedly shorter than Pu(IV)–O or Pu(IV)–OH_2, considering r_{OH^-} = 1.22 Å, $r_{O^{2-}}$ = 1.40 Å and r_{OH_2} = 1.38 Å reported previously [179-181]. However, as the number of Pu(III)–OH bonds in $PuO_x(OH)_{3-2x}{\cdot}yH_2O$(am) is unknown, the impact on the Pu-O distances cannot be properly assessed.

The shrinking of Pu-O and Pu-Pu distances in the solid phases containing Pu(III) is unexpected because of the larger size of the Pu^{3+} ion (1.12 ± 0.02 Å, CN = 8) compared to

Pu^{4+} (1.01 ± 0.02 Å, CN = 9) [173]. Only a limited number of experimental studies [167, 182-186] have investigated the structure and stability of sub-stoichiometric phases PuO_{2-x}(s). Most of these studies focused on the behavior of $PuO_{2\pm x}$(s) phases at elevated temperature, and reported the destabilization of PuO_{2-x}(s) below 300°C. Haschke *et al.* [184] investigated the reaction of Pu metal (both α-phase and δ-stabilized alloy) with water at 25°C, and reported the formation of several PuO_{2-x}(s) phases ($PuO_{1.714}$, $PuO_{1.778}$, $PuO_{1.8}$ and $PuO_{1.833}$) besides Pu_2O_3, PuO_2 and two Pu(III) oxo-hydrides (PuOH and $Pu_7O_9H_3$). Recent publications [185, 186] by the same research team combining their own experimental results with the re-interpretation of data available in the literature concluded that the Pu-O system is not accurately described by the currently accepted Pu phase diagram, and that the formation and predominance of PuO_{2-x}(s) phases should be also expected at room temperature. Both experimental and theoretical studies report however the expansion of the unit cell in PuO_{2-x}(s) compared to PuO_2(s), which expectedly should correlate with an elongation of the Pu-O distance [167, 187]. It is evident from the discussion above that relevant uncertainties still affect to this system, especially in the conditions investigated in the present study, *i.e.* in aqueous systems at room temperature.

Although, the presence of up to 30% of Pu(III) has been confirmed in the Pu solid phases equilibrated in Sn(II)-buffered systems, based upon the structural changes associated with the partial reduction of $Pu(IV)_s$, the currently available XAFS data cannot unambiguously differentiate between the following two cases:

1. Formation of a homogeneous phase, PuO_{2-x}(s), with reduced lattice constant
2. Mixture of predominantly fluorite type $Pu(IV)O_2$ and amorphous $Pu(III)(OH)_3$ phase.

Further experimental efforts are definitely needed to elucidate these uncertainties (see Section 3.1.1.8 for related discussion).

Table 6. *Data range and metric parameters extracted by least-squares fitting of EXAFS spectra to the EXAFS equation.*

Sample	***k-range [Å^{-1}] fit-range [Å]***	***shell***	***N***	***R [Å]***	***ΔE$_0$ [eV]***	***σ^2 [Å^2]***	***r-factor [%]***
PuO_2(ncr,hyd), starting material	1.85-12.13	O	4.3 (8.0[f])	2.33	2.06 [g]	0.0046 [C3] (0.0140)	2.9
	1.29-4.17	Pu	2.3	3.84		0.0004	
Pu(IV)$(OH)_4$(am) (sample H) [169]	1.71-12.5	O	4.0	2.32	2.38	0.0104	1.6
	1.35-3.99	Pu	2.4	3.87	1.84	0.0066	
HQ pH_m = 9	1.65-12.23	O	5.2	2.32	0.09 [g]	0.0068 [C3]	1.3
	1.01-4.08	Pu	3.2	3.83		0.0021	
HQ pH_m = 12	1.60-12.10	O	5.0	2.33	2.32 [g]	0.0044 [C3]	1.2
	1.01-4.08	Pu	3.2	3.83		0.0027	
Sn(II) pH_m = 9	1.90-12.22	O	6.2	2.28	-1.43 [g]	0.0071 [C3]	2.5
	0.83-4.17	Pu	3.7	3.78		0.0014	
Sn(II) pH_m = 12	1.90-12.18	O	4.9	2.28	-1.34 [g]	0.0061 [C3]	2.9
	0.83-4.17	Pu	3.2	3.78		0.0014	

S_0^2 = 1.0 fixed (slightly underestimating N in all fits)
[g] global parameter for both shells
[f] fixed parameter
[C3] asymmetry parameter (3rd cumulant) applied in fit
errors: R_{Pu-O} 0.01 Å, R_{Pu-Pu} 0.02 Å

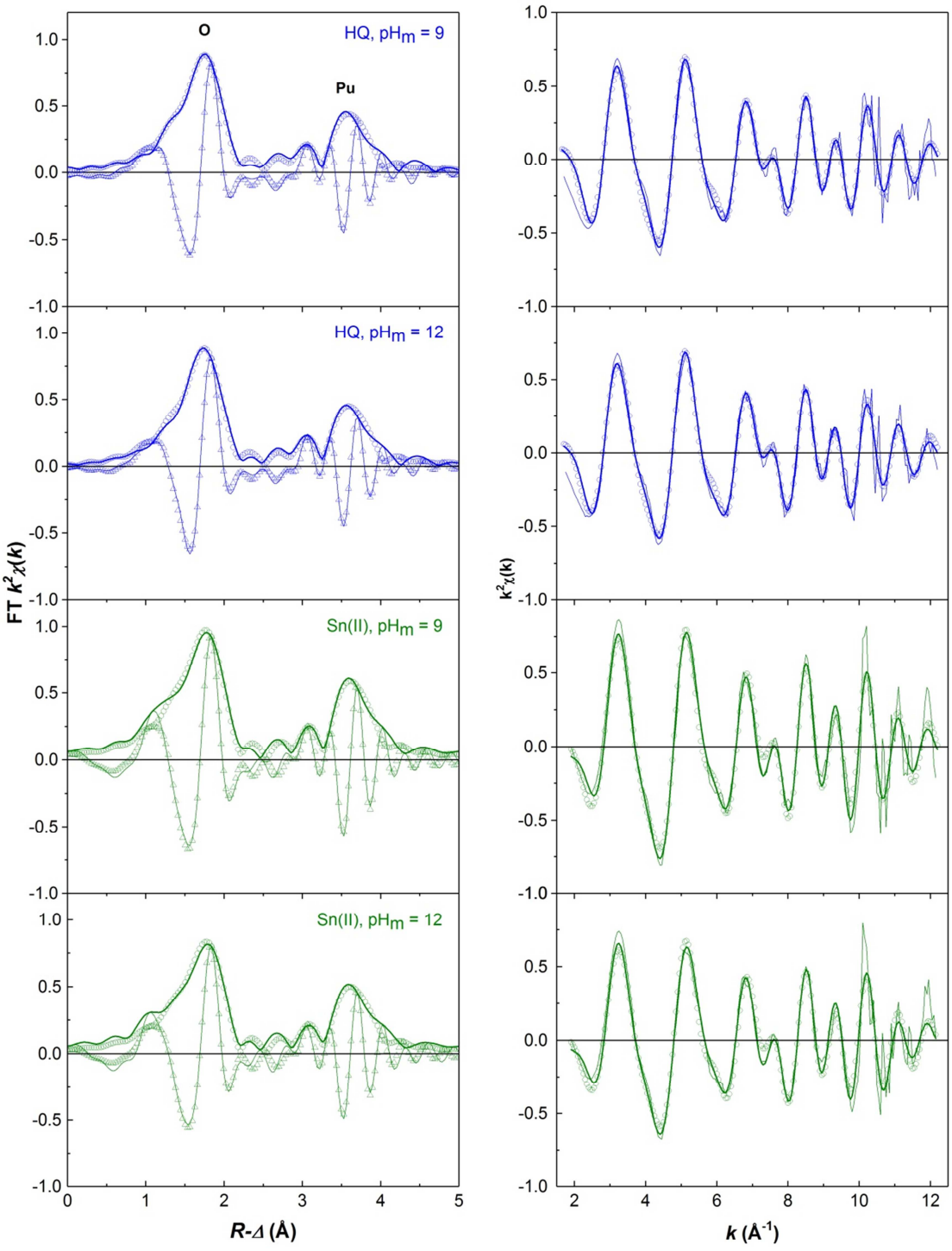

Figure 11. *Pu L_{III}–edge EXAFS fit results for hydroquinone and Sn(II) systems in R-space - left panel: FT magnitude (solid line), fit magnitude (open circles), FT real part (thin solid line) and fit real part (open triangles); right panel: Fourier-filtered data (solid line), raw data (thin solid line), back-transformed fit (open circles).*

3.1.1.5 Thermodynamic calculations

Chemical reactions (32), (35) and (38) are expected to control the solubility of Pu within the experimental conditions considered in this study. The corresponding Equations (33, 34), (36, 37) and (39, 40) have been used in combination with stability constants and SIT ion interaction coefficients summarized in Table A1 and Table A2 of the Appendix to calculate the solubility lines in Figure 7 and Figure 12: PuO_2(am,hyd) in equilibrium with Pu(IV) aqueous species (black line); PuO_2(am,hyd) in equilibrium with $Pu(IV)_{aq}$ and $Pu(III)_{aq}$ at pe + pH_m = 2 (grey line); and $Pu(OH)_3$(s) in equilibrium with $Pu(III)_{aq}$ (green and purple lines). The two solubility curves plotted for $Pu(OH)_3$(s) have been calculated using log $^*K°_{IIIs,0}$ = 15.8 and 14.35, as reported in [9] (taken from [30]) and [40], respectively.

$$Pu(III)(OH)_3(am) + n\ H^+ \Leftrightarrow Pu(III)(OH)_{3-n}^{n+} + n\ H_2O(l) \quad (32)$$

$$\log\ ^*K°_{IIIs,(3-n)} = \log\ ^*K'_{IIIs,(3-n)} + \log\ \gamma_{Pu(III)(OH)_{3-n}^{n+}} + n \log a_w - n \log \gamma_{H^+} \quad (33)$$

$$\log\ ^*K'_{IIIs,(3-n)} = \log m_{Pu(III)(OH)_{3-n}^{n+}} + n\ pH_m \quad (34)$$

$$Pu(IV)O_2(am,hyd) + n\ H^+ \Leftrightarrow Pu(IV)(OH)_{4-n}^{n+} + (n-2)\ H_2O(l) \quad (35)$$

$$\log\ ^*K°_{IVs,(4-n)} = \log\ ^*K'_{IVs,(4-n)} + \log\ \gamma_{Pu(IV)(OH)_{4-n}^{n+}} + n \log a_w - n \log \gamma_{H^+} \quad (36)$$

$$\log\ ^*K'_{IVs,(4-n)} = \log m_{Pu(IV)(OH)_{4-n}^{n+}} + n\ pH_m \quad (37)$$

$$Pu(IV)O_2(am,hyd) + (1+n)\ H^+ + e^- \Leftrightarrow Pu(III)(OH)_{3-n}^{n+} + (n-1)\ H_2O(l) \quad (38)$$

$$\log\ ^*K°_{IVs/III,(3-n)} = \log\ ^*K'_{IVs/III,(3-n)} + \log\ \gamma_{Pu(III)(OH)_{3-n}^{n+}} + pe + \\ + (1+n) \log a_w - (1+n) \log \gamma_{H^+} \quad (39)$$

$$\log\ ^*K'_{IVs/III,(3-n)} = \log m_{Pu(III)(OH)_{3-n}^{n+}} + (1+n)\ pH_m \quad (40)$$

3.1.1.6 Redox conditions in unbuffered systems

The redox-unbuffered systems after an equilibration time of ca. 8 years are considered to be in a well-established steady state with constant redox potential values. Liquid–liquid extraction method on the ultra-filtrates determined Pu(V) as the prevailing redox state of Pu in the investigated systems at pH_m = 3.76 and 3.86. The quantified $Pu(V)_{aq}$ concentrations

($\log m(Pu)_{tot}$ = –5.63 and –6.18) together with the contributions of $Pu(VI)_{aq}$ ($\log m(Pu)_{tot}$ = –7.3 and –7.9) and $Pu(IV)_{aq}$ ($\log m(Pu)_{tot}$ = –8.0 and –8.3, respectively) are suitable to calculate the theoretical redox potentials of the solutions, based on the corresponding redox-equilibria: $Pu(IV)_s \leftrightarrow Pu(V)_{aq}$ and $Pu(V)_{aq} \leftrightarrow Pu(VI)_{aq}$. According to the hydrolysis scheme of Pu(V) and Pu(VI) [9], the dominant species of the given oxidation states of Pu in solutions at pH_m = 3.76 and 3.86 were found to be the oxo-cations: PuO_2^{+} and PuO_2^{2+}. Hence, the theoretical pe values were then derived from redox-reactions (28) and (31), through the corresponding Equations (30) and (33), respectively, by using the thermodynamic values (29) and (32), reported in [5] and [9], corrected to 0.1 m NaCl via the SIT formulism.

$$Pu(IV)O_2(am,hyd) \Leftrightarrow Pu(V)O_2^{+}(aq) + e^{-} \quad (41)$$

$$\log {}^{*}K^{\circ}_{IVs/Vaq} = -(19.78 \pm 0.89) \quad (42)$$

$$pe_{(IVs\text{-}Vaq)} = -(\log {}^{*}K'_{IVs/Vaq} - \log m_{Pu(V)O_2^{+}(aq)}) \quad (43)$$

$$Pu(V)O_2^{+}(aq) \Leftrightarrow Pu(VI)O_2^{2+}(aq) + e^{-} \quad (44)$$

$$\log {}^{*}K^{\circ}_{Vaq/VIaq} = -(15.82 \pm 0.09) \quad (45)$$

$$pe_{(Vaq\text{-}VIaq)} = -(\log {}^{*}K'_{Vaq/VIaq} - \log m_{Pu(V)O_2^{+}(aq)} - \log m_{Pu(VI)O_2^{2+}(aq)} \quad (46)$$

The experimentally measured redox potential values: pe = 12.39, 11.35 in the unbuffered samples at pH_m = 3.76 and 3.86, respectively were found to be remarkably lower than those, calculated by the corresponding equilibria: $Pu(IV)_s/Pu(V)_{aq}$ with $pe_{(IVs\text{-}Vaq)}$ = 13.94, 13.39 and the $Pu(V)_{aq}/Pu(VI)_{aq}$ with $pe_{(Vaq\text{-}VIaq)}$ = 13.75, 13.74. In the absence of other redox buffers, the redox potential is directly controlled by the available plutonium in solution. In this framework, measured E_h values of systems with relatively low Pu total concentrations (below 10^{-5} M) are affected by large uncertainties and shall be treated carefully. Nonetheless, the good agreement in the pe values measured for the couples $Pu(IV)_s/Pu(V)_{aq}$ and $Pu(V)_{aq}/Pu(VI)_{aq}$ gives further confidence in the quantitative evaluation of the different redox states of Pu in solution.

3.1.1.7 Determination of $\log {}^{*}K^{\circ}_{IVs,0}$ for PuO_2(ncr,hyd) starting material

The accurate characterization of the PuO_2(ncr,hyd) solid phase and the quantification by liquid-liquid extraction of $m(Pu(IV))_{tot}$ in equilibrium with this phase under acidic conditions allows the quantification of $\log {}^{*}K^{\circ}_{IVs,0}$ of the starting material used in the solubility

experiments under alkaline to hyperalkaline pH conditions. Solid phase characterization (Section 3.1.1.4) has also confirmed the predominance of the same solid phase in hydroquinone systems, and thus the solubility data in this system expressed by the same log $*K°_{IVs,0}$. The case of Sn(II)-buffered systems, where XANES has confirmed the presence of Pu(III) in the solid phase is discussed in detail in Section 3.1.1.8.

Total concentration of Pu(IV) in equilibrium with PuO_2(ncr,hyd) at pH_m = 3.76 and 3.86 was quantified by liquid-liquid extraction. Based on the experimentally measured $m(Pu(IV))_{tot}$, the concentration of free Pu^{4+}(aq) was calculated using Equation (47):

$$m_{Pu^{4+}(aq)} = m(Pu(IV))_{tot} \cdot \left(1 + \sum_{n=1}^{4} (*\beta'_{1,n} \cdot m_{H^+}{}^{-n})\right)^{-1} \quad , \qquad (47)$$

where log $*\beta'_{1,n}$ are the hydrolysis constants of Pu(IV) (corresponding to the reactions: Pu^{4+} + n H_2O(l) ⇔ $Pu(IV)(OH)_n^{(4-n)+}$ + n H^+ with n = 1 – 4) corrected to 0.1 m NaCl using the SIT formalism. Based on the calculated $m_{Pu^{4+}(aq)}$ and according with chemical reaction (35) for n = 4, the conditional solubility product of PuO_2(ncr,hyd) in 0.1 m NaCl (log $*K'_{IVs,0}$) can be calculated based on Equation (47), and corrected to the standard state (log $*K°_{IVs,0}$) using Equation (36).

The resulting mean value of the solubility product of the PuO_2(ncr,hyd) phase used in this study was determined as log $*K°_{IVs,0}$ = –(58.1 ± 0.3), which is in excellent agreement with the selected reference value of –(58.3 ± 0.5), reported in Neck *et al.* [5] and NEA-TDB [9].

3.1.1.8 On the role of Pu(III)s/aq under alkaline reducing conditions

According to the current thermodynamic data selection, provided by NEA-TDB [9] for Pu(IV) and Pu(III) solid compounds and aqueous species, the redox transition for the transformation of PuO_2(am,hyd) + e^- ↔ $Pu(OH)_3$(s) lays at (pe + pH) = –(0.4 ± 1.6), is just below the lower border line of the stability field of water (see Section 1.1.1 for more details). Consequently, $Pu(OH)_3$(s) is not foreseen to form under the redox-influence of Sn(II) in aqueous systems, defined by the mildly higher (pe + pH_m) values (see Figure 6). It has to be emphasized however, that taken into account the uncertainty of ± 1.6 log-units assigned to the log $*K°_{IIIs,0}$ solubility product, the redox conditions defining the given transition are very ill-defined.

In contrast to the above mentioned thermodynamic expectations, XANES results provide evidence on the presence of relevant fractions of Pu(III) in the solid phases, controlling the

solubility of Pu in Sn(II)-buffered systems at pH_m = 9 and 12. Under the given conditions at pH_m = 9 the solubility of Sn(II) (originally: $m(Sn(II))_{tot}$ = 2 mM) is controlled by the $Sn_6O_4(OH)_4$(s) and SnO(s) phases, limiting $m(Sn(II))_{tot}$ to ~10^{-6} m, whilst at pH_m = 12, Sn(II) is quantitatively dissolved by the formation of $Sn(OH)_2^0$ and (mostly) $Sn(OH)_3^-$ [126]. Reproduction of the observed Pu L_{III}-edge XANES spectra by the linear combination of $Pu(III)_{aq}$ and $Pu(IV)_{aq}$ reference spectra from [140] determined an overall average $Pu(III)_s$ content of (30 ± 5) n% for both retrieved solids from the Sn(II)-buffered systems, regardless of the present pH_m condition in the supernatant solutions. Based on these observations, the influence of different Sn(II)-containing solid phases on the redox state of Pu within the investigated solids (through possible sorption effects) can be discarded. Furthermore, provided the different hydrolysis speciation and thus, the chemical behavior of Sn(II) at the given pH_m within the investigated systems, the detected reduction of Pu(IV)s to Pu(III)s (in comparison with the identical HQ system) could only be imposed by the lower ($pe + pH_m$) conditions, *i.e.* by the more reducing nature of the media.

Previously reported experimental observations [33, 40] point towards the greater stability of $Pu(OH)_3$(s) compared to the current thermodynamic NEA-TDB selection [9]. According to Equation (34) using the log $^*K°_{IIIs,0}$ for $Pu(OH)_3$(s) reported by Fellhauer and co-workers [40] the depicted calculation results in less reducing conditions for the given redox transition with ($pe + pH_m$) values of +1.05, consistently with the presence of Pu(III) in the solid phases of the Sn(II)-buffered solubility experiments. However, in the case of the simultaneous presence of two solid phases containing the same cation, the phase with the higher solubility (and thus less stable) controls the concentration of the cation in solution until its complete transformation into the thermodynamically stable solid phase (if equilibration processes between the solid and liquid phases are not kinetically hindered). In this context, the coexistence of two solid phases (PuO_2(ncr,hyd) and $Pu(OH)_3$(am)) along a broad pH-range (9–12, in the present study) is feasible but unlikely from a thermodynamic point of view. It requires $\Delta_r G$ = 0 within the considered ($pe + pH_m$) boundary conditions for the chemical reaction PuO_2(am,hyd) + H_2O(l) + H^+ + e^- ⇔ $Pu(OH)_3$(am). This observation suggests that the coexistence of both solid phases, if confirmed, would possibly correspond to a kinetically transient state evolving towards the complete transformation into a single phase, either PuO_2(ncr,hyd) or $Pu(OH)_3$(am), or a mixed-valent oxide forming.

For comparison reasons, the Pu solubility results of this study, gained in the Sn(II)-buffered system are plotted together in Figure 12 with the similar (above the given detection limit) data on $Pu(OH)_3$(s) solubility, conducted in distilled water by Felmy and co-workers [30]. Figure

12 also includes all the previously calculated Pu solubility curves corresponding to solutions in equilibrium with PuO_2(am,hyd) or $Pu(OH)_3$(s) solid phases.

The green line in Figure 12, showing the solubility of $Pu(OH)_3$(s) calculated with the NEA-TDB selection [9] clearly overestimates the experimentally measured Pu solubility in Sn(II)-buffered systems with $pH_m < 11$, supporting the hypothesis that the selected $\log {}^*K°_{IIIs,0}$ for this solid phase, reported in [30] is too large. Moreover the published raw data points of Felmy *et al.* also exhibit systematic differences (with negatively signed residuals) from the above mentioned solubility line. Worth mentioning also, that the corresponding solubility curve is corrected to 0.1 m (NaCl) ionic strength by the SIT formalism. Hence, changes in the residuals with respect to the "real" curve at infinite dilution are indeed expected, (since the experiments were conducted in distilled water by Felmy *et al.*), but the effect is irrelevant to the overall trend. This phenomena implies that the optimized solubility product of $Pu(OH)_3$(s) ($\log {}^*K°_{IIIs,0}$) is overestimated, which is partly originating from the incorrectly applied hydrolysis scheme of Pu(III) (see Section 1.1.1 for more details). The possible reevaluation of the raw data reported in [30], using the selected hydrolysis constants from the latest NEA-TDB review [9] for $Pu(III)_{aq}$, would already provide a moderately lower $\log {}^*K°_{IIIs,0}$ by approximately 0.6 log-units, also in accordance with the work of Cho *et al.* [33].

On the contrary, the identical solubility curve (purple line in Figure 9) of $Pu(OH)_3$(s), calculated with the $\log {}^*K°_{IIIs,0}$ determined in [40] provides a more consistent fit of the solubility data gained in this work at $pH_m \geq 9$. However, the large dispersion in the determined Pu concentrations under the near-neutral pH_m conditions does not allow us to refine theoretically the corresponding $\log {}^*K°_{IIIs,0}$ value of $Pu(OH)_3$(s) for the Sn(II)-buffered system.

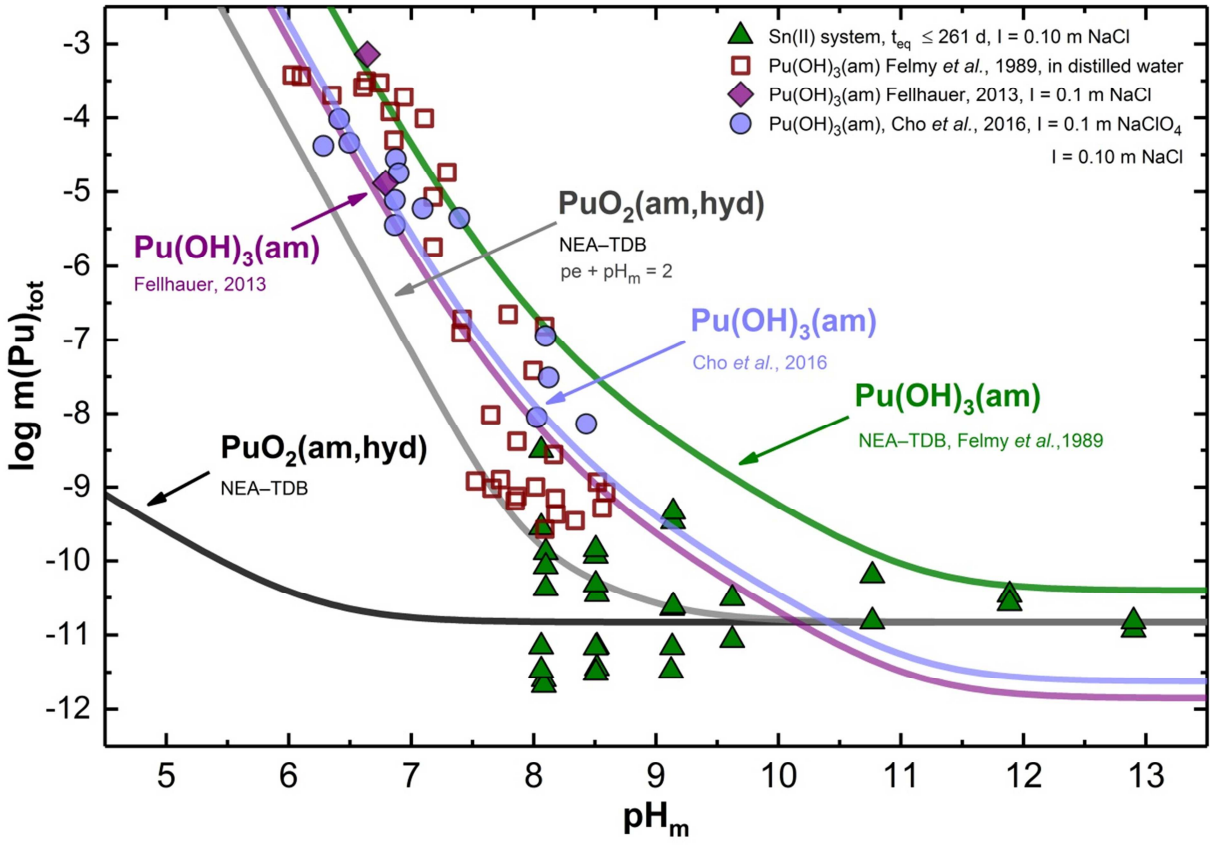

Figure 12. *Plutonium total concentrations in solution in equilibrium with $Pu(OH)_3$(am) in distilled water (Felmy et al. [30], symbol: □), in 0.10 m NaCl (Fellhauer [40], symbol: ♦), in 0.10 m $NaClO_4$ (Cho et al. [33], symbol: ●) or with PuO_2(ncr,hyd) in Sn(II)-buffered systems at I = 0.10 m NaCl (present study, symbol: ▲). Solid lines correspond to the thermodynamically calculated solubility of PuO_2(am,hyd) in equilibrium with $Pu(IV)_{aq}$ species (black line) and for pe + pH_m = 2 (grey line, predominance of $Pu(III)_{aq}$ at $pH_m \leq 9$). Green, purple and light blue lines show the calculated solubility lines of $Pu(OH)_3$(am) using log $*K°_{IIIs,0}$ values reported in NEA-TDB [9], in Fellhauer et al. [40] and in Cho et al. [33], respectively. Ionic strength corrections were performed using SIT formalism as described in Section 3.1.1.5.*

One plausible explanation for the presence of both Pu(IV) and Pu(III) in the solid phase controlling the solubility of Pu under alkaline to hyperalkaline reducing conditions would be the formation of the substoichiometric plutonium dioxide: PuO_{2-x}(s). It is widely accepted [5, 6, 177, 188-190] that the fluorite-type structure of PuO_2 can easily accommodate additional oxygen atoms to charge-balance the presence of Pu(V) in PuO_{2+x}(s), which readily forms in the presence of traces of O_2. A far more limited and discrepant literature is available on the

formation of the sub-stoichiometric phase PuO_{2-x}(s). Most of the available studies [167, 182, 183] deal with dry solid material synthesized and characterized at elevated temperature (300–1000°C), and thus, are hardly comparable to the present work. The study by Haschke and co-workers [184] dealing with the corrosion of Pu metal with water at room temperature provides a somehow closer basis to be compared with the material obtained in the presently. The authors could not explain their observations with the formation of either $Pu(OH)_3$(s) or PuO_2(s) solid phases plus H_2, but claimed the formation of several PuO_{2-x}(s) phases. Unfortunately, no structural data was reported for such phases and no information on the Pu concentrations in solution were provided either.

In spite of the multiple experimental evidence collected in the present work (solubility, (pe + pH) measurements, extensive solid phase characterization, redox speciation), this still does not allow us to formulate a final conclusion on the role of Pu(III) in the solid phases controlling the solubility of Pu under alkaline reducing conditions. However, the solubility behavior of Pu(IV) and Pu(III) solid phases in the presence of strongly complexing ligands (such as ISA) is expected to provide additional insights on the character of the solid phases controlling the solubility of Pu under these boundary conditions.

3.1.2 Pu–ISA system

3.1.2.1 pH and E_h measurements

The experimentally measured pH_m and E_h (converted into pe) values of all the evaluated samples are shown in the Pourbaix diagram of Pu in Figure 13. The thermodynamic calculations for the construction of the diagram were executed identically as it was detailed before in Section 3.1.1.2.

Solubility experiments in HQ or Sn(II) redox buffered systems in the presence of ISA showed stable pH_m (± 0.05) and E_h (± 15–30 mV, depending upon pH-region) readings within the time frame of this study (3 months).

In accordance with the findings of the present study conducted in the absence of ISA (see Section 3.1.1), the use of HQ as a redox buffering agent set moderately reducing conditions with $(pe + pH_m) = (9 \pm 1)$. These conditions fall within the stability field of $Pu(IV)_s$ and $Pu(IV)_{aq}$, and thus this system is considered as the reference case to assess the interaction of $Pu(IV)_{aq,s}$ with ISA. The presence of Sn(II) maintained strongly reducing conditions in solution. Redox potentials observed in all Sn(II)-buffered systems with shorter measurement time (approximately 15 mins) could be described by the correlation of $(pe + pH_m) = (1 \pm 1)$. However, as discussed in Section 2.2, longer allowed contact time for the measurements of E_h values resulted in a more stable mean value at each investigated pH_m condition. The obtained values showed significantly smaller uncertainty after 1 hour of measurement time. Table 7 summarizes the average of the E_h values (*versus* Ag/AgCl reference electrode) together with the associated uncertainties (2σ) collected in the Sn(II) system at different pH_m conditions with more than 1 hour of equilibration time. The small absolute drift for the measurements of the values listed in Table 7 (below < 0.08 mV/min) together with the clearly lower associated uncertainties (± 15 mV) ensured the validity of the obtained conditions.

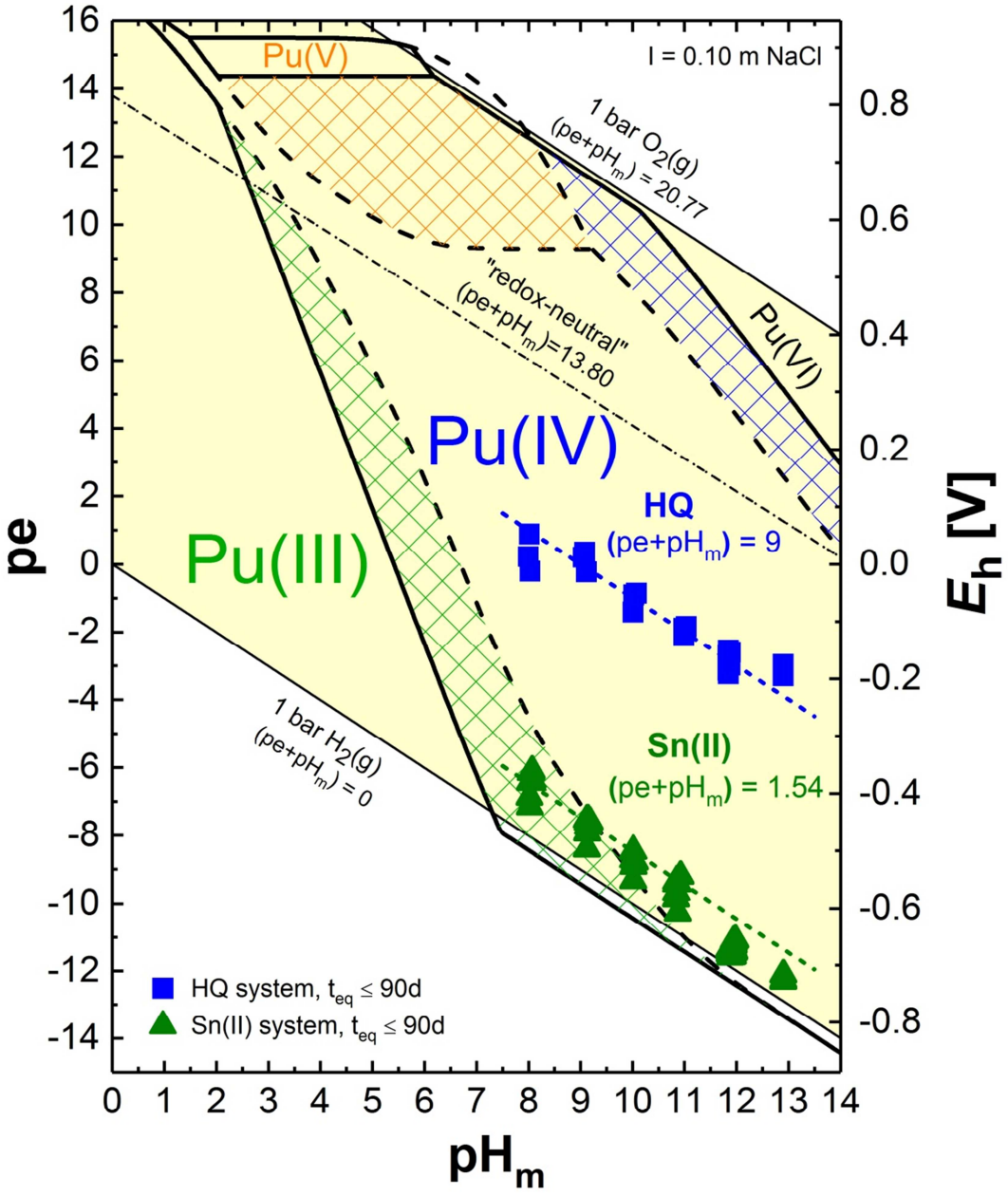

Figure 13. *Pourbaix diagram of Pu calculated for $m(Pu)_{tot} = 10^{-5}$ m and I = 0.1 m NaCl using thermodynamic and (SIT) activity models as described in the text. pH_m and E_h values experimentally determined for Pu(IV) solubility experiments in the presence of ISA and redox-buffering agents: HQ (■) and Sn(II) (▲).Thick lines correspond to redox borderlines between Pu(IV) and other Pu redox states: solid line is the borderline between Pu solid phases; dashed line is the borderline between Pu aqueous species. Colored regions indicate equilibrium between $Pu(IV)_s$ and $Pu(III)_{aq}$ (green), $Pu(V)_{aq}$ (orange) and $Pu(VI)_{aq}$ (blue). The borderlines of the stability field of water at $(pe + pH_m) = 20.77$ and $(pe + pH_m) = 0$, the "redox-neutral" line at $(pe + pH_m) = 13.8$ and the lines at $(pe + pH_m) = 1.54$ and 9 are shown for comparison.*

Table 7. *Mean pH_m and E_h values (versus Ag/AgCl reference electrode) with associated uncertainties collected in Sn(II)-buffered systems with extended measurement times (for 1, 2 and 6 hours).*

pH_m	***E_h (mV) vs. Ag/AgCl ref. electrode***	***Associated uncertainty, 2σ (mV)***
8.05	–580.0	14.5
9.15	–657.9	9.2
10.02	–714.8	14.2
10.85	–771.2	14.2

Using the results of 1, 2 and 6 hours of E_h measurements, an averaged redox condition with $(pe + pH_m) = (1.54 \pm 0.14)$ can be derived. This is considered to be the overall valid thermodynamic value and adapted for the interpretation of the data gained in the Sn(II) system (see Section 3.1.2.4.2 for further details on the evaluation procedure of the given results). Under the redox-influence of Sn(II) findings of the previous study conducted in the absence of ISA indicated the coexistence of Pu(IV) (~70%) and Pu(III) (~30%) in the solid phases recovered from experiments at $pH_m = 9$ and 12 after 146 days of contact time.

3.1.2.2 Solubility measurements

Total concentrations of plutonium in equilibrium with PuO_2(ncr,hyd) and in the presence of NaISA measured after phase separation (ultrafiltration and ultracentrifugation) are shown in Figure 14 ($pH_m = 8 – 12.9$; $m(ISA)_{tot}$ = constant = 10^{-3} m) and Figure 15 (pH_m = constant = 12; $m(ISA)_{tot} = 10^{-6} – 0.10$ m). Figure 12 also includes the total Pu concentration measured (without any phase separation applied) in the supernatant of the solubility experiments. The latter data give insight on the possible presence of colloidal Pu(IV) species. The solubility of PuO_2(ncr,hyd) in equilibrium with $Pu(IV)_{aq}$ (HQ system) and for $(pe + pH_m) = 1.54$ (reductive dissolution), as well as the solubility of $Pu(OH)_3$(am) using log $^*K°_{IIIs,0}$ reported in Cho *et al.* [33], are appended to the figures for comparison purposes.

3.1.2.2.1 Series with constant ISA total concentrations

Figure 14 shows that very stable values of $m(Pu)_{tot}$ are obtained for both HQ and Sn(II) systems after 90 days, indicating that thermodynamic equilibrium has been attained within this timeframe. The trends observed in the solubility curves in HQ and Sn(II) systems can be divided into three different cases:

1) pH_m = 8 – 11 in HQ-buffered systems: moderate and pH_m-independent enhancement in the solubility of PuO_2(ncr,hyd) is detected, indicating that no H^+ are involved in the equilibrium reaction controlling the solubility of Pu. The increase in solubility with respect to the ISA-free systems is attributed to the formation of Pu(IV)–ISA aqueous complexes.
2) pH_m = 8 – 11 in Sn(II) systems: compared to the HQ system, a greater impact of ISA on the solubility of PuO_2(ncr,hyd) is observed. The solubility shows also a clear pH-dependency. Such differential behavior can only be attributed to the formation of Pu(III)–ISA aqueous complexes. Although these observations do not provide any direct insight on the solid phase controlling the solubility, the lower $m(Pu)_{tot}$ measured at pH_m = 8 compared to the calculated solubility line of $Pu(OH)_3$(am) (light blue line in Figure 14) hints towards the possible retainment of the initial $Pu(IV)O_2$(am,hyd) phase within these boundary conditions.
3) pH_m > 11 for both HQ and Sn(II) systems: a clear increase in the total Pu concentrations is observed with a slope ($\log m(Pu)_{tot}$ *vs.* pH_m) ≈ +1, indicating that one H^+ is released in the equilibrium reaction controlling the solubility of Pu. The identical behavior observed in HQ and Sn(II) suggests that $Pu(IV)_s$ and $Pu(IV)_{aq}$ prevail in both systems.

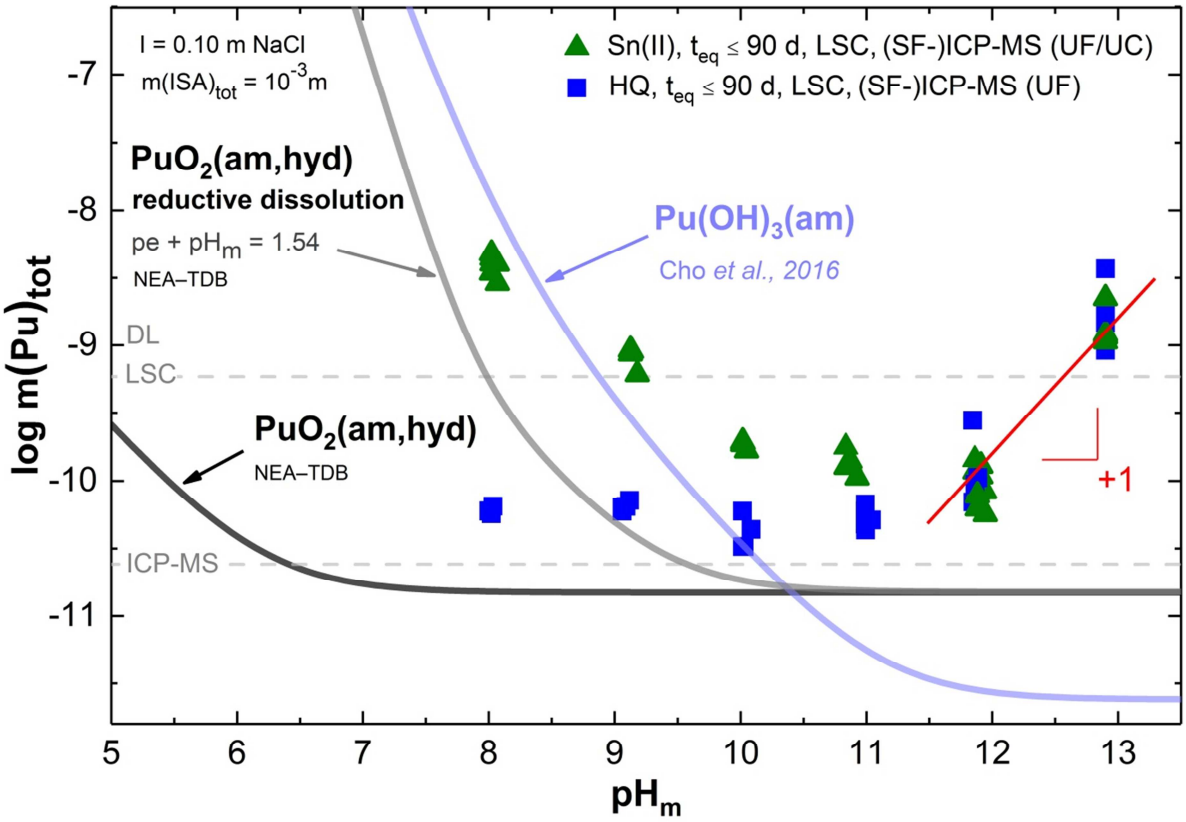

Figure 14. *Experimentally measured $m(Pu)_{tot}$ in equilibrium with PuO_2(ncr,hyd) in 0.10 m NaCl for redox buffered systems with HQ (■) and Sn(II) (▲) at pH_m = 8 – 12.9 and $m(ISA)_{tot}$ = 10^{-3} m. Solid lines correspond to the thermodynamically calculated solubility of PuO_2(am,hyd) in the absence of ISA in equilibrium with $Pu(IV)_{aq}$ (black line) and for pe + pH_m = 1.54 (grey line, predominance of $Pu(III)_{aq}$ below $pH_m \approx 10.5$, see text for more details), and for $Pu(OH)_3$(am) (light blue line) in equilibrium with $Pu(III)_{aq}$ species (calculated by using log $*K°_{IIIs,0}$ reported in Cho et al. [33]). Red line with a slope of +1 is shown for comparison purposes.*

3.1.2.2.2 Series at constant pH conditions

Figure 15 shows the solubility of Pu at pH_m = 12 as a function of increasing $m(ISA)_{tot}$ in solution after various applied phase separation methods and in the supernatants as well. Virtually identical solubility behavior is observed for the HQ- and Sn(II)-buffered systems, indicating that the same chemical equilibrium is controlling the solubility in both systems. Consistent values were obtained using ultrafiltration and ultracentrifugation as phase separation technique. A large scattering in $m(Pu)_{tot}$ is observed at $m(ISA)_{tot} < 10^{-3}$ m, in line with the results gained in the absence of ISA. More precise values of $m(Pu)_{tot}$ are visible at $m(ISA)_{tot} \geq 10^{-3}$ m, indicating the formation of a new Pu(IV)-ISA complex. The latter

phenomena: increasing precision of solubility measurements upon the formation of charged aqueous complexes was previously reported for the Th(IV)–carbonate system as well [106].

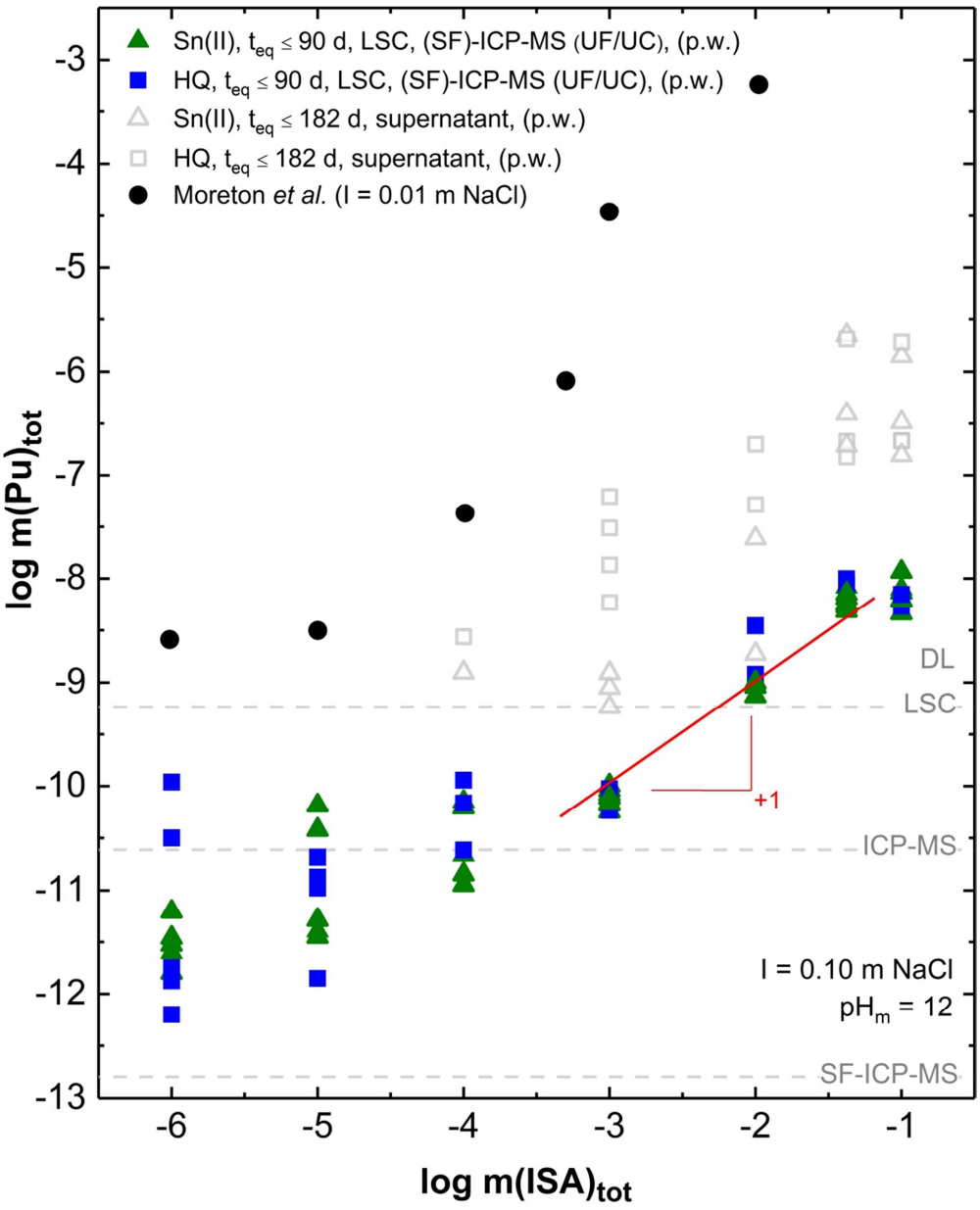

Figure 15. *Experimentally measured $m(Pu)_{tot}$ in equilibrium with PuO_2(ncr,hyd) in 0.10 m NaCl for redox buffered systems with HQ (■) and Sn(II) (▲) at pH_m = 12 and 10^{-6} m ≤ $m(ISA)_{tot}$ ≤ 0.10 m. Open symbols mark the total concentrations of Pu in the supernatants of the Sn(II)– (Δ) and HQ–buffered (□) systems (measured without any phase separation method applied). Black, filled circles (●) correspond to experimental solubility data reported in [93] obtained from undersaturation conditions at I = 0.01 m NaCl. Red line with a slope of +1 is shown for comparison purposes.*

At $m(ISA)_{tot} \geq 10^{-3}$ m, the solubility of Pu increases with a well-defined a slope of +1, indicating that the Pu:ISA stoichiometry of the complex at $pH_m = 12$ is 1:1.

Quantification of Pu in the supernatant solutions without any phase separation method (open symbols in Figure 15) show a significantly greater $m(Pu)_{tot}$ than the values obtained after ultracentrifugation or ultrafiltration, indicating the gradually larger fraction of colloidal Pu(IV) aqueous species in solution with increasing $m(ISA)_{tot}$. Special care was taken to avoid artefacts caused by the re-suspension of solid particles. The reproducibility of these observations was counterchecked with independent samples prepared with different total volumes and types of containers. Although $m(Pu)_{tot}$ values obtained after phase separation are representative of the thermodynamic equilibrium between the solid phase and monomeric aqueous species, the colloidal fraction must be also considered when assessing the impact of ISA on the mobilization of Pu under repository-relevant conditions.

Solubility data of Pu(IV) in the presence of ISA previously determined in [93] are also shown for comparison purposes in Figure 15. Substantial discrepancies arise between these data and the Pu solubility determined in the present work (for both, HQ- and Sn(II)-buffered systems). Relevant experimental shortcomings identified in [93] (see Section 1.3.3.1) could explain these observations, such as: the use of oversaturation approach without phase separation for the quantification of $m(Pu)_{tot}$, non-redox buffered conditions, among others. Indeed, the $m(Pu)_{tot}$ concentrations measured in the present work in the absence of phase separation already point out that the presence of colloids might represent a relevant contribution to the overall solubility measured by Moreton and co-workers. Because of these limitations, the data reported in [93] are disregarded in the development of chemical and thermodynamic models for the system Pu(IV)–ISA.

3.1.2.3 Solid phase characterization

Synchrotron-based in-situ XRD

Figure 16 and Figure 17 show the *in-situ* XRD patterns of the solid phases controlling the solubility of Pu in HQ and Sn(II) systems, respectively, equilibrated in solutions with $m(ISA)_{tot} = 10^{-3}$ m, $pH_m = 9$ or $m(ISA)_{tot} = 0.10$ m, $pH_m = 12$ for 260 days. Figure 16 also shows the diffractogram of the empty double containment used in the synchrotron-based measurements at the INE–Beamline as described in Section 2.6.6.

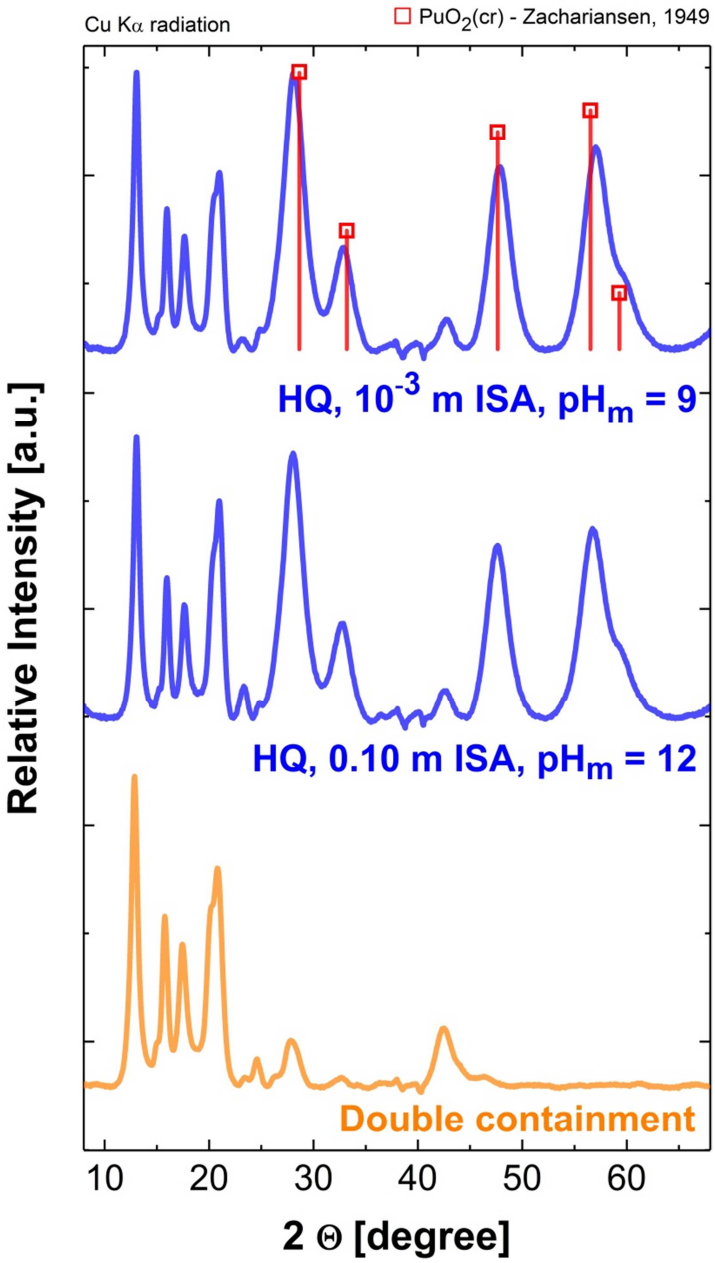

Figure 16. *In-situ XRD patterns collected at the INE-Beamline for the Pu solid phases recovered from HQ-buffered solubility experiments with* $m(ISA)_{tot} = 10^{-3}$ *m,* $pH_m = 9$ *and* $m(ISA)_{tot} = 0.1$ *m,* $pH_m = 12$ *(*$t_{eq} = 260$ *days) and for the empty double containment. Squares indicate peak positions and relative intensities reported for* PuO_2*(cr) [166].*

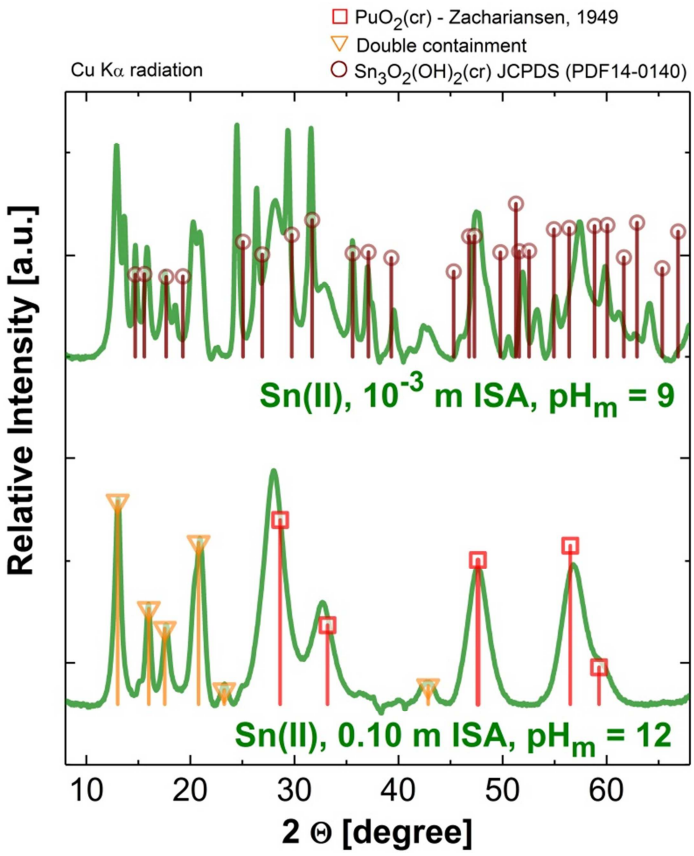

Figure 17. *In-situ XRD patterns collected at the INE-Beamline for the Pu solid phases recovered from Sn(II)-buffered solubility experiments with* $m(ISA)_{tot}$ *=* 10^{-3} *m,* pH_m *= 9 and* $m(ISA)_{tot}$ *= 0.1 m,* pH_m *= 12 (*t_{eq} *= 260 days). Square and circle marks show peak positions and relative intensities reported for* PuO_2*(cr) [166] and for* $Sn_6O_4(OH)_4$*(s) (PDF 14-0140 from JCPDS database [136]), respectively. The triangle marks indicate the corresponding signals of the empty double containment used.*

All collected diffractograms of the retrieved Pu solid phases equilibrated in the presence of ISA are perfectly matching with the reference pattern of PuO_2(cr) reported in [166]. Under identical conditions to those of the present work, previous experimental study conducted in the absence of ISA found the signals of the PuO_2(cr) reference pattern significantly decreased in the solid phases retrieved from the Sn(II)-buffered samples at pH_m = 9 and 12, in comparison with the analogous data obtained in the HQ system. The Pu L_{III}-edge XANES spectra indicated a relevant contribution of Pu(III) in the solid phases treated with Sn(II), but the presence of the cubic Pu_2O_3(cr) (PDF 06328) and/or PuO_{2-x}(cr) (PDF 41-1171) phases could not be ruled out. However, in the course of the current study, all XRD pattern collected on the solid phases equilibrated in the presence of ISA are identical and such differences are not observed between the data of different redox buffered systems. These results are hinting

towards the retainment and predominance of $Pu(IV)O_2$(am,hyd) in both the HQ- and Sn(II)-buffered Pu-ISA system. Besides the pattern of PuO_2(cr), a number of additional reflections are also observed in the Sn(II) system at pH_m = 9. The latter show moderate agreement with the diffractogram of $Sn_6O_4(OH)_4$(s) (PDF 14-0140, as identified solid phase available in the JCPDS database [136]) and SnO(s) (PDF 13-0111), which are the expected solid phases controlling the solubility of Sn(II) at this pH_m [126]. Just as previously (Section 3.1.1.4), Sn(II)-containing solid phases in the retrieved solid phases of the Sn(II)-buffered system at pH_m = 12 were not detected, due to the complete dissolution of Sn(II) under this condition.

XANES

Pu L_{III}–edge XANES spectra collected for the solid phases controlling the solubility of Pu in HQ and Sn(II)-buffered solutions with $m(ISA)_{tot} = 10^{-3}$ m, pH_m = 9 or $m(ISA)_{tot}$ = 0.10 m, pH_m = 12 (t_{eq} = 260 days) are shown in Figure 18. The figure also includes the XANES spectra of the reference spectra reported in [140] for aqueous Pu(III) and Pu(IV) species under acidic conditions.

The edge energies of the XANES spectra collected for all the retrieved Pu solid phases are in excellent agreement with the Pu(IV) reference spectrum reported in [140]. Furthermore, these spectra perfectly match the previously XANES spectrum collected for the starting material, and clearly show the existence of a PuO_2 fluorite-like structure in the analyzed solid.

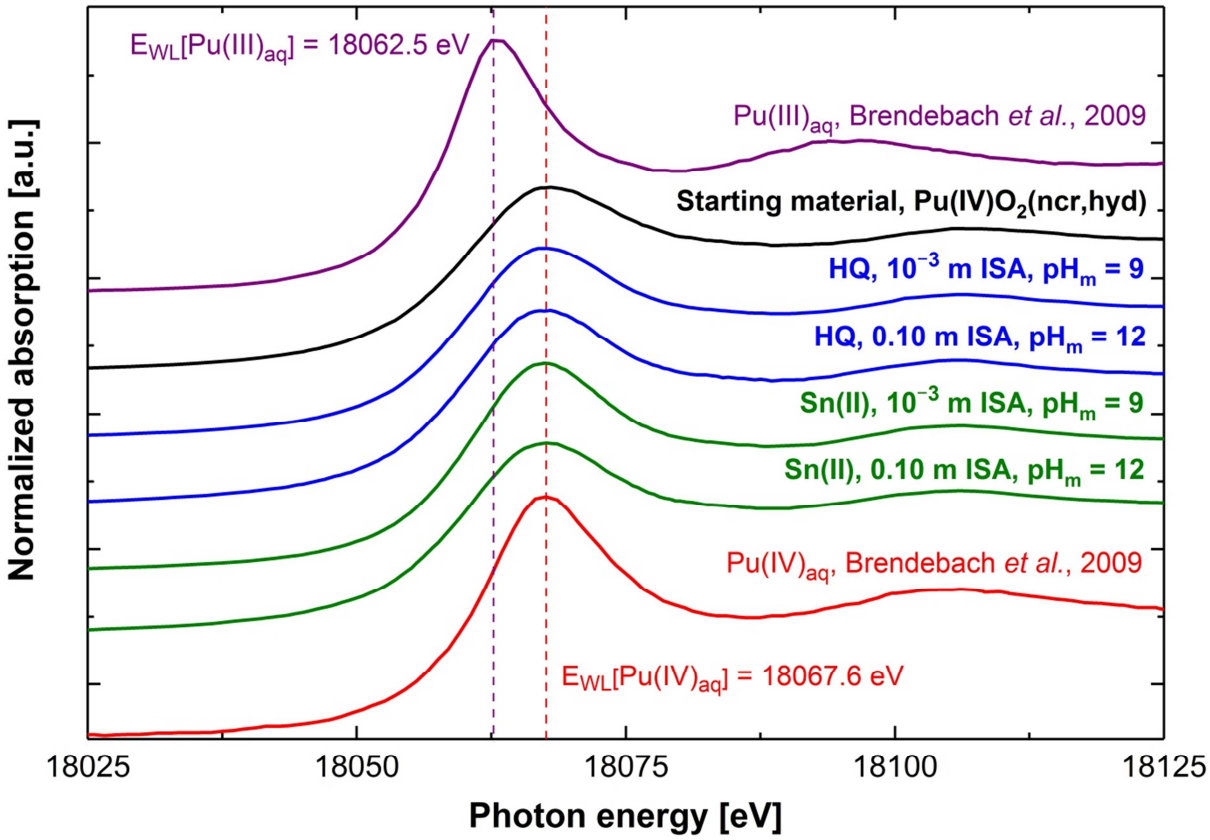

Figure 18. *Pu L_{III}–edge XANES spectra of solid phases recovered from HQ- (blue lines) and Sn(II)-buffered (green lines) systems equilibrated in solutions with $m(ISA)_{tot}$ = 10^{-3} m, pH_m = 9 and $m(ISA)_{tot}$ = 0.10 m, pH_m = 12 for 260 days. The spectra of the references for the aqueous species of Pu(III) (purple line, position of E_{WL} = 18062.5 eV) and Pu(IV) (red line, position of E_{WL} = 18067.6 eV) reported in Brendebach et al. [140] and the spectra of the initially characterized Pu(IV)O_2(am,hyd) phase (starting material, also used for the present study, see section 3.1.1.1 and references [1, 2])*

Experimental evidences from *in-situ* XRD and XANES measurements unequivocally confirm that the initial nanocrystalline Pu(IV)O_2(am,hyd) remains stable and controls the solubility of Pu in all system in the presence of ISA.

As the redox conditions imposed by HQ fall within the stability field of both, $Pu(IV)_s$ and $Pu(IV)_{aq}$, the predominance of Pu(IV) in the retrieved solid phases were *a priori* expected upon predictions of thermodynamic calculations. Previous solubility study conducted in the absence of ISA under identical redox conditions and ~8.0 ≤ pH_m ≤ ~13 showed very low (~$10^{-10.5}$ m) and pH-independent Pu solubility values, consistent with the control of the solubility equilibrium: PuO_2(am,hyd) + 2 H_2O(l) ⇔ $Pu(OH)_4$(aq). Hence, the HQ-buffered Pu-ISA series are treated as the reference case to separately assess the interaction of $Pu(IV)_{aq,s}$

with ISA. Findings of *in-situ* XRD and XANES gained on the retrieved Pu solid phases in the Sn(II) system show significant differences between the two cases: i, in the absence (t_{eq} = 146 days) and ii, in the presence of ISA (present work, t_{eq} = 260 days). The predominance of the tetravalent state of Pu, *i.e.* the complete lack of the previously detected Pu(III)-content in the retrieved solid phases dictates to evaluate the Pu-ISA solubility data of the Sn(II) system by the use of a reductive dissolution model. Under such circumstances, the concentrations of the free hydrolyzed Pu(III)-species are driven by the present redox condition, with ($pe + pH_m$) = (1.54 ± 0.14) in solution, through the chemical equilibrium: $Pu(IV)O_2(am,hyd) + (1+n)\ H^+ + e^- \Leftrightarrow Pu(III)(OH)_{3-n}^{n+} + (n-1)\ H_2O(l)$.

EXAFS

The Fourier-transformed (FT) representation of the k^2-weighted EXAFS data depicted in Figure 19 for HQ and Sn(II) systems (upper panel: FT magnitude, imaginary part and fit results in R-space, lower panel: raw data, Fourier-filtered data and fit results in k-space) corresponds to a radial pair distribution function uncorrected for photoelectron central and neighbor atom phase-shifts. Two coordination shells are discernible for all samples investigated in the present work: the first one around 1.75 Å (R−Δ) reflects Pu bonding to bridging oxygen atoms and to oxygen from terminal water and hydroxide units. These different oxygen neighbors exhibit a spread of bond distances generally leading to large Debye–Waller factors or requiring inclusion of an asymmetry parameter (3rd cumulant) in the fit - or even a second oxygen neighbor shell (*cf., e.g.* to Rothe *et al.* [169]). The second shell around 3.6 Å (R−Δ) reflects backscattering from second next Pu neighbors in the solid precipitates. All metric parameters are listed in Table 8.

As observed in the previous Pu solubility study in the absence of ISA [1], all solids investigated in the present work show a fluorite type signature as well. No clear trends are observed with pH_m (9 and 12) or with reducing agent (HQ and Sn(II)). In all cases, R_{Pu-O} scatters around 2.30 Å and R_{Pu-Pu} around 3.80 Å, whereas coordination numbers: N_O scatters around 6 and N_{Pu} around 4. As extensively discussed in previous publications [1, 179-181], the nanocrystalline character of the PuO_2(ncr,hyd) material used in this work leads to a significantly distorted local order around individual Pu centers, which importantly reduces the coordination number reported for ideal fluorite-type PuO_2: R_{Pu-O} = 2.32 Å, N_O = 8; R_{Pu-Pu} = 3.81 Å, N_{Pu} = 12. This is attributed to destructive interference of the backscattered photoelectron waves.

In summary, experimental evidences from *in-situ*-XRD, XANES and EXAFS measurements unequivocally confirm that the initial material, nanocrystalline Pu(IV)O_2(ncr,hyd) remains stable and controls the solubility of Pu in all systems in the presence of ISA. This observation was considered in Section 3.1.2.4 for deriving chemical and thermodynamic models for the Pu–ISA system in HQ- and Sn(II)-buffered systems.

Table 8. *Data range and metric parameters extracted by least-squares fitting of EXAFS spectra to the EXAFS equation.*

Sample name	***k-range [Å^{-1}] fit-range [Å]***	***shell***	***N***	***R [Å]***	***ΔE$_0$ [eV]^g***	***σ^2 [Å^2]***	***r-factor [%]***
HQ	1.80-13.28	O	5.9	2.30	-0.44	0.0081	2.7
pH_m = 9	0.95-4.14	Pu	3.4	3.81		0.0021	
Sn(II)	1.75-13.46	O	6.6	2.28	-2.28	0.0081	2.4
pH_m = 9	0.98-4.11	Pu	4.3	3.78		0.0030	
HQ	1.70-13.29	O	5.9	2.30	-1.11	0.0082	6.6!
pH_m = 12	1.04-4.11	Pu	4.1	3.80		0.0030	
Sn(II)	1.75-13.47	O	5.2	2.29	-2.31	0.0060	1.6*
pH_m = 12	0.90-4.06	Pu	3.5	3.80		0.0025	

S_0^2 = 1.0 fixed (slightly underestimating N in all fits)
^{g} global parameter for both shells
! worst fit in series, reason unclear, low frequency contribution not reproduced
* best fit in series
errors: R_{Pu-O} 0.01 Å, R_{Pu-Pu} 0.02 Å

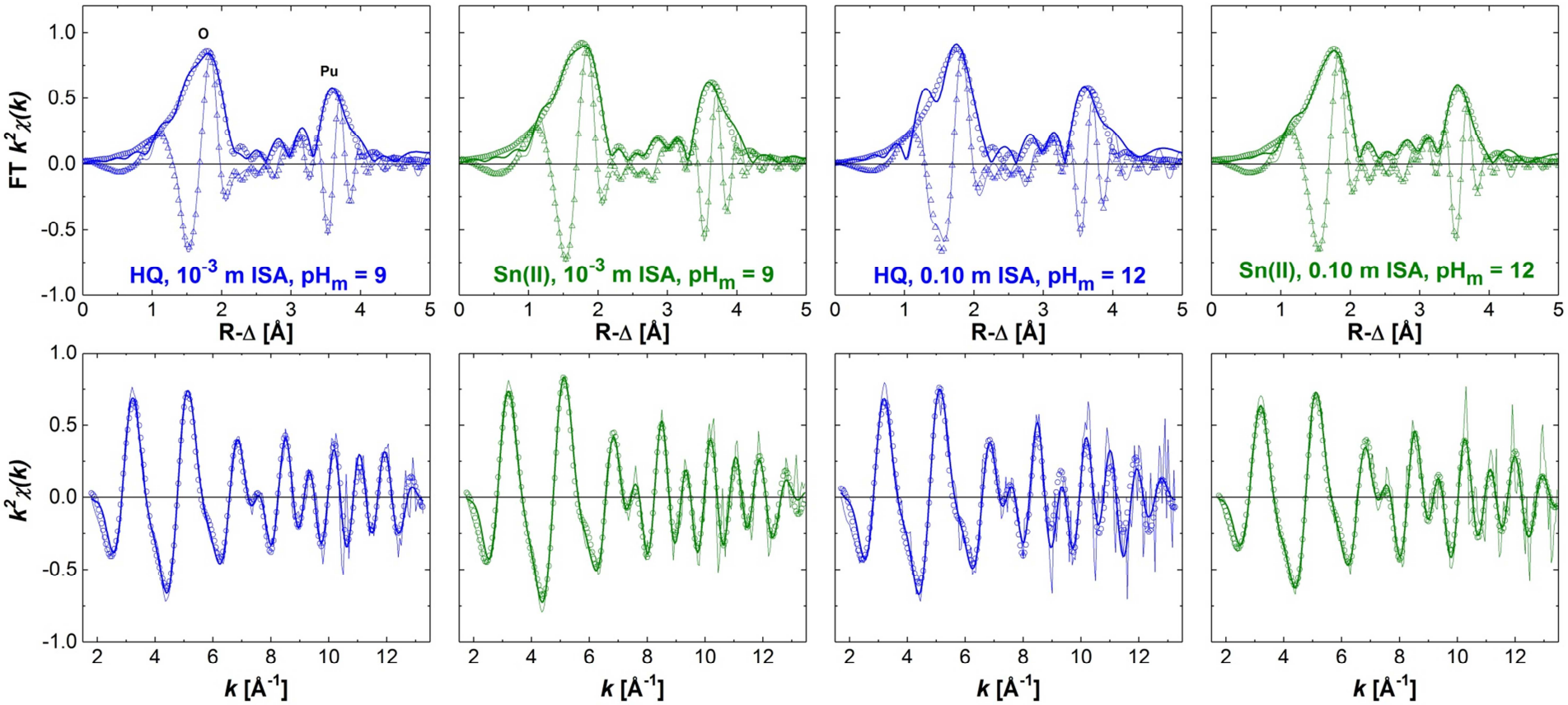

Figure 19. *Pu L_{III}–edge EXAFS fit results for Pu(IV)O_2(ncr,hyd) solid phases recovered from HQ and Sn(II)-buffered systems in the presence of ISA in R-space - upper panel: FT magnitude (solid line), fit magnitude (open circles), FT real part (thin solid line) and fit real part (open triangles); lower panel: Fourier-filtered data (solid line), raw data (thin solid line), back-transformed fit (open circles).*

3.1.2.4 Thermodynamic calculations

As discussed in Section 3.1.1.5, Chemical reactions (32), (35) and (38) are expected to control the solubility of Pu within the experimental conditions considered in this study. The corresponding Equations (33, 34), (36, 37) and (39, 40) have been used in combination with stability constants and SIT ion interaction coefficients summarized in Table A1 and Table A2 of the Appendix to calculate the solubility lines in Figure 20, Figure 21, Figure 22 and in Figure 28: PuO_2(am,hyd) in equilibrium with $Pu(IV)_{aq}$ (black line); PuO_2(am,hyd) in equilibrium with $Pu(IV)_{aq}$ and $Pu(III)_{aq}$ at (pe + pH_m) = 1.54 (grey line); and $Pu(OH)_3$(am) in equilibrium with $Pu(III)_{aq}$ (light blue line). The solubility curve plotted for $Pu(OH)_3$(am) were calculated using log $*K°_{IIIs,0}$ = 14.58, as reported in Cho *et al.* [33]. These thermodynamic and activity models and accordingly calculated solubility lines are the basis for the thermodynamic description of the systems Pu(IV)–OH–ISA and Pu(III)–OH–ISA, which are derived in Sections 3.1.2.4.1 and 3.1.2.4.2 based upon solubility data and solid phase characterization discussed above.

3.1.2.4.1 Chemical and thermodynamic model of the system Pu(IV)-OH-ISA

The solubility data obtained in HQ-buffered experiment series with $m(ISA)_{tot}$ < 0.10 m were used for the development of the chemical and thermodynamic models on the Pu(IV)–OH–ISA system. As demonstrated in the Pu solubility experiments in the absence of ISA (see Section 3.1.1) and also confirmed by the results of the solid phase characterization session in this chapter (see Section 3.1.2.3 for details), it can be safely assumed that HQ stabilizes the +IV redox state of Pu in both the aqueous and solid phases.

Based on the slope analyses described in Sections 3.1.2.2.1 and 3.1.2.2.2 (log $m(Pu)_{tot}$ *vs.* pH_m and log $m(Pu)_{tot}$ *vs.* log $m(ISA)_{tot}$), chemical reactions (48) and (49) are proposed to control the solubility and solution chemistry of Pu(IV) in the presence of ISA within the conditions investigated ($-6 \le \log m(ISA)_{tot} \le -2$ and $8 \le pH_m \le 13$) in HQ-buffered systems.

$$Pu(IV)O_2(am,hyd) + ISA^- + 2\ H_2O(l) \Leftrightarrow Pu(IV)(OH)_4ISA^- \quad (48)$$

$$Pu(IV)O_2(am,hyd) + ISA^- + 3\ H_2O(l) \Leftrightarrow Pu(IV)(OH)_5ISA^{2-} + H^+ \quad (49)$$

The species $Pu(OH)_4ISA^-$ is predominant at pH_m = 8 – 11, whereas $Pu(OH)_5ISA^{2-}$ forms in systems with pH_m > 11. Note, that the proposed stoichiometries for the Pu(IV)–ISA

complexes assume highly hydrolyzed Pu(IV) moieties ("$Pu(OH)_4$" and "$Pu(OH)_5^-$") coordinated to one ISA^- ligand. Analogous reactions can be proposed by assuming instead the deprotonation of one or more alcohol groups of the ISA ligand. Such uncertainty does not affect the mass action law in reactions (48) and (49) (except for the number of water molecules), and thus has no impact on the accordingly determined equilibrium constants. (In view of general knowledge on Pu coordination chemistry, however, it can already be clarified that the formation of the complex with the moiety of "$Pu(OH)_5^-$" should involve the simultaneous deprotonation of minimum one alcoholic groups of ISA.) The structures of the complexes forming are further investigated via quantum chemical calculations, as discussed in Section 3.1.2.5.1.

Internal data evaluation, using the non-linear regression analysis method of least-squares involved the application of the following model function:

$$f(K'_{IVs,4+x_1,y_1}\ldots, K'_{IVs,\,4+x_i,y_i}) = \left(\sum_{i=1}^{m}\left[\left(\log m^{exp}(Pu)_{tot,m} - \log m^{calc}(Pu)_{tot,m}\right)^2\right]\cdot(n-1)^{-1}\right)^{0.5}, \quad (50)$$

where $m^{exp}(Pu)_{tot,m}$ is the experimentally determined total concentration of Pu in solution (at a certain conditions, considering *m* number of data points in total). The parameters: ${}^*K'_{IVs,4+xi,yi}$ (with $i = 1, 2$) are the conditional equilibrium constants (at $I = 0.10$ m NaCl) corresponding to the solubility reactions (48) and (49), which can be expressed as in Equation (51):

$$\log {}^*K'_{IVs,4+x,y} = \log m_{Pu(IV)(OH)_{4+x}(ISA)_y^{-(x+y)}} + x \log m_{H^+} - y \log m_{ISA^-} \quad , \quad (51)$$

where ($y_1 = y_2 = 1$ and) $x_1 = 0$ for the first, ($Pu(OH)_4ISA^-$; $\log {}^*K'_{IVs,4,1}$) or ($x_2 =$) 1 for the second species ($Pu(OH)_5ISA^{2-}$; $\log {}^*K'_{IVs,5,1}$). The dependent variable: $m^{calc}(Pu)_{tot,m}$ is the total concentration of Pu in solution calculated according with Equation (52) and considering the total concentration of ISA ($m(ISA)_{tot}$) with the experimentally measured pH_m (converted to m_{H^+}) value at each experimental point. Taking into account the significantly higher total concentrations of ISA compared to the solubility of Pu, free concentration of ISA in solution: m_{ISA^-}, was set equal to the total: $m(ISA)_{tot}$.

$$m^{calc}(Pu)_{tot,m} = \sum_{n=1}^{4}\left({}^*K'_{IVs,(4-n)}\,(m_{H^+})^n\right) + \sum_{i=1}^{2}\left({}^*K'_{IVs,4+x_i,y_i}\,(m_{ISA^-})^{yi}\,(m_{H^+})^{-xi}\right) \quad (52)$$

In order to minimize the object function (Equation (50) - the square root of the averaged, squared residuals), firstly, the SIMPLEX method was applied [151].
In a second step, the gained, optimized values of ${}^{*}K'_{IVs,4,1}$ and ${}^{*}K'_{IVs,5,1}$ were then extrapolated to reference state, I = 0 using Equation (53) and SIT ion interaction coefficients with the values of $\varepsilon(Pu(OH)_4ISA^-; Na^+) = -(0.05 \pm 0.10)$ mol·kg^{-1} and $\varepsilon(Pu(OH)_5ISA^{2-}; Na^+) = -(0.10 \pm 0.10)$ mol·kg^{-1}, estimated according to empirical correlations with the charges of the newly forming complex species as described in [149].

$$\log {}^{*}K°_{IVs,4+x,y} = \log {}^{*}K'_{IVs,4+x,y} + \log \gamma_{Pu(IV)(OH)_{4+x}(ISA)_y^{-(x+y)}} + x \log \gamma_{H^+} - \\ - y \log \gamma_{ISA^-} - x \log a_w \quad (53)$$

As a last step, the resulting solubility constants $\log K°_{IVs,4,1}$ and $\log K°_{IVs,5,1}$ were converted (in accordance with chemical Equation (54) into the corresponding formation constants $\log {}^{*}\beta°_{1,4,1}$ and $\log {}^{*}\beta°_{1,5,1}$ using the $\log K°_{IVs,0}$ reported in the NEA-TDB [9] for PuO_2(am,hyd). As shown in analogous investigations conducted in the absence of ISA (see Section 3.1.1), this is consistent with the solubility control of the initial Pu(IV)O_2(ncr, hyd) phase used in this study as well.

$$Pu^{4+}(aq) + x\ ISA^- + (4+y)\ H_2O(l) \Leftrightarrow Pu(IV)(OH)_{4+y}ISA^{-(x+y)} + (4+y)\ H^+ \quad (54)$$

$$\log {}^{*}\beta°_{1,4+x,y} = \log a_{Pu(IV)(OH)_{4+x}(ISA)_y^{-(x+y)}} + (4+x) \log a_{H^+} - \log a_{Pu^{4+}} - y \log a_{ISA^-} \quad (55)$$

To validate the simplified fitting process described above, an independent data evaluation approach was also performed using the PHREEPLOT – PHREEQC (PP–PQC) program packages (see also Section 2.7). For this purpose, a database was constructed containing all necessary equilibrium constants and SIT ion interaction coefficients (including $\varepsilon(Pu(OH)_4ISA^-; Na^+)$ and $\varepsilon(Pu(OH)_5ISA^{2-}; Na^+)$ as summarized in Table A1 and Table A2 of the Appendix. With this database, the software package was used to optimize the values of $\log {}^{*}\beta°_{1,4,1}$ and $\log {}^{*}\beta°_{1,5,1}$. The applied objective function was the square root of the averaged sum of squared residuals (corresponding to the parameters). The refinement of the defined cumulative equilibrium constants (as in Equation (55), at the reference state) was combined with the internal calculation of the ionic strength, based upon the initially set m(NaCl), $m(ISA)_{tot}$ and pH_m values. In this case, the modified Levenberg-Marquardt method implemented in PP-PQC was used to optimize the constants [150].

Table 9 shows the values of log ${}^{*}\beta^{\circ}_{1,4,1}$ and log ${}^{*}\beta^{\circ}_{1,5,1}$ obtained with the two different data evaluation approaches. The nearly identical results from the two procedures provide further confidence in the optimized log ${}^{*}\beta^{\circ}_{1,4,1}$ and log ${}^{*}\beta^{\circ}_{1,5,1}$ values. Because of the higher internal consistency and the more accurate calculation of ionic strength, the outcome obtained with the PP–PQC software package was adopted as the final set of thermodynamic constants and uncertainties for the Pu(IV)–OH–ISA system.

Table 9. *Fitting results for the equilibrium constants (at I = 0, as expressed in Equation (55) for $Pu(OH)_4ISA^-$ with $\log {}^{*}\beta^{\circ}_{1,4,1}$ and $Pu(OH)_5ISA^{2-}$ with $\log {}^{*}\beta^{\circ}_{1,5,1}$) obtained through the non-linear regression analysis method of least–squares ("LS-method") or by using the PHREEPLOT – PHREEQC software package ("PP–PQC").*

$\log {}^{*}\beta^{\circ}_{1,4+x,1}$	Parameters of evaluated data sets (HQ system)		Approach	Fitting result
$Pu(IV)(OH)_{4+x}ISA^{-(1+x)}$	$m(ISA)_{tot}$ [m]	pH_m	(name)	(I → 0)
$\log {}^{*}\beta^{\circ}_{1,4,1}$	< 0.10	8 – 12.9	LS–method	–5.03
$\log {}^{*}\beta^{\circ}_{1,5,1}$	< 0.10	8 – 12.9	LS–method	–16.98
$\log {}^{*}\beta^{\circ}_{1,4,1}$	< 0.10	8 – 12.9	PP–PQC	**–(5.03 ± 0.12)**
$\log {}^{*}\beta^{\circ}_{1,5,1}$	< 0.10	8 – 12.9	PP–PQC	**–(16.92 ± 0.13)**

The solubility of $Pu(IV)O_2$(ncr,hyd) in the presence of ISA calculated using the chemical and thermodynamic models derived in the present work are shown in Figure 20 and in Figure 21 a, b, c, along with the corresponding experimental data sets obtained in this study. For comparison reasons, Figure 20 and Figure 21 also include experimental solubility data obtained in Sn(II) systems at $pH_m > 11$.

Figure 21 (a, b, c) show that the solubility of $Pu(IV)O_2$(am,hyd) in the presence of ISA calculated using the chemical and thermodynamic models derived in this work are in excellent agreement with the experimentally measured solubility in HQ systems. Although experimental data obtained in Sn(II) systems were not used for the refinement of the parameters, chemical and thermodynamic models derived from HQ systems properly explain solubility data in Sn(II) systems as well, where $pH_m > 11$. This observation further confirms the findings of the solid phase characterization as the chemical reaction controlling the solubility of Pu, *i.e.* PuO_2(ncr,hyd) ⇔ Pu(IV)–ISA(aq) is the same in both systems under the outlined conditions.

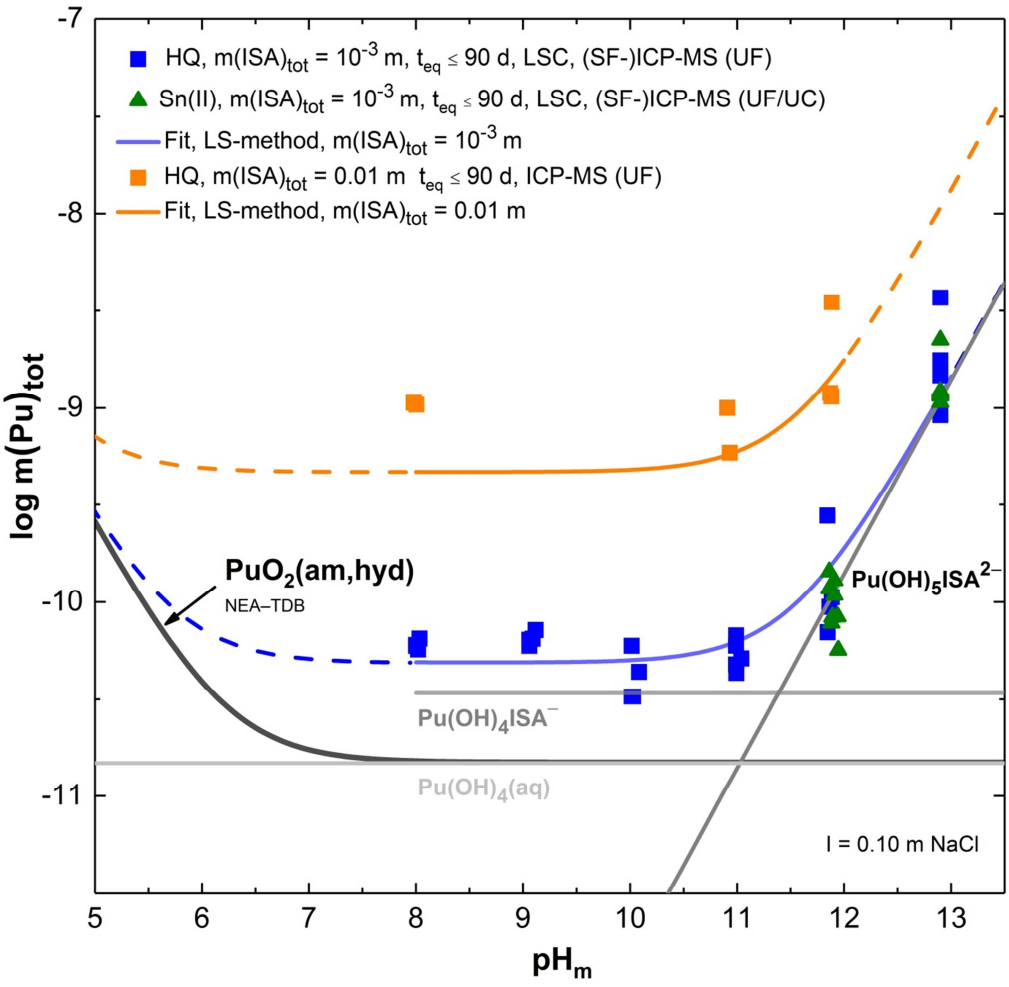

Figure 20. *Experimentally measured $m(Pu)_{tot}$ in equilibrium with PuO_2(ncr,hyd) at I = 0.10 m NaCl in HQ-buffered systems with pH_m = 8 – 12.9 in the presence of $m(ISA)_{tot} = 10^{-3}$ m (■) or $m(ISA)_{tot}$ = 0.01 m (■) and in Sn(II)-buffered systems (▲), at pH_m > 11 with $m(ISA)_{tot} = 10^{-3}$ m. Solubility lines (solid and dashed) in blue (with $m(ISA)_{tot} = 10^{-3}$ m) and in orange (with $m(ISA)_{tot}$ = 0.01 m) for Pu(IV)O_2(am,hyd) in the presence of ISA are calculated (at I = 0.10 m NaCl) using the chemical and thermodynamic models derived in this work. Black solid line corresponds to the thermodynamically calculated solubility of PuO_2(am,hyd) in the absence of ISA.*

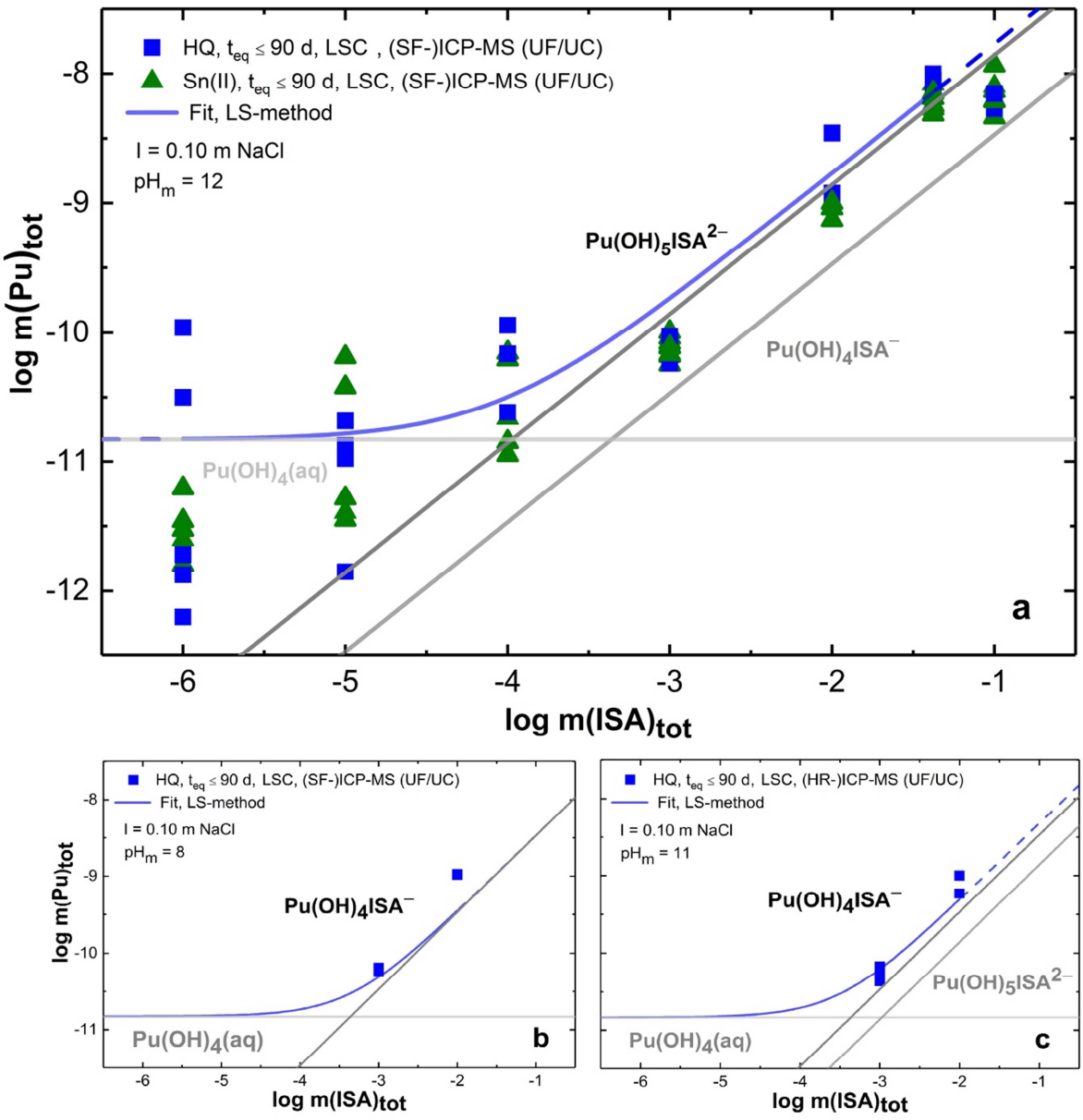

Figure 21. *Experimentally measured $m(Pu)_{tot}$ in equilibrium with PuO_2(ncr,hyd) at I = 0.10 m NaCl in HQ-buffered systems (■) or in Sn(II)-buffered systems (▲) at constant pH_m = 8 (**b**), 11 (**c**) or 12 (**a**) with 10^{-6} m ≤ $m(ISA)_{tot}$ = 0.10 m. Solubility lines (solid and dashed) in blue for Pu(IV)O_2(am,hyd) in the presence of ISA are calculated (at I = 0.10 m NaCl) using the chemical and thermodynamic models derived in this work. Straight lines are showing the individual contributions of the selected complex species.*

3.1.2.4.2 Chemical and thermodynamic model of the system Pu(III)–OH–ISA

The solubility data obtained in Sn(II)-buffered experiment series with $m(ISA)_{tot} = 10^{-3}$ m were used for the development of chemical and thermodynamic models on the Pu(III)--ISA-OH system. In comparison with the HQ series, the higher Pu solubility values obtained in the Sn(II)-buffered systems at $pH_m = 8 - 11$ supports the predominance of Pu(III)–ISA complex(es) in solution. As the solubility controlling phase (at $pH_m = 9$ and 12) was identified to be the initial $Pu(IV)O_2$(ncr,hyd) phase, the present Pu(III)-bearing ISA-complex species in solution originate from the reductive dissolution reaction of the initial $Pu(IV)_s$ phase. Hence, under such conditions, the concentration of free hydrolyzed Pu(III)-species are defined by Equations (39) and (40) through chemical equilibrium (38). The basis of data evaluation is the formerly determined chemical and thermodynamic model of the system Pu(IV)–OH–ISA.

Considering that the observed increase in Pu solubility with regard to the ISA-free case, *i.e.* solubility at $(pe + pH_m) = 1.54$ is pronounced within the near neutral pH-range, the formation reaction must undergo by involving either of the present hydrolyzed species: $Pu(III)(OH)^{2+}$, $Pu(III)(OH)_2^+$ and $Pu(III)(OH)_3$. The trend observed in the data set as function of the pH_m conditions however shows clear correlation with a slope of –1 ($\log m(Pu)_{tot}$ *vs.* pH_m), pointing towards the formation and predominance of only one, doubly hydrolyzed Pu(III)–ISA complex species: $Pu(III)(OH)_2ISA(aq)$. Nevertheless, the possible formation of a second species with several proposed stoichiometries as Pu(III):OH:ISA with values of 1:1:1, 1:3:1, 1:1:2, 1:3:2, 2:1:1 and 2:3:1 was also tested to represent the observed tendencies in the data set. However, as the overall fit throughout these procedures did not improve significantly (compared to the case of involving only the $Pu(III)(OH)_2ISA(aq)$ species), the existence of a second Pu(III)-ISA complex was finally disregarded (differences between the absolute values of the objective functions corresponding to the various fitting procedures were observed to be negligibly small: $\Delta\sum(\sigma^2) < 1\%$). Hence, the established speciation model consisted of only one species to be forming under the boundary conditions through chemical equilibrium (56).

$$Pu(III)(OH)_2^+ + ISA^- \Leftrightarrow Pu(III)(OH)_2ISA(aq) \qquad (56)$$

The newly defined species, $Pu(III)(OH)_2ISA(aq)$ is expected to be predominant under strongly reducing conditions at relatively wide range of pH_m values ($8 < pH_m < 10$, at $m(ISA)_{tot} = 10^{-3}$ m), whereas in solutions with $10 < pH_m$, the formerly identified $Pu(IV)(OH)_5ISA^{2-}$ complex gains relevance. (Just as previously, the proposed stoichiometry

for the Pu(III)–OH–ISA complex remains at a hypothetical level, provided that an analogous reaction can also be constructed by assuming instead the deprotonation of one or more alcohol groups of the ISA ligand. This again would not affect the mass action law or change the derived equilibrium constants related to the chemical reaction itself.)

The internal data evaluation, using the non-linear regression analysis method of least-squares involved the use of an analogous model function as previously established (see Equation (50) in Section 3.1.2.4.1). The optimized parameter in the present case was the conditional equilibrium constant ($^{*}K'_{III,2,1}$; at I = 0.10 m NaCl), corresponding to the chemical reaction (21), expressed as in Equation (57).

$$\log {}^{*}K'_{III,2,1} = \log m_{Pu(III)(OH)_2(ISA)(aq)} - \log m_{ISA^-} - \log m_{Pu(III)(OH)_2{}^{+}} \quad (57)$$

The total concentration of Pu in solution ($m^{calc}(Pu)_{tot,m}$) was calculated as expressed in Equation (58), considering the total concentration of ISA ($m(ISA)_{tot}$) with the experimentally measured pH_m (converted to m_{H^+}) and pe values as $-\log a_e$-, calculated from the ($pe + pH_m$) = 1.54 correlation, also taking into account the chemical model and the corresponding equilibrium constants of the system Pu(IV)–OH–ISA ($^{*}K'_{IVs,4,1}$ and $^{*}K'_{IVs,5,1}$ at I = 0.10 m NaCl calculated using the estimated SIT coefficients) optimized by the PP–PQC software package. Based on similar assumptions as formerly discussed, the free concentration of ISA in solution, m_{ISA^-}, was set equal to the $m(ISA)_{tot}$.

$$m^{calc}(Pu)_{tot,m} = \sum_{n=1}^{4}\left({}^{*}K'_{IVs,(4-n)}\cdot(m_{H^+})^{n}\right) + \sum_{n=1}^{3}\left({}^{*}K'_{IVs/III,(3-n)}\cdot(m_{H^+})^{n}\right) + \\ + \sum_{i=1}^{2}\left({}^{*}K'_{IVs,4+x_i,1}\,(m_{H^+})^{-xi}\cdot(m_{ISA^-})\right) + {}^{*}K'_{III,2,1}\,(m_{ISA^-})\cdot(m_{Pu(OH)_{2+y}}) \quad (58)$$

Minimization of the object function (optimization of the $^{*}K'_{III,2,1}$ parameter) was again performed using the SIMPLEX method [151].

The optimized value of $^{*}K'_{III,2,1}$ was then extrapolated to the reference state (I = 0) using Equation (59) where the SIT ion interaction coefficient was $\varepsilon(Pu(OH)_2ISA(aq); Na^+/Cl^-)$ = 0.00 mol·kg^{-1}, as given by definition for neutrally charged species within the SIT formalism.

$$\log {}^{*}K°_{III,2,1} = \log {}^{*}K'_{III,2,1} + \log \gamma_{Pu(OH)_2ISA(aq)} - \log \gamma_{ISA^-} \quad (59)$$

In the final stage, the resulting solubility constant log ${}^{*}K°_{III,2,1}$ was converted (in accordance with chemical Equation (60) into the corresponding cumulative formation constant: log ${}^{*}\beta°_{1,2,1}$, expressed in Equation (61) using the second hydrolysis constant of $Pu(III)_{aq}$, log ${}^{*}K°_{III,2}$ = 15.1 as reported in NEA-TDB [9].

$$Pu^{3+}(aq) + ISA^{-} + 2\ H_2O(l) \Leftrightarrow Pu(III)(OH)_2ISA(aq) + 2\ H^{+} \quad (60)$$

$$\log {}^{*}\beta°_{1,2,1} = \log a_{Pu(OH)_2ISA(aq)} + 2 \log a_{H^+} - \log a_{Pu^{3+}} - \log a_{ISA^-} \quad (61)$$

By the use of the previously established database for the system Pu(IV)–OH–ISA, the parameter log ${}^{*}\beta°_{1,2,1}$ was also optimized with the PP–PQC program packages. The procedure was executed analogously as previously described in Section 3.1.2.4.1, but in the present case the measured redox condition in solution with (pe + pH_m) = 1.54 also had to be taken in consideration as a second independent variable.

Provided that the measured E_h values were largely scattered, accounting for the uncertainty of the optimized parameter was executed using an optimized Monte Carlo approach. For this purpose, the following initial assumptions were set: 1. the mean pe values and the assigned uncertainties represent the final values and the statistical errors of the redox conditions present in solutions, 2. dependent (log $m(Pu)_{tot}$) and independent (pe, pH_m) variables follow Gaussian distribution when the number of variables is sufficiently large. In the course of the estimation procedure, the inverse Gaussian distribution function was applied together with the Monte-Carlo method to generate new sets of pe and log $m(Pu)_{tot}$ input values randomly scattered around the respective mean values (uncertainties assigned to the measured pH_m conditions are considered negligible). The standard deviations implemented in the functions were directly adapted from the errors assigned to the measured pe values and from the variance of the input log $m(Pu)_{tot}$ values corresponding to the best fit result of the initial data set. A total of 1000 new data sets were generated and independently re-fitted one by one using the PP–PQC program packages. The correctness of the used approach was attested through the re-calculation of the given standard deviations related to the new sets of the two variables, which were in perfect agreement with those of the initially collected data. Furthermore, as expected, the mean value of the optimized log ${}^{*}\beta°_{1,2,1}$ parameter was also found to be identical to the given best fit value. The uncertainty assigned to the log ${}^{*}\beta°_{1,2,1}$ parameter was finally calculated as the weighted average of all newly calculated uncertainties. The use of the latter approach enabled us to estimate coupled uncertainties accounting for individual errors of independent and dependent variables in strict correlation with the optimized parameter.

Table 10 shows the optimized values of the log ${}^{*}\beta^{\circ}_{1,2,1}$ obtained with the two different data evaluation procedures applied. Although small deviations arose between the two values, the one resulted from the internal data treatment still lay within the large uncertainty-range assigned by the Monte Carlo method. Due to the higher internal consistency and the more accurate calculation of ionic strength, the outcome obtained by the use of PP–PQC software package was again adopted as the recommended final thermodynamic constant together with the uncertainty calculated with the Monte Carlo method for the Pu(III)–OH–ISA system.

The solubility of $Pu(IV)O_2(ncr,hyd)$ in the presence of ISA under strongly reducing condition with $(pe + pH_m) = 1.54$ calculated using the chemical and thermodynamic models derived in the present work are shown in Figure 22, along with the corresponding experimental data sets obtained in the Sn(II)-buffered system. For the sake of comparison, Figure 22 also includes experimental solubility data obtained in HQ systems at $pH_m > 11$. The excellent agreement between the calculated and all the measured $\log m(Pu)_{tot}$ provides further confidence in the optimized parameter.

Table 10. *Fitting results for the equilibrium constants (at $I \rightarrow 0$), as expressed in Equation (61) for $Pu(III)(OH)_2ISA(aq)$ with $\log {}^{*}\beta^{\circ}_{1,2,1}$ obtained through the non-linear regression analysis method of least–squares ("LS-method") or by using the PHREEPLOT – PHREEQC software package ("PP–PQC").*

Parameters of evaluated data sets (Sn(II) system)		***Fitting approach***	***$\log {}^{*}\beta^{\circ}_{1,2,1}$***	***Uncertainty estimation***
$m(ISA)_{tot}$ [m]	***pH_m***	***(name)***	***(at $I \rightarrow 0$)***	***(description)***
10^{-3}	8 – 12.9	LS–method	–10.73	-
10^{-3}	8 – 12.9	PP–PQC	–(10.96 ± 0.10)	"± 3σ"
10^{-3}	8 – 12.9	PP–PQC	**–(10.96 ± 0.28)**	**"Monte Carlo"**

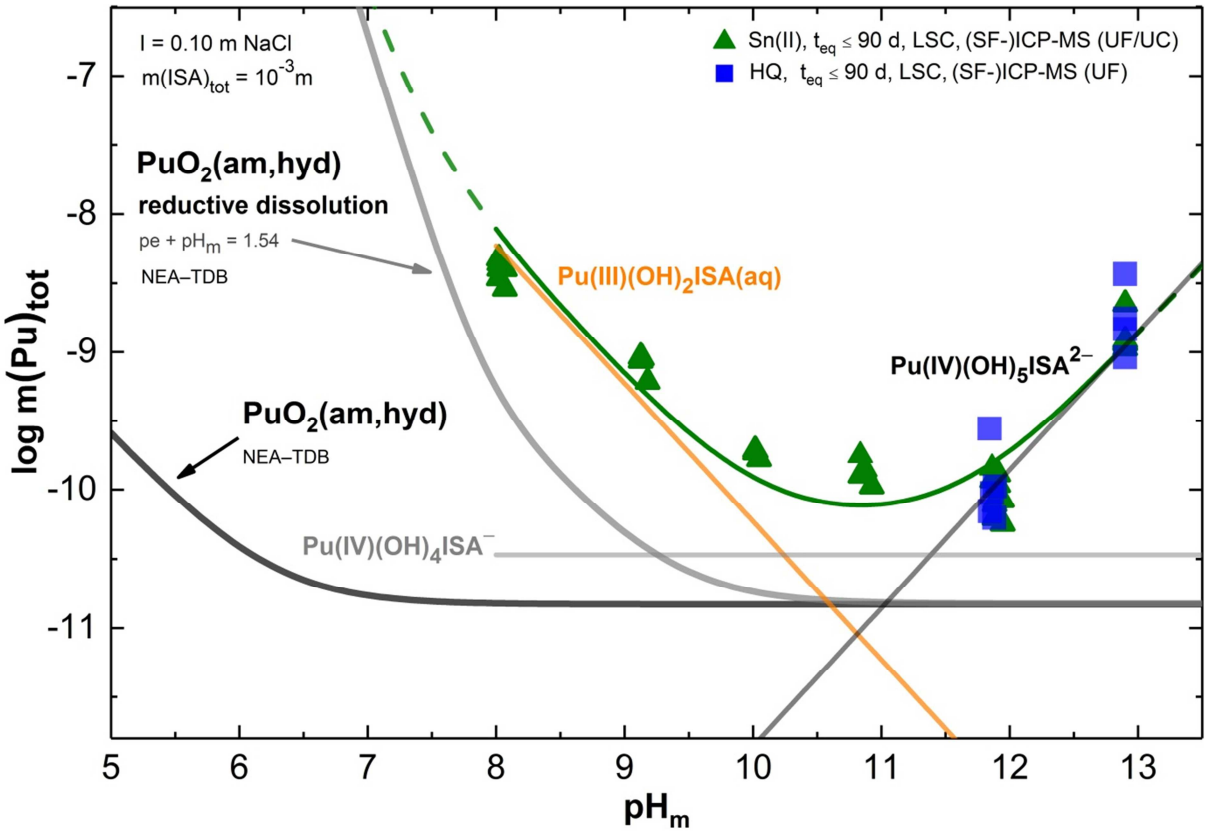

Figure 22. *Experimentally measured $m(Pu)_{tot}$ in equilibrium with PuO_2(ncr,hyd) at I = 0.10 m NaCl in Sn(II)-buffered systems (▲) with pH_m = 8 – 12.9 in the presence of $m(ISA)_{tot} = 10^{-3}$ m and in HQ-buffered systems (■), at pH_m > 11 with $m(ISA)_{tot} = 10^{-3}$ m. Solubility curves (solid and dashed) in green (with $m(ISA)_{tot} = 10^{-3}$ m) for Pu(IV)O_2(am,hyd) in the presence of ISA are calculated (at I = 0.10 m NaCl) using the chemical and thermodynamic models derived in this work. Black solid line corresponds to the thermodynamically calculated solubility of PuO_2(am,hyd) in the absence of ISA. Straight lines are showing the individual contributions of the selected complex species.*

3.1.2.5 Quantum chemical calculations

3.1.2.5.1 $Pu(IV)(OH)_4ISA^-$ and $Pu(IV)(OH)_5ISA^{2-}$ complexes

Based on experimental observations, the complexes $Pu(IV)(OH)_4ISA^-$ and $Pu(IV)(OH)_5ISA^{2-}$ were identified in Section 3.1.2.4.1 to dominate the aqueous speciation of Pu(IV) in HQ systems at $m(ISA)_{tot} \geq 10^{-3.5}$ m and $8 \leq pH_m \leq 13$. The analysis of solubility data provides only information on the stoichiometry of these complexes, in terms of Pu:OH:ISA ratios.

DFT calculations summarized in this section allow a further insight on the structure of these complexes, with focus on the hydrolysis of Pu^{4+} *vs.* deprotonation of OH-groups of the ISA

molecule. Because of the aqueous character of the complexes under investigation and as a simplified model for the solvent, a number of water molecules were included in the calculations (i) saturating the alcoholic groups of ISA and (ii) close to the metal ion in the first coordination shell of Pu^{4+}. Additional, a total of 8 water molecules were considered in a first approach, 4 at the ISA and 4 in the first coordination shell of Pu^{4+}. In a second step, DFT+COSMO was used to investigate the structure of the species in solution.

For both complexes under investigation, 8 oxygen atoms (belonging to ISA, water or to an OH-group) coordinated to Pu^{4+} in its first coordination shell. Formerly, through CASPT2 calculations, it was shown that coordination numbers of 8 and 9 are energetically similar for Pu(IV) [191]. Whilst keeping the charge of the complex constant, several configurations involving different number of hydrolysis groups (OH^-) and deprotonated alcohol groups of ISA (-C-O^-) were attempted: (i). $Pu(IV)(OH)_4ISA^-$, $Pu(IV)(OH)_3ISA_{-H}^-$, $Pu(IV)(OH)_2ISA_{-2H}^-$ and $Pu(IV)(OH)ISA_{-3H}^-$; (ii) $Pu(IV)(OH)_5ISA^{2-}$, $Pu(IV)(OH)_4ISA_{-H}^{2-}$, $Pu(IV)(OH)_3ISA_{-2H}^{2-}$ and $Pu(IV)(OH)_2ISA_{-3H}^{2-}$, where $ISA_{-x\mathrm{H}}$ corresponds to an ISA molecule with *x* deprotonated alcohol groups. In each case, several starting geometries were probed to confirm that a reasonable local minimum was found for the calculated structures. This procedure was carried out both with and without the approximation of the aqueous solution phases with COSMO.

For the complex "$Pu(IV)(OH)_4ISA^-$", calculations with and without COSMO indicate that the α-OH of ISA group (second carbon adjacent to the carboxylate group, see Figure 23) is deprotonated (labelled as ISA(C2) in Table 11). ISA interacts via the deprotonated α-OH and the COO^- group with Pu(IV). Additionally, 3 OH-groups and 3 water molecules remain in the first coordination shell of the Pu(IV) ion. The same is observed for the "$Pu(IV)(OH)_5ISA^{2-}$" complex, although in this case the alcohol group of the fourth carbon atom (labelled as ISA(C4) in Table 11) was also deprotonated and this O^- interacts directly with Pu(IV) and consequently one water molecule was removed from the first coordination shell of Pu(IV). The resulting structures as optimized by DFT can be described as $Pu(IV)(OH)_3ISA_{-H}^-$ and $Pu(IV)(OH)_3ISA_{-2H}^{2-}$ (see Figure 23). For both complexes, DFT calculations confirmed the presence of eight O-/O ions / atoms in the first coordination shell of the metal ion.

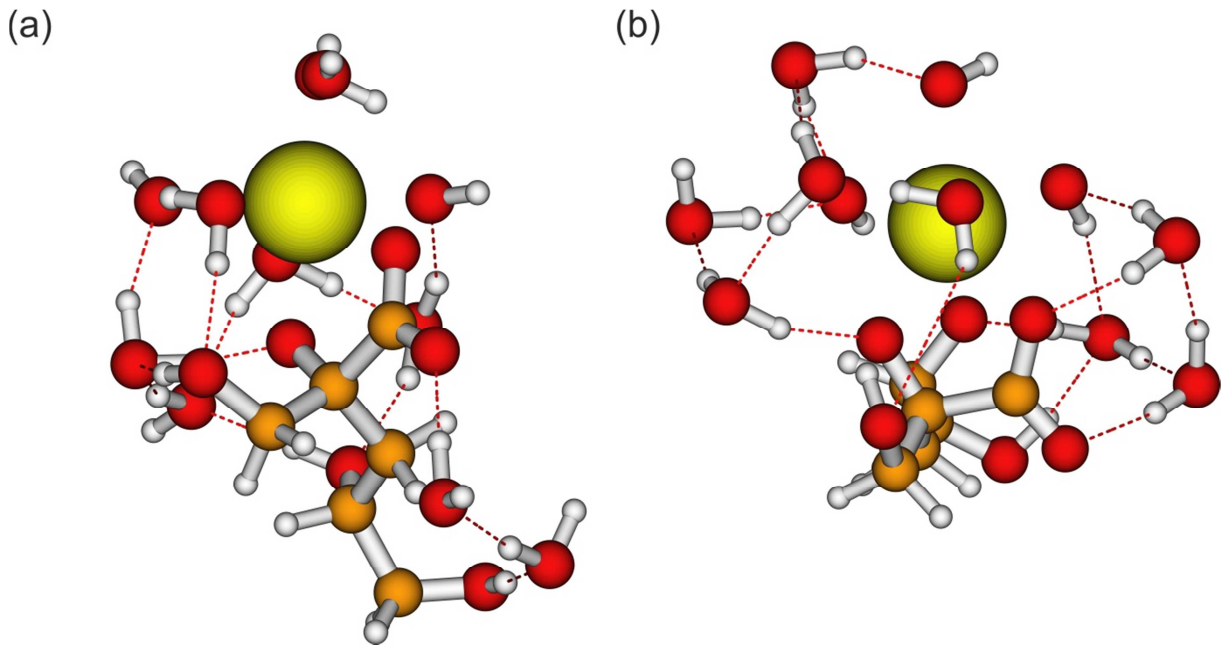

Figure 23. *Structures of the complexes (a) Pu(IV)(OH)$_3$ISA$_{-H}^-$ ("Pu(IV)(OH)$_4$ISA$^-$" in Section 3.1.2.4.1) and (b) Pu(IV)(OH)$_3$ISA$_{-2H}^{2-}$ ("Pu(IV)(OH)$_5$ISA^{2-}" in Section 3.1.2.4.1), as optimized in this work by DFT calculations with and without COSMO.*

Distances calculated by DFT and DFT+COSMO for the optimized structures of Pu(IV)(OH)$_3$ISA$_{-H}^-$ and Pu(IV)(OH)$_3$ISA$_{-2H}^{2-}$ are summarized in Table 11. Expectedly, shorter distances are found in the complex Pu(IV)(OH)$_3$ISA$_{-H}^-$ for Pu(IV)–OH$^-$ (average 232 pm / 231 pm for DFT / DFT+COSMO) and Pu(IV)–ISA(-C2-O$^-$) (average 231 pm / 230 pm), compared to the longer distances calculated for Pu(IV)–ISA(-COO$^-$) (239 pm / 240 pm) and Pu(IV)–H$_2$O (259 pm / 259 pm). Similar trends but with overall slightly longer distances are obtained in the case of Pu(IV)(OH)$_3$ISA$_{-2H}^{2-}$, with average distances Pu(IV)–OH$^-$ (233 pm / 233 pm), Pu(IV)–ISA(-C4-O$^-$) (233 pm / 232 pm), Pu(IV)–ISA(-C2-O$^-$) (240 pm / 237 pm), Pu(IV)–ISA(-COO$^-$) (248 pm / 249 pm) and Pu(IV)–H$_2$O (265 pm / 261 pm). The larger average distances in Pu(IV)(OH)$_3$ISA$_{-2H}^{2-}$ reflect the increased electronic density around the Pu^{4+} ion as a result of the additional coordination of the -C4-O$^-$ of ISA. The highly coordinating environment around Pu^{4+}, with 5 and 6 "-O$^-$" groups (as hydroxide ions: OH$^-$, alcoholate functional groups: -C*n*-O$^-$ or carboxylate functional group: -COO$^-$) is also responsible for the increased Pu(IV)–H$_2$O and Pu(IV)–OH$^-$ distances compared to values reported in the literature, *e.g.* d(Pu^{4+}–OH$_2$) = (239 ± 1) pm [173] and d(Pu^{4+}–OH$^-$) = $r_{Pu^{4+}}$ + r_{OH^-} = 101 + 122 = 223 pm [173, 179].

Table 11. *Pu–O distances (in pm) calculated by DFT and DFT+COSMO for the complexes $Pu(IV)(OH)_3ISA_{-H}^-$, $Pu(IV)(OH)_3ISA_{-2H}^{2-}$ and $Pu(III)(OH)ISA_{-H}(aq)$ as optimized in this work. For discussion on Pu(III) species see next chapter.*

$Pu(IV)(OH)_3ISA_{-H}^-$					
	DFT	+COSMO		DFT	+COSMO
Pu(IV)–OH^-	226	227	Pu(IV)–ISA(-COO^-)	239	240
Pu(IV)–ISA(-C2-O^-)	231	230	Pu(IV)–OH_2	250	251
Pu(IV)–OH^-	233	233	Pu(IV)–OH_2	260	259
Pu(IV)–OH^-	236	234	Pu(IV)–OH_2	267	267
$Pu(IV)(OH)_3ISA_{-2H}^{2-}$					
	DFT	+COSMO		DFT	+COSMO
Pu(IV)–OH^-	227	230	Pu(IV)–ISA(-C2-O^-)	240	237
Pu(IV)–ISA(-C4-O^-)	233	232	Pu(IV)–ISA(-COO^-)	248	249
Pu(IV)–OH^-	234	235	Pu(IV)–OH_2	264	260
Pu(IV)–OH^-	237	235	Pu(IV)–OH_2	266	261
Pu(III)(OH)ISA_{-H}(aq)					
	DFT	+COSMO		DFT	+COSMO
Pu(III)–ISA(-C2-O^-)	232	235	Pu(III)–OH_2	262	259
Pu(III)–OH^-	242	243	Pu(III)–OH_2	265	261
Pu(III)–ISA(-COO^-)	249	251	Pu(III)–OH_2	266	263
Pu(III)–OH_2	261	259	Pu(III)–OH_2	266	264

3.1.2.5.2 $Pu(III)(OH)_2ISA(aq)$ complex

The same approach as described in the previous section was used in the optimization of the structure of the $Pu(III)(OH)_2ISA(aq)$ complex. Here also several configurations with the same charge were evaluated: $Pu(III)(OH)_2ISA(aq)$, $Pu(III)(OH)ISA_{-H}(aq)$ and $Pu(III)ISA_{-2H}(aq)$. Both DFT and DFT+COSMO resulted in $Pu(III)(OH)ISA_{-H}(aq)$ as the energetically favored configuration. The optimized structure and resulting Pu–O distances are provided in Figure 24 and Table 11, respectively.

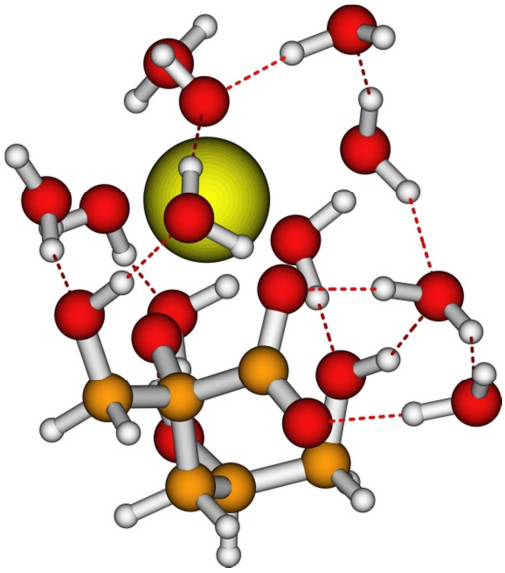

Figure 24. *Structure of the complexes Pu(III)(OH)ISA$_{-H}$(aq) ("Pu(III)(OH)$_2$ISA(aq)" in Section 3.1.2.4.2) and as optimized in this work by DFT calculations with and without COSMO.*

Pu–O distances summarized in Table 11 for the complex Pu(III)(OH)ISA$_{-H}$(aq) are systematically longer than the Pu(IV) counterparts, consistently with differences in the ionic radii of Pu^{4+} (101 pm for CN = 9) and Pu^{3+} (112 pm for CN = 8) [173] and the reduced charge at the metal ion. The distance calculated for Pu(III)–ISA(-COO^-) (251 pm) is in line with distances Cm(III)–L(-COO^-) reported in the literature for L = oxalate (239 – 251 pm)[192] and succinate (236 – 247 pm)[193] with side-on coordination, considering also differences in size between Pu^{3+} (112 pm) and Cm^{3+} (109 pm) [173].

3.1.2.6 Summary of the new Pu(III/IV)–OH–ISA thermodynamic model

Table 12 summarizes the equilibrium constants derived in the present work for the formation of Pu(III)–OH–ISA and Pu(IV)–OH–ISA complexes in alkaline to hyperalkaline pH_m conditions. Table 13 lists SIT ion interaction coefficients estimated for these complexes. Stoichiometry of these chemical reactions is provided by the combination of solubility data and solid phase characterization, whereas chemical formula for Pu(III/IV)–OH–ISA complexes are based upon DFT calculations.

Table 12. *Chemical equilibria and related equilibrium constants derived (for reference state, $I \rightarrow 0$ m) in the present study for the Pu(III/IV)–OH–ISA system.*

Chemical equilibria	*log*β° (I → 0)*
$Pu^{4+} + ISA^{-} + 3\ H_2O(l) \Leftrightarrow Pu(IV)(OH)_3ISA_{-H}^{-} + 4\ H^{+}$	–(5.03 ± 0.12)
$Pu^{4+} + ISA^{-} + 3\ H_2O(l) \Leftrightarrow Pu(IV)(OH)_3ISA_{-2H}^{2-} + 5\ H^{+}$	–(16.92 ± 0.13)
$Pu^{3+} + ISA^{-} + 2\ H_2O(l) \Leftrightarrow Pu(III)(OH)ISA_{-H}(aq) + 2\ H^{+}$	–(10.97 ± 0.28)

Table 13. *SIT ion interaction coefficients estimated for the Pu(III/IV)–ISA–OH species.*

species i	*species j*	*ε(i,j) [mol·kg^{-1}]*
$Pu(IV)(OH)_3ISA_{-H}^{-}$	Na^{+}	–(0.05 ± 0.10)[a)]
$Pu(IV)(OH)_3ISA_{-2H}^{2-}$	Na^{+}	–(0.10 ± 0.10)[a)]
$Pu(III)(OH)ISA_{-H}(aq)$	Cl^{-} / Na^{+}	0.00 [b)]

[a)] estimated values based on [149].
[b)] defined to be zero by definition within SIT formalism.

The chemical and thermodynamic models derived in this work provide the most accurate description available to date for the solubility of Pu in the presence of ISA. Thermodynamic data provided by Moreton and co-workers [93] are clearly superseded by the more accurate control of the experimental conditions achieved in the present study (especially in terms of phase separation techniques applied and monitored E_h values), as well as for the systematic variation of pH_m. The latter parameter was kept constant in the study by Moreton *et al.* [93], and thus the stoichiometry of the complexes proposed by the authors remains only at a speculative level.

Figure 25 a and b show the Pourbaix diagrams of Pu aqueous species in the presence of $\log m(ISA)_{tot} = -4$ and –2, respectively, calculated for $m(Pu(IV))_{tot} = 10^{-11}$ m and I = 0.1 m NaCl using the thermodynamic and (SIT) activity models derived in the present work. It is worth mentioning again that the formerly identified "Pu(IV)–ISA" colloids were not included in the present thermodynamic model.

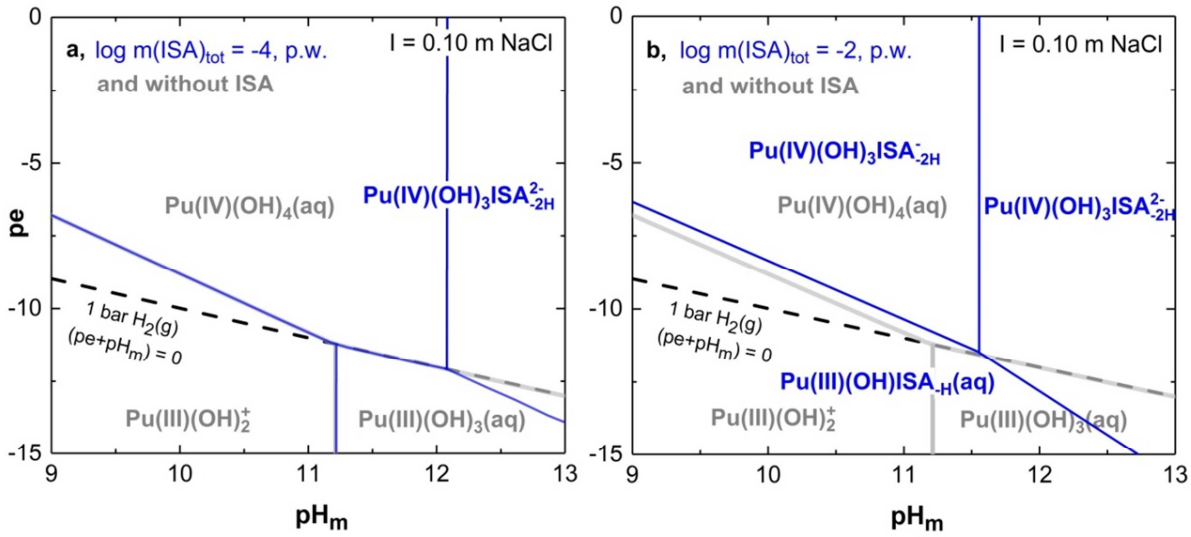

Figure 25. *Pourbaix diagram of Pu calculated for $m(Pu)_{tot} = 10^{-11}$ m and log $m(ISA)_{tot} = –4$: **a**, –2: **b,** (blue lines) and without ISA (grey lines) at I = 0.1 m NaCl using thermodynamic and (SIT) activity models as described in the text. Only aqueous species of Pu are displayed in the diagram. Dashed lines correspond to the borderline of water reduction to $H_2(g)$ at the given: $(pe + pH_m) = 0$ value.*

Figure 25 shows that the presence of ISA at $m(ISA)_{tot} \leq 10^{-4}$ m has a minor impact on the aqueous speciation of Pu, and the predominance of the complex $Pu(IV)(OH)_3ISA_{-2H}^{2-}$ is only predicted at $pH_m > 12$. However, at $m(ISA)_{tot} = 10^{-2}$ m, Pu(III/IV)–OH–ISA species become predominant within $9 \leq pH_m \leq 13$. At this $m(ISA)_{tot}$ and for $pH_m < 11.5$, the stability field of $Pu(III)_{aq}$ is slightly increased towards higher pe values compared to ISA-free systems. Above this pH_m, the complex $Pu(IV)(OH)_3ISA_{-2H}^{2-}$ becomes again predominant and is the only Pu–ISA complex forming above the border of water reduction. Note, however that other Pu(III)–ISA complexes beyond $Pu(III)(OH)ISA_{-H}(aq)$ possibly form under hyperalkaline conditions. For instance, the species $Eu(OH)_3ISA^-$ and $Am(OH)_3ISA^-$ (expectedly $Eu(OH)_2ISA_{-H}^-$ and $Am(OH)_2ISA_{-H}^-$) were proposed [100, 103, 105] to control the solution chemistry of Eu(III) and Am(III) in the presence of ISA at pH = 13.3.

3.1.2.7 Comparison with thermodynamic data available in the literature

Due to the absence of reliable thermodynamic data for the binary system Pu(IV)–ISA, the new chemical and thermodynamic models derived in the present work are compared to data available for Np(IV)–ISA and Th(IV)–ISA (Figure 26 a, b, cFigure 26) for a systematic

comparison. In both systems, data obtained in undersaturation solubility studies for Np(IV) [72] (re-evaluated in [12]) and Th(IV) [98, 107] were preferred[2], although the thermodynamic data derived in Vercammen *et al.*, 2001 [100] for the Th(IV)–ISA system from sorption studies (with large discrepancies to the work of Rai *et al.* [98] and also Colàs *et al.* [107]) are shortly discussed as well.

Figure 26 (a, b, c, d) shows the predominance diagrams of Pu(IV)–ISA, Np(IV)–ISA and Th(IV)–ISA calculated for $-6 \leq \log m(ISA)_{tot} \leq -1$ and $9 \leq pH_m \leq 13$ with I = 0.10 m NaCl using the thermodynamic data derived in the present work (Table 12) and summarized in Table 2 for Np(IV) and Th(IV). In spite of the clear insights gained by DFT on the structure of Pu(IV)–ISA complexes and for the sake of comparison with data reported in the literature, the notation assuming the hydrolysis of the An(IV) cation instead of the deprotonation of OH-groups of the ISA ligand has been used in the predominance diagram of Pu shown in Figure 26 d.

Figure 26 (a, c, d) shows significant differences in the calculated aqueous speciation of Pu(IV)–ISA, Np(IV)–ISA and Th(IV)–ISA systems. Thermodynamic data of the present work suggest the predominance of the 1:1 complex in the Pu(IV)–ISA system with $pH_m < 11.5$ and $m(ISA)_{tot} > 10^{-3.5}$ m. On the contrary, thermodynamic calculations conducted for Th(IV) show the predominance of the 1:2 complex above $m(ISA)_{tot} = 10^{-3}$ m, whereas the Np(IV) case results in the predominance of the 1:1 complex for $m(ISA)_{tot} \leq 10^{-2}$ m, and the predominance of the complex 1:2 above this $m(ISA)_{tot}$. Such observations could be rationalized by differences in the size of the An^{4+} cation, with Th^{4+} and Pu^{4+} having the largest (1.08 ± 0.02 Å) and smallest (1.01 ± 0.02 Å) size, respectively [173]. Hence, the formation of chelate complexes with An(IV):ISA ratio of 1:2 might be consequently favored for the largest cation as steric repulsions between the coordinated ligands are less pronounced. It has to be stressed, however that the uncertainties associated to these calculations are large and the number of An(IV)–ISA systems available are very limited, and thus the argumentation above does not represent any strong claim and must be only taken as a plausible hypothesis.

The predominance diagram in Figure 26 b calculated for the system Th(IV)–ISA using the equilibrium constants reported in Vercammen *et al.*, 2001 [100] shows a significantly different species distribution compared to Figure 26 a. Calculations in Figure 26 b predict the predominance of the species $Th(OH)_4ISA^-$ at $m(ISA)_{tot} \geq 10^{-5.9}$ m, whereas this species becomes only predominant at $m(ISA)_{tot} \geq 10^{-4.2}$ m (Figure 26 a). Vercammen and co-workers did not report the formation of the 1:2 complex $Th(OH)_4(ISA)_2^{2-}$, which therefore does not

[2] Sidenote: Colàs performed solubility experiments from both over- and undersaturation conditions.

appear in calculations shown in Figure 26 b, although they conducted their experiments with $m(ISA)_{tot} \leq 10^{-2}$ m. The use of the speciation scheme and equilibrium constants in Figure 26 b importantly overestimate experimental solubility data obtained from under- and oversaturation conditions in Rai *et al.* [98] and in Colàs *et al.* [107]. Although sorption experiments performed with ultra-trace concentrations of ^{228}Th or ^{234}Th may appear more susceptible to artefacts than solubility studies with macroscopic amounts of ^{232}Th, the discussion remains open and a final proof of concept for the proposed hypothesis is still missing.

Figure 26 a, c, d also show significant differences in the aqueous speciation of the systems An(IV)–ISA as a function of pH_m. Both Np(IV)–ISA and Th(IV)–ISA show a pH-independent behavior of the aqueous speciation at $9 \leq pH_m \leq 13$, whereas the formation of the complex: $Pu(OH)_3ISA_{-2H}^{2-}$ is predicted for the system Pu(IV)–ISA at $pH_m \geq 11.5$. Some relevant notes on these observations:

- Th(IV) solubility experiments in Rai *et al.* [98] and in Colàs *et al.* [107] were performed at $pH_m \leq 12$. Consequently, these authors may simply have missed the formation of the complex "$Th(OH)_5ISA^{2-}$", which according to the Z_{eff} of Th(IV) may form at greater pH values.
- Due to differences in the ionic radii of the An^{4+} ions, the effective charges (Z_{eff}) of the An(IV) systems under consideration follow the pattern $Pu^{4+} \geq Np^{4+} > Th^{4+}$. Such differences are for instance responsible for the much weaker hydrolysis observed for Th^{4+}, compared to both Np^{4+} and Pu^{4+}. It can be hypothesized that differences in Z_{eff} are also responsible for the differences in the aqueous speciation of the Np(IV)–ISA and Pu(IV)–ISA systems.
- Np(IV) solubility experiments in Rai *et al.*, 2003 [72] were performed over a relatively short timeframe (≤ 20 days). A close inspection of their solubility data suggests that the authors may have not attained equilibrium conditions in their experiments. Hence, Figure 5 in Rai *et al.*, 2003 [72] shows systematic and very relevant differences (0.3 to 0.5 log-units) between solubility data at t = 12 days and t = 20 days (the latter showing systematically greater solubility). Solubility data reported at pH_m = 13 and 13.8 were only collected for t = 5 and 13 days (Figure 4 in [72]). These experimental shortcomings may cast some doubts on the speciation scheme proposed by Rai and co-workers.

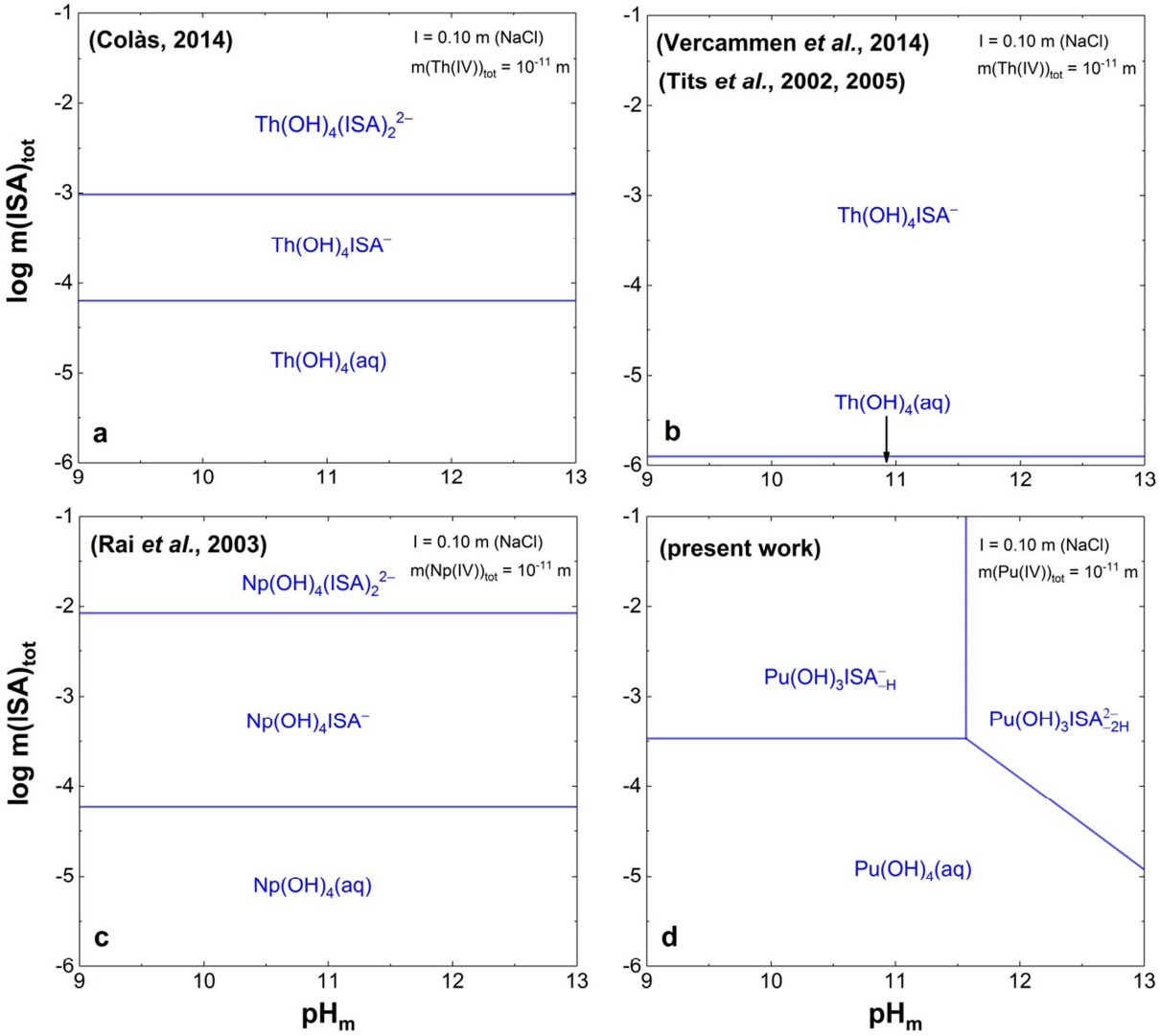

Figure 26. *Predominance diagrams of An(IV) in the presence of ISA ($-6 \leq \log m(ISA)_{tot} \leq -1$) with $m(An(IV))_{tot} = 10^{-11}$ m, $9 \leq pH_m \leq 13$ and I = 0.10 m NaCl, calculated for* ***a, Th(IV)*** *using thermodynamic data in Colàs et al. [107];* ***b, Th(IV)*** *using thermodynamic data in Vercammen et al., 2001 [100], as recalculated in [12];* ***c, Np(IV)*** *using thermodynamic data in Rai et al., 2003 [72] as recalculated in [12] and* ***d, Pu(IV)*** *using thermodynamic data derived in the present work.*

The discussion above does not provide a definitive explanation for the differences observed in the trends of An(IV)–ISA complexation with pH. As the current study (using a combination of solubility studies including XAFS techniques and theoretical DFT methods) in the system Pu(IV)–ISA represents the most comprehensive effort to characterize the systems and complexes forming under alkaline to hyperalkaline pH conditions, further experimental studies following a similar systematic and strategic approach like the one applied in the present work on the systems Th(IV)–ISA, U(IV)–ISA and Np(IV)–ISA would prove very

helpful in understanding the overall picture of An(IV)–ISA complexation under conditions relevant for L/ILW disposal.

The only thermodynamic data available for the system An(III)–ISA under alkaline conditions was reported by Tits *et al.* [105] for Am(III) based upon sorption experiments with calcite (see discussion in Section 1.3.3.4). Experiments were performed only at pH = 13.3, and thus the stoichiometry of the complex forming ($Am(OH)_3ISA^-$) was proposed in analogy with Eu(III) [100].

Figure 27 shows the predominance diagrams of Am(III)–ISA (a,) and Pu(III)–ISA (b,) calculated for $-6 \leq \log m(ISA)_{tot} \leq -1$ and $9 \leq pH_m \leq 13$ at I = 0.10 m NaCl using the thermodynamic data derived in the present work (Table 12 and Table 13) and summarized in Table 2 for Am(III).

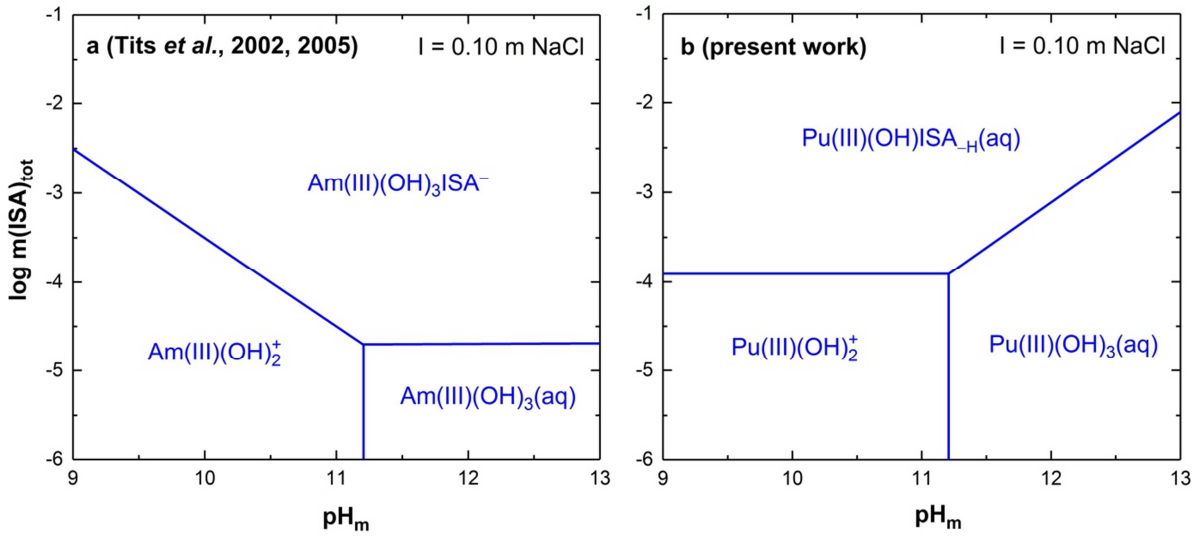

Figure 27. *Predominance diagrams of An(III) in the presence of ISA ($-6 \leq \log m(ISA)_{tot} \leq -1$) with $9 \leq pH_m \leq 13$ at I = 0.10 m NaCl, calculated for* ***a, Am(III)****: $m(Am(III))_{tot} = 10^{-10}$ m using thermodynamic data reported by Tits et al. [105] and* ***b, Pu(III)****: $m(Pu(III))_{tot} = 10^{-10}$ m, using thermodynamic data derived in the present work.*

Figure 27 displays different speciation schemes for Am(III)–ISA and Pu(III)–ISA systems, which basically reflect the experimental conditions in which the corresponding thermodynamic models were derived (pH = 13.3 for Am(III)–ISA in Tits *et al.* [105], $pH_m \leq$ 11.5 for Pu(III)–ISA in this work). As the sorption study by Vercammen *et al.* [100] on the system Eu(III)–ISA (basis for the chemical model proposed by Tits *et al.* [105]) was performed at pH > 10.7, these authors could not observe the formation of the complex

$Eu(III)(OH)_2ISA(aq)$ proposed in the present work for Pu(III). Indeed, the combination of chemical and thermodynamic models available for Am(III)–ISA and Pu(III/IV)–ISA provides a satisfactory explanation of the present solubility data collected in Sn(II) systems (see Figure 28).

Although the incorporation of the species 1:3:1 in the model did not result in a significantly improved fit for the solubility data of the present work, the consideration of $\log {}^*\beta^\circ_{1,3,1} = -(21.4 \pm 1.0)$ as reported in Tits *et al.* for the chemical reaction $Am^{3+} + 3\ H_2O(l) + ISA^- \Leftrightarrow Am(OH)_3ISA^- + 3\ H^+$ can be adapted as a reasonable upper limit for the Pu(III) as well. In the case of Pu(III), however, the predominance of this complex is limited to strongly alkaline and reducing conditions with $pH_m > 11.5$ and $(pe + pH_m) < 1.5$.

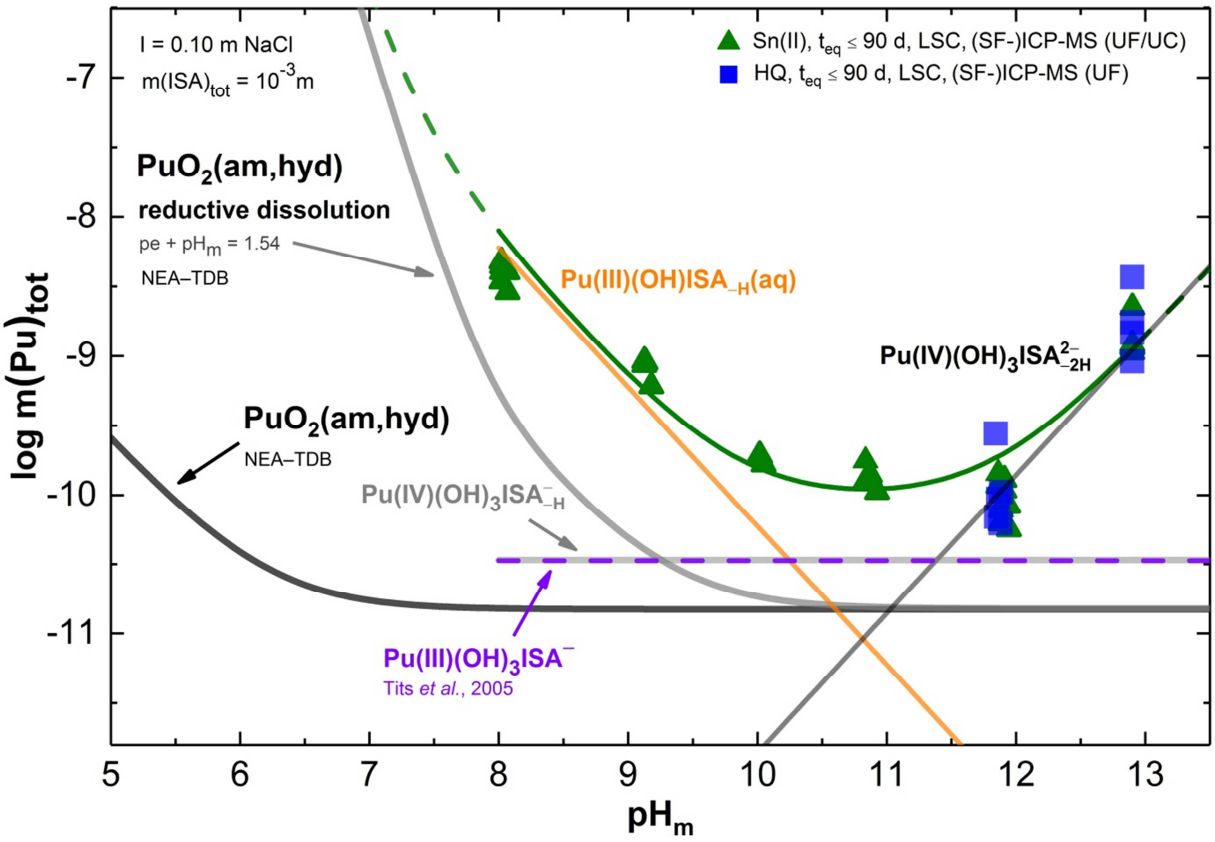

Figure 28. *Experimentally measured $m(Pu)_{tot}$ in equilibrium with PuO_2(ncr,hyd) at I = 0.10 m NaCl in Sn(II)-buffered systems (▲) with pH_m = 8 – 12.9 in the presence of $m(ISA)_{tot}$ = 10^{-3} m and in HQ-buffered systems (■), at pH_m > 11 with $m(ISA)_{tot}$ = 10^{-3} m. Solubility curves (solid and dashed) in green (with $m(ISA)_{tot}$ = 10^{-3} m) for Pu(IV)O_2(ncr,hyd) in the presence of ISA are calculated (at I = 0.10 m NaCl) using the chemical and thermodynamic models derived in the present work and additionally including the formation of the $Pu(III)(OH)_3ISA^-$ species (not detected in the p. w.) where the equilibrium constant (log $*\beta^\circ_{1,3,1}$ = (–21.4 ± 1.0)) reported by Tits et al. [105] was adapted (purple line indicates the individual contribution of this species to the overall calculated Pu total concentrations). Black and grey solid lines correspond to the thermodynamically calculated solubility of PuO_2(am,hyd) in the absence of ISA, calculated using equilibrium constants reported in NEA-TDB [9].*

3.1.3 Ca–Pu–ISA system

3.1.3.1 pH and E_h measurements

The collected pH_m and E_h (converted into pe) values of all evaluated samples are shown in the Pourbaix diagram of Pu in Figure 29. The thermodynamic calculations for the construction of the diagram were performed as indicated in Section 3.1.1.2.

Solubility experiments with HQ or Sn(II) redox buffered systems in the presence of ISA and Ca(II) show stable pH_m (± 0.05) and E_h (± 15–30 mV, depending upon pH-region) readings within the time frame of this study (~3 months).

In accordance with the findings of work conducted in the absence and presence of ISA [1, 2], HQ in solution imposed moderately reducing conditions. However, the obtained (pe + pH_m) values in the present case were found to be at a slightly lower level (~8.5 ± 0.5) than those of the previously[2] determined values: (pe + pH_m) = 9 ± 1 (whilst also having lower associated uncertainties), but still within the range of the expected values considering the originally assigned uncertainty. Apart from the latter minor discrepancy, the newly assessed redox conditions are again clearly located within the stability field of Pu(IV) for both, aqueous species and solid Pu compounds. Evaluation of Pu solubility data collected in the HQ system under the presence of only ISA in solution, formerly resulted in the identification of two Pu(IV)–OH–ISA species: $Pu(IV)(OH)_3ISA_{-H}^{-}$, $Pu(IV)(OH)_3ISA_{-2H}^{2-}$ [2]. Hence, the HQ-buffered system of the present study is considered as the reference case to investigate the interaction of $Pu(IV)_{aq,s}$ with ISA and Ca(II) in solution.

As it was also discussed in Sections 3.1.1.2 and 3.1.2.1, the presence of sparingly soluble Sn(II)-oxides and -oxy-hydroxide precipitates forming under $pH_m < 11$ conditions (SnO(cr), or $Sn_6O_8H_4(s)$ / $Sn_6O_4(OH)_4(s)$) [126], dictates longer equilibration times for E_h measurements in these Sn(II)-buffered systems. The formerly established redox condition with (pe + pH_m) values of (1.54 ± 0.14) for the Sn(II)-buffered system were found to be slightly higher but agreeing within the uncertainties with the average values measured in the presence of Ca(II), (pe + pH_m) = (1.0 ± 0.5). However, it has to be highlighted that the thermodynamic evaluation of the Sn(II) solubility data collected in the current case for the presence of Ca(II) did not necessitate the acquired pe values to be included as input values in the development of the thermodynamic model. Hence, E_h values were not measured further with longer equilibration times. In this sense, the determined log $K°$ values were not affected by the newly set conditions in the presence of Ca(II) ions in solution. In the absence of Ca(II) in solution, reductive dissolution reaction: PuO_2(ncr, hyd) ⇔ Pu(III)(aq) + Pu(IV)(aq) was

determined formerly as the Pu solubility controlling reaction in the Sn(II) system (see Section 3.1.2.4.2) [2]. In this aspect, the Sn(II)-buffered solubility experiment series in the presence of Ca(II) was aimed to assess the impact of Ca(II) ions on the latter equilibria, where below pH_m = 11, the predominance of the Pu(III)-ISA species was observed.

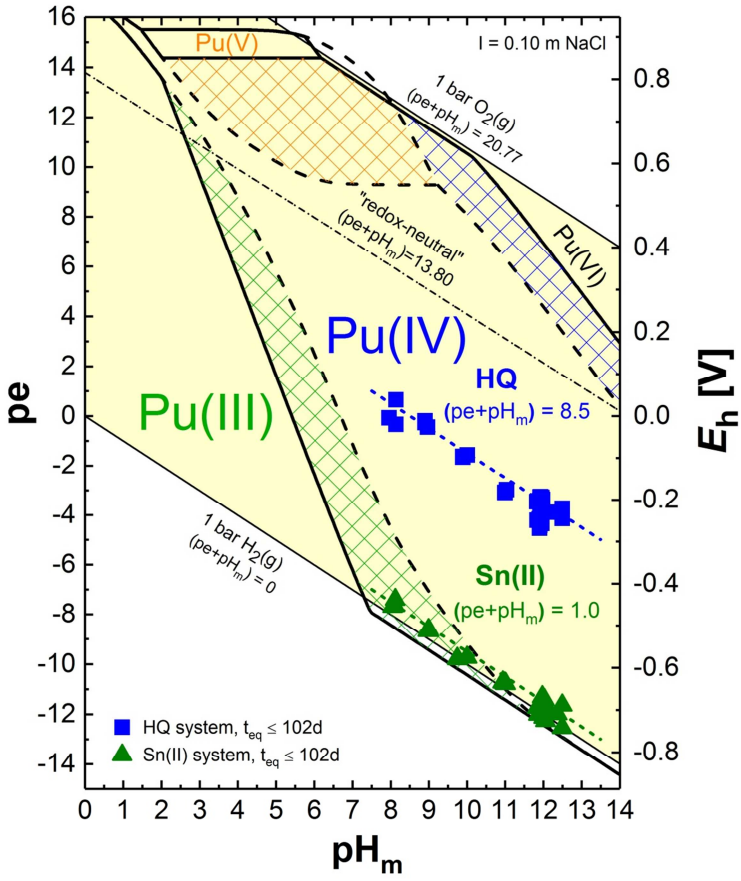

Figure 29. *Pourbaix diagram of Pu calculated for $m(Pu)_{tot}$ = 10^{-5} m and I = 0.1 m NaCl using thermodynamic and (SIT) activity models as described in the text. pH_m and E_h values experimentally determined for Pu(IV) solubility experiments in the presence of ISA and Ca(II) ions in solution with redox-buffering agents: hydroquinone (■) and Sn(II) (▲). Thick lines correspond to redox borderlines between Pu(IV) and other Pu redox states: solid line is the borderline between Pu solid phases; dashed line is the borderline between Pu aqueous species. Colored regions indicate equilibrium between $Pu(IV)_s$ and $Pu(III)_{aq}$ (green), $Pu(V)_{aq}$ (orange) and $Pu(VI)_{aq}$ (blue). The borderlines of the stability field of water at ($pe + pH_m$) = 20.77 and ($pe + pH_m$) = 0, the "redox-neutral" line at ($pe + pH_m$) = 13.8 and the lines at ($pe + pH_m$) = 1.54 and 9 are shown for comparison.*

3.1.3.2 Solubility measurements

Figure 30 shows the experimentally measured total concentrations of Pu in equilibrium with PuO_2(ncr,hyd) at $m(ISA)_{tot}$ = constant = 10^{-3} m and $m(Ca)_{tot}$ = constant = 0.01 m with pH_m = 8 – 12.5 in HQ-buffered system (■). The analogous Sn(II)-buffered system (▲) is displayed in Figure 31. Figure 32 summarizes the solubility of Pu in HQ- (■) and Sn(II)-buffered (▲) systems at pH_m = 12 with $m(Ca)_{tot}$ = constant = 0.01 m and 10^{-5} m ≤ $m(ISA)_{tot}$ ≤ 10^{-2} m. Figure 33 shows the solubility of Pu determined at pH_m = 12 in the presence of $m(ISA)_{tot}$ = constant = 10^{-3} m with $3 \cdot 10^{-4} \leq m(Ca)_{tot} \leq 2 \cdot 10^{-2}$ m, for both HQ- (■) and Sn(II) (▲) systems. All figures also display the solubility curves of Pu(IV)O_2(am,hyd) in the presence of ISA (and absence of Ca), calculated for identical conditions (at I = 0.10 m) applying chemical and thermodynamic models derived in the present study as well as reported in [2]. (For further details regarding the calculations of the reference solubility curves, see Section 3.1.1.5.)

3.1.3.2.1 Series at constant $m(ISA)_{tot}$ and $m(Ca)_{tot}$

Figure 30 shows a clear and systematic increase in the solubility of PuO_2(ncr,hyd) in HQ systems (■) with $m(ISA)_{tot}$ = 10^{-3} m and $m(Ca)_{tot}$ = 0.01 m, compared to the solubility of the ternary Pu(IV)-OH-ISA system in the absence of Ca (blue line in the figure). This observation strongly supports the formation of quaternary Ca(II)–Pu(IV)–OH–ISA aqueous complexes in HQ systems. For this redox buffer, same/similar pH-dependency of the solubility is observed in the absence and presence of Ca(II), suggesting that Pu(IV)–ISA complexes in the presence of Ca hold similar Pu:OH ratios in their apparent stoichiometries as those reported in the absence of Ca: 1:4 and 1:5.

Less precise data (especially at pH_m = 9 – 10) were obtained for the Sn(II)-buffered systems (Figure 31), although in general terms experimentally measured $m(Pu)_{tot}$ are of the same order than those determined in HQ systems. In both cases, the solubility of Pu remains in all samples bellow 10^{-8} m, suggesting the lack of quaternary species forming between Ca(II) and the formerly identified Pu(III)(OH)ISA_{-H}(aq) species. This observation is in line with results of previous studies [59, 100] on analogous systems, where the formation of a quaternary complex of Eu(III)-ISA species with Ca(II) ion under alkaline conditions was not detected. Due to these ambiguities, development of a chemical and thermodynamic model for the Ca(II)–Pu–ISA system was based entirely on the HQ-buffered solubility data.

Considering the limitations existing for the Sn(II) system, the following tendencies can be outlined for the solubility of Pu in HQ solutions (Figure 30):

1. **pH_m = 8 – 11**: as in the absence of Ca(II), a clear and pH-independent enhancement in the solubility of PuO_2(ncr,hyd) is observed. This indicates that within this pH-range no protons are involved in the equilibrium reaction controlling the solubility of Pu in the presence of ISA and Ca(II).

2. **pH_m = 11 – 12**: a pH-dependent increase of the solubility is observed with a slope of ($\log m(Pu)_{tot}$ *vs.* pH_m) ≈ +1. This finding suggests that one H^+ is released in the equilibrium reaction controlling the solubility of Pu. A similar behavior can be claimed for the solubility of Pu in Sn(II) systems. Note however that because of the limited number of experimental points defining this pH_m-region, a slope of +2 (with the corresponding implications for the stoichiometry Pu:OH in the Ca-Pu-OH-ISA complex) was also tested in the development of a thermodynamic model (see Section 3.1.3.4).

3. **pH_m = 12.4**: experimental data show a clear decrease in the solubility of Pu with respect to the sample at pH_m = 12. A similar behavior is observed for the solubility of Pu in the Sn(II) system. Indeed, the solubility data at this pH_m value is very similar to the solubility in the absence of Ca(II). TOC and ICP-OES measurements performed after 2 weeks of equilibration of the inactive system (before the addition of Pu solid phases) indicated that no loss of ISA and/or Ca took place. The working hypothesis refers to the possible formation of a quaternary, Ca(II)–Pu–OH–ISA solid phase, although so far, no conclusive evidence is available in this respect. Consequently, solubility data obtained in the presence of Ca at pH_m = 12.4 has been disregarded in the development of the thermodynamic model for the system Ca(II)–Pu–ISA.

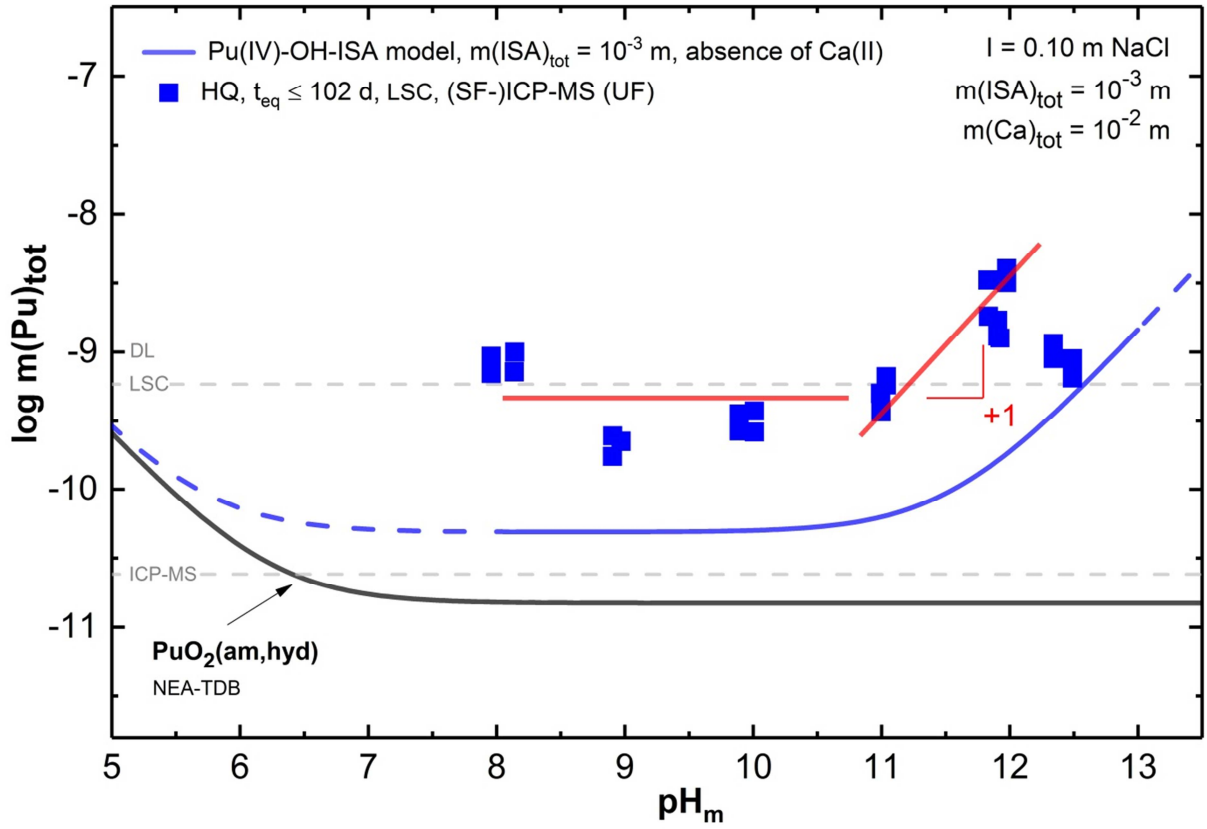

Figure 30. *Experimentally measured $m(Pu)_{tot}$ in equilibrium with PuO_2(ncr,hyd) in 0.10 m NaCl at $m(ISA)_{tot}$ = 10^{-3} m and $m(Ca)_{tot}$ = 0.01 m with pH_m = 8 – 12.5 in HQ-buffered solutions (■). Blue line (solid and dashed) corresponds to the solubility of Pu(IV)O_2(am,hyd) at I = 0.10 m NaCl, in the presence of $m(ISA)_{tot}$ = 10^{-3} m calculated using the chemical and thermodynamic models derived in the present work for the system Pu(IV)–OH–ISA [2]. Black solid line corresponds to the thermodynamically calculated solubility of PuO_2(am,hyd) in the absence of ISA, adapted from NEA-TDB [9].*

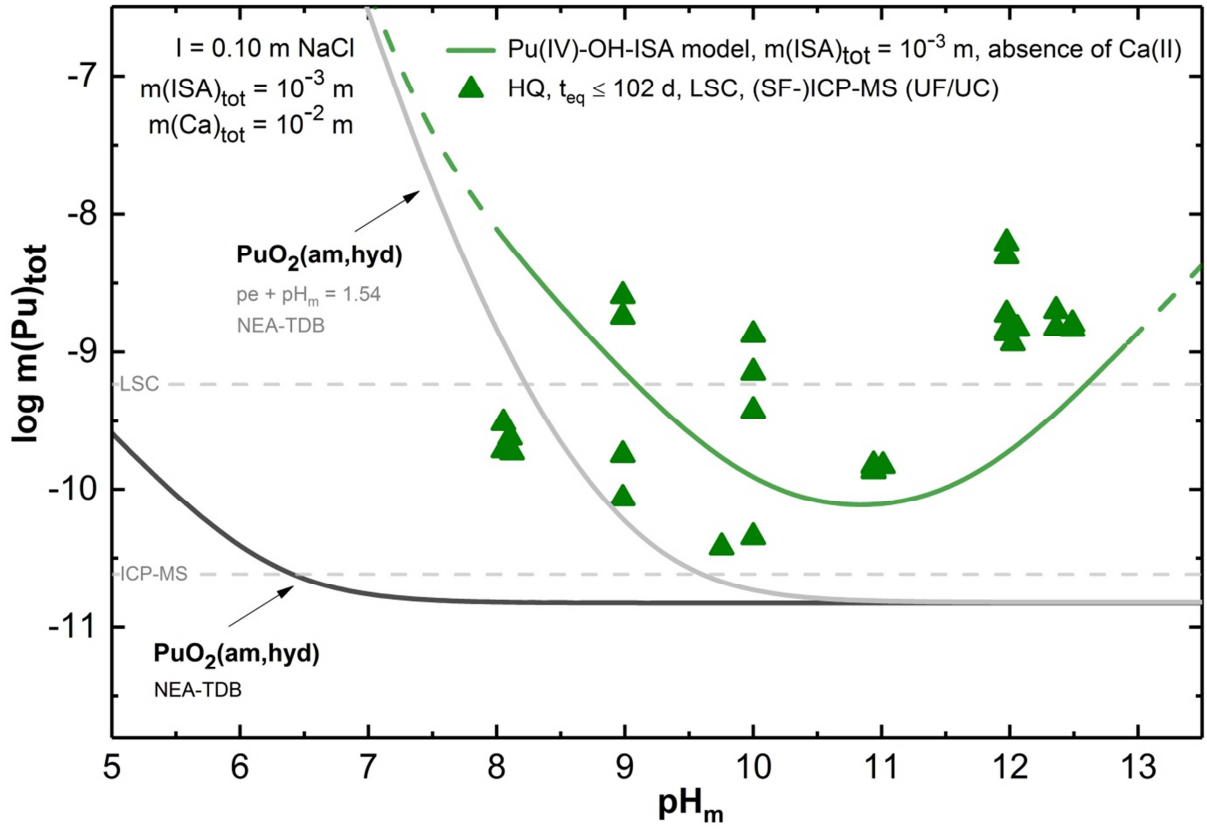

Figure 31. *Experimentally measured $m(Pu)_{tot}$ in equilibrium with PuO_2(ncr,hyd) in 0.10 m NaCl at $m(ISA)_{tot}$ = 10^{-3} m and $m(Ca)_{tot}$ = 0.01 m with pH_m = 8 – 12.5 in Sn(II)-buffered solutions (▲). Green lines (solid and dashed) correspond to the solubility of Pu(IV)O_2(am,hyd) at I = 0.10 m NaCl, in the presence of $m(ISA)_{tot}$ = 10^{-3} m calculated using the chemical and thermodynamic models derived for the binary system Pu(III/IV)–OH–ISA (listed in Table 12) [2]. Black and grey solid lines correspond to the thermodynamically calculated solubility of PuO_2(am,hyd) in the absence of ISA in equilibrium with $Pu(IV)_{aq}$ and for ($pe + pH_m$) = 1.54 (predominance of $Pu(III)_{aq}$ below $pH_m \approx 10.5$, see Section details), respectively.*

3.1.3.2.2 Solubility at constant pH_m and $m(Ca)_{tot}$

A clear and systematic enhancement of PuO_2(ncr,hyd) solubility is observed with increasing $m(ISA)_{tot}$ at constant pH_m = 12 and $m(Ca)_{tot}$ = 10^{-2} m. The trend is very similar in HQ and Sn(II) systems, suggesting that the chemical reactions controlling the solubility of Pu are the same in both systems. The clear increase in the solubility with respect to the Ca(II)-free system (solid line in Figure 32), again supports the formation of a quaternary Ca(II)–Pu(IV)–OH–ISA complex. Although the formation of binary/ternary Ca(II)–ISA complexes ($CaISA^+$ and $CaISA_{-H}^0$(aq)) hinders a straightforward interpretation of the data, a slope of +1 (and thus

a stoichiometry Pu:ISA of 1:1) can be postulated both for HQ and Sn(II) systems. In order to further test the validity of the proposed model, a Pu:ISA stoichiometry of 1:2 was also considered in the development of the thermodynamic model (see Section 3.1.3.4 for further details).

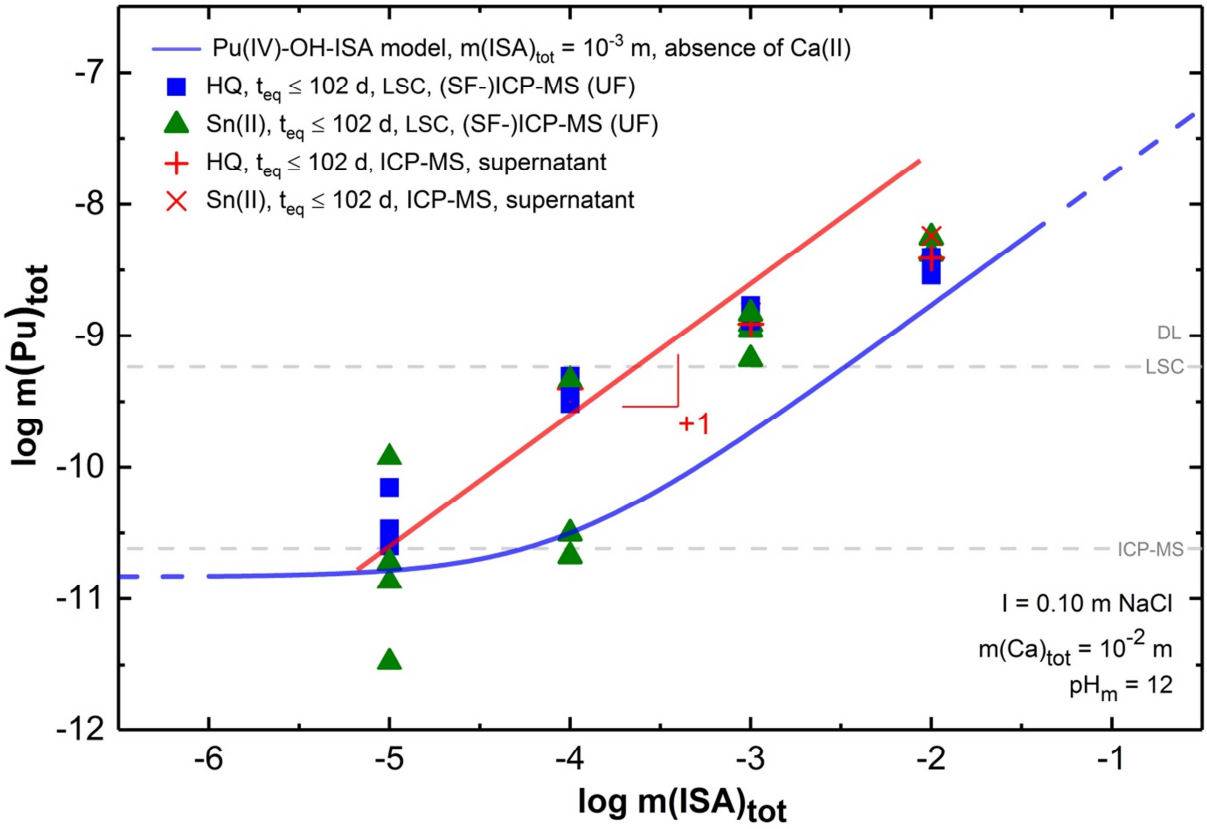

Figure 32. *Experimentally measured $m(Pu)_{tot}$ in equilibrium with PuO_2(ncr,hyd) in 0.10 m NaCl at pH_m = 12 and $m(Ca)_{tot}$ = 0.01 m conditions with 10^{-5} m ≤ $m(ISA)_{tot}$ ≤ 10^{-2} m in HQ-(■) or Sn(II)-buffered solutions (▲). Cross, red symbols are the total concentrations of Pu in the supernatants (sampled without any phase separation) of the Sn(II)– (×) and HQ-buffered (+) systems. Blue lines (solid and dashed) correspond to the solubility of Pu(IV)O_2(am,hyd) at I = 0.10 m NaCl, in the presence of $m(ISA)_{tot}$ = 10^{-3} m calculated using the chemical and thermodynamic models derived for the binary system Pu(IV)–OH–ISA (listed in Table 12) [2].*

To assess the presence of colloidal Pu(IV) species, total Pu concentrations in the supernatants of the samples were additionally measured without any phase separation method applied (cross symbols in Figure 32). The detected Pu concentrations from the directly supernatants after an equilibration time of 102 days were virtually the same as the $m(Pu)_{tot}$ values collected

after ultracentrifugation or ultrafiltration phase separation methods. This is different from the previous findings on the system in the absence of Ca(II) ions in solution, where the enhanced formation of Pu(IV) colloidal species was seen with increasing total ISA concentration in solution (see Figure 15 in Section 3.1.2.2.2). Although the mechanism driving to these observations is not understood, it points out the relevant role of Ca(II) in the destabilization of Pu colloids in ISA containing systems. Similar phenomena was also observed for clay colloid suspensions, where the Ca(II) concentration set close to the critical coagulation concentration caused the gradual agglomeration of the colloidal particles due to the Ca^{2+} ion exchange against Li^{+} and Na^{+} ions at the charged basal clay planes [194].

3.1.3.2.3 Solubility at constant pH_m and $m(ISA)_{tot}$

Figure 33 shows a clear increase in the solubility of Pu with increasing $m(Ca)_{tot}$. A very similar trend in the solubility data is observed for HQ and Sn(II) systems, suggesting again that the chemical equilibria controlling the solubility of Pu at pH_m = 12 are the same for both redox-buffered systems. In solutions with the lowest Ca(II) total concentration ($m(Ca)_{tot}$ = –3.5) Pu solubility values are in close agreement with the concentration determined in the absence of Ca(II) and same $m(ISA)_{tot}$. This observation further supports the experimental results and thermodynamic model derived in Section 3.1.2.4 for the system Pu(III/IV)–OH–ISA in the absence of Ca(II).

The increase of log $m(Pu)_{tot}$ with increasing log $m(Ca)_{tot}$ follows a slope ≈ +1, indicating that the Ca:Pu stoichiometry of the Pu–ISA complex forming at pH_m = 12 is 1:1. As in the evaluation process of the previously collected data with pH_m = 12 (log $m(Pu)_{tot}$ *vs.* pH_m and log $m(Pu)_{tot}$ *vs.* log $m(ISA)_{tot}$), the fitting of the data considered also the possible formation of complexes with Ca:Pu stoichiometry of 2:1 to test the reliability of the model (see Section 3.1.3.4 for further details).

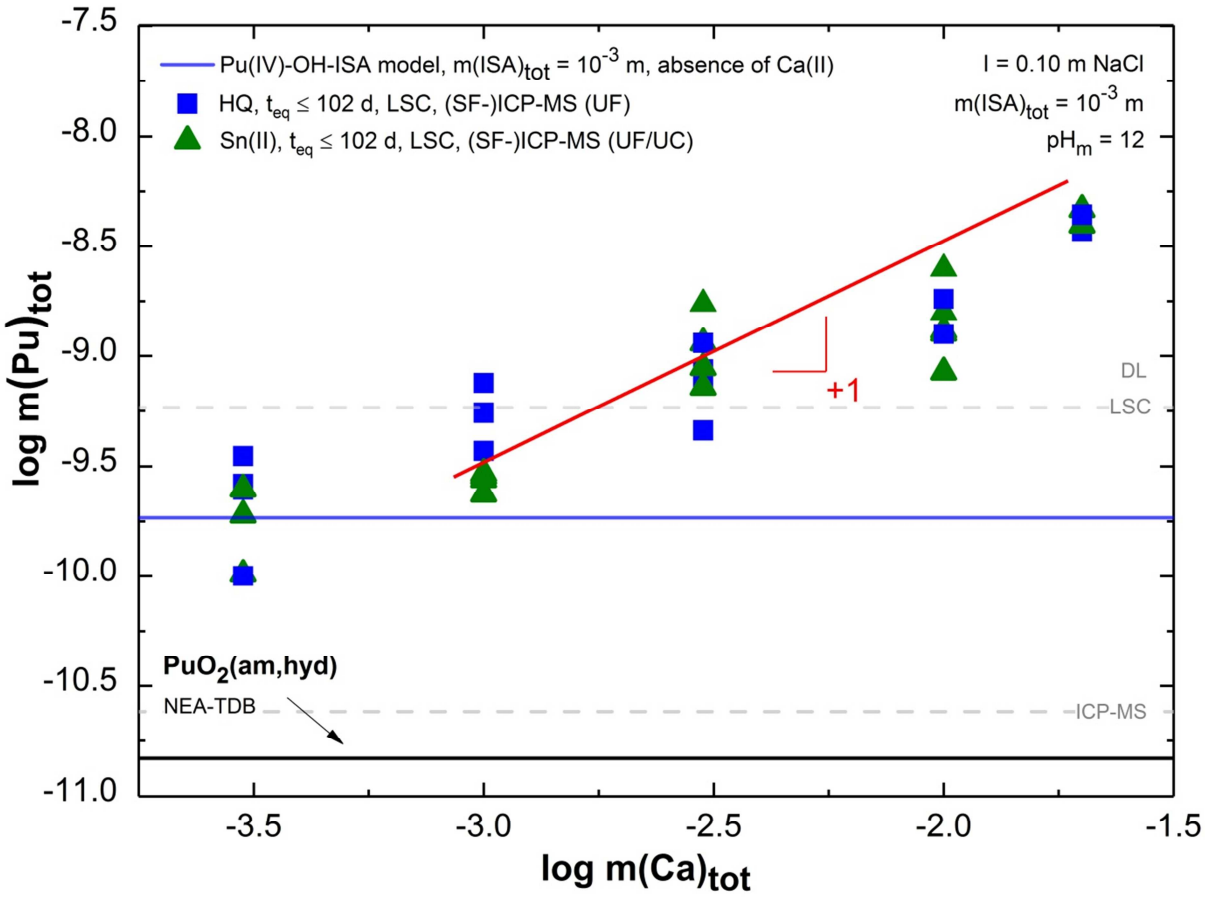

Figure 33. *Experimentally measured total $m(Pu)_{tot}$ in equilibrium with PuO_2(ncr,hyd) in 0.10 m NaCl at pH_m = 12 and $m(ISA)_{tot} = 10^{-3}$ m, with $3 \cdot 10^{-4}$ m ≤ $m(Ca)_{tot} \leq 10^{-3}$ $2 \cdot 10^{-2}$ m, in HQ-(■) or Sn(II)-buffered solutions (▲). Solid blue line corresponds to the solubility of Pu(IV)O_2(am,hyd) at I = 0.10 m NaCl, in the presence of $m(ISA)_{tot} = 10^{-3}$ m calculated using the chemical and thermodynamic models derived for the binary system Pu–ISA (listed in Table 12) [2]. Black solid line corresponds to the thermodynamically calculated solubility of PuO_2(am,hyd) in the absence of ISA adapted from NEA-TDB [9].*

3.1.3.3 Solid phase characterization

Synchrotron-based in-situ XRD

Figure 34 shows the *in-situ* XRD patterns of the solid phases controlling the solubility of Pu in HQ and Sn(II) systems, equilibrated in solutions with $m(ISA)_{tot} = 10^{-3}$ m, $m(Ca)_{tot}$ = 0.01 m at pH_m = 12 for 150 days. It also displays the diffractogram of the empty double containment used in the course of the synchrotron-based measurements at the INE–Beamline as described in Section 2.6.6.

The collected patterns of the retrieved Pu solid phases equilibrated in the presence of ISA and Ca(II) in solution are in perfect agreement with the reference pattern of PuO_2(cr) reported by Zachariansen [166]. Under identical conditions to those of the present work, previous experimental study conducted in the absence of Ca(II) also pointed out the retainment and predominance of Pu(IV)O_2(ncr,hyd) in both redox-buffered systems after long equilibration times (260 days) in contact with 10^{-3} m and 0.01 m ISA solutions at pH_m = 9 and 12 [2]. The present observations also conclude that the initially inserted solid phase remained in its original state, just as in the case when it was only equilibrated with ISA in solution.

As stated before (in Sections 3.1.1.4 and 3.1.2.3), Sn(II) is completely dissolved at pH_m = 12, which was again underlined by the lack of reflexes corresponding to Sn(II)-containing phases in the Sn(II)-buffered system at this pH_m. Additionally, the absence of any XRD peaks related to the $Ca(ISA)_2$(cr) phase (detection limit at ~5-10%) confirms that Ca(II) and ISA dominantly exist as solution species in the system. This confirms the previous quantitative analysis and also the predictions of thermodynamic calculations made prior to the initialization of the solubility experiments, *i.e.* no differences are to be expected in the originally introduced total concentrations of these species.

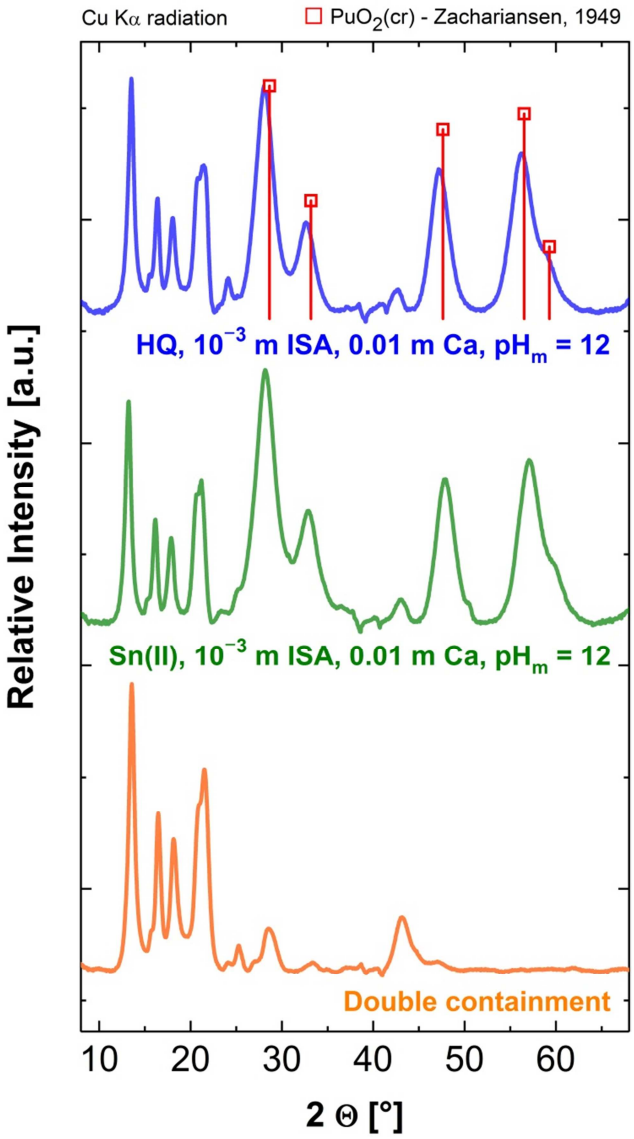

Figure 34. *In-situ XRD patterns collected at the INE-Beamline for the Pu solid phases recovered from HQ-buffered (blue, top) and Sn(II)-buffered (green, lower) solubility experiments solubility with* $m(ISA)_{tot}$ *=* 10^{-3} *m,* $m(Ca)_{tot}$ *=* 10^{-2} *m and* pH_m *= 12 (*t_{eq} *= 150 days) and for the empty double containment used in the synchrotron-based measurements (orange). Squares indicate peak positions and relative intensities reported for* PuO_2*(cr) [166].*

XANES

Pu L_{III}–edge XANES spectra collected for the solid phases recovered from HQ and Sn(II)-buffered solubility experiments with $m(ISA)_{tot}$ = 10^{-3} m, $m(Ca)_{tot}$ = 10^{-2} m and pH_m = 12 (t_{eq} = 150 days) are shown in Figure 35. The figure also includes the XANES spectra of the references reported in Brendebach *et al.* [140] for aqueous Pu(III) and Pu(IV) species under acidic conditions and furthermore it also depicts the spectra of the formerly reported

PuO_2(IV)(ncr,hyd) solid phase (starting material from Section 3.1.1.1 and previous studies [1, 2]), which was used as the initial solid phase in the present series of experiments as well.

The edge energies of the XANES spectra collected for all the retrieved Pu solid phases are in excellent agreement with the Pu(IV) reference spectrum reported by Brendebach and co-workers [140]. The newly collected spectra were also found to be virtually identical to the previously reported [1] XANES spectrum of the PuO_2(ncr,hyd), starting material. In accordance with *in-situ* XRD data, XANES analysis also unequivocally confirm the retainment of the original Pu(IV)O_2(ncr,hyd) solid phase introduced to the solubility batch experiments with ISA and Ca(II) in solution.

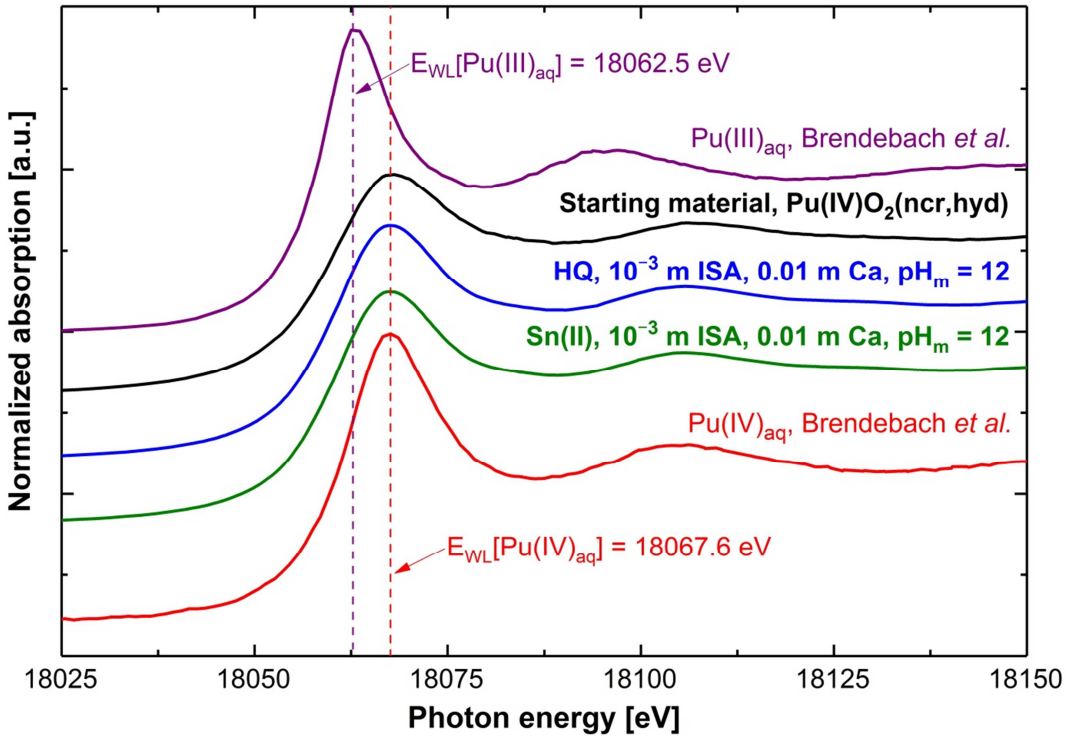

Figure 35. *Pu L_{III}–edge XANES spectra of solid phases recovered from HQ- (blue lines) and Sn(II)-buffered (green lines) systems equilibrated in solutions with with $m(ISA)_{tot}$ = 10^{-3} m, $m(Ca)_{tot}$ = 10^{-2} m and pH_m = 12 (t_{eq} = 150 days). The spectra of the references for the aqueous species of Pu(III) (purple line, position of WL = 18062.5 eV) and Pu(IV) (red line, position of WL = 18067.6 eV) reported in Brendebach et al. [140] and the spectra of the initially characterized Pu(IV)O_2(ncr,hyd) phase (starting material, also used for the present study, see section 3.1.1.1 and references [1, 2]) are shown for comparison.*

EXAFS

The k^2-weighted EXAFS data shown in Figure 36 for Pu solid phases recovered from solubility experiments in HQ- and Sn(II)-systems (top row: Fourier-transform magnitude,

imaginary part and fit results in R-space, bottom row: raw data, Fourier-filtered data and fit results in k-space) are perfectly in agreement with our previous results obtained in the absence of Ca(II) (see section 3.1.2.3 and reference [2]). The corresponding metric parameters are listed in Table 14. The fit results obtained for both Pu phases are identical within the error margins and very similar to those obtained for the "starting material", PuO2(ncr,hyd) solid phase as discussed previously (see section 3.1.1.1 and reference [1]). This observation underlines our *in-situ* XRD and XANES results, confirming that the initial PuO_2(ncr,hyd) starting material remains stable in the presence of ISA and Ca(II) in solution and it is the solid phase controlling the solubility of Pu in given systems. It is also worth mentioning that the results obtained by EXAFS indicate the presence of significant local disorder and deviations from the ideal PuO_2 fluorite-type crystal structure, which are not visible in the XRD pattern.

Table 14. *Data range and metric parameters extracted by least-squares fitting of EXAFS data on selected retrieved solid phases as shown in Figure 36.*

Sample	***k-range [Å^{-1}] fit-range [Å]***	***shell***	***N***	***R [Å]***	***ΔE_0*** [a] ***[eV]***	***σ^2 [Å^2]***	***r-factor [%]***
HQ	1.75-13.58	O	6.2	2.28	-2.19	0.0086	3.1
	0.92-4.11	Pu	4.6	3.78		0.0047	
Sn(II)	1.75-12.92	O	6.0	2.29	-1.90	0.0085	2.9
	0.92-4.11	Pu	4.3	3.78		0.0039	

S_0^2 = 1.0 fixed (slightly underestimating N in all fits)
[a] global parameter for both shells
errors: R_{Pu-O} 0.01 Å, R_{Pu-Pu} 0.02 Å

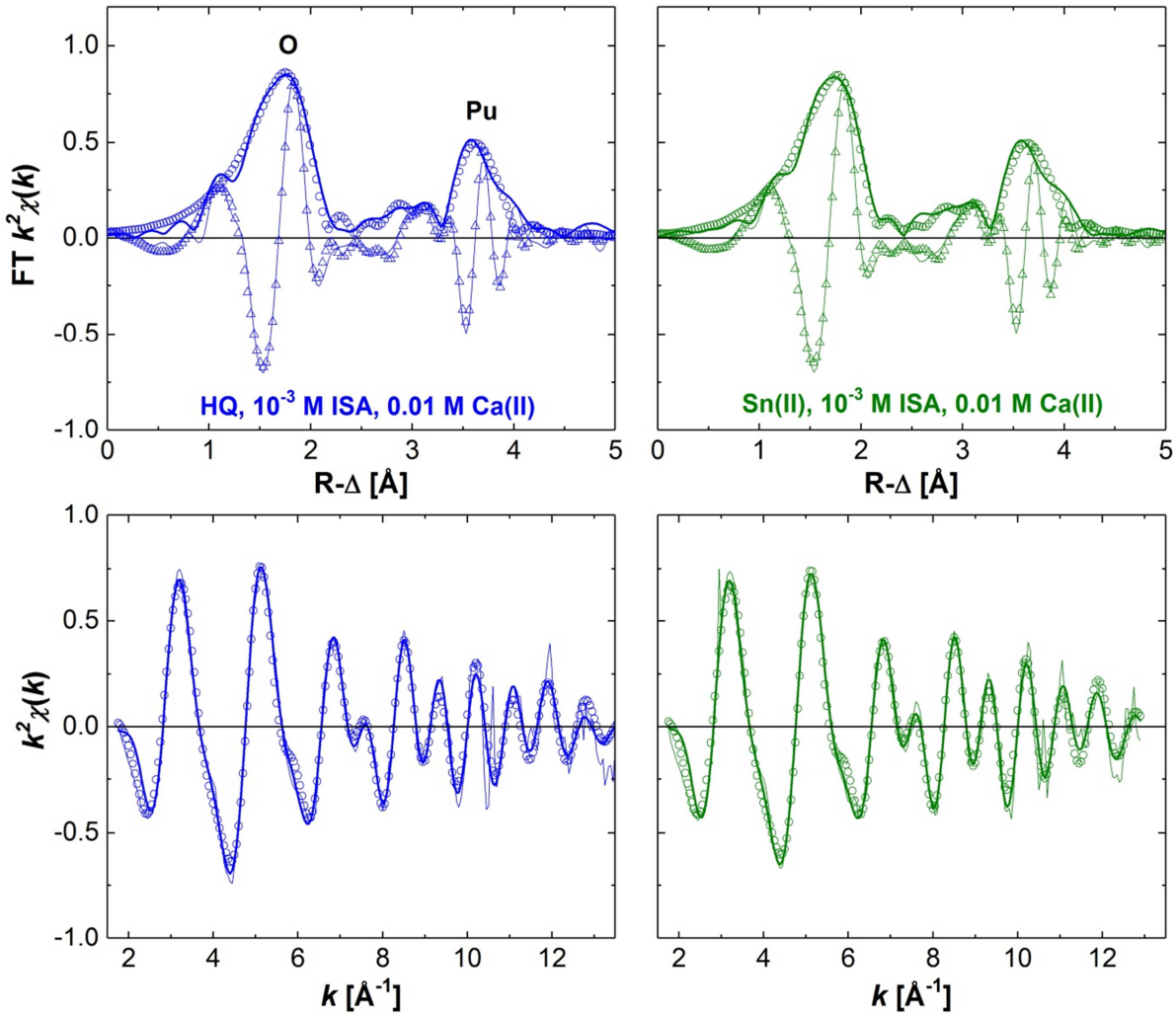

Figure 36. *Pu L_{III}–edge EXAFS fiting results for solid phases recovered from HQ- (blue) and Sn(II)-buffered (green) samples equilibrated with $m(ISA)_{tot}$ = 10^{-3} m, $m(Ca)_{tot}$ = 10^{-2} m in solution at pH_m = 12 (t_{eq} = 150 days) – top row: FT magnitude (solid line), fit magnitude (open circles), FT real part (thin solid line) and fit real part (open triangles); bottom row: Fourier-filtered data (solid line), raw data (thin solid line), back-transformed fit (open circles).*

3.1.3.4 Thermodynamic calculations

As discussed in Section 3.1.1.5, chemical reactions (32), (35) and (38) are expected to control the solubility of Pu within the experimental conditions considered in this study. The corresponding Equations (33, 34), (36, 37) and (39, 40) have been used in combination with stability constants and SIT ion interaction coefficients summarized in Table A1 and Table A2 of the Appendix to calculate the solubility lines in Figure 30, Figure 31, Figure 33: PuO_2(am,hyd) in equilibrium with $Pu(IV)_{aq}$ (black line, calculated using equilibrium constants

reported in NEA-TDB [9]); PuO_2(am,hyd) in equilibrium with $Pu(IV)_{aq}$ and $Pu(III)_{aq}$ at (pe + pH_m) = 1.54 (grey line); and $Pu(OH)_3$(am) in equilibrium with $Pu(III)_{aq}$ (light blue line).
Under identical conditions with the presence of ISA in solution, besides the abovementioned hydrolysis equilibria, chemical reactions (54) (with y = 1 and x = 0 or 1) and (55) are governing the speciation of Pu in solution. In these cases, Equations (55), (62) (with y = 1 and x = 0 or 1) and (61), (63) were used in combination with stability constants and SIT ion interaction coefficients summarized in Table 12 and Table 13, respectively, together with the auxiliary thermodynamic data (Table A1 and Table A2 of the Appendix) to calculate the solubility lines in Figure 30, Figure 31, Figure 32, Figure 33, Figure 37, Figure 38, Figure 39: PuO_2(ncr,hyd) in equilibrium with Pu(IV)–OH–ISA species (blue lines); PuO_2(ncr,hyd) in equilibrium with Pu(IV)–OH–ISA and Pu(III)–OH–ISA species at (pe + pH_m) = 1.54 (green lines).

$$\log {}^{*}\beta^{\circ}_{1,4+x,y} = \log {}^{*}\beta'_{1,4+x,y} + \log \gamma_{Pu(IV)(OH)_{4+x}ISA^{-(y+1)}} + (4+x) \log \gamma_{H^+} - \log a_{Pu^{4+}(aq)} - \\ - y \log \gamma_{ISA^-} - (4+x) \log a_w \quad (62)$$

$$\log {}^{*}\beta^{\circ}_{1,2,1} = {}^{*}\beta'_{1,2,1} + \log \gamma_{Pu(III)(OH)_2ISA(aq)} + 2 \log \gamma_{H^+} - \log a_{Pu^{3+}(aq)} - \log \gamma_{ISA^-} - \\ - 2 \log a_w \quad (63)$$

3.1.3.4.1 Chemical and thermodynamic model of the system Ca(II)-Pu(IV)-OH-ISA

Based on the analyses of the data set described in Section 3.1.3.2 ($\log m(Pu)_{tot}$ *vs.* pH_m, $\log m(Pu)_{tot}$ *vs.* $\log m(ISA)_{tot}$ and $\log m(Pu)_{tot}$ *vs.* $\log m(Ca)_{tot}$) and considering PuO_2(ncr, hyd) as solid phase controlling the solubility of Pu(IV) in all HQ systems with the presence of ISA and Ca(II), chemical reactions (13) and (14) are proposed to control the solubility and solution chemistry of Pu(IV) under alkaline to hyperalkaline conditions.

$$Pu(IV)O_2(ncr,hyd) + ISA^- + Ca^{2+}(aq) + 2\ H_2O(l) \Leftrightarrow Ca(II)Pu(IV)(OH)_4ISA^+ \quad (64)$$

$$Pu(IV)O_2(ncr,hyd) + ISA^- + Ca^{2+}(aq) + 3\ H_2O(l) \Leftrightarrow Ca(II)Pu(IV)(OH)_5ISA^0(aq) + H^+ \quad (65)$$

The species $Ca(II)Pu(OH)_4ISA^+$ is predominant in solutions with pH_m = 8 – 11, whereas $Ca(II)Pu(OH)_5ISA^0$(aq) forms at pH_m > 11. In the present case as well, the proposed stoichiometries for the Ca(II)–Pu(IV)–ISA complexes assume highly hydrolyzed metal centers ("$Pu(OH)_4$" and "$Pu(OH)_5^-$") within the quaternary complex species where only the

carboxylic group is deprotonated on the ligand. In view of Section 3.1.2.5, the DFT calculation results for the stoichiometries of the Pu(III/IV)-ISA species, possibly the formation of the newly identified, quaternary complexes also involve the deprotonation of one or several alcohol groups of ISA. As of now, no theoretical study has been conducted to assess the stoichiometry of the Ca(II)-Pu(IV)-OH-ISA species. Hence, for the sake of consistency with the study on the binary system, the nomenclature assuming the retainment of the stoichiometries of the existing, binary species was adapted in the present section.

The limitations and assumptions of the proposed chemical model can be summarized as follows:

1. The proposed chemical model is based on solubility data at $pH_m < 12$. Above this value of pH_m, other phenomena not yet understood affect the solubility equilibrium, decreasing (or limiting) $m(Pu)_{tot}$ in solution. The use of this chemical model (and the accordingly derived thermodynamic model) beyond this pH value seemingly overestimates experimental solubility data (according to so-far available data), (thus proving to be conservative when estimating upper-limit concentration levels).
2. Solubility experiments with varying $m(ISA)_{tot}$ and $m(Ca)_{tot}$ were only conducted at $pH_m = 12$, thus the stoichiometries Pu:ISA and Pu:Ca in reaction (13) are based on the assumption that the same stoichiometry of the Pu-ISA complex in the absence of Ca(II) is retained, and that only one Ca^{2+} ion is attached to this structure. The complexation of a second Ca^{2+} ion to the $Ca(II)Pu(IV)(OH)_4ISA^+$ moiety appears to be unlikely for evident electrostatic reasons.

The data interpretation of the ternary system Ca(II)–Pu(IV)–OH–ISA was performed taking into consideration the chemical and thermodynamic data for the system Pu(IV)–OH–ISA derived in Section 3.1.2.6, applying stability constants and SIT ion interaction coefficients summarized in Table 12 and Table 13, respectively, together with the auxiliary thermodynamic data (Table A1 and Table A2 of the Appendix) as well as for the system Ca(II)–OH–ISA (see thermodynamic data provided in Table 1).

As discussed in the previous sections, to gain further confidence on the proposed model, different plausible “apparent” stoichiometries of Ca(II)–Pu(IV)–OH–ISA complexes were also evaluated in the fitting procedure of the experimental data. General equilibrium constants

of the newly forming quaternary species $(Ca_zPu(IV)(OH)_{4+x}(ISA)_y^{(2z-x-y)}$, chemical reaction (66)) can be calculated according to Equation (67).

$$Pu^{4+}(aq) + y\ ISA^{-} + (4+x)\ H_2O(l) + z\ Ca^{2+}(aq) \Leftrightarrow$$
$$\Leftrightarrow Ca_zPu(IV)(OH)_{4+x}(ISA)_y^{(2z-x-y)} + (4+x)\ H^{+} \quad (66)$$

$$\log {}^{*}\beta^{\circ}_{z,1,4+x,y} = \log a_{Ca_zPu(IV)(OH)_{4+x}(ISA)_y^{(2z-x-y)}} + (4+x) \log a_{H^+} - \log a_{Pu^{4+}(aq)} - y \log a_{ISA^-} - z \log a_{Ca^{2+}} \quad (67)$$

The total concentration of Pu in solution at I = 0.10 m NaCl was calculated by PP-PQC software packages using Equation (68), which besides the formation of the newly identified Ca(II)–Pu(IV)–OH–ISA complexes also took into account the presence of the ternary Pu(IV)–OH–ISA and Ca(II)–Pu(IV)–OH complexes.

$$\log m^{calc}(Pu)_{tot,m} = \sum_{n=1}^{4} \left({}^{*}K'_{IVs,(4-n)} \cdot (m_{H^+})^n \right) + {}^{*}K'_{IVs,0} \cdot \left[\left({}^{*}\beta'_{1,4,1} \cdot (m_{ISA^-}) + {}^{*}\beta'_{1,5,1} \cdot (m_{H^+})^{-1} \cdot (m_{ISA^-}) \right) \right] + {}^{*}K'_{IVs,0} \cdot \left[\sum_{i=1}^{2} \left({}^{*}\beta'_{zi,1,4+xi,yi} (m_{H^+})^{-x_i} \cdot (m_{ISA^-})^{y_i} \cdot (m_{Ca^{2+}})^{z_i} \right) \right] + {}^{*}K'_{IVs,4,1,8} (m_{H^+})^{-4} \cdot (m_{Ca^{2+}})^4 \quad (68)$$

In the first step of the fitting exercise, the effect of ionic strength for the newly forming quaternary species was calculated considering only the Debye–Hückel term within the SIT formulism. At the second stage, once the definite chemical model was set, a final fit, considering estimated values for SIT ion interaction coefficients of the quaternary Ca(II)–Pu(IV)–OH–ISA complexes was also performed.

Although the chemical model involving the formation of the complex species with Ca(II):Pu(IV):OH:ISA ratios of 1:1:4:1 ($CaPu(IV)(OH)_4ISA^+$) and 1:1:5:1 ($CaPu(IV)(OH)_5ISA(aq)$) was initially favored based on the slope analysis and chemical reasoning discussed previously, several additional stoichiometries: 1:1:6:1, 1:1:5:2, 2:1:5:1, 2:1:5:2 and 2:1:6:2 were also tested for the second complex (see Table 15). Due to the limited experimental data available under less alkaline conditions (*e.g.* only data at $m(ISA)_{tot}$ = constant and $m(Ca)_{tot}$ = constant), the evaluation of different stoichiometries was disregarded for the first species. In this respect, this species remains bound to the given assumptions. For

all evaluated chemical models, the values of the two respective equilibrium constants (67) were optimized to obtain the best fit of the solubility data set.

Table 15 shows values of the R^2 and the objective function ($f_{obj}(*\beta°_{z,1,4+x,y})$, square root of the averaged sum of squared residuals with regard to the measured and calculated $m(Pu)_{tot}$) resulting from the fitting procedures using the different chemical models proposed above.

Table 15. *Fitting results: values of the applied objective functions (square root of the averaged sum of squared residuals) and the coefficients of determination (R-squared values in percentage) provided by the evaluation of the available solubility data on the Ca(II)-Pu-OH-ISA system at $pH_m \leq 12$, executed via PHREEPLOT – PHREEQC software packages. The values are presented with regard to the applied stoichiometries of the two, newly forming Ca(II)–Pu(IV)–OH–ISA complexes.*

	Ca (z) : Pu(IV) : OH (4+x) : ISA (y) ratios					
1st species	**1:1:4:1**	1:1:4:1	1:1:4:1	1:1:4:1	1:1:4:1	1:1:4:1
2nd species	***1:1:5:1***	*1:1:6:1*	*1:1:5:2*	*2:1:5:1*	*2:1:5:2*	*2:1:6:2*
R^2 [%]	**73.14**	73.26	39.46	69.35	39.46	39.46
$f_{obj}(*\beta°_{z,1,4+x,y})$	**0.273**	0.273	0.410	0.293	0.410	0.410

Chemical models involving the formation of (1:1:4:1 + 1:1:5:1) or (1:1:4:1 + 1:1:6:1) complexes gave an almost identical statistical representation of the data set. Although acknowledging that both models describe equally well the experimental data, the first option is favored for the sake of simplicity and to retain a closer consistency with the chemical model reported for the system Pu(IV)–OH–ISA (Table 12).

It has to be mentioned also that the correlation coefficient related to the two optimized equilibrium constants was sufficiently low in all cases. This indicates that the formation of two species is required to describe the data set, and moreover, that the addition of further species to the model would only be an overparameterized representation for the given system.

In the following step, equilibrium constants of the selected two complexes (through chemical reaction (66), defined in Equation (67), with y = z = 1 and x = 0 and 1) were optimized to obtain the lowest residuals between the calculated, as in Equation (68) and experimentally measured total Pu total concentrations.

SIT formalism through Equation (69) was used to calculate the effect of ionic strength on the equilibrium constants of the related complex species $CaPu(IV)(OH)_4ISA^+$ (with x = 0) and $CaPu(IV)(OH)_5ISA(aq)$ (with x = 1), respectively. The SIT ion interaction parameter of the complex $CaPu(IV)(OH)_4ISA^+$ with Cl^- was estimated as $\varepsilon(CaPu(IV)(OH)_4ISA^+, Cl^-) = -(0.05 \pm 0.10)$ mol·kg^{-1}, following the charge analogy described in the work of Hummel *et al.* [149]. The ion interaction coefficient of the neutral complex $CaPu(IV)(OH)_5ISA(aq)$ is zero as defined within SIT formalism.

$$\log {}^{*}\beta^{\circ}_{1,1,4+x,1} = \log {}^{*}\beta'_{1,1,4+x,1} + \log \gamma_{CaPu(IV)(OH)_{4+x}ISA}{}^{(1-x)} + (4+x) \log \gamma_{H^+} - \\ - \log \gamma_{Pu^{4+}(aq)} - \log \gamma_{ISA^-} - \log \gamma_{Ca^{2+}(aq)} - (4+x) \log a_w \quad (69)$$

The optimization of $\log {}^{*}\beta^{\circ}_{1,1,4,1}$ and $\log {}^{*}\beta^{\circ}_{1,1,5,1}$ resulted in:

$$\log {}^{*}\beta^{\circ}_{1,1,4,1}(CaPu(IV)(OH)_4ISA^+) = -(1.66 \pm 0.10) \quad (70)$$

$$\log {}^{*}\beta^{\circ}_{1,1,5,1}(CaPu(IV)(OH)_5ISA(aq)) = -(12.70 \pm 0.08) \quad (71)$$

The solubility curves of Pu calculated, using Equation (68) for the system Ca(II)–Pu(IV)–OH–ISA using the chemical and thermodynamic models derived in this work are shown in Figure 37, Figure 38 and Figure 39, together with the corresponding experimental data for HQ-buffered systems in the presence of Ca(II) as well as the solubility calculated (described in Section 3.1.2.4.1) for the binary system Pu(IV)–OH–ISA.

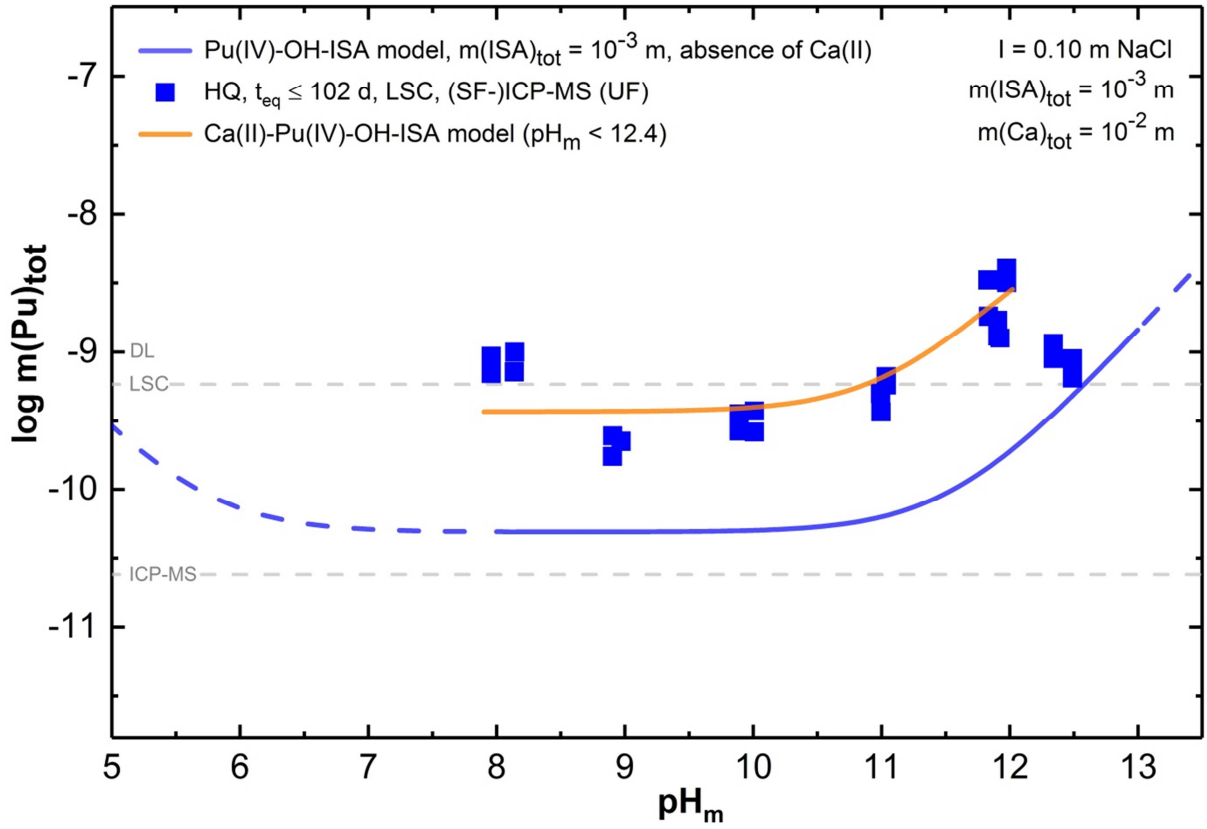

Figure 37. *Experimentally measured $m(Pu)_{tot}$ in equilibrium with PuO_2(ncr,hyd) in HQ-buffered systems (■) at pH_m = 8 – 12.4 with $m(ISA)_{tot}$ = 10^{-3} m and $m(Ca)_{tot}$ = 0.01 m. Solubility line in orange is calculated with the chemical and thermodynamic models derived in this work for the system Ca(II)–Pu(IV)–OH–ISA. Blue lines (solid and dashed) correspond to the solubility of Pu(IV)O_2(am,hyd) at I = 0.10 m NaCl, in the presence of $m(ISA)_{tot}$ = 10^{-3} m calculated using the chemical and thermodynamic models derived for the binary system Pu(IV)–OH–ISA (listed in Table 12).*

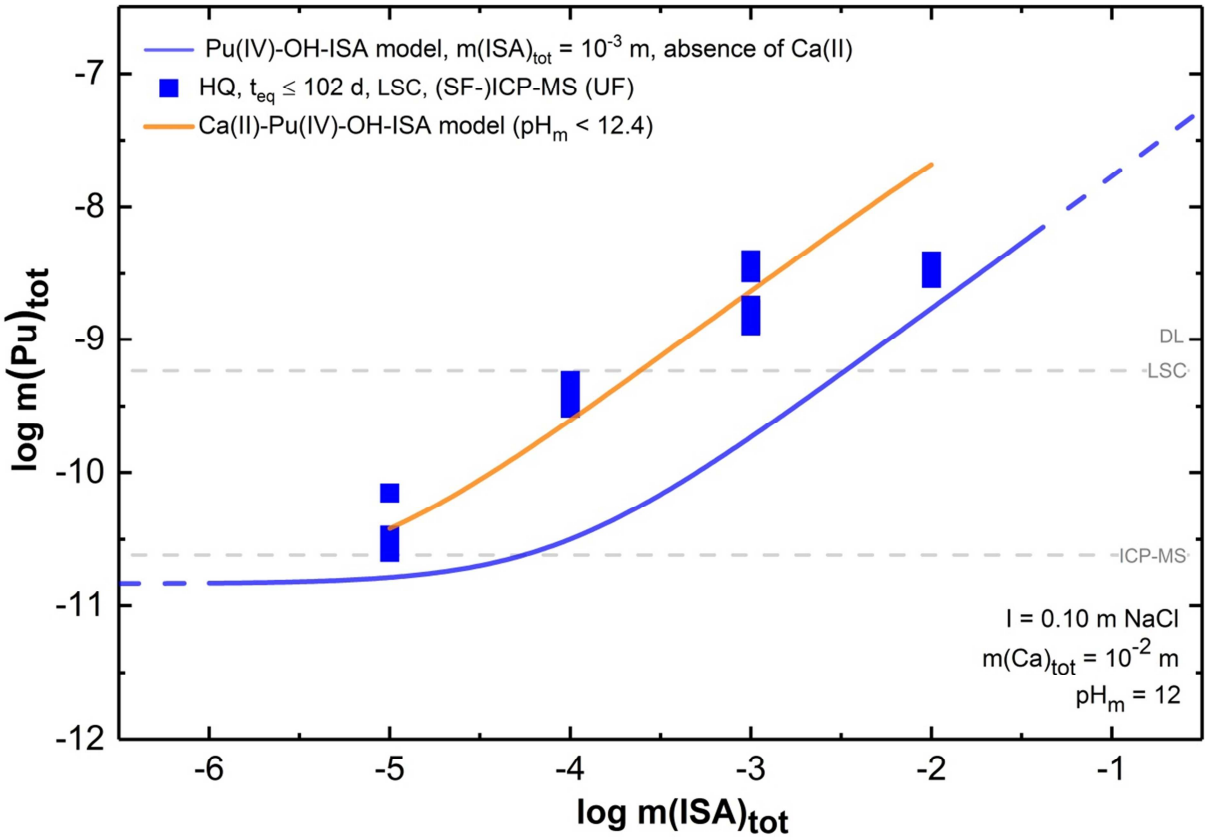

Figure 38. *Experimentally measured $m(Pu)_{tot}$ in equilibrium with PuO_2(ncr,hyd) in HQ-buffered systems (■) at pH_m = 12 and $m(Ca)_{tot}$ = 0.01 m with 10^{-6} m ≤ $m(ISA)_{tot}$ ≤ 0.10 m. Solubility line in orange is calculated with the chemical and thermodynamic models derived in this work for the system Ca(II)–Pu(IV)–OH–ISA. Blue lines (solid and dashed) correspond to the solubility of Pu(IV)O_2(am,hyd) at I = 0.10 m NaCl, in the presence of $m(ISA)_{tot}$ = 10^{-3} m calculated using the chemical and thermodynamic models derived for the binary system Pu(IV)–OH–ISA (listed in Table 12).*

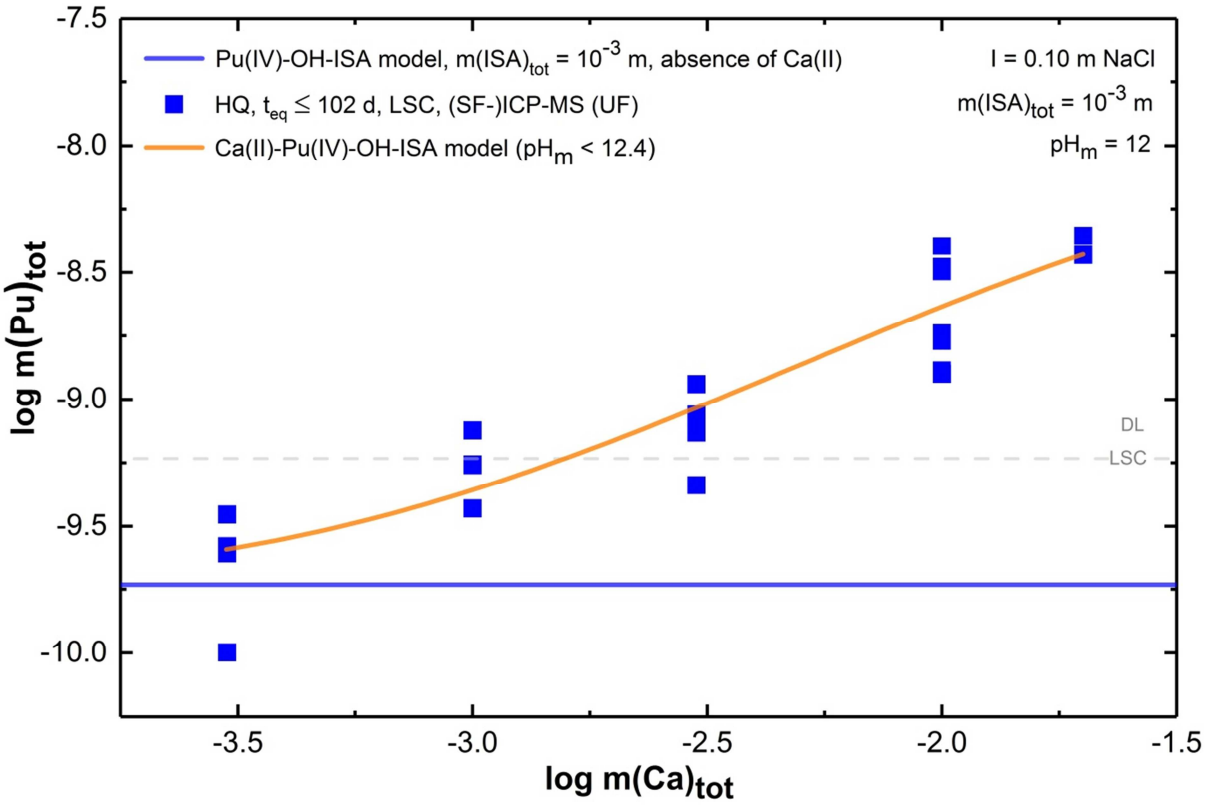

Figure 39. *Experimentally measured $m(Pu)_{tot}$ in equilibrium with PuO_2(ncr,hyd) at constant pH_m = 12 and $m(ISA)_{tot}$ = 10^{-3} m with $3 \cdot 10^{-4}$ m ≤ $m(Ca)_{tot}$ ≤ $2 \cdot 10^{-2}$ m, in HQ-buffered (■) solutions. Solubility line in orange is calculated with the chemical and thermodynamic models derived in this work for the system Ca(II)–Pu(IV)–OH–ISA. Blue lines (solid and dashed) correspond to the solubility of Pu(IV)O_2(am,hyd) at I = 0.10 m NaCl, in the presence of $m(ISA)_{tot}$ = 10^{-3} m calculated using the chemical and thermodynamic models derived for the binary system Pu(IV)–OH–ISA (listed in Table 12).*

In all cases, the proposed chemical and thermodynamic model describes equally well most experimental data collected within the given boundary conditions. However, relatively large deviations are observed at high ISA concentration ($m(ISA)_{tot}$ > 0.01 m), where the model overestimates the experimentally measured Pu solubility by *ca.* 0.5 log-units. Overestimations with similar magnitude are also observed for experimental data at pH_m = 12.4 (with $m(ISA)_{tot}$ = 10^{-3} m and $m(Ca)_{tot}$ = 0.01 m conditions). Presumably this trend is also progressing above this pH. Note that the data points collected within systems at the latter pH value were excluded from the fitting process as discussed in Section 3.1.3.2.1. These observations could hint to an additional solubility phenomena not yet identified, taking place under these conditions (*e.g.* precipitation of a new solid phase). In view of the so-far available data, the

proposed thermodynamic model overestimates the experimentally measured solubility values for pH > 12.4 and/or $m(ISA)_{tot}$ > 0.01 m conditions, and thus provides conservative results with respect to the potential release of Pu from the repository under these particular conditions. Based upon this observation, within the sorption study, separate solubility experiments were additionally conducted where the focus was put on the validity of the established thermodynamic model under porewater conditions for the system Ca(II)–Pu(IV)––OH–ISA (see Section 3.2.6.6.1 for results).

It has to be emphasized that the new thermodynamic model in systems with pH_m > 11 provides reasonable predictions for Pu solubility values under strongly reducing conditions as well, despite that the experimental points collected in the Sn(II)-buffered solubility series were excluded from the input dataset.

3.1.3.5 Comparison of the new Ca(II)-Pu(IV)-OH-ISA model with literature data

Table 16 summarizes the equilibrium constants derived in the present work for the formation of Ca(II)-Pu(IV)–ISA–OH complexes prevailing under reducing, alkaline to hyperalkaline conditions. Table 17 lists SIT ion interaction coefficients estimated in the present work for the newly defined species.

Table 16. *Chemical equilibria and related equilibrium constants (at zero ionic strength) derived in the present study describing Ca(II)–Pu(IV)–OH–ISA system.*

Chemical equilibria	***log*β° (I → 0)***
$Pu^{4+}(aq) + ISA^{-} + 4\ H_2O(l) + Ca^{2+}(aq) \Leftrightarrow$ $\Leftrightarrow Ca(II)Pu(IV)(OH)_3ISA_{-H}^{+} + 4\ H^{+}$	–(1.66 ± 0.10)
$Pu^{4+}(aq) + ISA^{-} + 5\ H_2O(l) + Ca^{2+}(aq) \Leftrightarrow$ $\Leftrightarrow Ca(II)Pu(IV)(OH)_3ISA_{-2H}^{0}(aq) + 5\ H^{+}$	–(12.70 ± 0.08)

Table 17. *SIT ion interaction coefficients used in the present study.*

species i	*species j*	*ε(i,j) [mol·kg^{-1}]*
$Ca(II)Pu(IV)(OH)_4ISA^+$	Cl^-	$-(0.05 \pm 0.10)$ [a)]
$Ca(II)Pu(IV)(OH)_5ISA^0(aq)$	Cl^- / Na^+	0.00 [b)]

[a)] estimated values based on the work of Hummel *et al.* [149]
[b)] zero by definition within SIT formalism

The thermodynamic model established for the system Ca(II)–Pu(IV)–OH–ISA can only be compared with the analogous data on the Th(IV) system reported in the works of Vercammen *et al.* [100] and Tits *et al.* [103, 105] (see Introduction, Section 1.3.3.5 for detailed discussion). Figure 40 (a, b, c, d) shows the predominance diagrams of Pu(IV) (based upon the results of the present study) and Th(IV) (adapted from Vercammen *et al.* [100] and Tits *et al.* [103, 105], later re-evaluated in [12]) for conditions: pH_m = constant = 9 and 12, with $-6 \leq \log m(ISA)_{tot} \leq -1$ and $-4 \leq \log m(Ca)_{tot} \leq -1.5$ applying thermodynamic calculations as described in Section 3.1.3.4.

Figure 40 a, b, c, d show significantly different aqueous speciations for Pu(IV) and Th(IV) in the presence of ISA and Ca. An interesting feature of the predominance diagrams is the lack of equilibrium line between the hydrolyzed Th(IV) species and the quaternary Ca(II)–Th(IV)–OH–ISA species. The latter observation indicates that under any experimental conditions within the displayed window, the increase of ISA total concentration always results in the formation and predominance of the Th(IV)–OH–ISA species first, even when there is a significant excess of Ca(II) ions (compared to the ligand) in solution. In view of the effect of Ca(II) on the Pu(IV)–OH–ISA system, this feature is highly unexpected, as the overestimated stability of the Th(IV)–OH–ISA species was also proved by a number of independently performed solubility studies [59, 107]. This points out that the thermodynamic data on the Th(IV)–OH–ISA system based on the sorption study conducted by Vercammen *et al.* [100] are strongly overestimating Th(IV) solubility limits in the presence of the ligand. The predominance of complexes with the same 1:1 An(IV):ISA ratio for both, Pu(IV) and Th(IV) is again invalid and it was shown that in solutions with $m(ISA)_{tot} > 10^{-3}$ m, (within the alkaline pH-range) the complex with 1:2 ratio ($Th(OH)_4(ISA)_2^{2-}$) is dominating for the Th(IV) case [107]. The former observation was also found to be consistent with literature data

available for analogous An(IV)–OH–ISA systems (for further details see discussion in Sections 1.3.3 and 3.1.2.7).

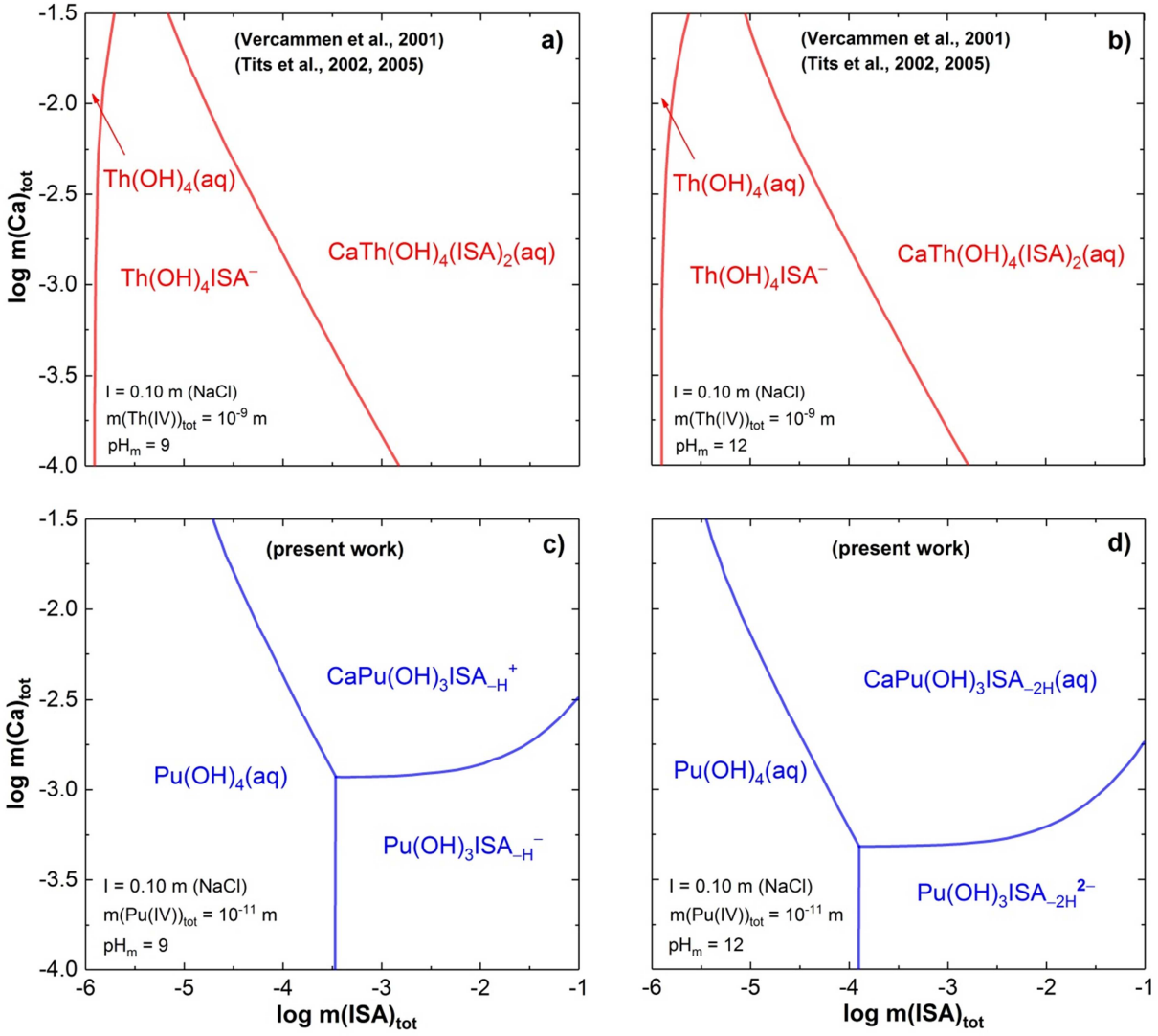

Figure 40. *Predominance diagrams of An(IV) in the presence of ISA ($-6 \leq \log m(ISA)_{tot} \leq -1$) and Ca ($-4 \leq \log m(Ca)_{tot} \leq -1.5$), at I = 0.10 m NaCl, calculated for* ***Th(IV)****: $m(Th(IV))_{tot} = 10^{-9}$ m, at pH_m = 9* ***(a,)****; 12* ***(b,)*** *using thermodynamic data reported by Vercammen et al. [100] for Th(IV)-OH-ISA system and Tits et al. [103, 105] for Ca(II)-Th(IV)-OH-ISA system recalculated in [12] and for* ***Pu(IV)****: $m(Pu(IV))_{tot} = 10^{-11}$ m, at pH_m = 9* ***(c,)****; 12* ***(d,)*** *using thermodynamic data derived in the present work.*

Despite that the results of the present work confirm the role of Ca(II) in stabilizing ternary Pu(IV)–OH–ISA complexes, the "enhanced" stability of the resulting quaternary complexes does not match the predictions based on Th(IV) data. The clearly increased stability predicted

for the Ca(II)–Th(IV)–OH–ISA species compared to the Pu(IV) case is not considered to be "thermodynamically real", but rather caused by differences between solubility and sorption experiments. A definitive explanation for this major discrepancy is not yet found. Nonetheless, the systematic, wide-range variation of experimental parameters, coupled with a combined thermodynamic fit on a collected dataset is the key element in deriving a reliable thermodynamic model for such a system. In this aspect, the extensive study on the system Ca(II)–Pu(IV)–OH–ISA together with the thermodynamic model derived on the Pu(III/IV)–OH–ISA system accomplished in this work represent the most comprehensive effort to characterize quaternary Ca(II)–An(III/IV)–OH–ISA complexes. However, further experimental studies (considering both solubility and sorption experiments) following a similar systematic and strategic approach applied in the present work on systems Ca(II)–Th(IV)–ISA, Ca(II)–U(IV)–ISA and Ca(II)–Np(IV)–ISA would provide essential information in understanding the role of Ca(II) on the An(IV)–ISA complexation under conditions relevant for L/ILW disposal.

3.2 Sorption study

Prior to the discussion of the obtained data on sorption experiments, characterization results on the applied cement powder and porewater are presented in Section 3.2.1. Subsequently, results on sorption investigations are provided in four main parts:

(i) Redox conditions prevailing in the investigated systems (Section 3.2.2);
(ii) Obtained sorption data and evaluation on the system ISA-Cement (Section 3.2.3);
(iii) Sorption data collected on the binary, Cement-Pu system is presented (Section 3.2.4)
(iv) Experimental results and data evaluation on the ternary, Cement-Pu-ISA system (Sections 3.2.5 and 3.2.6).

3.2.1 Characterization of the cement powder and porewater

3.2.1.1 Initial cement powder

In view of the solid phase characterization results on the initial cement powder (provided in the Appendix, Section 6.5), it can be stated that the chemical composition of the cement material has not been modified by the powdering procedure and the main, hydrated solid phases present in the generated OPC powder are the amorphous C-S-H phases and the Portlandite. Based on the assumption that in the course of the hydration process all Ca-content of the clinker-components is consumed by the forming Portlandite and the C-S-H phases, while the Si-content is taken up solely by the C-S-H phases, an estimate of 1.7 – 1.9 can be calculated for Ca:Si atom-concentration ratio for the present C-S-H phases using the various quantification results of ICP-OES/-MS, TG-DSC and XPS techniques. This value is found to be in close agreement with the reported data of 1.8, resulting from model calculations on OPC pastes with similar chemical characteristics [195-197].
In this respect, the generated cement powder to be applied for the sorption experiments can be taken as a representative material for the original cement specimens in terms of the main chemical properties.

3.2.1.2 Chemical compositions of equilibrated cement pastes and porewater solutions

Identically as in the case of the initial cement powder, two equilibrated cement pastes were also characterized after hydration stoppage by the before mentioned techniques. The solid phases were retrieved from: 1. the batch sample used for generating the porewater (which was

the solution applied for all sorption studies simulating stage II of the cement degradation process) and from 2. a batch sample of the Cement-ISA sorption experiment series (at $[ISA]_{tot}$ = 0.01 M and S:L ratio = 2 $g \cdot dm^{-3}$). Data on the sample 1 (named as "porewater cement") was collected after the preparation of all sorption experiments (~1 year of contact time), whilst on the 2nd sample (denoted as "ISA-cement") all analysis were performed after an equilibration time of 14 days (final t_{eq} of Cement-ISA sorption investigations). In addition to the solid phase characterization, equilibrium chemical compositions of the aqueous phases were also assessed for the above listed two samples. A more detailed discussion on the results are provided in the Appendix (Section 6.6).

In summary, it can be concluded that the generated porewater to be applied as the liquid phase for later sorption experiments is a chemically representative solution of cement pore fluids expected at stage II of the cement degradation process. Solid phase characterization results on the retrieved cement solid paste coincide with the latter observation. As for the ISA-cement sample, the total ligand concentration of 0.01 M in the supernatant with S:L ratio = 2 $g \cdot dm^{-3}$ was determined to bear with a negligible effect on both: the governing chemical parameters in solution of interest (pH_c, $[Ca]_{tot}$) and also on the main chemical composition (presence of Portlandite and C-S-H phases) of the HCP. It is of note, that a slightly enhanced calcification was observed on the surface of the retrieved specimens.. Observed changes can be modelled assuming Portlandite dissolution equilibria in combination with Ca(II)-OH-ISA complex formation reactions in solution, which is in agreement with the observation of previous studies [104].

Table 18 contains the concentrations of the major and minor elements in the liquid phases of the abovementioned two samples: porewater cement sample and the ISA-cement sample as quantified by ICP-OES and ICP-MS measurements.

The initial composition of the porewater together with the determined pH condition of pH_c = (12.55 ± 0.08) (averaged value of multiple measurements on the porewater) are in good agreement with the calculated and the previously reported porewater conditions (with pH_c = 12.50) representing stage II of the cement degradation process [4, 198]. Slightly lower value has been quantified for Na(I) concentration, whereas concentration of K(I) was found to be in good agreement with reference data, both indicating the successfulness of the pre-washing step aimed to remove the alkali-content of the initial cement powder. Reference values for Mg(II) and Fe(III) are not provided in the literature, whilst the concentration of Si(IV) is below the detection limit of the in-house quantification by ICP-MS, in agreement with the low level reported [198].

Table 18. *Compositions quantified by ICP-OES/-MS techniques of the liquid phases in contact with different cement pastes: "porewater" designates the solution generated by equilibrating Milli-Q water with the pre-washed cement powder (t_{eq} = 1 year), "ISA-cement porewater" is the supernatant of the sample prepared using the latter porewater, the initial cement powder and the ISA-stock solution to reach $[ISA]_{tot}$ = 0.01 M at S:L ratio = 2 g·dm^{-3}, analyzed at t_{eq} = 14 days. Reference values are adapted from literature data on analogous OPC porewater [4, 198].*

Sample name	***Ca(II)***	***Na(I)***	***K(I)***	***Al(III)***	***Si(IV)***	***Mg(II)***	***Fe(III)***
	[M]	***[M]***	***[M]***	***[M]***	***[M]***	***[M]***	***[M]***
Porewater	0.02	$7\cdot10^{-5}$	$3\cdot10^{-4}$	$2\cdot10^{-6}$	< D.L.[a)]	$8\cdot10^{-7}$	$3\cdot10^{-8}$
ISA-cement porewater	0.02	0.02	$8\cdot10^{-4}$	$2\cdot10^{-5}$	$7\cdot10^{-5}$	$2\cdot10^{-6}$	$5\cdot10^{-6}$
Reference[b)]	0.02	$3\cdot10^{-3}$	$1\cdot10^{-4}$	$2\cdot10^{-6}$	$3\cdot10^{-6}$	–	–

a) below detection limit means a concentration of < 1 10^{-5} M for Si(IV)
b) reference values are taken from literature data on analogous systems [4, 198]

The measured pH value of the ISA-cement porewater sample: $pH_c = 12.60 \pm 0.03$ was observed to be within the uncertainty-range of the values collected in the absence of ISA (calculated theoretical value under identical conditions is: $pH_c = 12.57$). The chemical composition of the equilibrated porewater with $[ISA]_{tot}$ = 0.01 M at S:L ratio of 2 g·dm^{-3} show distinct changes in the depicted elemental concentrations especially with regard to Na(I) ion concentration. These discrepancies are originating from the introduction of ISA-stock solution to the system, which was later confirmed by the characterization of identical solutions prepared in the absence of cement solid phases. Ca(II) ion concentration was found to be negligibly affected by the high ligand concentration in solution, which is in agreement with thermodynamic calculations, assuming that the concentration of Ca^{2+} is governed by the dissolution of Portlandite and by its complex formation reactions with ISA in solution (when $[ISA]_{tot}$ does not exceed ~0.1 M, *i.e.* precipitation of $Ca(ISA)_2(s)$ does not occur). Accounting for the latter chemical equilibria, the calculated theoretical increase (without taking into account the sorption of the ligand) in $[Ca^{2+}]_{tot}$ with the level of $2.7\cdot10^{-3}$ M is located closely to

the uncertainty-range (± 3 10^{-3} M) associated to the quantification of $[Ca^{2+}]_{tot}$ by ICP-OES technique in analogous systems.

3.2.2 Redox conditions

The redox conditions in terms of averaged (pe + pH_c) values collected in all HQ-, Sn(II)- and dithionite-buffered batch sorption experiments in the absence and in the presence of ISA are summarized in Table 19.

A general trend in the collected pH_c and pe values as function of $[ISA]_{tot}$ in solution or the S:L ratio applied was not found. Measured pH conditions in the course of all sorption studies were identical to the previously collected values in pure porewater solutions, indicating the retainment of Portlandite as the pH- (and $[Ca]_{tot}$-) controlling phase in the system. Thermodynamic evaluations were used to derive theoretically calculated pH_c (and $[Ca]_{tot}$) values, accounting for the given $[ISA]_{tot}$ concentration and Portlandite solubility equilibria.

Table 19. *List of averaged pH_c values and redox conditions, (pe + pH_c) values (with associated uncertainties) collected on all HQ-, Sn(II)- and dithionite-buffered batch sorption experiments conducted in the present study.*

Redox buffer (2mM)	***$pH_{c,av.}$***	***$pe_{av.}$***	***$(pe + pH_c)_{av.}$***
HQ	(12.54 ± 0.16)	–(3.5 ± 1.0)	(9.2 ± 0.8)
Sn(II)	(12.50 ± 0.16)	–(11.6 ± 1.1)	(1.0 ± 0.7)
$S_2O_4^{2-}$	(12.50 ± 0.17)	–(12.4 ± 1.3)	–(0.3 ± 0.6)

In agreement with the findings of previous studies performed in the absence and presence of ISA and Ca(II) (see results of solubility study Section 3.1 and references [1, 2]), HQ in solution imposed moderately reducing conditions. Detected overall conditions with an averaged (pe + pH_c) value of (9.2 ± 0.8) were in good agreement with the previously assigned value of (pe + pH_m) = (9 ± 1). The related E_h measurements show fast equilibration times. Sorption of HQ on the cement can be excluded based on NPOC data. The redox conditions in HQ-buffered systems are within the stability field of Pu(IV) for both, aqueous species and

solid compounds. Hence, sorption data of these samples can serve as reference for evaluating processes and interactions within the Cement–Pu(IV)(–ISA) system.

The formerly reported redox conditions (pe + pH_m) of (1.54 ± 0.14) for the Sn(II)-buffered system were in moderate agreement with the new value of (pe + pH_c) = (1.0 ± 0.7). The thermodynamic evaluation of Sn(II) sorption data in the course of the present study did not necessitate the acquired pe values to be included as input values in the thermodynamic model (in the presence of ISA the predominance of Ca(II)–Pu(IV)–OH–ISA species are expected in the solution). In this respect, E_h values in the present case were not measured further with longer equilibration times. As the reliability of E_h values acquired under short equilibration times are sometimes questionable, newly obtained (pe + pH_c) values (still overlapping with uncertainty field of the formerly detected ranges) should be taken as orientative values. Sorption data collected in the presence of Sn(II) under strongly reducing conditions will be used as the representative system expected for deep geological repositories. In this study it is used to evaluate the chemical interactions within the Cement–Pu(III/IV) and Cement–Pu(IV)(–ISA) systems.

Similar but slightly more reducing redox conditions with (pe + pH_c) values of -0.3 ± 0.6 were obtained in the presence of dithionate in solution. Data plotting below the lower decomposition line of water are in close agreement with previous literature data on analogous systems [40]. Dithionate ions are unstable in near neutral solutions. However, under highly alkaline, anaerobic conditions at T = 22 ± 2°C the decomposition process is known to be kinetically hindered [199, 200]. This was confirmed in the course of the present experiments, as constant strongly reducing conditions were detected in the investigated systems over the entire time-frame of the study. In this aspect, the dithionate-buffered experiments are taken as an analogous system to the Sn(II)-buffered experiments, representing strongly reducing aqueous conditions but a chemically significantly different redox buffer.

3.2.3 Cement-ISA system

Prior to the investigations on the cement-ISA system, blank samples in the absence of the ligand were analyzed to account for the leaching of organic impurities from the OPC paste and the consequent increase in the background-level of NPOC within the porewater solutions at various S:L ratios.

Figure 41 shows the background-corrected NPOC values obtained (after centrifugation) on the supernatants of the porewater samples equilibrated with the initial cement powder at S:L ratios of 0.2, 2, 4, 8, 15, 20 and 50 gdm^{-3}.

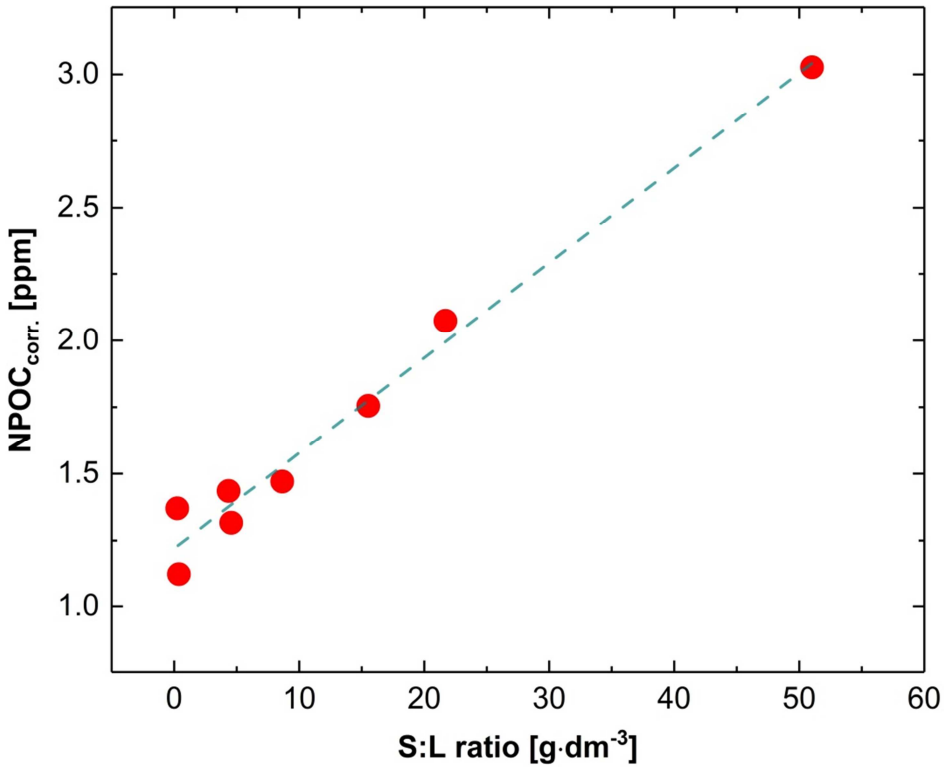

Figure 41. *Background-corrected total NPOC values measured in the centrifuged supernatant solutions of blank samples without ISA in solution prepared by mixing the porewater solution and the initial cement powder to reach S:L ratios of 0.2, 2, 4, 8, 15, 20 and 50 gdm^{-3}. The dashed blue line depicts the linear fit performed on the data set.*

Organic impurities were found to be representing a negligible amount: 1 – 3 ppm of the total NPOC values in the S:L ratio-range of 0.2 – 50 gdm^{-3}. Assuming a linear correlation between the leached organic-content and the amount of cement powder added to porewater, a fit was performed on the data set and the resulting empirical expression: Equation (72) was later applied to correct NPOC values quantified at a specific S:L ratio in the cement-ISA system under analogous conditions.

$$NPOC_{impurities}\ (ppm) = 0.036 \cdot S{:}L\ ratio\ (gdm^{-3}) + 1.22\ (ppm) \quad (72)$$

Figure 42 summarizes all results in terms of $[ISA]_{sorbed}$, calculated using Equation (18) as function of the equilibrium concentrations of ISA, with $[ISA]_{eq}$ determined from the background-corrected NPOC values acquired in the cement-ISA experiments. Figure 43

displays quantified $[ISA]_{eq}$ concentrations within the experimental series with $[ISA]_{tot} = 10^{-3}$ M as function of the S:L ratios.

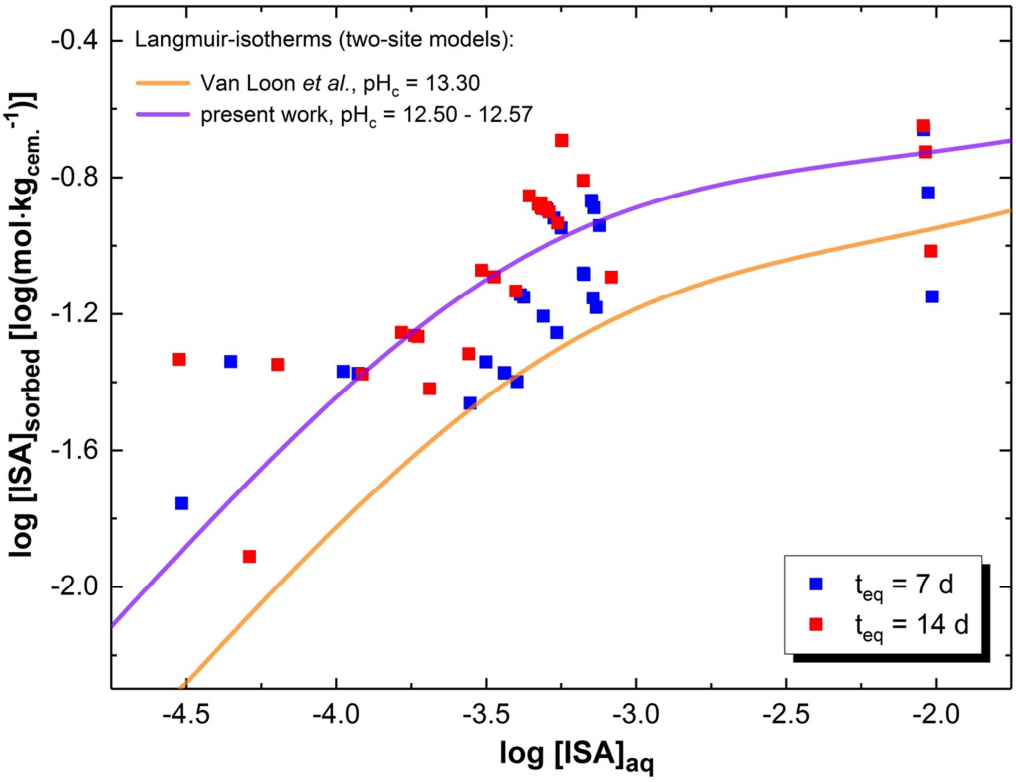

Figure 42. *Sorption isotherm of ISA on the initial OPC powder collected in porewater solutions (pH_c = 12.50 – 12.57) with $[ISA]_{tot} = 10^{-2}$, 10^{-3}, 10^{-4}, 10^{-5} M and S:L ratios of 0.2, 2, 4, 8, 15, 20 and 50 gdm^{-3} at t_{eq} = 7 (blue symbols) and 14 d (red symbols). Solid lines represent the calculated two-site Langmuir-isotherms, expressed as in Equation (19) based on: i. the model reported by Van Loon et al. [57, 84] with values from Equation (20): orange line and ii. the results from the combined fitting exercise performed in the present work on the displayed data set with values from Equation (76): purple line.*

Despite the slightly enhanced sorption of ISA at t_{eq} = 14 d, compared to the case of t_{eq} = 7 d, a definite chronological trend could not be identified within the data set as the associated uncertainties of the detected $[ISA]_{eq}$ concentrations were relatively high (~5 – 50 %, depending on the absolute value). Considering also that ISA-sorption is known to be a fast process [57, 84, 87], taking place usually within 2 days of contact-time with cement pastes, both data sets were evaluated and fitted.

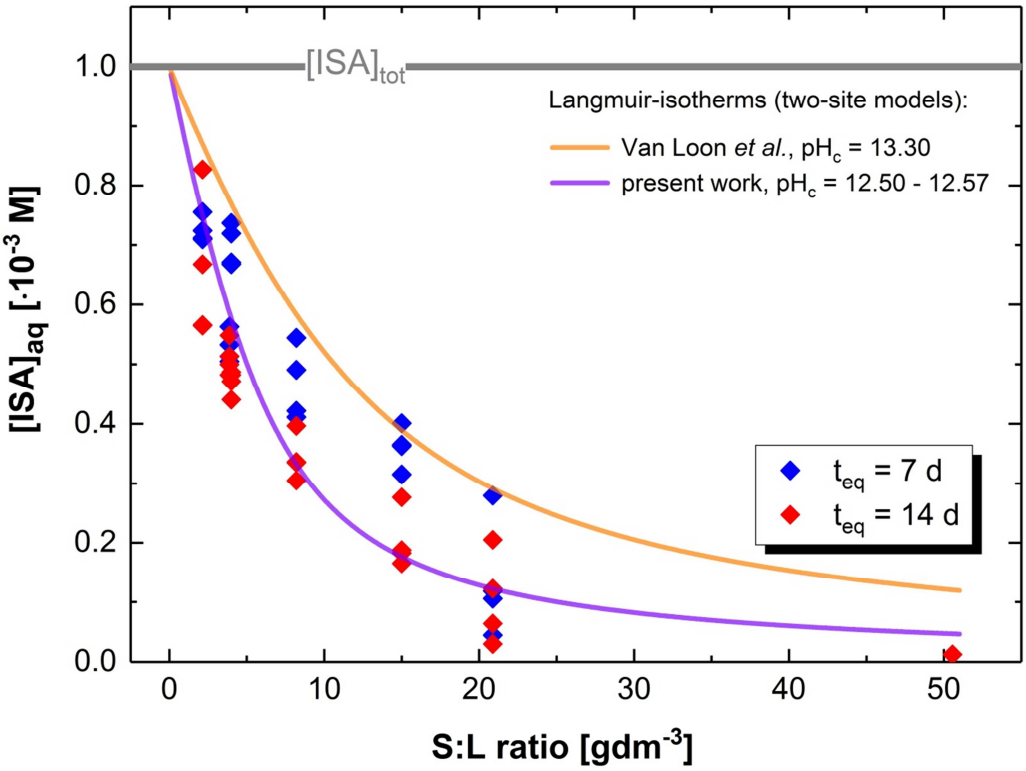

Figure 43. *Concentrations of ISA in porewater solutions (pH_c = 12.50 – 12.57) in equilibrium with the initial OPC powder at $[ISA]_{tot} = 10^{-3}$ M (grey line) and S:L ratios of 2, 4, 8, 15, 20 and 50 gdm^{-3} at t_{eq} = 7 (blue symbols) and 14 d (red symbols). Solid lines represent the calculated concentrations using the two-site Langmuir-isotherms from Equation (19), based on: (i) the model reported by Van Loon et al. [57, 84] with values from Equation (20): orange line and (ii) the results from the combined fitting exercise performed in the present work on the displayed data set with values from Equation (76): purple line.*

Sorption data on the series with constant $[ISA]_{tot} = 10^{-3}$ M, a significant decrease in $[ISA]_{eq}$ was witnessed with increasing S:L ratios, *e.g.* in the sample with 51 gdm^{-3} the determined equilibrium concentration of the ligand was found to be $5 \cdot 10^{-5}$ M. The latter value represents a high retention for ISA by HCP with R_d = 403, *i.e.* a four times larger value than as expected from the work of Pointeau *et al.* under the given conditions [87]. This demonstrates that the distribution ratios are dependent on the applied S:L ratios and furthermore, the use of a surface complexation model may not be applicable to significantly different conditions (especially taking into account the variation of available specific surface areas of the applied cement phases). The evaluation of the collected sorption data was limited to the isotherm type of representation, due to the lack of additional thermodynamic parameters related to the conditions of the present study.

The isotherm representation (Equation (19)) of the data set, (calculation of $[ISA]_{sorbed}$ from $[ISA]_{eq}$ using q_1, q_2 and K_1, K_2 parameters as in Equation (20) from values reported by Van Loon and co-workers [84], orange line in Figure 42) provides a good empirical prediction for expected $[ISA]_{eq}$ values within a wide-range of $[ISA]_{tot}$ concentrations. The expression slightly overestimates $[ISA]_{eq}$ for all the evaluated of S:L ratios (Figure 43). Also, the expression (as in Equation (19)), owing to the strong correlation between the "q" and the "K" parameters, fails to provide accurate predictions for $[ISA]_{eq}$ with regard to the variation of S:L ratios at a constant total concentration of the ligand. Since the main aim of the study was to assess the $[ISA]_{eq}$ values in the function of S:L ratios, evaluation of the data set using the Langmuir-isotherm model was executed with a slight modification. The parameter optimization procedure was performed simultaneously by the minimization of two separate objective functions expressed using Equation (73) (resulting from the combination of Equation (18) and (19)):

$$([ISA]_{tot} - [ISA]_{eq})\cdot V_L\cdot(\text{porewater, dm}^3)\cdot m(\text{cement, kg})^{-1} =$$
$$= [ISA]_{sorbed} = K_1\cdot q_1\cdot[ISA]_{eq}\cdot(1 + K_1\cdot[ISA]_{eq})^{-1} + K_2\cdot q_2\cdot[ISA]_{eq}\cdot(1 + K_2\cdot[ISA]_{eq})^{-1} \quad (73)$$

The expression above raises two possibilities for the determination of q_1, q_2 and K_1, K_2 parameters: (1) correlating measured and calculated $[ISA]_{sorbed}$ values from the Langmuir-isotherm type of representation (using only the Equation on the right hand side), just as described before or (2) correlating measured and calculated $[ISA]_{eq}$ concentrations expressed from the combination of the two equations (using both the right and the left expression within Equation (73)). The first possibility is proven to be more sensitive to the variation of the theoretical sorption capacities of the two sites, whilst option two is more prone to the variation of the adsorption affinity constants.

In Option 1, $[ISA]_{sorbed}$ values were calculated using initial input values for q_1, q_2 and K_1, K_2 parameters (values taken from Equation (20)), as provided by the original Langmuir-isotherm and the objective function (F_1), expressed as in Equation (74) was minimized in order to gain the optimized values of the parameters (given *n* number of data points).

$$F_1(q_1, q_2, K_1, K_2) = \left(\sum_{i=1}^{n}(\log [ISA]_{sorbed,calc.} - \log [ISA]_{sorbed,meas.})^2\cdot(n-1)^{-1}\right)^{0.5} \quad (74)$$

Option 2 was based on Equation (73), where $[ISA]_{eq}$ values were calculated using initial input values for q_1, q_2 and K_1, K_2 parameters in addition to the total volumes of the samples and the

applied weights of the cement powder. In this case, objective function, expressed as in Equation (75) was minimized to get the best-fit values for the given parameters:

$$F_2(q_1, q_2, K_1, K_2) = \left(\sum_{i=1}^{n} (\log [ISA]_{eq,calc.} - \log [ISA]_{eq,meas.})^2 \cdot (n-1)^{-1}\right)^{0.5} \quad (75)$$

The combined fit was executed by the simultaneous minimization of both objective functions (F_1 and F_2) on all experimental data points. The optimized sorption capacities and affinity constants of the two sorption-sites are as follows:

$$q_1 = (0.18 \pm 0.02)\ mol \cdot kg^{-1},\ K_1 = 2510 \pm 500\ dm^3 \cdot mol^{-1} \text{ and}$$
$$q_2 = (0.17 \pm 0.02)\ mol \cdot kg^{-1},\ K_2 = 12 \pm 2\ dm^3 \cdot mol^{-1} \quad (76)$$

Associated uncertainties were estimated upon the variation of the calculated and measured $[ISA]_{sorbed}$ and $[ISA]_{eq}$ values. (Depicted values exceed the associated statistical uncertainties.) Model calculations using the best-fit values are shown in Figure 42 and Figure 43 as purple solid lines. Predictions of the previously published model by Van Loon *et al.* [84] are displayed as orange solid lines for comparison.

The established Langmuir-isotherm provides good predictions in both representations with small deviations from the data points, plotting within the uncertainty-range of NPOC measurements. A one-site isotherm was also tested within the fitting procedure, however, in accordance with observation formerly made by the PSI team, the presented, two-site model appeared to be more precise, especially for high $[ISA]_{sorbed}$ values. (The application of the Freundlich-type isotherm has failed in the present case as well.)

Using the optimized parameters, the maximum uptake of the ISA ligand by the cement powder, *i.e.* the total sorption capacity, can be calculated as $q_1 + q_2 = 0.35\ mol \cdot kg^{-1}$. The latter value is in good agreement with the value of $0.27\ mol \cdot kg^{-1}$ derived from sorption studies [57, 84] and also with the estimate of $0.32\ mol \cdot kg^{-1}$ provided in the work of Bradbury and Sarott [85]. The slightly higher value obtained in the present study can be caused by many factors such as difference in specific surface area or in the chemical characteristics of the applied HCP. Furthermore, as discussed before, ISA sorption is also known to be highly influenced by pH_c conditions and the $[Ca]_{tot}$ concentration within the porewater. Pointeau *et al.* formerly showed [87] that the uptake of ISA by OPC pastes reaches a maximum at $pH_c = \sim 12.5$, thus, in comparison with the model reported by Van Loon *et al.* [57, 84], the presently observed enhanced sorption of the ligand is reasonable.

In the subsequent sections, the newly established cement-ISA sorption model (in the form of the two-site Langmuir isotherm with the best-fit parameters, as provided in Equation (76)) is used as an empirical formula to account for ISA uptake by the initial cement powder at a specific S:L ratio and $[ISA]_{tot}$ concentration.

3.2.4 Cement-Pu system

Pu sorption data for the Cement-Pu system are presented in two separate sections, according to the experimental set-up given in Section 2.4.5:

1. Screening experiments: Section 3.2.4.1, HQ-buffered systems, S:L ratio = ~0.2 gdm^{-3} – 4 gdm^{-3}, at log $[Pu]_{in}$ ~ -6 or -9, and
2. Redox experiments: Section 3.2.4.2, HQ-, Sn(II)-, dithionate-buffered systems, S:L ratio = ~0.2 gdm^{-3} and 2 gdm^{-3}, at log $[Pu]_{in}$ ~ -6 or -9).

3.2.4.1 Screening experiments

Figure 44 and Figure 45 show the total concentrations of Pu, log $[Pu]_{aq}$ in centrifuged, HQ-buffered porewater solutions in contact with the initial cement powder quantified after ultrafiltration as function of applied S:L ratios at two total Pu initial concentrations: log $[Pu]_{in}$ = -5.3 and -8.3, respectively.

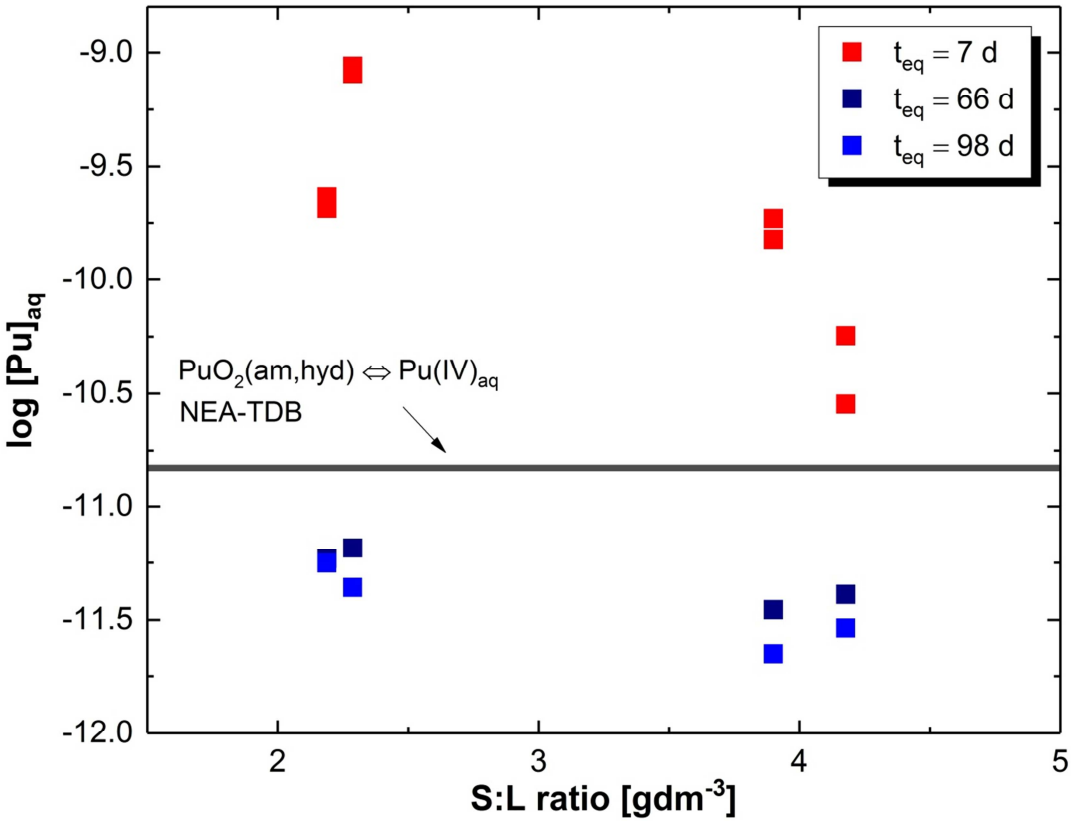

Figure 44. *Aqueous total concentrations of Pu quantified after ultrafiltration phase separation method in HQ-buffered cement powder – porewater systems at t_{eq} = 7 d (red), 66 d (dark blue) and 98 d (blue symbols) with S:L ratios of ~2 gdm^{-3} and ~4 gdm^{-3}, at the applied initial Pu concentration of log [Pu]$_{in}$ = -5.3. Solid, black line corresponds to the solubility of PuO$_2$(am,hyd) in equilibrium with Pu(IV)$_{aq}$ species calculated for porewater conditions (at pH$_c$ = 12.60) using thermodynamic data reported in NEA-TDB[9] (related calculations are adapted from a previous study [1]).*

At a high initial total concentration of Pu (log [Pu]$_{in}$ = -5.3), the detected log [Pu]$_{aq}$ values were observed to show a significant decrease after 7 days of equilibration time (Figure 45, red symbols). Concentrations quantified after t_{eq} = 66 and 98 days (blue symbols) were found to be constant and located close to the solubility of PuO$_2$(am,hyd), indicating the potential separate precipitation of Pu solid phase from the system. Taking into account the high uncertainty associated to Pu(IV) solubility and hydrolysis equilibria (± ~1.1 log [Pu]$_{tot}$), part of the results measured at t_{eq} = 7 days with S:L ratio = ~4 and all results at t_{eq} = 66 and 98 days are collectively falling in the range of Pu total concentrations expected for solubility controlled concentrations in the presence of PuO$_2$(am,hyd) solid phase in the system.

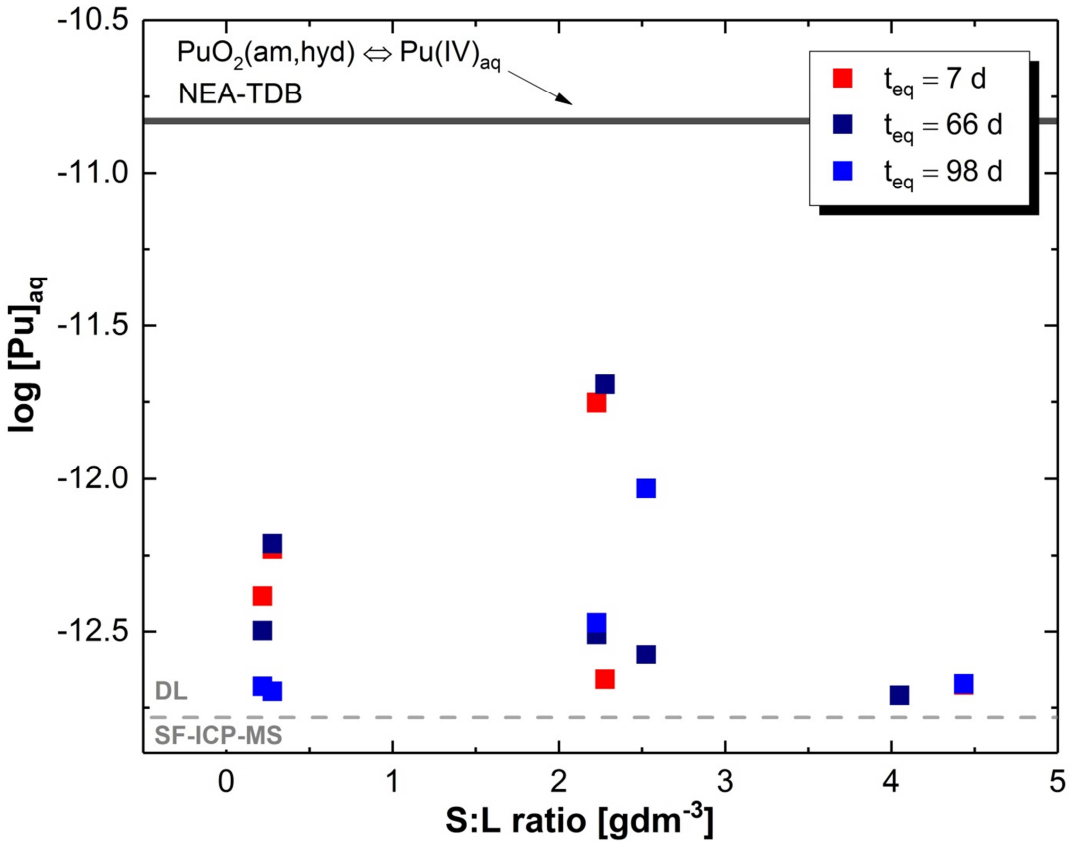

Figure 45. *Aqueous total concentrations of Pu quantified after ultrafiltration phase separation method in HQ-buffered cement powder – porewater systems at t_{eq} = 7 d (red), 66 d (dark blue) and 98 d (blue symbols) with S:L ratios of ~0.2 gdm^{-3} – ~4 gdm^{-3}, at the applied initial Pu concentration of log [Pu]$_{in}$ = -8.3. Solid, black line corresponds to the solubility of PuO$_2$(am,hyd) in equilibrium with Pu(IV)$_{aq}$ species calculated for porewater conditions (at pH$_c$ = 12.60) using thermodynamic data reported in NEA-TDB[9] (related calculations are adapted from [1]).*

Pu in the systems with the lower initial level of log [Pu]$_{in}$ = -8.3 showed steady values throughout the entire sampling period, well below the calculated solubility values expected for the presence of PuO$_2$(am,hyd). As most Pu concentrations were but slightly higher than the detection limit of SF-ICP-MS (at log [Pu]$_{tot}$ ~ -12.8), associated analytical uncertainties were rather large (usually with ± 0.5 – 1 log-units).

All sorption results transformed from concentrations to distribution ratios (R_d values calculated according to Equation (25), in dm^{3}kg^{-1} units) collected in the course of the screening experiments are shown in Figure 46.

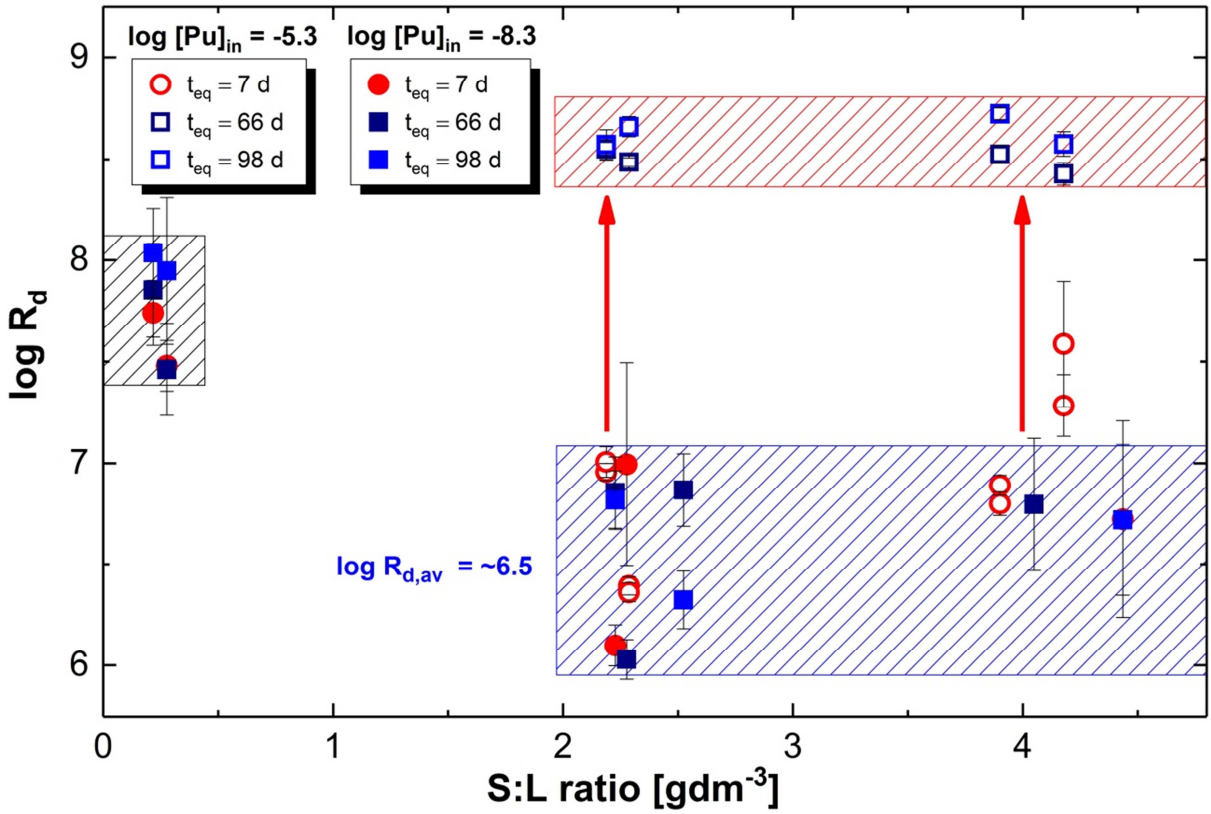

Figure 46. *Distribution ratios (R_d values, in dm^3kg^{-1} units) of Pu quantified after ultrafiltration in HQ-buffered cement powder – porewater systems at t_{eq} = 7 d (red), 66 d (dark blue) and 98 d (blue symbols) with S:L ratios of ~0.2 gdm^{-3} – ~4 gdm^{-3}, at applied initial Pu concentrations of log $[Pu]_{in}$ = -5.3 (opened symbols) and -8.3 (filled symbols). (The displayed error bars are originating only from the analytical uncertainties associated to the quantification of Pu total concentrations by SF-ICP-MS technique.)*

At the S:L ratio of ~0.2 gdm^{-3}, the determined log R_d values were generally larger by 1 – 1.5 log-units than those corresponding to the analogous systems with higher S:L ratios present. However, most results of the series at S:L ratio = ~2 and 4 gdm^{-3} with log $[Pu]_{in}$ = -5.3 at t_{eq} = 7 days and all results obtained with log $[Pu]_{in}$ = -8.3 at the higher S:L ratios applied were found to be consistent (all values are located within the blue shaded area in Figure 46), showing an approximate averaged value of log R_d (dm^3kg^{-1}) = ~6.5.

The steep decrease in concentrations detected in systems with log $[Pu]_{in}$ = -5.3 after t_{eq} = 7 days resulted in a significant shift (illustrated by the red arrows in Figure 46) for calculated log R_d values, reaching an averaged final level of log $R_{d,av}$ = ~8.5 (located within the red shaded area in Figure 46). As the $[Pu]_{aq}$ concentrations detected at these longer equilibration times within the given systems were close to the level of PuO_2(am,hyd) solubility, the latter

apparent increase in log R_d values might be caused by the precipitation of Pu solid phase from the solution.

The higher log R_d values obtained at low S:L ratios and low initial Pu-concentration are in agreement with experimental findings of previous studies on the analogous Th(IV) system [13]. As the absolute amount of the cement powder at S:L ratio ~0.2 gdm^{-3} is relatively small, distribution ratios are considered to be more sensitive to factors such as the non-negligible sorption of Pu(IV) onto the walls of the sample vials or uncertainties in the homogeneity of the weighed amount of cement powder. In this respect, determined log R_d values related to low S:L ratios generally feature rather high uncertainties and may as a consequence also be strongly overestimated.

3.2.4.2 Redox experiments

Figure 47 and Figure 48 show the total concentrations of Pu in centrifuged, HQ- Sn(II)- and dithionate-buffered porewater solutions in contact with the initial cement powder at various S:L ratios (~0.2 or ~2 gdm^{-3}) with log $[Pu]_{in}$ = -5.8 and -8.5, respectively. Data were quantified at $t_{eq} \leq 108$ days using ultrafiltration (UF) and/or ultracentrifugation (UC) phase separation methods.

The detected $[Pu]_{aq}$ concentrations in HQ-buffered systems were in accordance with the analogous system (at log $[Pu]_{in}$ = -5.3) of the screening experiments, indicating the possible presence of PuO_2(am,hyd) solid phase and the solubility controlled Pu total concentrations in solution. Regardless of the different redox-buffering agents used, all values are located at the same concentration level. This suggests the predominance of the $Pu(IV)_s$ solid phase even under the strongly reducing conditions imposed by Sn(II) and dithionate in solution. Pu total concentrations of the latter samples are in excellent agreement with those of the previous solubility study (conducted in the absence of ISA [1], see Figure 7), where identical values were determined under the redox control by Sn(II) at pH_c = ~12.9 in NaCl media. This however, does not exclude the potential formation of $Pu(III)_{aq}$ species in the course of the sorption experiments, since Pu L_{III}-edge XANES results indicated the presence of $Pu(III)_s$ in the solid phases retrieved from the undersaturation solubility experiments.

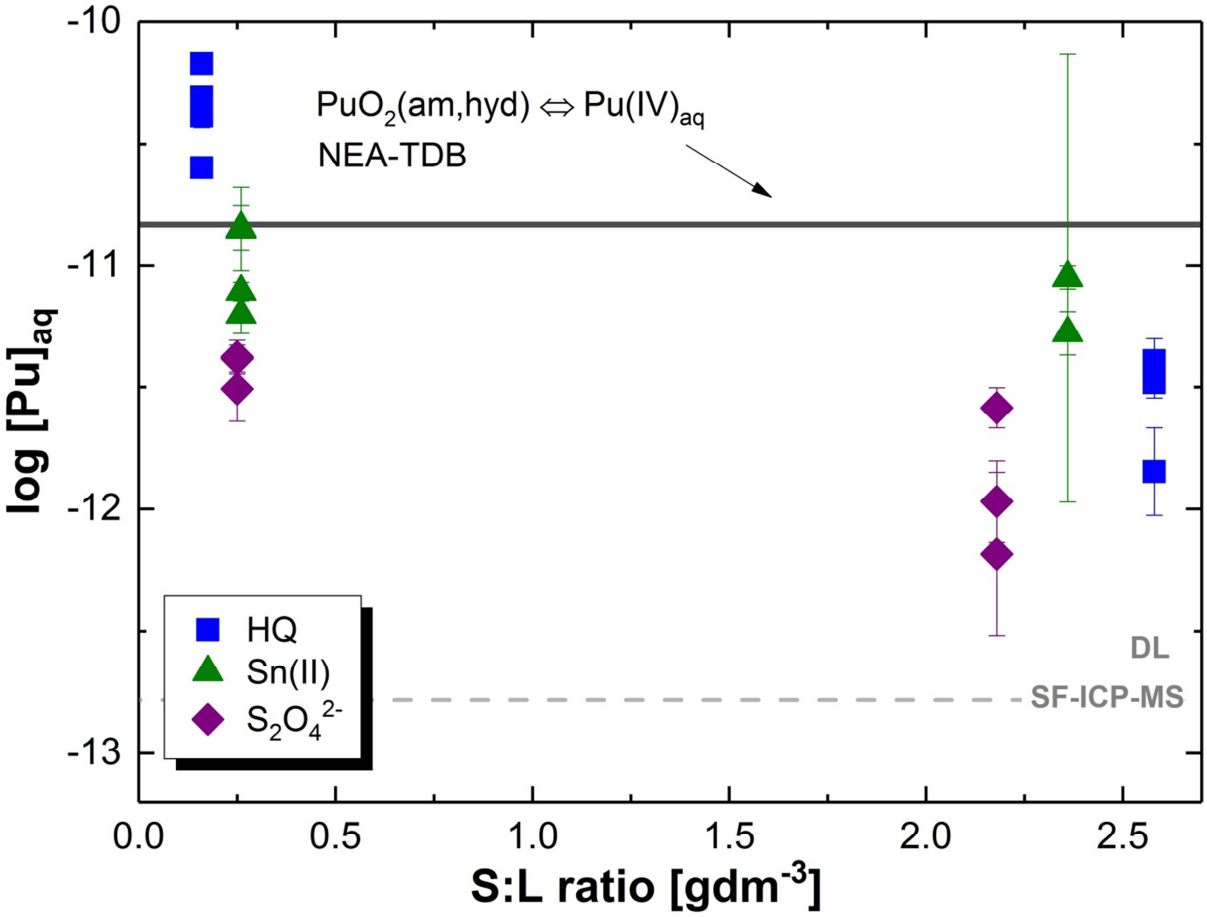

Figure 47. *Aqueous total concentrations of Pu quantified after ultrafiltration or ultracentrifugation phase separation methods in HQ- (blue), Sn(II)- (green) or dithionate-buffered (purple symbols) cement powder – porewater systems with $t_{eq} \leq 108$ d at S:L ratios of ~0.2 gdm^{-3} and ~2 gdm^{-3} and initial Pu concentration of log $[Pu]_{in}$ = -5.8. Solid, black line corresponds to the solubility of PuO_2(am,hyd) in equilibrium with $Pu(IV)_{aq}$ species calculated for porewater conditions (at pH_c = 12.60) using thermodynamic data reported in NEA-TDB [9] (related calculations are adapted from [1]). (The error bars are originating from the analytical uncertainties associated to the quantification of Pu total concentrations by SF-ICP-MS).*

To assess Pu precipitation and the Pu redox stages in the systems with high initial Pu total concentration (log $[Pu]_{in}$ = -5.3), equilibrated hydrated cement pastes at t_{eq} = 132 days were retrieved from samples with S:L ratio = 0.2 gdm^{-3} and characterized *in-situ* by means of XANES analysis (for Sn(II) and HQ-buffered systems) and in the form of dried powders (without hydration stoppage) by XPS (for the HQ-buffered sample). Solid phase characterization is summarized in Section 3.2.4.3.

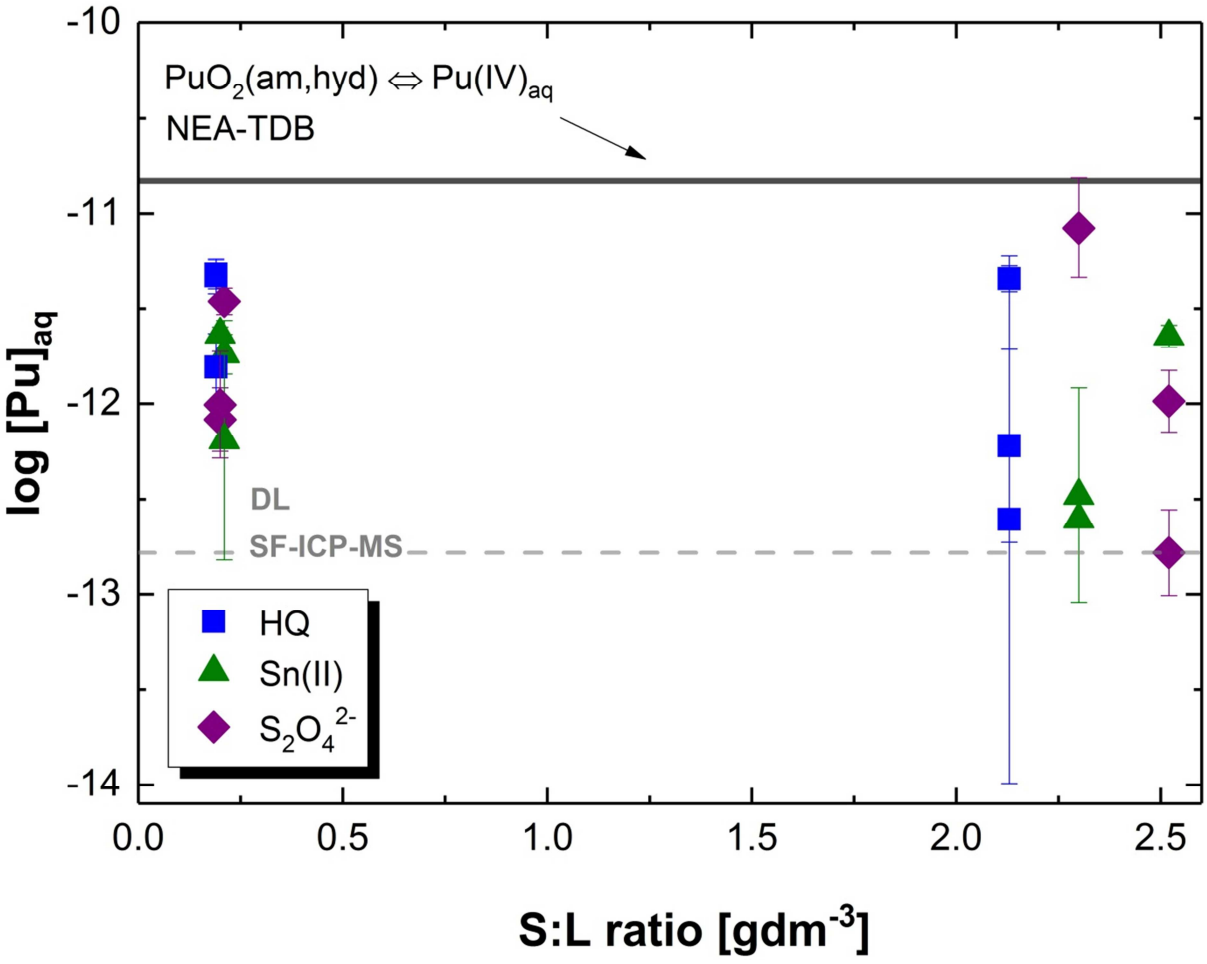

Figure 48. *Aqueous total concentrations of Pu quantified after ultrafiltration or ultracentrifugation in HQ- (blue), Sn(II)- (green) or dithionate-buffered (purple symbols) cement powder – porewater systems with* $t_{eq} \leq 108$ *d at S:L ratios of ~0.2 gdm*$^{-3}$ *and ~2 gdm*$^{-3}$ *and initial Pu concentration of log* $[Pu]_{in} = -8.5$*. Solid, black line corresponds to the solubility of* PuO_2*(am,hyd) in equilibrium with* $Pu(IV)_{aq}$ *species calculated for porewater conditions (at* $pH_c = 12.60$*) using thermodynamic data reported in NEA-TDB[9] (related calculations are adapted from [1]). (The displayed error bars are originating only from the analytical uncertainties associated to the quantification of Pu total concentrations by SF-ICP-MS).*

All Pu total aqueous concentrations quantified in systems with log $[Pu]_{in}$ = -8.5 were showing low values within the entire time-frame of the sampling period (see Figure 48), which is in close agreement with the results of the analogous HQ-buffered system from the experimental screening series (at least for the series with 2 gdm^{-3} S:L ratio). Different results in the two redox-buffered systems was again not observed, suggesting either, that: (i) the sorption of

$Pu(III)_{aq}$ species onto the cement phase are indistinguishable from the case of $Pu(IV)_{aq}$, or (ii) that the contribution of $Pu(III)_{aq}$ species are negligible compared to total Pu concentration in solution. As the Pu concentrations in the present case are close to the detection limit of SF-ICP-MS (mostly below the solubility level of $Pu(IV)_s$ expected under porewater conditions, see black line in Figure 48), associated uncertainties are significant and likely exceeding the displayed analytical uncertainties as shown in Figure 48. In this respect, any of the two above listed hypotheses can be neither denied nor confirmed. Thus, considering the sorption results collected in the HQ-buffered systems, all data of the present series are treated equally to represent the uptake of $Pu(IV)_{aq}$ by the present HCP.

The sorption results obtained within the above described redox experiments, transformed from concentrations to distribution ratios (R_d values calculated according to Equation (25), in dm^3kg^{-1} units) are presented in Figure 49.

The trends observed in the derived distribution ratios are consistent with the results of the screening experiments. All experimental results provide Pu aqueous concentrations located close to or below expected solubility limits with regard to PuO_2(am,hyd). At higher initial concentration of Pu, precipitation of the solid phase is considered to be more probable, which then determines aqueous Pu concentrations. In those studies with lower $\log [Pu]_{in}$, solution concentrations for Pu lie significantly below the solubility line. Assuming that Pu surface sorption dominates in the latter systems and that no PuO_2(am,hyd) forms, an estimate for the distribution coefficient for Pu between aqueous solution and HCP can be derived, as expressed in Equation (77).

$$\log R_{d,in} \, (dm^3kg^{-1}) = (6.3 \pm 0.6) \qquad (77)$$

This value together with the high associated uncertainty accounting for the variation of the determined R_d values collected at different S:L ratios, considering especially $[Pu]_{aq}$ concentrations detected on or close to the detection limit of SF-ICP-MS. Results of the screening experiments at S:L ratio = 0.2 gdm^{-3} with the largest observed deviations were omitted from the evaluation process.

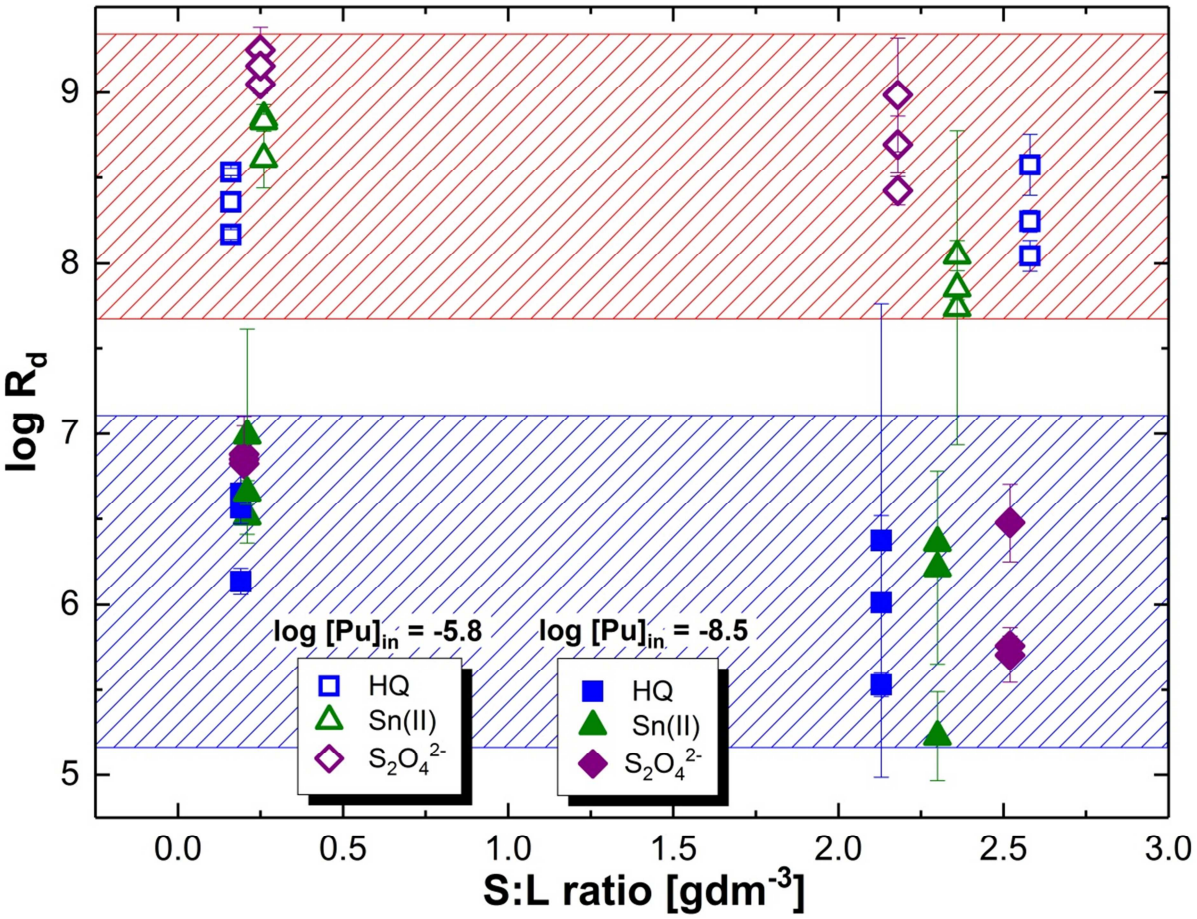

Figure 49. *Distribution ratios (R_d values, in dm^3kg^{-1} units) of Pu quantified after ultrafiltration or ultracentrifugation in HQ- (blue), Sn(II)- (green) or dithionate-buffered (purple symbols) with $t_{eq} \leq 108$ d at S:L ratios of ~0.2 gdm^{-3} and ~2 gdm^{-3} with initial Pu concentration of log $[Pu]_{in}$ = -5.8 (opened symbols) or -8.5 (filled symbols). (The displayed error bars are originating solely from the analytical uncertainties associated to the quantification of Pu total concentrations by SF-ICP-MS).*

The value of log $R_{d,in}$ (dm^3kg^{-1}) = (6.3 ± 0.6) determined in this work is larger than the average log R_d calculated from data reported in the literature for An(IV) (log R_d (dm^3kg^{-1}) ≈ 5, see Section 1.3.4.1 in the Introduction). Such discrepancy may support the hypothesis that the value of log $R_{d,in}$ (dm^3kg^{-1}) determined in the present work might be impacted by solubility phenomena and thus (slightly) overestimated. Nevertheless, a final conclusion cannot be deduced at this point, since certain available literature data (Baston *et al.* [120] with log R_d = ~6.1 – ~6.8) also provided experimentally similar values for the case of Pu under analogous conditions.

3.2.4.3 Solid phase characterization in cement-Pu systems

The *in-situ* Pu L_{III}–edge XANES spectra collected for the hydrated cement pastes recovered from HQ and Sn(II)-buffered cement-Pu sorption experiments with S:L ratio = 0.2 gdm^{-3} and log $[Pu]_{in}$ = -5.8 at t_{eq} = 132 days are shown in Figure 53 (Section 3.2.5.2). The figure also includes Pu reference spectra reported by Brendebach *et al.* [140] for aqueous Pu(III) and Pu(IV) species acquired under acidic conditions and the spectra collected on the PuO_2(IV)(ncr,hyd) solid phase, as taken from a previous study (provided in 3.1.1.1 or in [1]).

The position of the most intense energy-resonance white line (WL, listed in Table 20) of the XANES spectra collected for the HQ-buffered cement paste sample ("HQ, no ISA") is in excellent agreement with the previously reported XANES spectrum for the Pu(IV)O_2(ncr,hyd) solid phase [1]. The spectral features (WL position, post-edge resonances) of the Pu(IV) XANES reference spectrum reported by Brendebach and co-workers [140] were very close to the newly obtained spectra, indicating the predominance of Pu(IV) in the potential precipitates and/or sorbed species of Pu in the given systems. Small deviations with regard to the absorption edge energy, Δ(first inflection points) = 0.3 eV, can be caused by differences in speciation as well as by the lower signal to noise ratios of the newly recorded spectra.

A notable shift in the WL position to lower energy (≈ 1.0 eV) was observed for Pu present in the Sn(II)-buffered cement sample ("Sn(II), no ISA" sample in Figure 53), which is found to be beyond the typical energy calibration error margin (≈ 0.5 eV). This unambiguously shows the presence of Pu(III) in the system. Considering the high initial concentration of Pu (with log $[Pu]_{in}$ = -5.8) applied in the sample, and the detected $[Pu]_{aq}$ concentrations matching the level of analogous undersaturation Pu solubility experiments, the presence of a PuO_2(am,hyd) solid phase with a similar $Pu(III)_s$ contribution of ~30% as formerly determined under identical conditions (see Section 3.1.1.4) [1] seems possible.

The X-ray photoelectron spectrum of the dried, HQ-buffered cement powder at t_{eq} = 132 days (retrieved from batch sorption experiment with S:L ratio = 0.2 gdm^{-3} and log $[Pu]_{in}$ = -5.8) is displayed with regard to the Pu 4f photoemission peak in Figure 50.

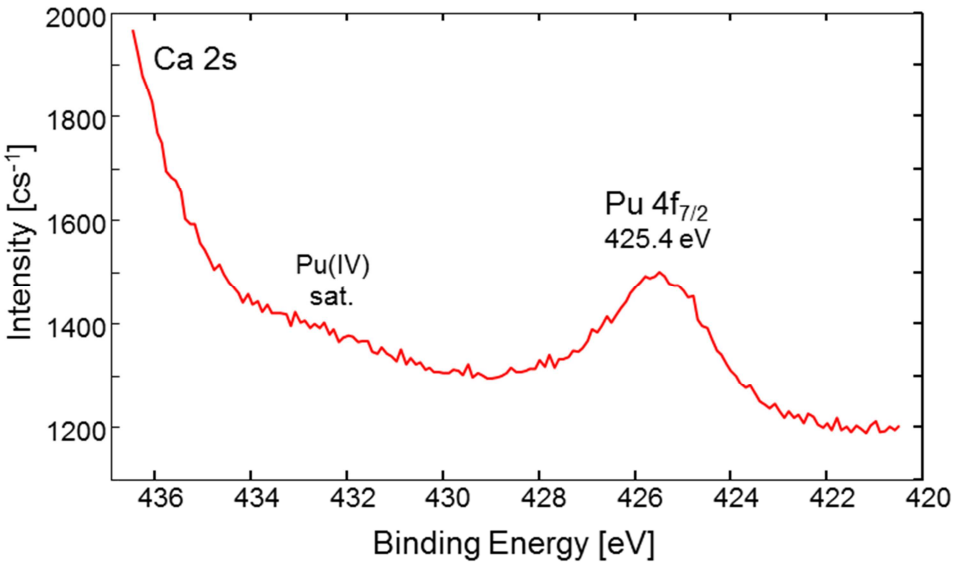

Figure 50. *XPS narrow scan of the Pu $4f_{7/2}$ elemental line of the dried cement powder sample retrieved from cement-Pu sorption experiment at t_{eq} = 132 days with S:L ratio = 0.2 gdm^{-3} and log $[Pu]_{in}$ = -5.8.*

The observed binding energy of the Pu $4f_{7/2}$ elemental line at about 425.4 eV is located between the reference values of Pu_2O_3 (424.7 eV) and the previously reported value of 426.2 eV determined for the PuO_2(ncr,hyd) solid phase equilibrated under analogous conditions in the course of the former solubility study [1]. The detected binding energy is also in moderate agreement with other literature values ranging from 425.0 eV to 426.7 eV for PuO_2 solid phases [170-172]. A weak-intensity satellite, characteristic for PuO_2 is observed at approximately 6.7 eV higher binding energy than the Pu $4f_{7/2}$ main line. This energy-difference between the main line and the satellite is found to be in agreement with data previously reported for PuO_2(cr) [170]. Relative intensity ratios for the two signals however, could not be determined, since the satellite appears to be superimposed by the Ca 2s elemental line. The lower binding energy for the Pu $4f_{7/2}$ elemental line is possibly originating from the presence of sorbed Pu(IV) species, neighboring an atom with lower Pauling's electronegativity (potentially Ca).

Combining all evidence, it can be clearly concluded that the Pu concentrations in the sorption experiments performed at high initial Pu concentrations (log $[Pu]_{in}$ = -5.8) are solubility controlled. The dominant presence of Pu(IV) species in the retrieved solid phases confirms the complete reduction of Pu(VI) to Pu(IV) in the course of sample equilibration. Information

obtained by solid phase characterization methods additionally show that Pu(IV) is partly bound to the surface of solid cement phases in the investigated systems.

3.2.5 Cement-Pu-ISA system

Sorption results for the Cement-Pu-ISA system are presented in three separate sections in accordance with the experimental details:

1. *0.2 gdm^{-3} S:L series* (Section 3.2.5.1, HQ-, Sn(II)- or dithionate-buffered systems with S:L ratio = ~0.2 gdm^{-3} and $[ISA]_{tot}$ = 10^{-3} or 10^{-2} M at log $[Pu]_{in}$ ~ -6 or -9)
2. *2 gdm^{-3} S:L series* (Section 3.2.5.4, HQ- or dithionate-buffered systems with S:L ratio = ~2 gdm^{-3} and $[ISA]_{tot}$ = 10^{-3} or 10^{-2} M at log $[Pu]_{in}$ ~ -6 or -9)
3. *0.2 – 50 gdm^{-3} S:L series* (Section 3.2.5.5, HQ- or dithionate-buffered systems with S:L ratio = ~0.2 – 50 gdm^{-3} and $[ISA]_{tot}$ = 10^{-3} or 10^{-2} M at log $[Pu]_{in}$ ~ -6).

3.2.5.1 Experiments at 0.2 gdm^{-3} S:L ratio

Figure 51 and Figure 52 show the total concentrations of Pu in centrifuged, HQ- Sn(II)- and dithionate-buffered porewater solutions in contact with the initial cement powder quantified at $t_{eq} \leq 109$ days. Data are measured directly in the supernatant solution or after ultrafiltration (UF) / ultracentrifugation (UC) as a function of $[ISA]_{tot}$ (10^{-3} and 10^{-2} M) at S:L ratio = 0.2 gdm^{-3} using two total Pu initial concentrations log $[Pu]_{in}$ = -5.8 and -8.5, respectively. The figures also include the solubility curve of PuO_2(ncr,hyd) under the given porewater conditions in the presence of ISA and Ca(II) in solution. Calculations were done as in the course of the solubility study (see Section 3.1 and references [1, 2] for more details) considering experimentally measured parameters (pH_c = 12.60, $[Ca]_{tot}$ = 0.02 M, with SIT formalism) and the Ca^{2+}–Pu^{3+}–Pu^{4+}–OH^-–Cl^-–ISA^-–H_2O(l) thermodynamic data (listed in Table 12, Table 13, Table 16 and Table 17, together with the auxiliary thermodynamic data in Table A1 and Table A2 of the Appendix).

Regardless of the phase separation method applied, detected Pu concentrations in solutions were in good agreement for each analyzed sample at a given contact time. Furthermore, concentrations measured in the supernatants were matching roughly the data quantified after UF or UC methods, indicating the insignificant impact of “Pu(IV)-ISA” colloids under these conditions. This observation is in line with previous experimental findings of the solubility

study conducted in the presence of Ca(II) ions in solution (see Section 3.1.3.2 for further details).

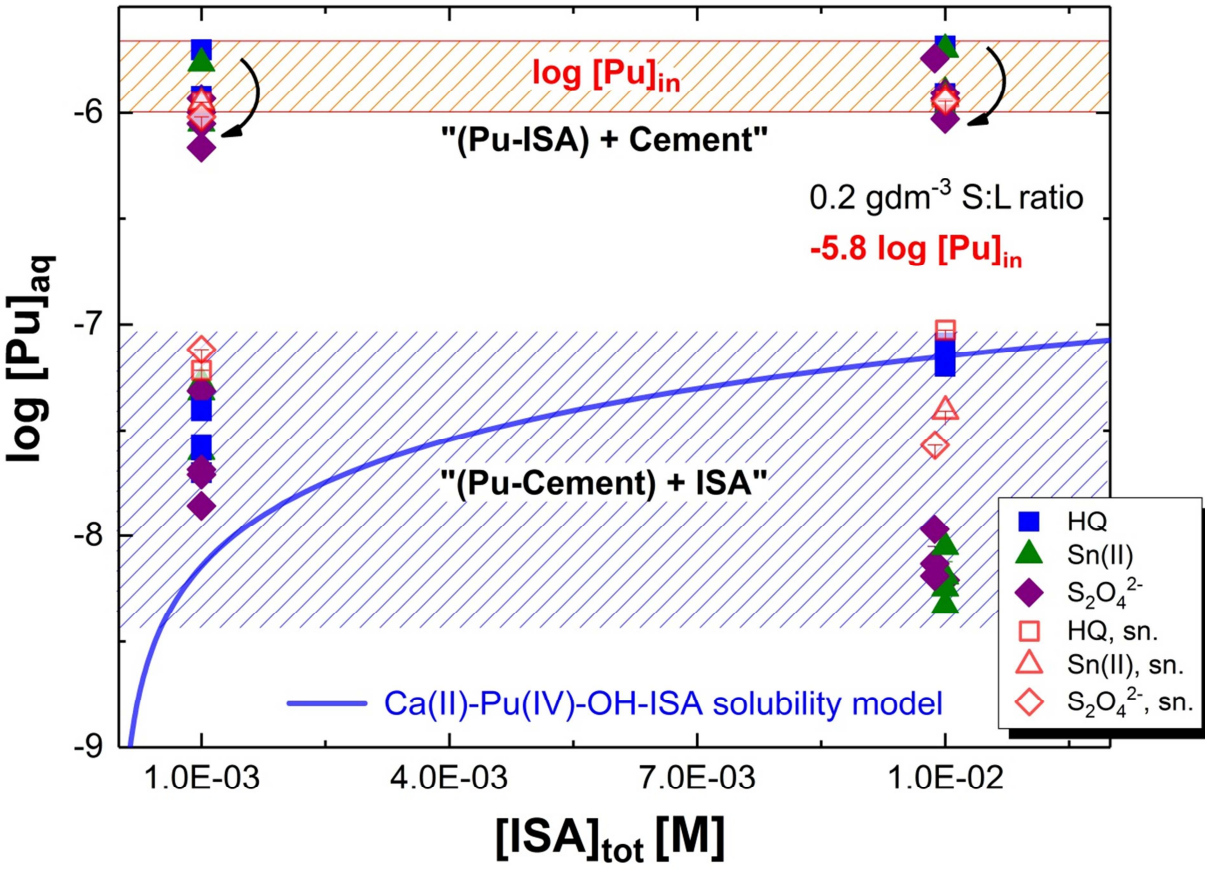

Figure 51. *Aqueous total concentrations of Pu in HQ- (blue), Sn(II)- (green) or dithionate-buffered (purple symbols) cement powder – porewater systems with $t_{eq} \leq 109$ d at S:L ratio of 0.2 gdm^{-3} and $[ISA]_{tot} = 10^{-3}$ or 10^{-2} M with initial Pu concentration of log $[Pu]_{in}$ = -5.8. Concentrations were quantified either without any phase separation method applied (directly in the supernatant solutions, opened symbols) or after ultrafiltration / ultracentrifugation methods (filled symbols). Values located within the blue shaded area correspond to experiments prepared in the "(Pu + Cement) + ISA" order, whilst the rest of the experiments were conducted following the "(Pu + ISA) + Cement" order. Solid, blue line corresponds to the solubility of PuO_2(ncr,hyd) under porewater conditions in the presence of ISA and Ca(II) calculated analogously as in Section 3.1 applying SIT formalism (see text for details).*

In the sorption data with high initial concentration of Pu, log $[Pu]_{in}$ = -5.8, significant deviations were identified with regard to the different sequence of addition in sample preparation. The $[Pu]_{aq}$ values collected in experiments following the "(Pu + ISA) + cement"

experimental preparation order (meaning Pu and ISA were put together in a first step and only later contacted with cement) were found to be located closely to the initially introduced concentration values after t_{eq} = 109 days (the latter data lie close to the red shaded area of Figure 51), depicting a transient state with concentrations higher than the predicted solubility level for the related Ca(II)-Pu(IV)-OH-ISA system. Nonetheless, a slightly decreasing tendency in Pu concentration was observed as function of allowed equilibration time, indicating a potentially hindered slow formation of a $Pu(IV)O_2$(am,hyd) precipitate in the system.

In selected samples with high initial Pu total concentration: $\log [Pu]_{in}$ = -5.3 equilibrated hydrated cement pastes at t_{eq} = 130 days were retrieved from samples with S:L ratio = 0.2 gdm^{-3} with $[ISA]_{tot} = 10^{-2}$ M and characterized *in-situ* by means of Pu L_{III}-edge XANES analysis (for Sn(II) and HQ-buffered systems). Solid phase characterization results are detailed in Section 3.2.5.2.

All Pu aqueous concentrations measured in the "(Pu + cement) + ISA" batch experiments were in moderate agreement with the expected solubility for the Ca(II)-Pu(IV)-OH-ISA system taking into account also the uncertainties of the model. The latter data set demonstrates that at the high applied $\log [Pu]_{in}$ = -5.8, just as in the analogous binary cement-Pu sorption investigations, the main chemical equilibria controlling the total concentration of Pu in the experiments is the solubility of the PuO_2(am,hyd) solid phase. Hence, under these conditions the effect of sorption processes on $[Pu]_{aq}$ concentrations cannot be analyzed.

Results of the sorption studies conducted at lower, $\log [Pu]_{in}$ = -8.5 concentration (see Figure 52), show no dependence on the experimental preparation order and all $[Pu]_{aq}$ values are near to the initially introduced Pu concentration level. In comparison with the concentrations measured in the absence of ISA under analogous conditions (shown as solid black line in Figure 52, calculated using $\log R_{d,in}$ = 6.3 at S:L = 0.2 gdm^{-3}), the present data set shows a significant sorption reduction effect for ISA.

In view of these experimental observations a simplified sorption model was derived, in order to model the effect of the ISA ligand on the uptake of Pu by HCP. The final aim was to predict variations in $[Pu]_{aq}$ concentrations as the function of ISA total concentrations and S:L ratios, considering also the sorption of the ISA ligand onto the cement paste. Details on the model together with the list of the required assumptions are provided in Section 3.2.5.3.

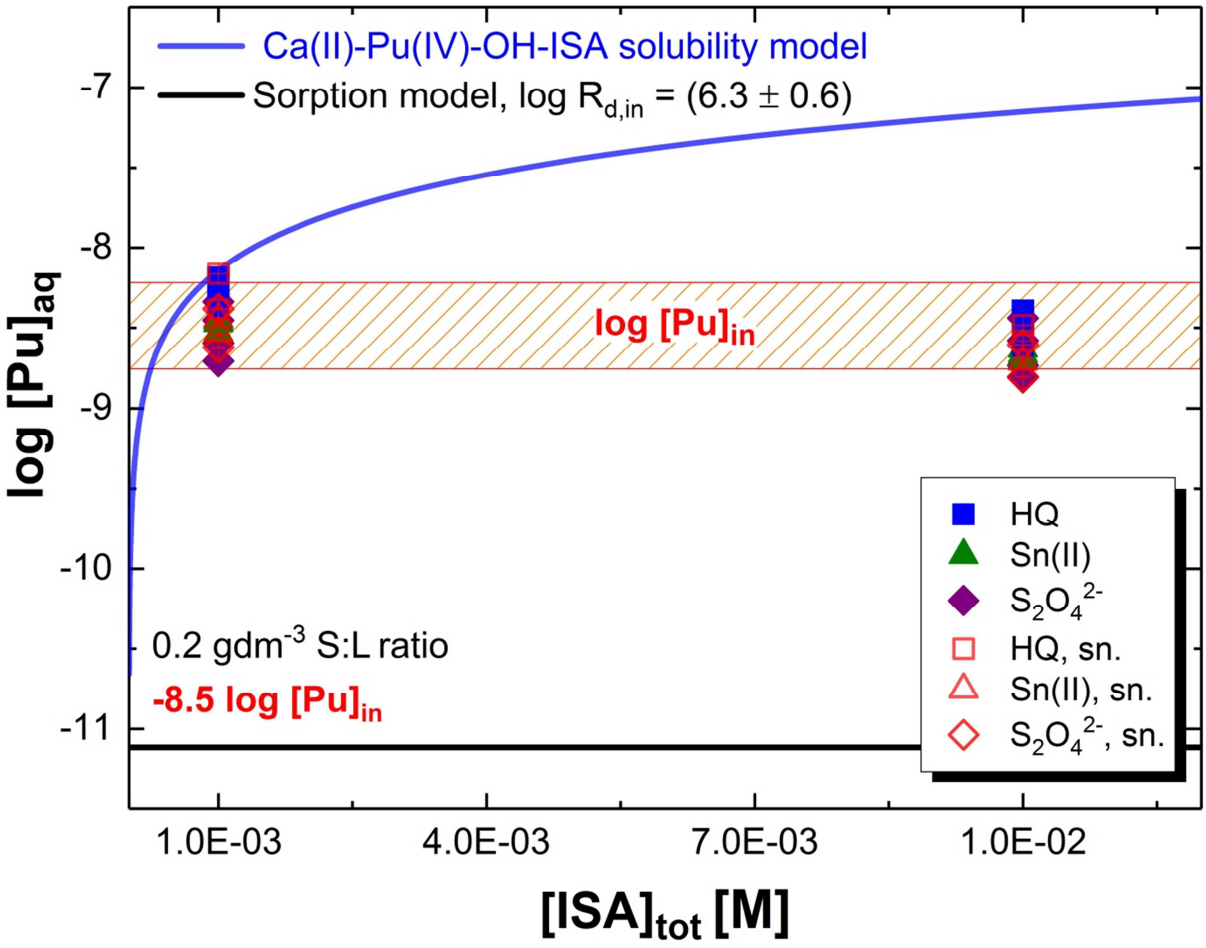

Figure 52. *Aqueous total concentrations of Pu in HQ- (blue), Sn(II)- (green) or dithionate-buffered (purple symbols) cement powder – porewater systems with $t_{eq} \leq 109$ d at S:L ratios of 0.2 gdm^{-3} and $[ISA]_{tot} = 10^{-3}$ or 10^{-2} M with initial Pu concentration of log $[Pu]_{in}$ = -8.5. Concentrations were quantified either without any phase separation method applied (directly in the supernatant solutions, opened symbols) or after ultrafiltration / ultracentrifugation methods (filled symbols). (Displayed data related to different experimental preparation orders, i.e.: "(Pu + cement) + ISA" or "(Pu + ISA) + cement" in the present case are indistinguishable.) Solid, blue line corresponds to the solubility of PuO_2(ncr,hyd) under porewater conditions in the presence of ISA and Ca(II) calculated analogously as in Section 3.1 applying SIT formalism (see text for details). Solid black line indicates $[Pu]_{aq}$ concentrations calculated using $\log R_{d,in} = 6.3$ at S:L = 0.2 gdm^{-3} (for the absence of ISA).*

3.2.5.2 Solid phase characterization in cement-Pu systems

Figure 53 shows the *in-situ* Pu L_{III}-edge XANES spectra of hydrated cement pastes retrieved from HQ- and Sn(II)-buffered batch sorption experiments equilibrated for 130 days in the presence of ISA ($[ISA]_{tot} = 10^{-2}$ M) under porewater conditions. Analogous data on experiments without ISA in solution are also included in the figure together with the reference spectra formerly reported by Brendebach *et al.* [140] for aqueous Pu(III) and Pu(IV) species under acidic conditions and for the PuO_2(IV)(ncr,hyd) solid phase, taken from previous study [1].

The edge energies (listed in Table 20) of the XANES spectra collected for the HQ- and Sn(II)-buffered cement paste samples ("Pu-I+C, HQ, 10^{-2} M ISA" and "Pu-C+I, Sn(II), 10^{-2} M ISA) are in excellent agreement with the analogous data of the HQ-buffered system equilibrated in the absence of ISA and also with the previously reported [1] XANES spectrum for the Pu(IV)O_2(ncr,hyd).

Small energy differences with regard to the WL positions and first inflection points are considered to be due to changes in speciation (see for instance the case of "sample H" from the work of Rothe *et al.* [169] for data on amorphous $Pu(OH)_4$ precipitate) for example caused by the possible presence of sorbed Pu(IV) species. However, taking into account the uncertainty in the energy calibration (± 0.5 eV) and the low signal to noise ratios of the newly recorded spectra, the observed deviations are negligible and unequivocally confirm the presence of $Pu(IV)_{s,aq}$ species in the system.

The almost identical results obtained in systems prepared with different experimental order of addition "(Pu + ISA) + cement" in HQ- and "(Pu + cement) + ISA" in Sn(II)-buffered samples indicate the predominance of $Pu(IV)_{s/aq}$ under both, moderate and strongly reducing conditions applied in course of the sorption study. This observation is in excellent agreement with the previous findings from undersaturation solubility experiments with PuO_2(ncr,hyd) conducted in the presence of ISA and Ca(II) (Section 3.1.2 and 3.1.3).

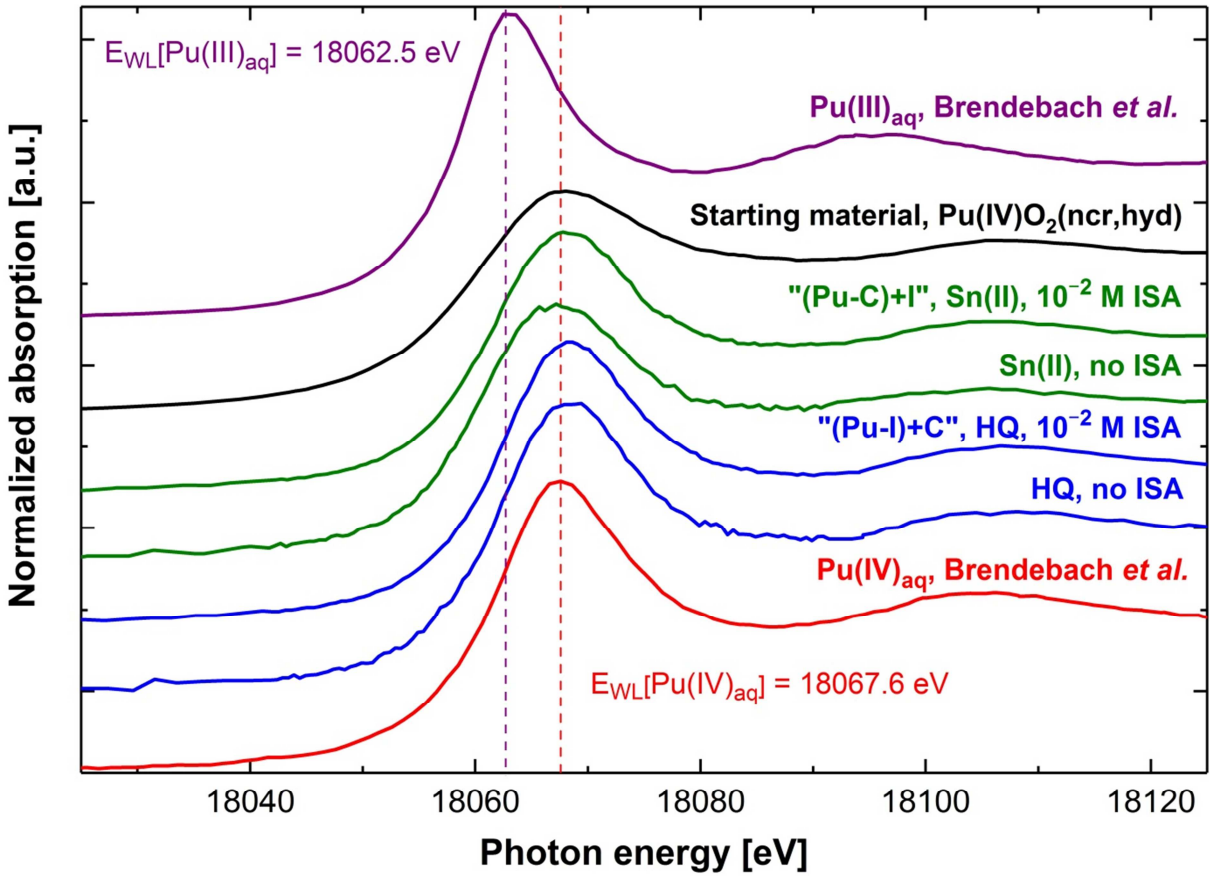

Figure 53. *In-situ Pu L_{III}–edge XANES spectra of cement pastes recovered from HQ- (blue lines) and Sn(II)-buffered (green lines) cement-Pu(-ISA) sorption experiments with S:L ratio of 0.2 gdm^{-3} and log $[Pu]_{in}$ = -5.8, equilibrated in solutions in the absence and presence of $[ISA]_{tot}$ = 10^{-2} M for ~4 months. The "(Pu-C)+I" and the "(Pu-I)+C" designates the different orders of preparation applied for the Cement-Pu-ISA sorption experiments, as "(Pu + cement) + ISA" and "(Pu + ISA) + cement", respectively. Spectra of the references for the aqueous species of Pu(III) (purple line, position of WL = 18062.5 eV) and Pu(IV) (red line, position of WL = 18067.6 eV) reported in Brendebach et al. [140] and the spectra of the formerly characterized Pu(IV)O_2(ncr,hyd) phase used for a previous solubility study adapted from [1] are shown for comparison reasons.*

Table 20. *Pu L_{III}–edge inflection points and white-line positions of the XANES spectra in Figure 53: PuO_2(ncr,hyd) solid phase used in former solubility studies [1], HCPs recovered from cement-Pu(-ISA) sorption experiments with S:L ratio of 0.2 gdm^{-3} at log $[Pu]_{in}$ = -5.8 equilibrated for ~4 months in the absence and presence of ISA (with $[ISA]_{tot} = 10^{-2}$ M) in HQ- or Sn(II)-buffered porewater solutions. The "PuC+I" and the "PuI+C" designates the different orders of preparation applied for the Cement-Pu-ISA sorption experiments, following the "(Pu + cement) + ISA" or the "(Pu + ISA) + cement" order, respectively. Reference values for $Pu(III)_{aq}$ and $Pu(IV)_{aq}$ species[140] and for $Pu(OH)_4$(am) are appended for comparison.*

Sample name	***First inflection point*‡ [eV]***	***White line (WL)* [eV]***
$Pu(IV)O_2$(ncr,hyd)	18060.3	18068.3
HQ, no ISA	18062.7	18068.3
HQ, $[ISA]_{tot} = 10^{-2}$ M, PuI+C	18062.5	18068.4
Sn(II), no ISA	18061.2	18067.3
Sn(II), $[ISA]_{tot} = 10^{-2}$ M, PuC+I	18062.1	18068.0
$Pu(III)_{aq}$ (HCl, pH = 0) [140]	18059.9	18062.5
$Pu(IV)_{aq}$ (HCl, pH = 3) [140]	18062.4	18067.6
$Pu(IV)(OH)_4$(am) (sample H) [169]	18060.5	18068.4

*Energy calibration relative to first infection point of Zr K-edge XANES assigned to 17998 eV (E 1s). Calibration error (due to DCM motor encoder step uncertainty): ± 0.5 eV.
‡Note that the position of the first inflection point is affected also by the Pu aggregation state (*i.e.*, aqua ion vs. colloidal oxy/hydroxide species or solid precipitates.

3.2.5.3 Simplified sorption model for the Cement-Pu-ISA system

Prior to setting up a simplified quantitative model to describe the sorption of Pu(IV) onto hydrated cement phases in the presence of ISA, the obtained experimental results are discussed. Considering all experimental observations derived in this study, the sorption model is bound to the following list of assumptions:

Absence of ISA:

I. The uptake of Pu(IV) by the OPC paste is a fast process involving the sorption of the $Pu(OH)_4(aq)$ species. It can be represented by a general distribution ratio, provided in Equation (77) ($logR_{d,in}$) as derived from the results of the cement-Pu sorption experiments.

Presence of ISA:

II. Sorption of ISA onto the cement paste involves different sorption sites than those for Pu (*i.e.* non-competitive sorption of ISA and Pu). Total concentration of ISA remaining in solution can be properly quantified using the two-site Langmuir-isotherm established in the present study in the form of Equation (19) with values from Equation (76).

III. The in-solution complexation reaction of $Pu(IV)_{aq}$ with ISA (and Ca(II) ions) and the sorption process of $Pu(IV)_{aq}$ onto the hydrated cement phases are the only competitive reactions governing $[Pu]_{aq}$ concentrations in solution.

IV. The aqueous complexes Pu(IV)-OH-ISA and Ca(II)-Pu(IV)-OH-ISA do not sorb on cement.

V. The thermodynamic model on the Ca(II)-Pu(IV)-OH-ISA system derived in the previous studies is applicable for the investigated porewater conditions (pH_c = 12.60; $[Ca]_{tot}$ = 0.02 M; I ~ 0.06 M). Therefore, Pu(IV) speciation calculations for the presence of ISA and Ca(II) are executed upon the experimentally determined conditions using the Ca^{2+}–Pu^{3+}–Pu^{4+}–OH^-–Cl^-–ISA^-–$H_2O(l)$ thermodynamic data (listed in Table 12, Table 13, Table 16 and Table 17, together with the auxiliary thermodynamic data in Table A1 and Table A2 of the Appendix).

The simplified sorption model, expressed in Equation (78) following the work of the PSI research team [13, 100, 103, 104] (Equation (29)) is aimed to reproduce the reduction effect of ISA on Pu(IV) sorption in a semi-empirical way by applying $logR_{d,in}$ ($\log R_{d,in}$ (dm^3kg^{-1}) =

(6.3 ± 0.6) determined in the absence of ISA and the complex formation constants for the Ca(II)-Pu(IV)-OH-ISA system as derived within the previous studies of the present work.

$$\log R_d = \log R_{d,in} - \log (1 + {}^*\beta'_{1,4,1}\cdot[ISA^-]\cdot(A\cdot[H^+]^4)^{-1} + {}^*\beta'_{1,5,1}\cdot[ISA^-]\cdot(A\cdot[H^+]^5)^{-1} + \\ + {}^*\beta'_{1,1,4,1}\cdot[ISA^-]\cdot[Ca^{2+}]\cdot(A\cdot[H^+]^4)^{-1} + {}^*\beta'_{1,1,5,1}\cdot[ISA^-]\cdot[Ca^{2+}]\cdot(A\cdot[H^+]^5)^{-1}) \quad (78)$$

The overall stability constants ${}^*\beta'_{1,4,1}$, ${}^*\beta'_{1,5,1}$ and ${}^*\beta'_{1,1,4,1}$, ${}^*\beta'_{1,1,5,1}$ are corresponding to the formation of the previously identified four (Ca(II)-)Pu(IV)-OH-ISA species, whilst the *A* term accounts for the hydrolysis equilibria of Pu(IV) at the ionic strength prevailing under porewater conditions:

$$A = 1 + {}^*\beta'_{1,4}\cdot[H^+]^{-4} \quad , \quad (79)$$

where ${}^*\beta'_{1,4}$ is the overall stability constant related to the formation of the $Pu(OH)_4(aq)$ species under the given condition.

The free proton concentration in solution was calculated from the experimentally determined pH_c = 12.60 value. The free concentrations of $Ca^{2+}$and ISA^- ions were obtained from Equation (80) and (81), respectively.

$$[Ca]_{tot} = [Ca^{2+}] + [CaOH^+] + [CaISA^+] + [CaISA_{-H}^0] + [Ca_4Pu(OH)_8^{4+}] + \\ + [CaPu(OH)_3ISA_{-H}^+] + [CaPu(OH)_3ISA_{-2H}^0] = 0.02\ M \quad (80)$$

$$[ISA]_{eq} = [ISA^-] + [CaISA^+] + [CaISA_{-H}^0] + [Pu(OH)_3ISA_{-H}^-] + [Pu(OH)_3ISA_{-2H}^{2-}] + \\ + [CaPu(OH)_3ISA_{-H}^+] + [CaPu(OH)_3ISA_{-2H}^0] \quad (81)$$

The contributions of all Pu-bearing species to the total concentrations of the ions were neglected. (Related thermodynamic constants on complementary systems: Ca(II)-OH and Ca(II)-HISA-OH were adapted from Table 1 in the present case as well.) The stability constants were corrected for the ionic strength present in porewater solutions as provided by experimental quantifications, for I = 0.06 M (NaCl) using SIT formalism with ion interaction coefficients listed in Table 17 and Table 13 and in the Appendix (Table A2). (Further details on the calculations performed are provided in previous sections.) In comparison to the Debye-Hückel term, the contribution of the binary ion interaction coefficients to the overall effect of the ionic strength correction is negligible, thus, the latter simplification (assumption of the

presence of a pure NaCl media with identical ionic strength) has only been made for the sake of consistency with the previous studies.

The $[ISA]_{eq}$ concentrations were calculated from the initially introduced total concentrations of the ligand: $[ISA]_{tot}$ using the two-site Langmuir-isotherm, in the form of Equation (19), based on the results from the combined fitting exercise performed in the present work with parameters, as provided in Equation (76).

The application of Equation (78) in combination with Equations (79 – 81), enables to evaluate the effect of ISA on the log $R_{d,in}$ value, accounting solely for the solution speciation and the free concentration of the ligand, corresponding to a certain S:L ratio and $[ISA]_{tot}$ concentration. The resulting, new log R_d value can be used to re-calculate $[Pu]_{aq}$ concentrations for the cement-Pu(IV)-ISA system under a wide-range of experimental conditions, independently of the newly collected data set.

Figure 54 shows the predictions of the simplified sorption model transformed to $[Pu]_{aq}$ concentrations in the function of $[ISA]_{tot}$ concentrations together with the analogous data set obtained at log $[Pu]_{in}$ = -8.5 and the S:L ratio = 0.2 gdm^{-3}.

At $[ISA]_{tot}$ = 10^{-3} M, a relatively large deviation was observed between the experimentally determined values and the simplified model calculations for $[Pu]_{aq}$ concentrations. For the data collected in systems with $[ISA]_{tot}$ = 10^{-2} M, the sorption model provides a reasonable agreement between the derived and the obtained concentrations. However it can be stated, as the measured $[Pu]_{aq}$ values were located close to the initially added total concentration of Pu in all cases, the simplified model predicts a lower sorption reduction effect of ISA at the given S:L ratio of 0.2 gdm^{-3}. This discrepancy can originate from different factors, such as: (i) the overestimation of log $R_{d,in}$ (related to assumption I.), (ii) from the incorrect speciation scheme applied for the Ca(II)-Pu(IV)-OH-ISA system (assumption V.), or (iii) from an unidentified effect of ISA on the sorption behavior of Pu and/or the HCP (targeting assumption II.).

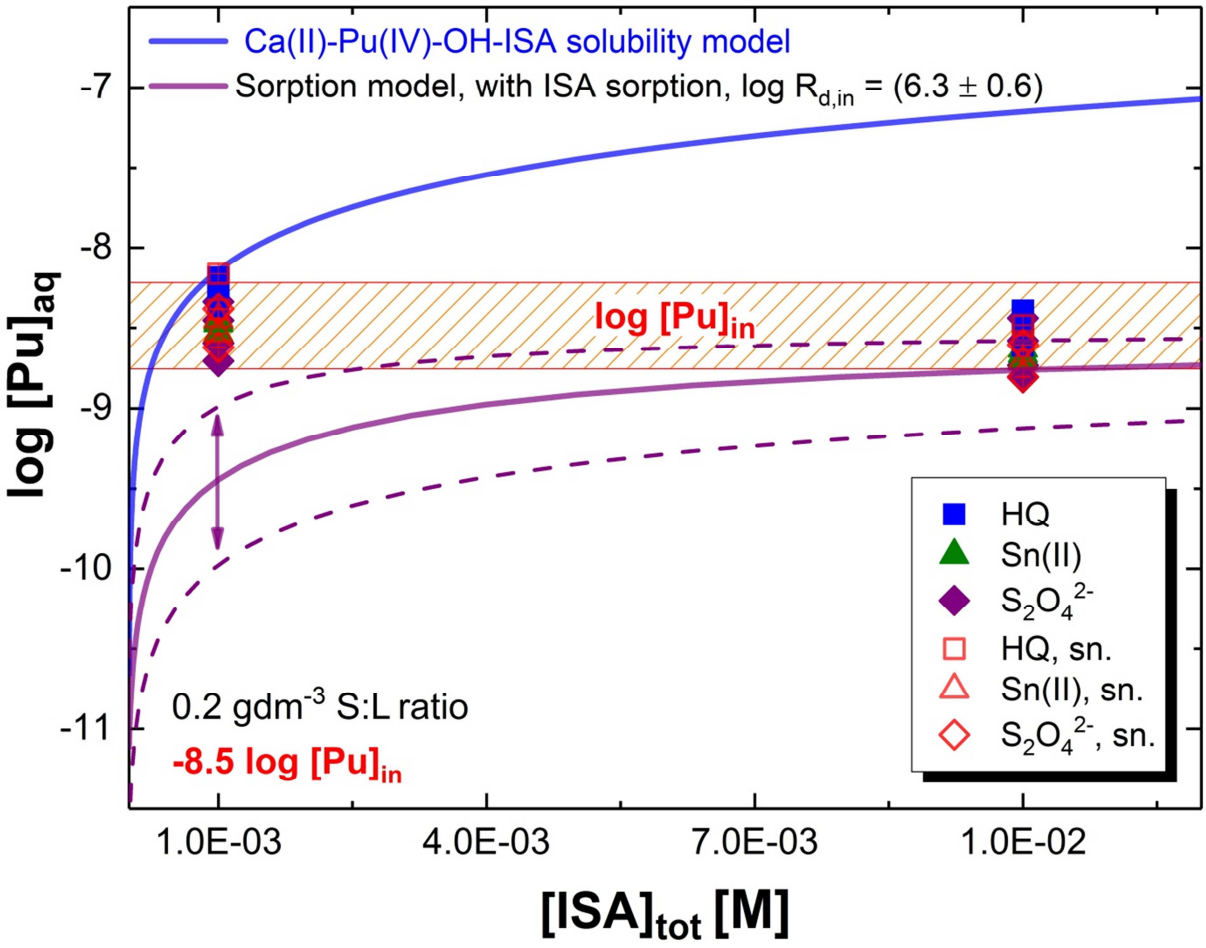

Figure 54. *Aqueous total concentrations of Pu in HQ- (blue), Sn(II)- (green) or dithionate-buffered (purple symbols) cement powder – porewater systems with $t_{eq} \leq 109$ d at S:L ratios of 0.2 gdm^{-3} and $[ISA]_{tot} = 10^{-3}$ or 10^{-2} M with initial Pu concentration of log $[Pu]_{in}$ = -8.5. Concentrations were quantified either without any phase separation method applied (directly in the supernatant solutions, opened symbols) or after ultrafiltration / ultracentrifugation methods (filled symbols). Solid lines correspond to the solubility of PuO_2(ncr,hyd) (blue) and to the simplified sorption model predictions (purple) using Equation (77) and (78) calculated for porewater conditions in the presence of ISA and Ca(II) applying SIT formalism (see text for details). The dashed purple lines reflect the uncertainty of log $R_{d,in}$.*

As it was pointed out before, in many sorption experiments with log $[Pu]_{in}$= –8.5, the existence of a solubility control could not be ruled out unequivocally. For clarification, see *e.g.* Figure 15, where the quantified Pu total concentrations in the solubility experiments ($m(Pu)_{tot}$ values at log m(ISA) = –6) considerably overlap with $[Pu]_{aq}$ values detected in the course of the latter sorption study (see Figure 48). Thus, the application of a lower intial value for the distribution coefficient of Pu (for instance: log $R_{d,in}$ = 5 as the reasonable average

value from literature data, see Section 1.3.4.1) would significantly change the predictions of the simplified model, eventually resulting in a better agreement with the collected data set. On the other hand, deviations can also be caused by the unknown impact of ISA on the sorption behavior of the system. The latter effect can be apprehended as a competitive sorption process, imposing changes in the surface properties of the hydrated cement phases (as steric, electrostatic or other effects). Indeed, differences in surface potential are undoubtly expected, given the excessive surface-coverage of the cement phases caused by the sorption of the ligand. As a consequence, the new, differing surface charge can significantly alter the properties of the HCP and could potentially prohibit / limit the uptake of Pu.

3.2.5.4 Experiments at 2 gdm^{-3} S:L ratio

Figure 55 and Figure 56 show the total concentrations of Pu, log $[Pu]_{aq}$ in centrifuged, HQ- and dithionate-buffered porewater solutions in contact with the initial cement powder quantified. Data are at $t_{eq} \leq 112$ days after ultrafiltration as function of $[ISA]_{tot}$ (10^{-3} and 10^{-2} M) at S:L ratio = 2 gdm^{-3} with two total Pu initial concentrations of log $[Pu]_{in}$ = -5.8 and -8.5, respectively. The figures also include the solubility curve of PuO_2(ncr,hyd) under porewater conditions in the presence of ISA and Ca(II) in solution (see Section 3.2.5.1 for more details). Figure 56 also shows values for $[Pu]_{aq}$ provided by the simplified sorption model, expressed in Equation (78) in the function of $[ISA]_{tot}$ concentrations under the given condition.

At log $[Pu]_{in}$ = -5.8, a significant difference was detected in Pu concentrations related to the experimental preparation order. As in the data of the previously discussed series (see Section 3.2.5.1) measured Pu concentrations in the "(Pu + ISA) + cement" samples were located significantly higher than the data for the "(Pu + cement) + ISA" system. Although a definite decrease was not observed in the data set with increasing equilibration times, the values were found to be slightly lower than the initially introduced Pu concentration level, indicating the hindered formation of a PuO_2(am,hyd) precipitate.

As in the case of 0.2 gdm^{-3} (Fig. 57) the data for the "(Pu + cement) + ISA" system at 10^{-3} M ISA show somewhat higher values as predicted by the solubility model which cannot be sufficiently explained at the moment.

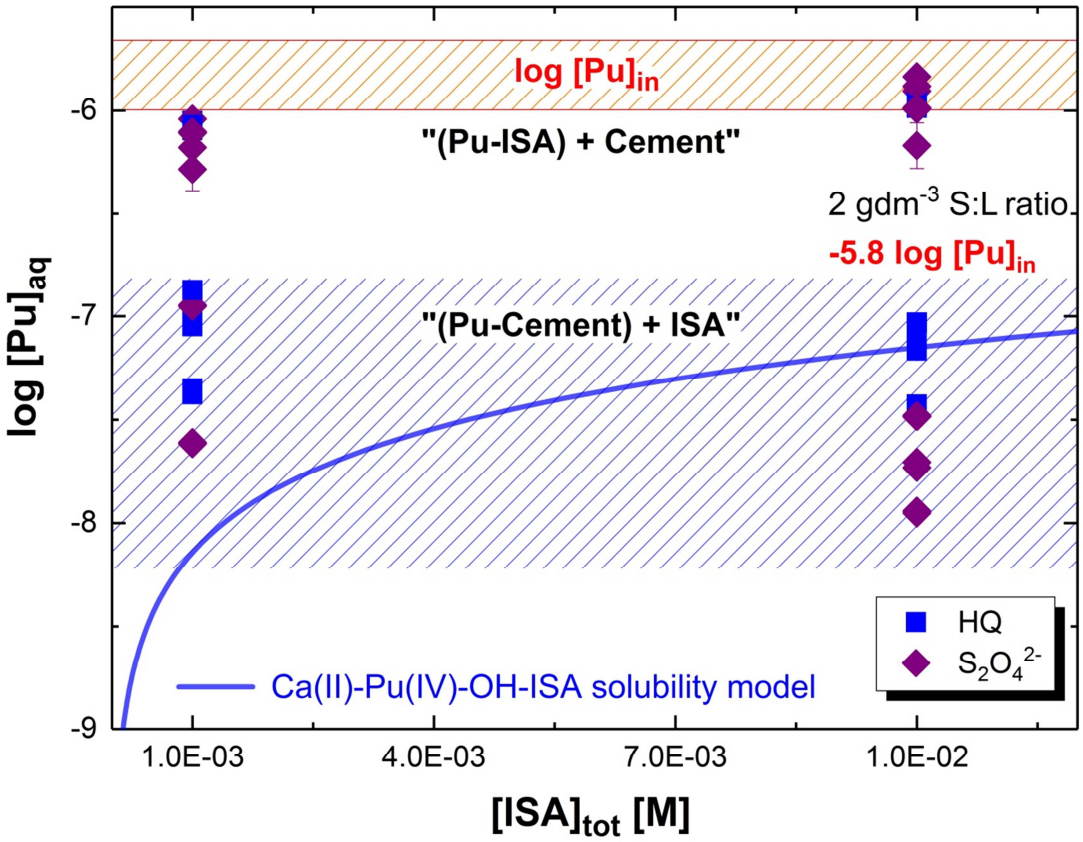

Figure 55. *Aqueous total concentrations of Pu quantified after ultrafiltration method in HQ-(blue) or dithionate-buffered (purple symbols) cement powder – porewater systems with* $t_{eq} \leq$ *112 d at S:L ratio of 2* gdm^{-3} *and* $[ISA]_{tot} = 10^{-3}$ *or* 10^{-2} *M with initial Pu concentration of* $\log [Pu]_{in} = -5.8$*. Values located within the blue shaded area correspond to experiments prepared in the "(Pu + cement) + ISA" order, whilst the rest of the experiments were conducted following the "(Pu + ISA) + cement" order. Solid, blue line corresponds to the solubility of* PuO_2*(ncr,hyd) under porewater conditions in the presence of ISA and Ca(II) calculated analogously as in Section 3.1 applying the SIT formalism (see text for details).*

For $\log [Pu]_{in} = -8.5$, the trend in the data set with time again show an unexpectedly large reduction effect of ISA on the uptake of Pu(IV) by HCP. Combining observations from Figure 54 and Figure 56, it can be stated that the simplified model in general underestimates $[Pu]_{aq}$ concentrations quantified in the experimental series at both S:L ratios 0.2 and 2 gdm^{-3}. Results indicate that the cement-Pu(IV)-ISA system cannot be precisely modelled by the combination of the chemical and thermodynamic models set up for the individual systems. As mentioned before, such deviations could potentially be caused by the overestimation of $\log R_{d,in}$ or by the competitive sorption process of the ligand onto HCP. For example, the use of a lower value for $\log R_{d,in}$ as an input would already result in a better overall prediction of the obtained

sorption data by the simplified model. Taking also into account the excessive surface-coverage of the ligand on HCP (about 50 % of the maximum ISA loading is observed at 10^{-3} – 10^{-2} M ISA), the imposed changes in the surface properties of the cement phase (steric, electrostatic or others) could be significant. However, as the discrepancies are larger at the lower total ligand concentration of log $[ISA]_{tot}$ = -3, the influence of the ISA sorption cannot be the single reason for the observed phenomena.

Considering the solubility of PuO_2(ncr,hyd) in the presence of ISA at log $[ISA]_{tot}$ = -3 under porewater conditions (blue line), the initial concentration of Pu (log $[Pu]_{in}$ = -8.5) is observed to be located close to the saturation level. This implies that for the latter experiments as well, the solubility control cannot be fully excluded. Regarding systems with log $[ISA]_{tot}$ = -2, the theoretical Pu solubility level under analogous condition, however, exceeds the introduced concentration of Pu by more than one order of magnitude. Thus, $[Pu]_{aq}$ concentrations collected in these systems are not impacted by prevailing Pu solubility equilibria. This is also in accordance with the $[Pu]_{aq}$ values quantified to be below the calculated solubility limit.

The preparation order in experiments with log $[Pu]_{in}$ = -8.5 again has no impact as observed for experiments with lower S:L ratio. A distinct difference was only observed at log $[ISA]_{tot}$ = -2. For the "(Pu + cement) + ISA" system, all aqueous Pu concentrations in porewater solutions for log $[ISA]_{tot}$ = -2 fall within the predicted range of the model, considering also the uncertainty-range related to the log $R_{d,in}$ value (dashed purple lines are indicating the variation of the model calculations with regard to parameter, as in Equation (76)). For log $[ISA]_{tot}$ = -3, the model underestimates the measured Pu concentrations by about one order of magnitude. However, it is important to highlight that the use of lower log $R_{d,ini}$ (see discussion in Sections 1.3.4.1 and 3.2.5.3) would improve the agreement of model and experimental data at log $[ISA]_{tot}$ = -3, whilst retaining the same agreement for log $[ISA]_{tot}$ = -2.

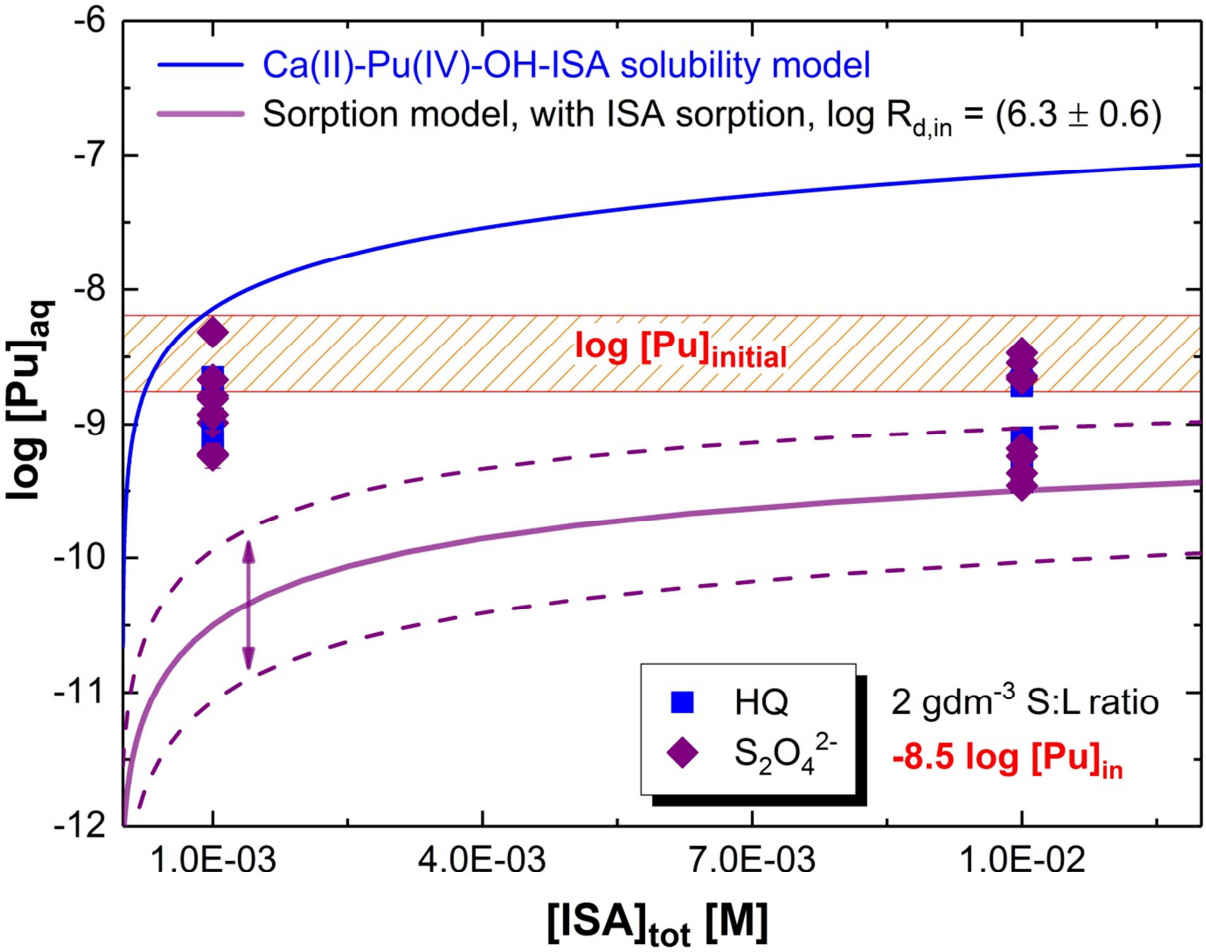

Figure 56. *Aqueous total concentrations of Pu in HQ- (blue) or dithionate-buffered (purple symbols) cement powder – porewater systems quantified after ultrafiltration method with* $t_{eq} \leq$ *112 d at S:L ratio of 2 gdm*$^{-3}$ *and* $[ISA]_{tot} = 10^{-3}$ *or* 10^{-2} *M and initial Pu concentration of* $\log [Pu]_{in} = -8.5$*. Solid lines correspond to the solubility of* PuO_2*(ncr,hyd) (blue) and to the simplified sorption model predictions (purple) using Equation (77) and (78) calculated for porewater conditions in the presence of ISA and Ca(II) applying SIT formalism (see text for details). The dashed purple lines reflect the uncertainty of log* $R_{d,in}$*.*

3.2.5.5 Experiments at 0.2 – 50 gdm^{-3} S:L ratios

Figure 57 shows aqueous total Pu concentrations in centrifuged, HQ-buffered porewater solutions at $[ISA]_{tot} = 10^{-2}$ M in contact with the initial cement powder quantified at $t_{eq} \leq 112$ days. Data after ultrafiltration as function of S:L ratio = 0.2 – 50 gdm^{-3} at the total Pu initial concentration of log $[Pu]_{in}$ = -5.8. For a better overview, data corresponding to the system prepared with the "(Pu + ISA) + cement" experimental addition order are omitted from the display as they are all located close to the initially introduced Pu concentration level. The

figure also includes the solubility curve (blue solid line) of PuO_2(ncr,hyd) under porewater conditions in the presence of ISA and Ca(II) in solution including the new cement-ISA sorption model, *i.e.* applying $[ISA]_{eq}$ concentrations (dashed green line) provided by the two-site Langmuir-isotherms from Equation (19), using the constants from Equation (76) at $[ISA]_{tot} = 10^{-2}$ M with S:L ratios = 0.2 – 50 gdm^{-3}.

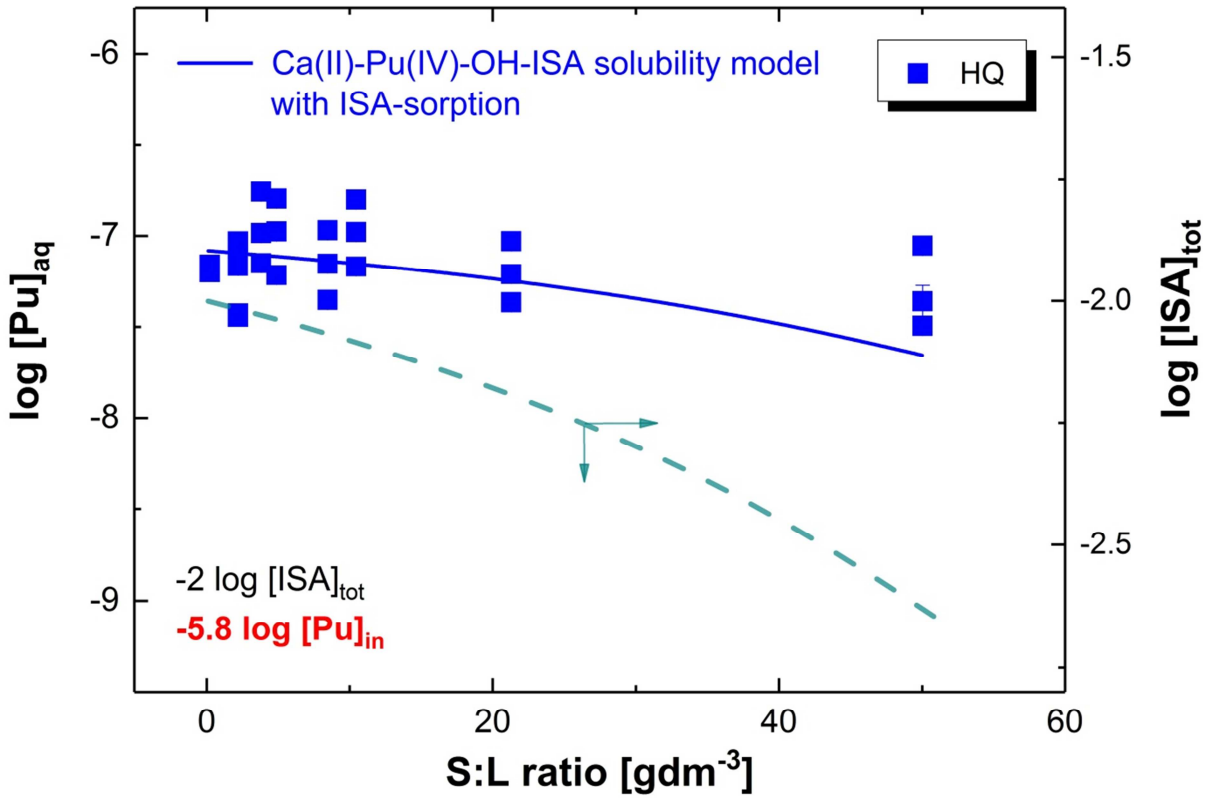

Figure 57. *Aqueous total concentrations of Pu quantified after ultrafiltration in HQ-buffered (blue symbols) cement powder – porewater systems with* $t_{eq} \leq 112$ *d at* $[ISA]_{tot} = 10^{-2}$ *M in the function of the S:L ratios: 0.2 – 50* gdm^{-3} *with initial Pu concentration of* $\log [Pu]_{in} = -5.8$. *All displayed data are collected in experiments prepared following the "(Pu + cement) + ISA" order. Solid, blue line corresponds to the solubility of* PuO_2*(ncr,hyd) under porewater conditions in the presence of ISA and Ca(II) calculated analogously as in Section 3.1 applying the SIT formalism (see text for details) and using* $[ISA]_{eq}$ *concentrations (dashed green line) accounting the sorption of ligand onto HCP (by Equation (19) with values from Equation (76)).*

In agreement with the previous findings for sorption experiments at $\log [Pu]_{in} = -5.8$, the obtained data related to the present system conducted in the "(Pu + cement) + ISA" preparation order indicate $[Pu]_{aq}$ concentrations controlled by the solubility equilibria of a

PuO_2(am,hyd) solid phase. Additionally, a decreasing trend with time was observed in the data set, which has been successfully assigned to the decrease in the equilibrium concentrations of the ligand caused by its sorption onto HCP. However, as the changes in $[ISA]_{eq}$ is not significant at $\log [ISA]_{tot} = -2$, the consequent effect, *i.e.* the decreasing ligand concentration on the Ca(II)-Pu(IV)-OH-ISA solubility is not pronounced.
All data lie within the assigned uncertainty range of the solubility model ($\sim \pm 1.0 \log [Pu]_{tot}$), indicating its extended validity-range compared to the originally set limits (with $pH_m < 12.4$).

3.2.5.6 Complementary experiments

The complementary experiments consisted of two types of investigations:

i. "*Undersaturation solubility coupled sorption experiments"* (Section 3.2.5.6.1, where undersaturation solubility experiments were performed with the previously prepared PuO_2(ncr,hyd) solid phase equilibrated in HQ-buffered porewater solutions with $[ISA]_{tot} = 10^{-5} – 10^{-2}$ M. Then coupled with sorption experiments at S:L ratios of ~0.2 – 50 gdm^{-3} by using the separated supernatants of the latter experiments), and
ii. *Desorption experiments* (Section 3.2.5.6.2, HQ-buffered systems with S:L ratio = ~0.2 or 2 gdm^{-3} and $[ISA]_{tot} = 10^{-3}$ or 10^{-2} M at $\log [Pu]_{in} \sim -6$ or -9 using the retrieved equilibrated hydrated cement phases of the screening experiments).

The first experimental series was dedicated to validate the applicability of the previously established Ca(II)-Pu(IV)-OH-ISA solubility model under the present porewater conditions (tackling assumption IV. from Section 3.2.5.3) and to test the sensitivity of the sorption process at lower $\log [Pu]_{in}$ concentrations, provided by the solubility equilibria of the PuO_2(ncr,hyd) solid phase. In the course of these experiments, the potential oversaturation of Pu in the system is directly excluded.
The desorption experiments were aimed to the assess the reversibility of the system, *i.e.* to validate the reliability of former results corresponding to systems conducted by following the "(Pu + cement) + ISA" experimental preparation order. These experiments are addressing the nature of the Pu(IV) uptake process by HCP, testing the reproducibility of the detected distribution factors (R_d vs. K_d) and the effect of the potential incorporation of $Pu(IV)_{sorbed}$ species into the hosting cement phases (C-S-H phases) with increasing allowed contact time.

3.2.5.6.1 Undersaturation solubility coupled sorption experiments

Figure 58 shows the total Pu concentrations measured after UF phase separation at $t_{eq} \leq 54$ days as function of log $[ISA]_{tot}$ in undersaturation solubility experiments performed with the formerly used PuO_2(ncr,hyd) solid phase. The figure also includes the solubility curve of PuO_2(ncr,hyd) under porewater conditions in the presence of ISA and Ca(II) in solution (see Section 3.2.5.1 for more details).

Detected log $[Pu]_{tot}$ values were in good agreement with the predictions of the previously established thermodynamic model for the Ca(II)-Pu(IV)-OH-ISA system, indicating its wider applicability than originally assigned ($pH_m < 12.4$).

Despite the slightly overestimated Pu concentrations provided by the model for certain conditions, at log $[ISA]_{tot}$ = -3, where results of 7 independent batch experiments are displayed together, a large dispersion can be seen in the collected data points. As no definite chronological trend was detected within these data, this indicates the high uncertainty for the prevailing solubility equilibrium. Deviations observed at log $[ISA]_{tot}$ = -4 and -5 (located close to or on the detection limit of ICP-MS in the present case) can be explained by the uncertainty of the solubility equilibria under the given condition. In the experiment with the lowest ligand concentration applied (log $[ISA]_{tot}$ = -5), Pu total concentrations after t_{eq} = 14 days were quantified at or slightly below log $[Pu]_{tot}$ = -11, showing an unusually large deviation from the solubility model.

Differences between the model calculations and measured $[Pu]_{tot}$ concentrations at log $[ISA]_{tot}$ = -2 were already identified in the course of the former undersaturation solubility experiments and are clearly confirmed in the present study. A definite explanation for the phenomenon cannot be given without further experimental evidences.

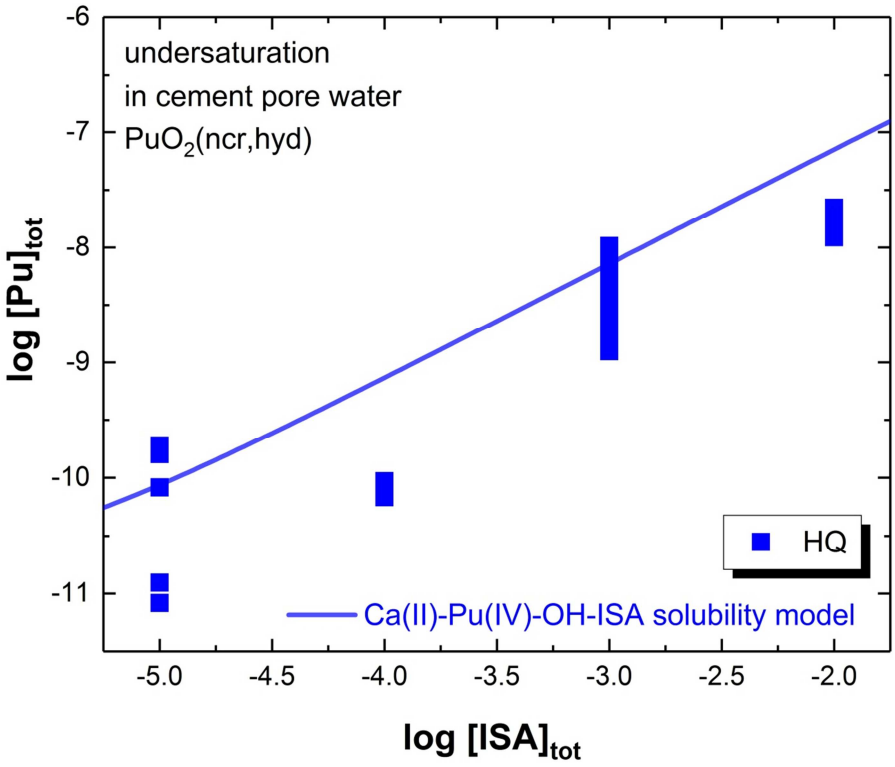

Figure 58. *Total concentrations of Pu quantified after ultrafiltration in HQ-buffered (blue) porewater solutions with $t_{eq} \leq 54$ d at $[ISA]_{tot} = 10^{-5} – 10^{-2}$ M in equilibrium with the formerly used PuO_2(ncr,hyd) solid phase (without HCP). Solid, blue line corresponds to the solubility of PuO_2(ncr,hyd) under porewater conditions in the presence of ISA and Ca(II) calculated analogously as in Section 3.1 applying SIT formalism (see text for details).*

As described before (Section 2.4.7), supernatants were quantified for $[Pu]_{tot}$ concentrations up to t_{eq} = 54 days, afterwards volumes of 5 cm^3 were separated from the PuO_2(ncr,hyd) phase and used for the coupled sorption experiments.

$[Pu]_{aq}$ concentrations at $t_{eq} \leq 31$ d after UF phase separation corresponding to the new sorption experiments with $[ISA]_{tot}$ = constant = 10^{-3} M and S:L ratio = 0.2 – 50 gdm^{-3} (coupled with the undersaturation solubility study) are shown in Figure 59. The figure also includes the solubility curve of a PuO_2(ncr,hyd) solid phase in the presence of ISA and Ca(II) ions ($[Pu]_{tot}$, blue solid line). The simplified sorption model predictions, $[Pu]_{aq}$ values under porewater conditions in the absence of ISA are displayed as a black solid line, whilst for the presence of ISA, it is indicated by a purple solid line. All calculations were performed accounting for the sorption of ISA onto HCP by applying $[ISA]_{eq}$ concentrations (shown separately as dashed green line) from the two-site Langmuir-isotherm, as in Equation (19) using the constants from Equation (76) at $[ISA]_{tot} = 10^{-3}$ M with S:L ratios = 0.2 – 50 gdm^{-3}.

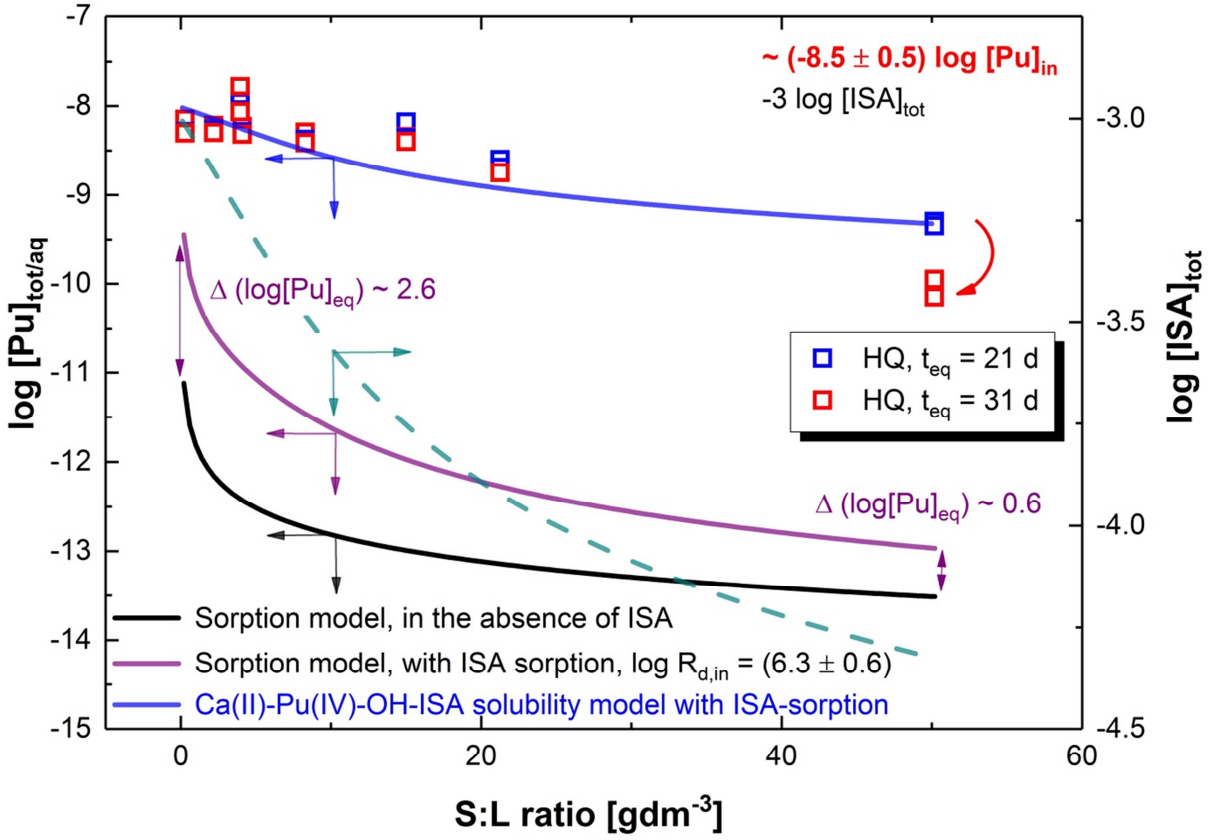

Figure 59. *Aqueous total concentrations of Pu quantified after ultrafiltration in HQ-buffered (blue symbols) cement powder – porewater systems with* $t_{eq} \leq 31$ *d at* $[ISA]_{tot} = 10^{-3}$ *M as function of the applied S:L ratios: 0.2 – 50* gdm^{-3} *at initial Pu concentration of* $log\ [Pu]_{in} = (-8.5 \pm 0.5)$*, as given by the results on the undersaturation solubility experiments. Solid lines correspond to: the solubility of* PuO_2*(ncr,hyd) under porewater conditions in the presence of ISA and Ca(II) (blue) and to the simplified sorption model predictions for porewater conditions in the absence (black) and presence of ISA (purple line). Calculations were executed by applying the SIT formalism as described in Sections 3.1 and 3.2.5.3 (see text for details) by using* $[ISA]_{eq}$ *concentrations (dashed blue line) accounting the sorption of ligand onto HCP (with Equation (19) with values from Equation (76)).*

In the coupled sorption experiments, 21 days after the introduction of the cement phases, all measured concentrations showed consistent values with the Ca(II)-Pu(IV)-OH-ISA solubility model predictions calculated from $[ISA]_{eq}$ concentrations after ISA sorption onto HCP. This observation suggests that even at the low Pu concentrations a similar effect occurs as seen in the results of the sorption experiments performed at $\log [Pu]_{in} = -5.8$, where the $[Pu]_{aq}$ concentrations did not decrease significantly even after 112 days of equilibration time. As

described before, this effect may be explained by kinetic processes or changes of the cement surface properties when ISA is sorbed. Pu might suffer an in-solution stabilization, which will result in a further prolonged sorption process in the case of the latter "(Pu + ISA) + cement" experiments. Nevertheless, the data set in the present series at S:L ratio = 50 gdm^{-3} already depict a slight concentration decrease by ~ 1 log $[Pu]_{aq}$ unit from t_{eq} = 21 d to 31 d, implying that at higher S:L ratios the increased availability of the sorption sites on the surface of the sorbing phases (with regard to $[ISA]_{tot}$ concentrations) are overcompensating the latter in-solution stabilization effect.

3.2.5.6.2 Pu desorption experiments

Prior to the initialization of the desorption experiments, the selected samples (6 batches) taken from the screening experiments with S:L ratios of 0.2 – 2.5 gdm^{-3} and log $[Pu]_{in}$ = -6 or -9, were quantified at t_{eq} = 167 d for $[Pu]_{aq}$ directly in the supernatant solutions and after UF phase separation to ensure steady-state conditions in the systems. Figure 60 shows sorption results of the latter samples at t_{eq} = 167 days expressed in the form of log R_d (dm^3kg^{-1}) values together with the log $R_{d,in}$ value and its associated uncertainty derived in the cement-Pu experiments within the present work (Equation (77)).

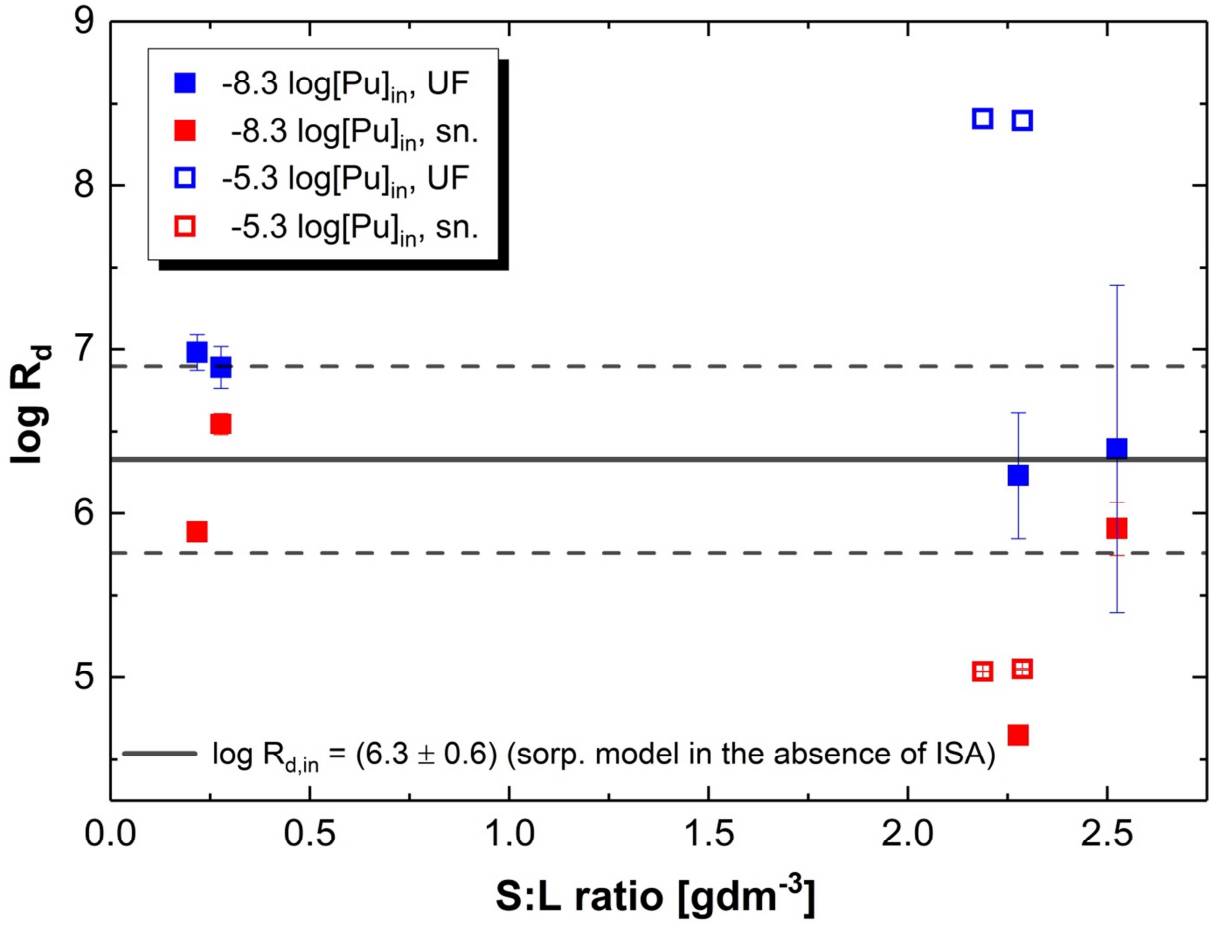

Figure 60. *Distribution ratios (R_d values, in dm^3kg^{-1} units) of Pu quantified at t_{eq} = 167 d directly in the supernatant solutions (red) or after ultrafiltration phase separation method (blue symbols) in HQ-buffered cement powder – porewater systems with S:L ratios of ~0.2 gdm^{-3} – ~2 gdm^{-3}, at applied initial Pu concentrations of log $[Pu]_{in}$ = -5.3 (opened) and -8.3 (filled symbols). The displayed error bars of data points are originating only from the analytical uncertainties associated to the quantification of Pu total concentrations after ultrafiltration phase separation method: UF or directly in the supernatants of the solutions: sn. by SF-ICP-MS technique. Black, solid and dashed lines are corresponding to the log $R_{d,in}$ = (6.3 ± 0.6) value and its uncertainties derived in the present study for the Cement-Pu system.*

In systems with log $[Pu]_{in}$ = -8.3, all newly determined log R_d values using the $[Pu]_{aq}$ concentrations quantified after UF phase separation method were in agreement with the log $R_{d,in}$ value of (6.3 ± 0.6), confirming the validity of the initially assigned value for longer equilibration times. Data related to S:L ratio = 0.2 gdm^{-3} were found to be slightly underestimated as expected (for explanation see related discussion in Section 3.2.4.2). These

data points still fall close to the upper limit of the predicted uncertainty-range. Distribution ratios related to $[Pu]_{aq}$ concentrations determined in the supernatants of these experiments are also showing a relatively good agreement with the estimates, indicating the lack of a large contribution of colloidal Pu(IV) species to the total Pu concentration in the solution.

In systems with log $[Pu]_{in}$ = -5.3 and S:L ratio = 2 gdm^{-3}, detected $[Pu]_{aq}$ concentrations after ultrafiltration were located in the range of the solubility level for the PuO_2(am,hyd) phase, in agreement with the previous experimental findings for the system.

As detailed in the related experimental Section (2.4.7), the hydrated cement solid phases of the latter samples were separated via centrifugation and the supernatants were replaced by identical but ISA-containing porewater solutions with $[ISA]_{tot} = 10^{-3}$ and 10^{-2} M. Figure 61 shows $[Pu]_{aq}$ concentrations detected after UF phase separation in the time-frame of $t_{eq} \leq$ 112 days after starting the desorption experiments with log $[Pu]_{in}$ = -5.3 and S:L ratio = 2 gdm^{-3} as function of $[ISA]_{tot}$ concentration. The figure also includes the solubility curve of PuO_2(ncr,hyd) under porewater conditions in the presence of ISA and Ca(II) in solution (see Section 3.2.5.1 for more details).

Similarly as in the Cement-Pu-ISA investigations at S:L ratios of 0.2 and 2 gdm^{-3} with log $[Pu]_{in}$ = -5.3, the analogous desorption experiments conducted in the presence of ISA resulted in the "reproduction" of Ca(II)-Pu(IV)-OH-ISA solubility experiments. This is shown by the good agreement between the model calculations and the measured values for $[Pu]_{aq}$ concentrations in the system. A notably larger discrepancy was observed between the predictions and the data collected at log $[ISA]_{tot}$ = -3, but still falling in the assigned uncertainty-range of the model (~± 1.0 log $[Pu]_{tot}$).

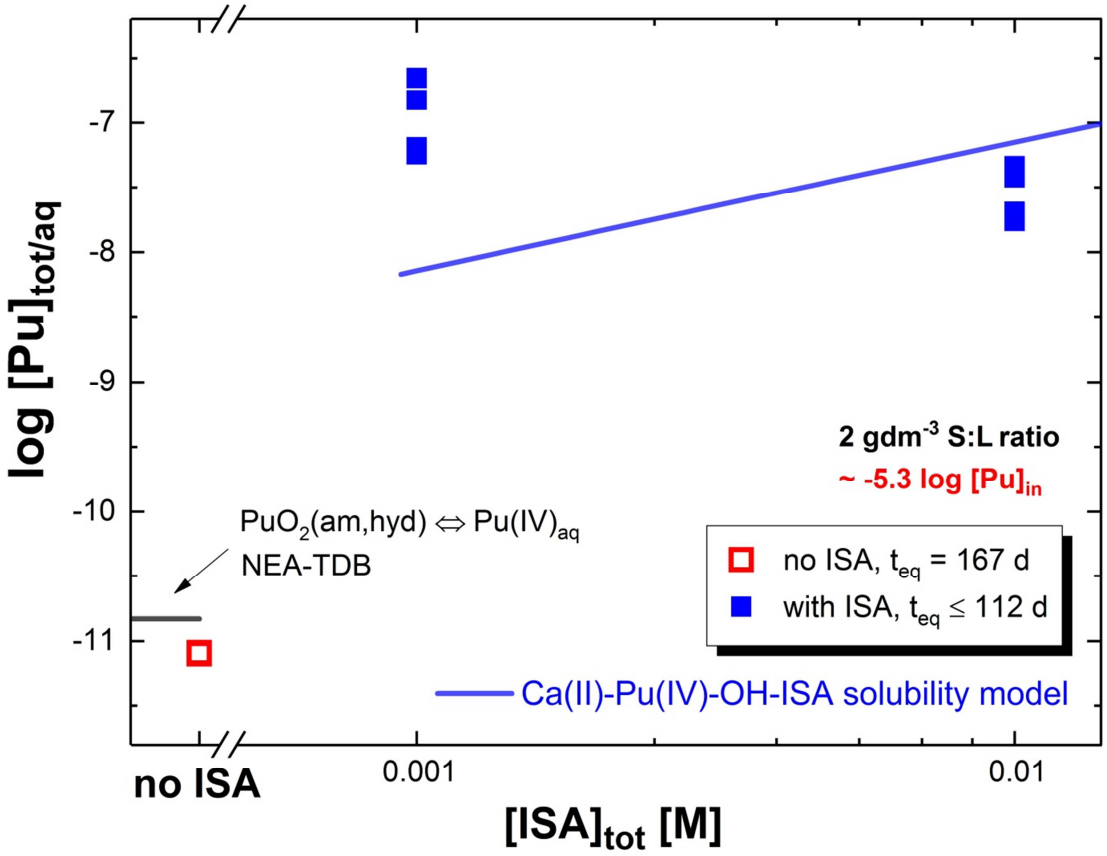

Figure 61. *Aqueous total concentrations of Pu obtained in desorption experiments in HQ-buffered cement powder – porewater systems with S:L ratio of 2 gdm^{-3} and the initial Pu concentration of log [Pu]$_{in}$ = -5.3 quantified after ultrafiltration phase separation at t_{eq} =167 d (in the absence of ISA in solution, red symbols) and at $t_{eq} \leq 112$ d with [ISA]$_{tot}$ = 10^{-3} or 10^{-2} M (blue symbols). Solid, blue line corresponds to the solubility of PuO$_2$(ncr,hyd) under porewater conditions in the presence of ISA and Ca(II) calculated analogously as in Section 3.1 applying the SIT formalism (see text for details).*

Figure 62 and Figure 63 show the results in terms of log R_d values related to the desorption experiments with log [Pu]$_{in}$ = -8.3 as function of ISA total concentrations at S:L ratio = 0.2 and 2 gdm^{-3}, respectively. The [Pu]$_{aq}$ concentrations collected in the presence of ISA were determined in ultrafiltrated solutions at $t_{eq} \leq 112$. The figures also shows log R_d values (and associated uncertainties with regard to Equation (77)) predicted by the simplified sorption model, expressed in Equation (78) as function of [ISA]$_{tot}$ concentrations for given conditions. Further details on the performed calculations are provided in previous sections (*e.g.* 3.2.5.3).

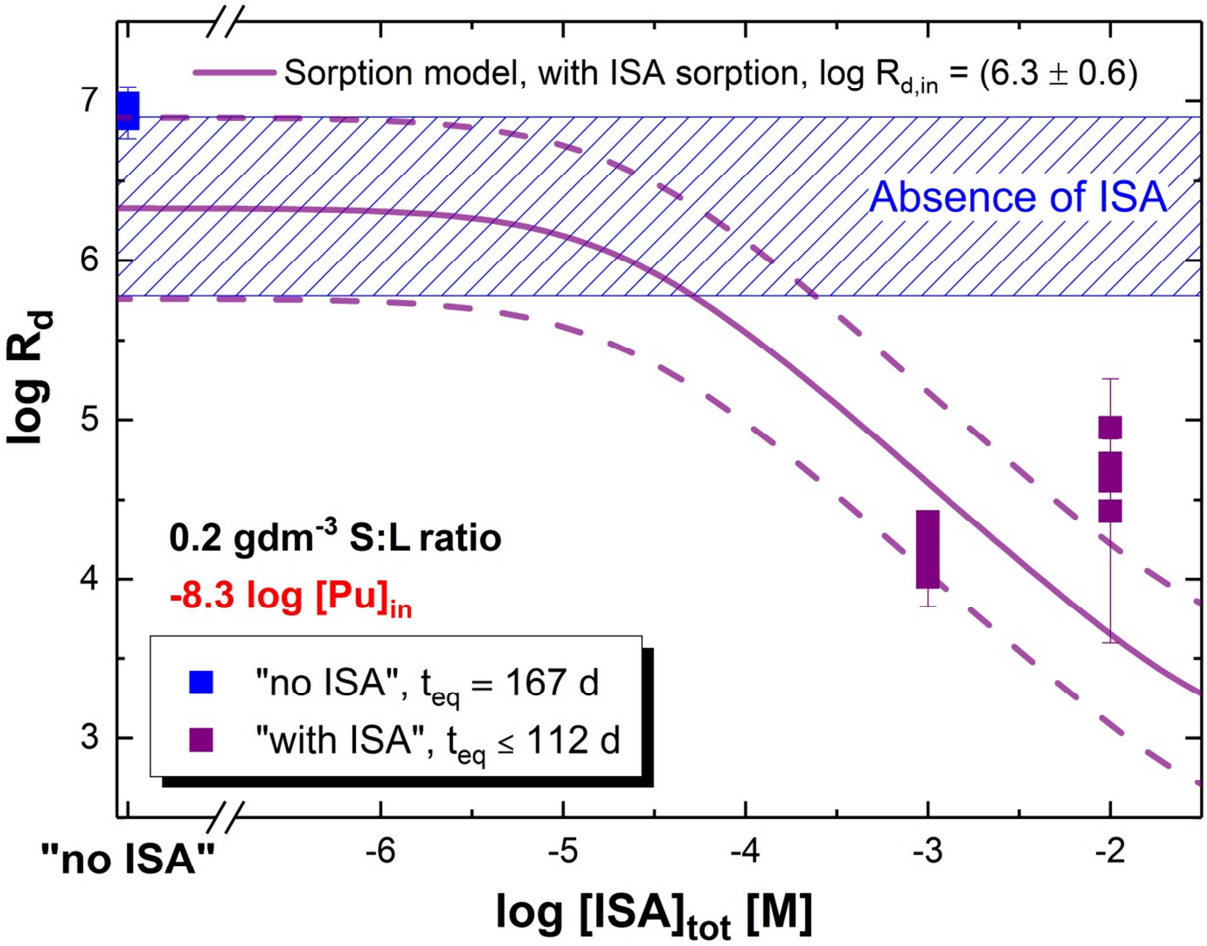

Figure 62. *Distribution ratios in desorption experiments (R_d values, in dm^3kg^{-1} units) of Pu quantified after ultrafiltration phase separation in HQ-buffered cement powder – porewater systems at t_{eq} = 167 d in the absence of ISA (blue) and at $t_{eq} \leq$ 112 d in the presence of ISA (purple symbols) at S:L ratio = ~0.2 gdm^{-3} and with the applied initial Pu total concentration of log $[Pu]_{in}$ = -8.3. (The displayed error bars are reflecting only the analytical uncertainties associated to the quantification of Pu aqueous total concentrations by SF-ICP-MS). Solid, and dashed purple lines correspond to log R_d values predicted by the simplified sorption model and its associated uncertainty through the variation of the log $R_{d,in}$ parameter. Calculations were executed by applying the SIT formalism as described in Section 3.2.5.3 (see text for details) by using $[ISA]_{eq}$ concentrations accounting for the sorption of the ISA ligand onto HCP.*

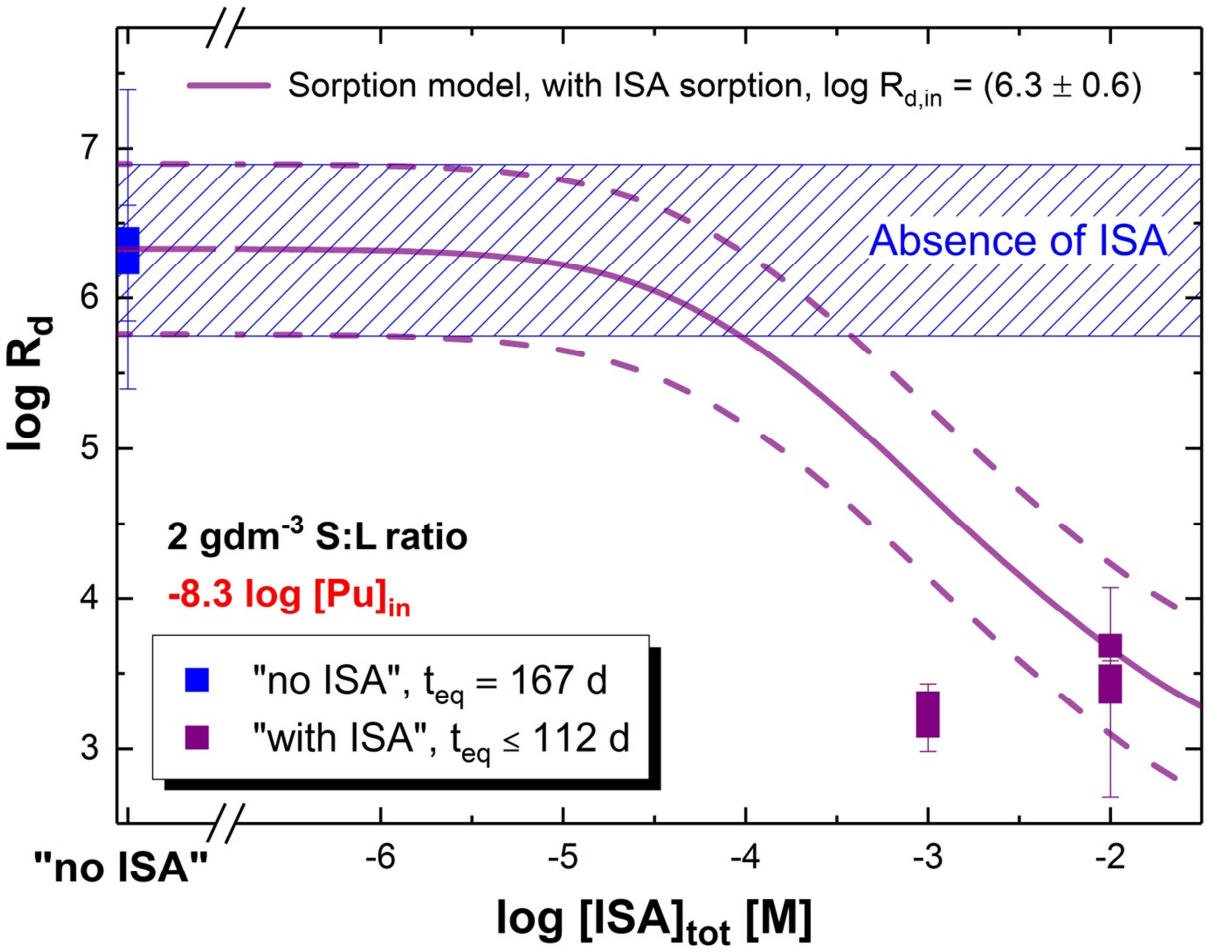

Figure 63. *Distribution ratios in desorption experiments (R_d values, in dm^3kg^{-1} units) of Pu quantified after ultrafiltration phase separation method in HQ-buffered cement powder – porewater systems at t_{eq} = 167 d in the absence of ISA (blue) and at $t_{eq} \leq$ 112 d in the presence of ISA (purple symbols) at S:L ratio = ~2 gdm^{-3} and with the applied initial Pu total concentration of log $[Pu]_{in}$ = -8.3. (The displayed error bars are reflecting only the analytical uncertainties associated to the quantification of Pu aqueous total concentrations by SF-ICP-MS). Solid, and dashed purple lines correspond to log R_d values predicted by the simplified sorption model and its associated uncertainty through the variation of the log $R_{d,in}$ parameter. Calculations were done by applying the SIT formalism as described in Section 3.2.5.3 (see text for details) by using $[ISA]_{eq}$ concentrations accounting the sorption of the ISA ligand onto HCP.*

One important observation was that the desorption data collected at t_{eq} = 5 d time already showed steady-state conditions in terms of $[Pu]_{aq}$ concentrations and the derived log R_d values compared well to the previously obtained data in "(Pu + cement) + ISA" experiments. The latter observation, especially at log $[ISA]_{tot}$ = -2, indicates the high reversibility of Pu(IV)

sorption onto the HCP, suggesting that the process is rather a surface reaction (reactions with incorporation into crystal structures are mostly significantly slower), *i.e.* can be apprehended as an adsorption process taking place on the surface of the hosting phase (R_d *vs.* K_d).

In the course of the present experiments, the simplified sorption model for both S:L ratios at 0.2 and 2 $g \cdot dm^{-3}$ provided only a moderate accuracy in simulating the detected log R_d values. A controversial aspect in both cases is that the distribution ratios show an increase in the data set from $[ISA]_{tot} = 10^{-3}$ to 10^{-2} M, *i.e.* the aqueous concentrations of Pu were quantified to be lower in systems with the higher ISA total concentration of log [ISA] = -2. This contradiction points out the possibility of different prevailing chemical equilibria within the two systems. As discussed before, in experiments with log [ISA] = -3, the initially introduced level of Pu concentration is close to the expected solubility level of PuO_2(am,hyd). A different perspective for the occurring problem is visualized when sorption and solubility data are shown together in concentration units (log $[Pu]_{aq}$ vs. log $[ISA]_{tot}$). Figure 64 a and b display the desorption data together with previously shown sorption results (taken from Sections 3.2.6.1 and 3.2.6.4) obtained at 0.2 and 2 $g \cdot dm^{-3}$ S:L ratios and with the undersaturation solubility data (taken from Section 3.2.5.6.1) collected under analogous conditions.

Figure 64 demonstrates for both cases with 0.2 and 2 $g \cdot dm^{-3}$ S:L ratios that two phenomena might occur at the two different log $[ISA]_{tot}$ concentrations. The substantial overlap between the $[Pu]_{aq}$ concentrations collected at log $[ISA]_{tot}$ = -3 in the course the solubility and sorption experiments show that under this condition a Pu solubility control in the investigated systems cannot be excluded. This effect originates from the high initial Pu total concentration, located close to the expected solubility limit of PuO_2(ncr,hyd). Conversely at log $[ISA]_{tot}$ = -2, solubility data are located above all sorption data as well as above the introduced concentration level of Pu in the system, underlining that under this conditions a sorption reaction is most likely responsible for the observed Pu solution concentrations.

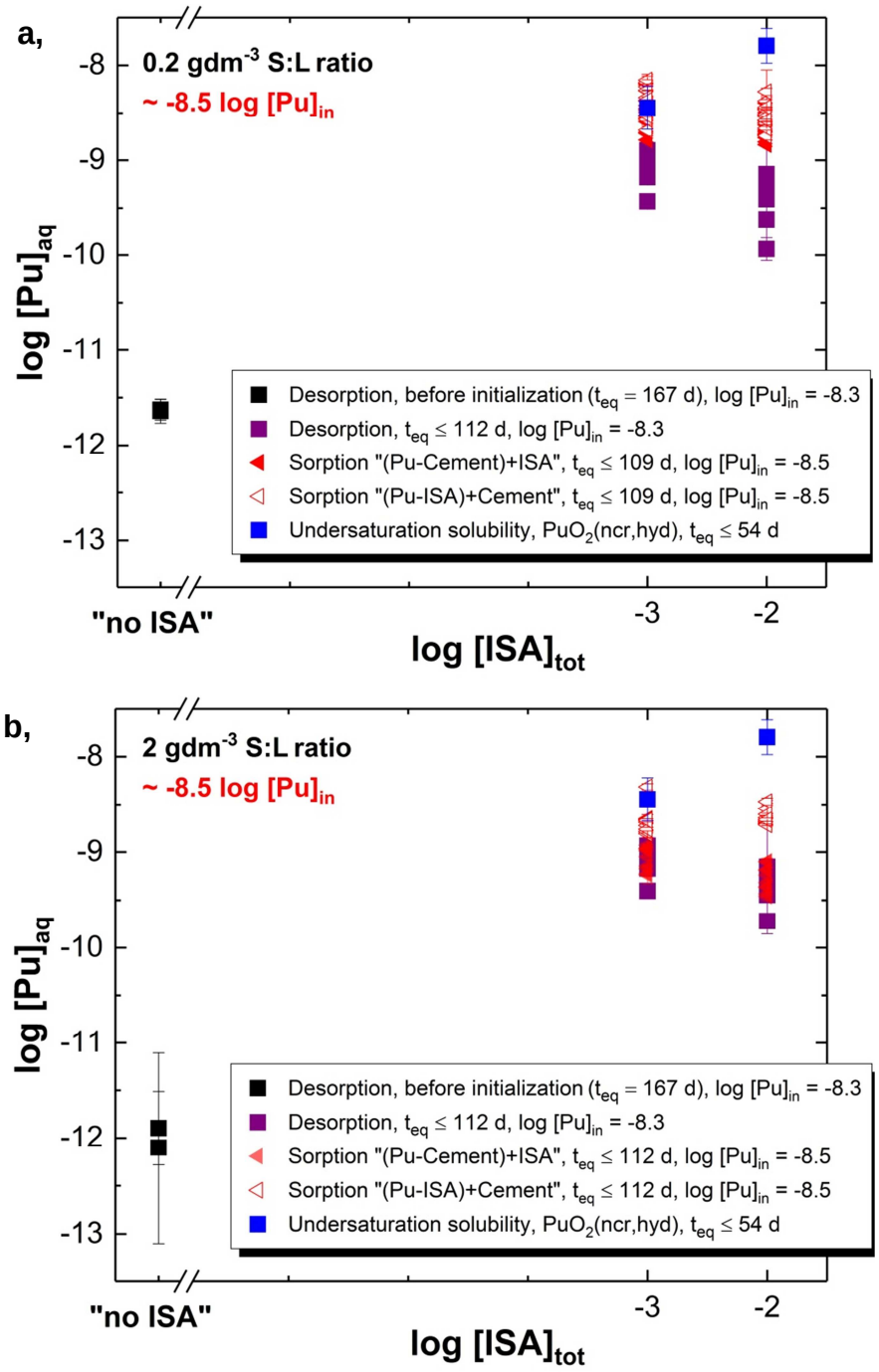

Figure 64. *Aqueous total concentrations of Pu in HQ-buffered cement powder – porewater systems with $t_{eq} \leq 112$ d at S:L ratios of ~0.2 (a) and 2 gdm^{-3} (b) without ISA (only for desorption experiments $t_{eq} = 167$ d) or at $[ISA]_{tot} = 10^{-3}$ or 10^{-2} M with initial Pu concentration of log $[Pu]_{in}$ = -8.3 (desorption experiments) and -8.5 (sorption experiments as adapted from Sections 3.2.5.1 and 3.2.5.4. Data collected within sorption experiments are displayed with regard to the experimental preparation orders, i.e.: "(Pu + cement) + ISA" (closed symbols) or "(Pu + ISA) + cement" (opened symbols).*

3.2.6 Sorption reduction factors in the presence of ISA

In order to the determine sorption reduction factors for the uptake of Pu(IV) by HCP in the presence of ISA at different total concentration-levels of the ligand, selected $[Pu]_{aq}$ data were combined. Results of the sorption experiments conducted with S:L ratios = ~2 – 4 $g \cdot dm^{-3}$ at various $[ISA]_{tot}$ concentrations (10^{-5} – 10^{-2} M) with log $[Pu]_{in}$ = -8.3 (or lower) were serving as the basis for the calculation. Considering the former observations and discussions on trends of collected data points, the data selection was based on the following criteria:

- Experiments at log $[Pu]_{in}$ = –5.5 were disregarded in this interpretation because they are largely oversaturated with respect to PuO_2(am,hyd). All data obtained for systems with log $[Pu]_{in}$ = –(8.4 ± 0.6) were taken into account to derive the respective F_{red} values, although, as discussed in previous sections, Pu aqueous concentrations in some of these systems might also be controlled by solubility equilibria.
- Narrowing the data set of log $[Pu]_{in} \leq$ –9 systems, experiments only with S:L ≈ 2 – 4 $g \cdot dm^{-3}$ were considered to be selected for F_{red} calculation. The argumentation is based on the fact that the obtained results in systems with S:L = 0.2 $g \cdot dm^{-3}$ may be affected by systematic errors due to the lower amount of cement introduced.
- Previous sections have shown that the order of addition has an impact on sorption (especially in systems with log $[ISA]_{tot}$ = –2). Consequently, two log F_{red} have been calculated corresponding to (i) "(Pu + cement) + ISA", and (ii) "(Pu + ISA) + cement". The present working hypothesis is that (i) likely represents equilibrium and (ii) might be kinetically hindered, but both log F_{red} are made available for the interpretation of the impact of ISA on Pu(IV) uptake by HCP.

Selected data were transformed to sorption reduction factors (F_{red}) of ISA, as expressed in Equation (27) using experimentally determined parameters and the log $R_{d,in}$ ($dm^3 \cdot kg^{-1}$) = (6.3 ± 0.6) value. The calculated factors are displayed in Figure 65 together with the single experimental data point provided by Baston and co-workers [120] and with model calculations reported previously by Bradbury and Sarott [85] applying the chemical model provided in the works of Moreton and Greenfield *et al.* [91-93]. The figure also includes the

calculated F_{red} values predicted by the simplified model (with implemented ISA-sorption). Further details on the calculations related to the present work are provided in Section 3.2.5.3. It is important to be noted that the plotted data in Figure 65 are originating from the 2 $g \cdot dm^{-3}$ S:L series, from the 0.2 – 50 $g \cdot dm^{-3}$ S:L series as well as from the complementary experimental series (undersaturation solubility coupled sorption and separate desorption experiments). The averaged values for the sorption reduction factors (and associated uncertainties) with regard to the experimental preparation order and $[ISA]_{tot}$ concentrations are provided in Table 21. The data in Table 22 correspond to data obtained for the selected experimental conditions, *i.e.* $\log [Pu]_{in} = -(8.4 \pm 0.6)$.

Table 21. *Averaged values and associated uncertainties (bold numbers, taken as three times the standard deviation of the depicted values at a certain $[ISA]_{tot}$ in Figure 65) for the sorption reduction factors (F_{red}) of ISA on the uptake of Pu(IV) by hydrated OPC paste under generated porewater conditions (pH_c = 12.60, $[Ca]_{tot}$ = 0.02 M) with $[ISA]_{tot} = 10^{-3}$ and 10^{-2} M, $\log [Pu]_{in} = -(8.4 \pm 0.6)$ and at S:L ratios of ~2 – 4 $g \cdot dm^{-3}$. Equilibrium concentration of the ligand was calculated upon the sorption model for the cement-ISA system under analogous conditions at S:L ratio = 2 $g \cdot dm^{-3}$. Data of the present work are distinguished with regard to the applied experimental preparation order. Estimates of the present study are calculated upon the simplified sorption model (see Section 3.2.5.3 for details). Reference values (considered to be valid under analogous conditions to the p.w.) are adapted from elsewhere as indicated.*

log $F_{red,av}$ ± 3·stand.dev. (p.w.)				***log F_{red} (ref.)***	
log $[ISA]_{tot}$	**log $[ISA]_{eq}$**	**"(Pu + cement) + ISA"**	**"(Pu + ISA) + cement"**	**Th(IV)**	**Pu(IV)**
-2	-2.01	**3.0 ± 0.4** (2.7*)	**4.4 ± 0.7**	4[a]	6[c]
-3	-3.12	**3.3 ± 0.4** (1.6*)	**4.6 ± 0.6**	2[a,b]	4.3[c] / 3[d]
-4	-4.25	(0.6*)	-	0[a,b]	2.7[c]
-5	-5.28	(0.1*)	-	0[a,b]	1.3[c]

* estimated values provided by the simplified sorption model derived in the present work
a, adapted from Ochs *et al.* [122]
b, adapted from Wieland *et al.* [13]
c, calculated values as provided by Bradbury and Sarott [85]
d, suggested by the review work of Wang *et al.* [109]

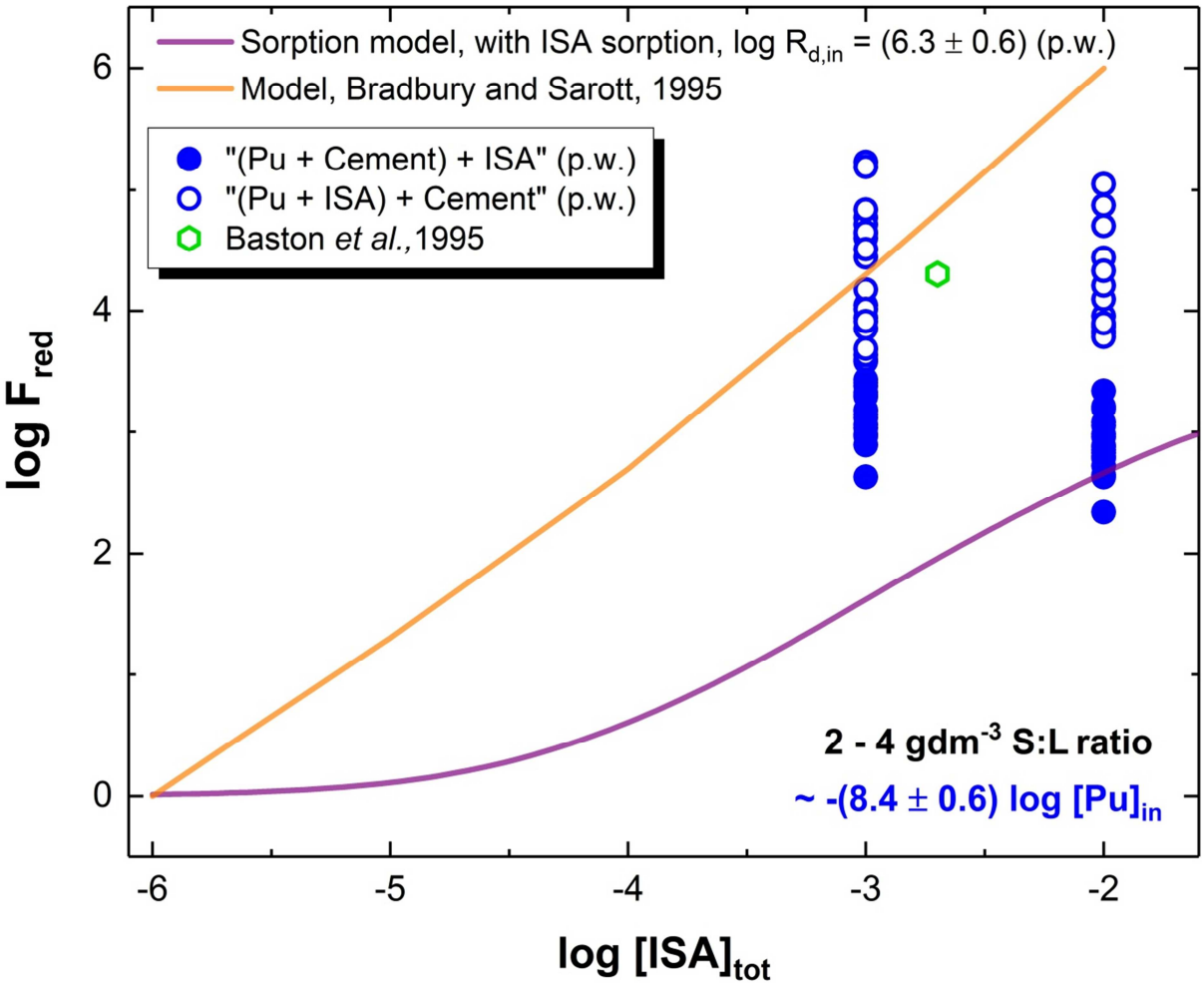

Figure 65. *Sorption reduction factors (F_{red}) of ISA on the uptake of Pu(IV) by hydrated OPC paste under porewater conditions (pH_c = 12.60, $[Ca]_{tot}$ = 0.02 M). Displayed values related to the present study (blue symbols) are derived via Equation (27) using log $R_{d,in}$ ($dm^3 \cdot kg^{-1}$) = (6.3 ± 0.6) from the results obtained in systems with S:L ratios of ~2 – 4 $g \cdot dm^{-3}$ at $[ISA]_{tot}$ = 10^{-3} or 10^{-2} M, where log $[Pu]_{in}$ = -(8.4 ± 0.6). The opened and closed symbols are denoting the preparation order of the experiments: "(Pu + ISA) + cement" and "(Pu + cement) + ISA", respectively. Literature values are taken from the work of Baston et al. [120] (green symbol) and from model calculations provided elsewhere [85] (orange solid line). Solid purple line corresponds to F_{red} values calculated using the simplified sorption model through Equation (77) and (78) for porewater conditions in the presence of ISA and Ca(II) applying the SIT formalism (see text for further details).*

As discussed before, an important parameter affecting the values for F_{red} at a certain $[ISA]_{tot}$ concentration (for S:L ratio = 2 $g \cdot dm^{-3}$) was found to be the applied preparation order of the experiments. In systems where Pu was first put in contact with ISA within the porewater and

the cement phase was introduced later, $[Pu]_{aq}$ concentrations were close to the initially introduced Pu concentration level, indicating an additional in-solution stabilization (sorption hindering) and a consequent potential kinetic effect on the system. As a result, F_{red} values related to the latter experiments might be highly overestimated, *i.e.* not representative of the prevailing adsorption equilibria of $Pu(IV)_{aq}$ species onto HCP in the presence of ISA.

In view of the available F_{red} values as function of log $[ISA]_{tot}$, the following discussion arises:

F_{red} values derived for $[ISA]_{tot} = 10^{-3}$ M:

- The only available experimental F_{red} value in the literature (for $[ISA]_{tot} = 2 \cdot 10^{-3}$ M, obtained at pH ~ 12.4, using OPC based, hydrated concrete and mortar powders with a S:L ratio of 20 $g \cdot dm^{-3}$) is reported by Baston *et al.* in [120].
- The latter value is found to be in good agreement with the results of the "(Pu + ISA) + cement" experiments. The closer inspection of their experimental details reveals that their investigations were indeed conducted in a similar way as in the course of the "(Pu + ISA) + cement" system of the present study. Consequently, the relatively high F_{red} value reported could be considered to be caused by the kinetic effect of ISA and it is in line with the observation made in the present work as well.
- The observed differences between the simplified model calculations and determined F_{red} values at $[ISA]_{tot} = 10^{-3}$ M can be attributed superposition of three separate phenomena: (i) the potential control of Pu aqueous concentrations by solubility phenomena (see Figure 64 for interpretation), (ii) changes in the physiochemical properties of the hydrated cement surface imposed by the excessive surface-coverage of HCP by the ligand and (iii) kinetical, in-solution stabilization effect of ISA on Pu aqueous species.

F_{red} values derived for $[ISA]_{tot} = 10^{-2}$ M:

- The "most representative" log F_{red} values for the impact of ISA might be obtained experimentally at log $[ISA]_{tot} = -2$ in the present work, as calculated from sorption and desorption experiments.
- As the Ca(II)-Pu(IV)-OH-ISA solubility of Pu(IV) is higher than $[Pu]_{in}$, the potential precipitation of PuO_2(am, hyd) controling $Pu(IV)_{aq}$ is more unlikely

and hence, sorption related processes can be exclusively responsible for the decrease in $[Pu]_{aq}$ concentrations in solution.

- The experimental value corresponding to the "(Pu + cement) + ISA" system was found to agree well with the log F_{red} value (2.7) calculated using the simplified model described in Section 3.2.5.3.
- Quantified F_{red} values in the "(Pu + ISA) + cement" system show large deviations from the results of the "(Pu + cement) + ISA" system and with the present model calculations as well. At the current stage of the investigation, the nature of the effect is not clear. F_{red} values in the "(Pu + ISA) + cement" system are nevertheless reported as a potential unfavorable situation.
- Reference values available in the literature for log F_{red} of An(IV) in the presence of log $[ISA]_{tot}$ = –2 (log F_{red} = 4 in [122]; log F_{red} = 6 in [85]) are clearly higher than the proposed data obtained in the present work.
- The predictions provided by Bradbury and Sarott in their review work [85] for F_{red} values valid under analogous conditions (cementitious environment, pH ~12.5, Stage II of the cement degradation process) are calculated using the previously reported chemical model by Moreton and co-workers [93]. However, the deviation of ~+1.5 log-units from the new experimental F_{red} values observed at log $[ISA]_{tot}$ = -2 reported in this work might at least partly be the result of incorrect assumptions related to the aqueous Pu speciation.
- On the basis of chemical analogy and a more extensive pool of available experimental work, previous review studies [13, 122] proposed the general use of the ISA sorption reduction factors for Th(IV) to describe cement-An(IV)-ISA systems (listed in Table 21). The use of Th(IV) as analogue for Pu(IV) results in significant errors regarding the prediction of solubility / speciation of Pu(IV) as it was demonstrated in this work. Since Th(IV) and Pu(IV) complexes with ISA show differing stoichiometries and stability, exploiting this analogy may lead to significant errors in the interpretation of sorption data.

Results of the present work provide important insight into the multiple parameter-dependence of the system. A better understanding on the complex Cement-Pu-ISA system has been achieved through the more precise chemical knowledge and accurate control of prevailing redox conditions, the correct assessment of solution speciation as well as by accounting for the sorption processes prevailing in the individual, binary systems.

4 Summary and conclusions

Within this PhD thesis four fundamental issues affecting the behavior of plutonium in the context of low- and intermediate-level radioactive waste disposal were successfully addressed:

i. Redox behavior of Pu in alkaline, reducing aquatic systems,
ii. Solubility, redox behavior and complexation of Pu: presence of ISA, *absence* of Ca,
iii. Solubility, redox behavior and complexation of Pu: presence of ISA, *presence* of Ca,
iv. Impact of ISA on the sorption of Pu onto cementitious materials.

These four processes have been comprehensively investigated in experiments under different well-controlled redox conditions, using a systematic variation of pH_m, ISA and Ca(II) concentrations, and in sorption experiments, considering key parameters such as S:L ratio or the order of addition of the components. The results are quantified within the concepts of equilibrium thermodynamics of aqueous systems, and provide key input for the quantitative interpretation of the uptake of Pu by cement in the presence of ISA. This significantly contributes to improved safety analysis for related nuclear waste disposal scenarios. The main achievements of this study can be summarized as follows:

1. Redox behavior of Pu in alkaline, reducing aquatic systems

The solubility of the Pu(IV)O_2(ncr,hyd) phase used in this study under alkaline, moderately reducing conditions (imposed by HQ) is very low (~10^{-11} m) and pH_m-independent. This is in good agreement with the solubility of Pu(IV) calculated using thermodynamic data currently selected in the NEA-TDB, and with the solubility product calculated for the same solid phase using solubility data obtained under acidic conditions. In the very reducing conditions defined by Sn(II) and $pH_m > 9$, the solubility of Pu remains low (~10^{-11} m) and pH_m-independent. *In-situ* XRD, XAFS and XPS indicate that Pu(IV)O_2(ncr,hyd) is the solid phase controlling the solubility of Pu in HQ-system. On the other hand, XANES confirms a significant contribution of Pu(III) (~30 ± 5 n%) in the solid phases controlling the solubility of Pu in Sn(II) systems. This observation can be explained with the formation of substoichiometric PuO_{2-x}(ncr,hyd) or by the transient coexistence of PuO_2(ncr,hyd) and $Pu(OH)_3$(am) solid phases. The redox and solubility data obtained in this first part of the PhD thesis add important input to the discussion of a current “hot-topic” in fundamental

plutonium chemistry and also provides a sound baseline for the subsequent quantitative experimental evaluation of the impact of ISA on Pu solubility under analogous chemical conditions.

2. Solubility, redox behavior and complexation of Pu: presence of ISA, *absence* of Ca

The solubility of Pu in the presence of ISA shows a systematic increase compared to the ligand-free case discussed above, thus supporting the formation of ternary complexes Pu–OH–ISA. Long-term experiments on the chemical stability of ISA were conducted in alkaline reducing systems in the absence of Pu, confirming that the ISA ligand remains stable within the time-frame of the solubility studies. Solid phase characterization confirms that, in the presence of ISA, PuO_2(ncr,hyd) is the solid phase controlling the solubility in HQ and Sn(II) systems. This reflects the potential impact of ISA on the redox chemistry of Pu under alkaline reducing conditions.

Based on slope analysis and statistical evaluation of the solubility data, three Pu–OH–ISA complexes were determined to be present under the conditions of interest, namely: $Pu(IV)(OH)_3ISA_{-H}^-$, $Pu(IV)(OH)_3ISA_{-2H}^{2-}$ and $Pu(III)(OH)ISA_{-H}$(aq). Stoichiometries and structures of these complexes were optimized via quantum chemical calculations. In mildly reducing environment (HQ-systems), Pu(IV)-OH-ISA complexes dominate the aqueous speciation of Pu. On the other hand, in strongly reducing solutions (Sn(II)-systems) at pH_m < 11.5, solubility is controlled by the reductive dissolution of $Pu(IV)O_2$(ncr,hyd) and consequent formation of the complex $Pu(III)(OH)ISA_{-H}$(aq). Above this pH_m, the $Pu(IV)(OH)_3ISA_{-2H}^{2-}$ complex becomes predominant as in HQ-systems. Based on the experimental and theoretical information, a comprehensive and robust thermodynamic model for the system Pu(III/IV)-OH-ISA was established using the SIT formalism. The new thermodynamic model derived in this work is valid for a wide-range of pH_m, pe and $m(ISA)_{tot}$ conditions.

Further experimental observations detected gradually increasing fractions of colloidal Pu(IV) species with increasing $m(ISA)_{tot}$ in solution (for both redox-buffered cases), indicating that “Pu–ISA colloids” importantly contribute to the total Pu concentration in Ca-free solution at high pH values (pH_m = 12). The formation of such colloids was not parametrized in the thermodynamic model derived for the system Pu(III/IV)-OH-ISA, but their contribution must be accounted for to provide realistic upper limit concentrations of Pu in the presence of ISA and absence of Ca(II).

3. Solubility, redox behavior and complexation of Pu: presence of ISA, *presence* of Ca

Analogous Pu solubility investigations performed in the presence of Ca(II) and ISA unequivocally confirm the formation of quaternary Ca(II)-Pu(IV)-OH-ISA species in addition to the ternary complexes identified under absence of Ca. No direct evidence on the formation of analogous Pu(III) quaternary complexes was observed. Slope analysis of solubility data in combination with solid phase characterization indicate the formation of the complexes $Ca(II)Pu(IV)(OH)_3ISA_{-H}^{+}$ and $Ca(II)Pu(IV)(OH)_3ISA_{-2H}^{0}(aq)$, which prevail below and above $pH_m \approx 11$, respectively. Chemical and thermodynamic models derived for the system Ca^{2+}–Pu^{4+}–OH^{-}–Cl^{-}–ISA^{-}–$H_2O(l)$ describe the experimental results obtained within this study, although relatively large deviations were observed for the highest pH_m and ISA concentration. Under these conditions, the formation of a yet undefined quaternary solubility controlling phase Ca(II)–Pu(IV)–OH–ISA(s) is suspected.

It is also of high importance, that the formerly identified fractions of "Pu–ISA colloids" in the supernatants of Ca-free systems at $pH_m = 12$ are clearly absent in the studies where Ca(II) ions are present in solution. Although the exact mechanism leading to this phenomenon is not resolved, it points out the important role of Ca(II) in the destabilization of colloids as previously described for clay systems.

4. Impact of ISA on the sorption of Pu onto cementitious materials

Plutonium is sorbing strongly on cement under reducing conditions and absence of ISA. Log R_d values determined in the present work are in good agreement with data available in the literature for An(IV) analogs. Sorption experiments conducted under comparable chemical conditions but absence of Pu indicate that ISA sorbs significantly on cement in the degradation stage II. A two-site Langmuir-isotherm was used to fit the experimental data of ISA sorption obtained in this work. This isotherm provides an empirical tool to evaluate the concentration of ISA remaining in solution after sorption.

Solubility experiments conducted with PuO_2(ncr,hyd) using the porewater in equilibrium with the investigated cement have been conducted for different ISA concentrations. The results obtained provide upper concentration limits for Pu in contact with cement.

All sorption experiments conducted in the presence of ISA with $\log [Pu]_{in} = -5.5$ are likely to be solubility controlled and have therefore been disregarded for the interpretation of sorption phenomena. Accordingly, the main conclusions of this chapter are derived from sorption experiments with $\log [Pu]_{in} = -8.5$. Although some systems at this $[Pu]_{in}$ might be as well solubility controlled (especially at log [ISA] = –3), such concentration is realistic

value for potential L/ILW repositories. An important feature observed under these conditions is that the order of addition of the components (Pu / ISA / cement) appears to have a relevant impact on Pu sorption, especially at $[ISA]_{tot} = 10^{-2}$ M. In the latter systems, the sequence "(Pu + cement) + ISA" shows log R_d values ≈ 1.5 log-units greater (or log F_{red} values 1.5 log-units lower) than the sequence "(Pu + ISA) + cement".
A simplified, quantitative model has been derived and compared to experimental sorption data obtained in this PhD thesis. The model considers log $R_{d,in}$ as determined experimentally in this work for Pu sorption in the absence of ISA, and assumes a decreased sorption caused only by formation of dissolved Ca(II)–Pu(IV)–OH–ISA complexes. Thermodynamic data derived in this PhD thesis are used to calculate the concentrations of the complexes Ca(II)–Pu(IV)–OH–ISA forming in solution.

The outcome of sorption experiments conducted with log $[Pu]_{in} = –8.5$ in the presence of ISA defines two different cases:

- **Case I**, showing the strongest Pu sorption. This case has been observed only in desorption experiments and sorption experiments following the sequence "(Cement + Pu) + ISA". Data in Case I can be explained approximately by the simplified model, especially at log $[ISA]_{tot} = –2$.
- **Case II**. This case corresponds to some sorption experiments performed following the order "(Pu + ISA) + Cement". Results in Case II show higher Pu concentrations in solution, and accordingly lower R_d and higher F_{red}. The hypothesis proposed to explain these results refers to a strong kinetic stabilization of aqueous Pu species in solution and/or the substantial coverage of the cement surface by ISA, which significantly affects the properties of this surface and accordingly impacts Pu sorption at least temporarily.

The conclusions summarized above highlight that solubility phenomena likely play a role in controlling the concentration of Pu for several of the investigated systems in the presence of cement. Further experiments with lower Pu concentrations (possibly using shorter-lived ^{238}Pu or ^{239}Pu isotopes) could help in providing a more insightful mechanistic view on the sorption phenomena controlling Pu retention / mobility in cementitious systems.

This extensive experimental work reflects the high complexity of the ternary system Pu–ISA–cement and clearly demonstrates the key impact of ISA on Pu retention on cement under reducing conditions. The results and conclusions summarized here represent a reasonable empirical basis to quantitatively assess the impact of ISA on the sorption of Pu, but so far cannot provide a final mechanistic insight on the uptake process itself.

5 References

[1] Tasi, Á., Gaona, X., Fellhauer, D., Böttle, M., Rothe, J., Dardenne, K., Schild, D., Grive, M., Colas, E., Bruno, J., Kallstrom, K., Altmaier, M., Geckeis, H., *Redox behavior and solubility of Plutonium under alkaline, reducing conditions.* Radiochimica Acta doi: 10.1515/ract-2017-2870, 2018.

[2] Tasi, Á., Gaona, X., Fellhauer, D., Böttle, M., Rothe, J., Dardenne, K., Polly, R., Grive, M., Colas, E., Bruno, J., Kallstrom, K., Altmaier, M., Geckeis, H., *Thermodynamic description of the plutonium - alpha-D-isosaccharinic acid system: solubility, complexation and redox behavior.* Submitted to Applied Geochemistry (Migration2017 special issue), 2018.

[3] Tasi, Á., Gaona, X., Fellhauer, D., Böttle, M., Rothe, J., Dardenne, K., Polly, R., Grive, M., Colas, E., Bruno, J., Kallstrom, K., Altmaier, M., Geckeis, H., *Thermodynamic description of the plutonium - alpha-D-isosaccharinic acid system II: formation of quaternary Ca(II)-Pu(IV)-OH-ISA complexes.* Submitted to Applied Geochemistry (Migration2017 special issue), 2018.

[4] SKB, *Safety analysis SFR 1. Long-Term Safety*, Svensk Kärnbränslehantering AB, Stockholm, Sweden, 2008.

[5] Neck, V., Altmaier, M., Fanghänel, T., *Solubility of plutonium hydroxides/hydrous oxides under reducing conditions and in the presence of oxygen.* Comptes Rendus Chimie 10, p. 959-977, 2007.

[6] Neck, V., Altmaier, M., Seibert, A., Yun, J.I., Marquardt, C.M., Fanghänel, T., *Solubility and redox reactions of Pu(IV) hydrous oxide: Evidence for the formation of PuO2+x(s, hyd).* Radiochimica Acta 95, p. 193-207, 2007.

[7] Walther, C., Rothe, J., Brendebach, B., Fuss, M., Altmaier, M., Marquardt, C.M., Büchner, S., Cho, H.-R., Yun, J.I., Seibert, A., *New insights in the formation processes of Pu(IV) colloids.* Radiochimica Acta 97, p. 199-207, 2009.

[8] Walther, C., *From Hydrolysis to the Formation of Colloids - Polymerization of Tetravalent Actinide Ions*, in *Faculty of Chemistry, Pharmaceutical Sciences and Geosciences*. 2008, Johannes Gutenberg University, Mainz: Forschungzentrum Karlsruhe Gmbh, Karlsruhe, Germany.

[9] Guillaumont, R., Fanghänel, T., Neck, V., Fuger, J., Palmer, D.A., Grenthe, I., Rand, M.H., *Chemical Thermodynamics, Vol. 5. Update on the Chemical Thermodynamics of Uranium, Neptunium, Plutonium, Americium and Technetium*. OECD, NEA-TDB, Elsevier, North Holland, Amesterdam, 2003.

[10] Glaus, M.A., Van Loon, L.R., *Degradation of cellulose under alkaline conditions: new insights from a 12 years degradation study.* Environ Sci Technol 42, p. 2906-2911, 2008.

[11] Glaus, M.A., Van Loon, L.R., Achatz, S., Chodura, A., Fischer, K., *Degradation of cellulosic materials under the alkaline conditions of a cementitious repository for low and intermediate level radioactive waste. Part I: Identification of degradation products.* Analytica Chimica Acta 398, p. 111-112, 1999.

[12] Gaona, X., Montoya, V., Colàs, E., Grivé, M., Duro, L., *Review of the complexation of tetravalent actinides by ISA and gluconate under alkaline to hyperalkaline conditions.* J Contam Hydrol 102, p. 217-27, 2008.

[13] Wieland, E., *Sorption Data Base for the Cementitious Near Field of L/ILW and ILW Repositories for Provisional Safety Analyses for SGT-E2*, Paul Scherrer Institut, Wettlingen, Switzerland, 2014.

[14] Poinssot, C., Geckeis, H., *Radionuclide Behaviour in the Natural Environment*, Woodhead Publishing Ltd., Cambridge, UK, 2012.

[15] Seaborg, G.T., Loveland, W.D., *The elements beyond uranium*, J. Wiley and Sons Publishing Co., New York, U.S.A., 1990.
[16] Katz, J.J., Seaborg, G.T., Morss, L.R., *The Chemistry of the Actinide Elemements*. 2nd ed, Springer Netherlands, Chapman and Hall Ltd., 1986.
[17] Tananaev, I.G., Nikonov, M.V., Myasoedov, B.F., Clark, D.L., *Plutonium in higher oxidation states in alkaline media.* Journal of Alloys and Compounds 444-445, p. 668-672, 2007.
[18] Nikonov, M.V., Kiselev, Y.M., Tananaev, I.G., Myasoedov, B.F., *Plutonium volatility in ozonization of alkaline solutions of Pu(VI) hydroxo complexes.* Doklady Chemistry 437, p. 69-71, 2011.
[19] Seaborg, G.T., Katz, J.J., Manning, W.M., *Division IV. - Plutonium Project Record*, in *The Transuranium Elements*. 1949, McGraw-Hill Book Co., Inc. p. 345-347.
[20] Clark, D.L., *The chemical complexities of plutonium.* Los Alamos Science 26, p. 364-381, 2000.
[21] Clark, D.L., Hecker, S.S., Jarvinen, G.D., Neu, M.P., *Plutonium*, in *The Chemistry of the Actinide and Transactinide Elements*, L.R. Morss, N.M. Edelstein, and J. Fuger, Editors. 2006, Springer Netherlands: Dordrecht. p. 813-1264.
[22] Newton, T.W., Rabideau, S.W., *A Review of the Kinetics of the Aqueous Oxidation–Reduction Reactions of Uranium, Neptunium and Plutonium.* The Journal of Physical Chemistry 63, p. 365-370, 1959.
[23] Choppin, G.R., Bond, A.H., Hromadka, P.M., *Redox speciation of plutonium.* Journal of Radioanalytical and Nuclear Chemistry 219, p. 203-210, 1997.
[24] Knopp, R., Neck, V., Kim, J.I., *Solubility, Hydrolysis and Colloid Formation of Plutonium(IV)* Radiochimica Acta 86, p. 101-108, 1999.
[25] Icker, M., Walther, C., Neck, V., Geckeis, H., *The redox potential of Pu containing acidic solutions and the fate of "Pu(IV)-colloids": Direct measurement versus optical absorption spectroscopy.* IOP Conference Series: Materials Science and Engineering 9, p. 012060, 2010.
[26] Reilly, S.D., Neu, M.P., *Pu(VI) Hydrolysis: Further Evidence for a Dimeric Plutonyl Hydroxide and Contrasts with U(VI) Chemistry.* Inorg Chem 45, p. 1839-1846, 2006.
[27] Rao, L., Tian, G., Di Bernardo, P., Zanonato, P., *Hydrolysis of plutonium(VI) at variable temperatures (283-343 K).* Chemistry 17, p. 10985-93, 2011.
[28] Runde, W., *The chemical interactions of actinides in the environment.* Los Alamos Science 26, p. 392-411, 2000.
[29] Altmaier, M., Neck, V., Lützenkirchen, J., Fanghänel, T., *Solubility of plutonium in MgCl2 and CaCl2 solutions in contact with metallic iron.* Radiochimica Acta 97, 2009.
[30] Felmy, A.R., Rai, D., Schramke, J.A., Ryan, J.L., *The Solubility of Plutionium Hydroxide in Dilute Solution and in High-Ionic-Strenght Cloride Brines.* Radiochimica Acta 48, p. 29-35, 1989.
[31] Lemire, R.J., Fuger, J., Nitsche, H., Potter, P.E., Rand, M.H., Rydberg, J., Spahiu, K., Sullivan, J.C., Ullman, W.J., Vitorge, P., Wanner, H., *Chemical Thermodynamics, Vol. 4. Chemical Thermodynamics of Neptunium and Plutonium.* OECD, NEA-TDB, Elsevier, North Holland, Amsterdam, 2001.
[32] Nilsson, H., *The Chemistry of Plutonium Solubility, Ph.D. Thesis*, Chalmers University of Technology (Nuclear Chemistry, Department of Materials and Surface Chemistry), Göteborg, Sweden, 2004.
[33] Cho, H.R., Youn, Y.S., Jung, E.C., Cha, W., *Hydrolysis of trivalent plutonium and solubility of Pu(OH)3 (am) under electrolytic reducing conditions.* Dalton Transactions 45, p. 19449-19457, 2016.
[34] Fujiwara, K., Yamana, H., Fujii, T., Moriyama, H., *Solubility product of plutonium hydrous oxide.* Journal of Nuclear Fuel Cycle and Environment (Jpn) 7, p. 17-24, 2001.

[35] Fujiwara, K., Yamana, H., Fujii, T., Moriyama, H., *Solubility product of plutonium hydrous oxide and its ionic strength dependence.* Radiochimica Acta 9, p. 857, 2002.
[36] Rai, D., Gorby, Y.A., Fredrickson, J.K., Moore, D.A., Yui, M., *Reductive Dissolution of PuO2(am): The Effect of Fe(II) and Hydroquinone.* Journal of Solution Chemistry 31, p. 433-453, 2002.
[37] Kraus, K.A., Dam, J.R., *Hydrolytic Behavior of Plutonium (III) Acid-Base Titrations of Plutonium (III).* Technical Report, AECD-2543 (CN-2832), 1945.
[38] Hubert, S., Hussonnois, M., Guillaumont, R., *Comportement du plutonium trivalent lors de son extraction par la thenoyltrifluoroacetone.* Journal of Inorganic Nuclear Chemistry 37, p. 1255-1258, 1975.
[39] Nair, G.M., Chander, K., Joshi, J.K., *Hydrolysis constants of plutonium(III) and americium(III)* Radiochimica Acta 30, p. 37-40, 1982.
[40] Fellhauer, D., *Untersuchungen zur Redoxchemie und Löslichkeit von Neptunium und Plutonium, PhD-thesis*, Ruprecht-Karls-Universität Heidelberg, Heidelberg, Germany, 2013.
[41] Powell, B.A., Fjeld, R.A., Kaplan, D.I., Coates, J.T., Serkiz, S.M., *Pu(V)O2+ Adsorption and Reduction by Synthetic Magnetite (Fe3O4).* Environmental Science & Technology 38, p. 6016-6024, 2004.
[42] Powell, B.A., Duff, M.C., Kaplan, D.I., Fjeld, R.A., Newville, M., Hunter, D.B., Bertsch, P.M., Coates, J.T., Eng, P., Rivers, M.L., Serkiz, S.M., Sutton, S.R., Triay, I.R., Vaniman, D.T., *Plutonium Oxidation and Subsequent Reduction by Mn(IV) Minerals in Yucca Mountain Tuff.* Environmental Science & Technology 40, p. 3508-3514, 2006.
[43] Kirsch, R., Fellhauer, D., Altmaier, M., Neck, V., Rossberg, A., Fanghänel, T., Charlet, L., Scheinost, A.C., *Oxidation State and Local Structure of Plutonium Reacted with Magnetite, Mackinawite, and Chukanovite.* Environmental Science & Technology 45, p. 7267-7274, 2011.
[44] Felmy, A.R., Moore, D.A., Rosso, K.M., Qafoku, O., Rai, D., Buck, E.C., Ilton, E.S., *Heterogeneous reduction of PuO(2) with Fe(II): importance of the Fe(III) reaction product.* Environ Sci Technol 45, p. 3952-8, 2011.
[45] Felmy, A.R., Moore, D.A., Pearce, C.I., Conradson, S.D., Qafoku, O., Buck, E.C., Rosso, K.M., Ilton, E.S., *Controls on soluble Pu concentrations in PuO2/magnetite suspensions.* Environ Sci Technol 46, p. 11610-11617, 2012.
[46] Felmy, A.R., Moore, D.A., Qafoku, O., Buck, E., Conradson, S.D., Ilton, E.S., *Heterogeneous reduction of 239PuO2 by aqueous Fe(II) in the presence of hematite.* Radiochimica Acta 101, p. 701-710, 2013.
[47] González-Siso, M.R., Gaona, X., Duro, L., Schild, D., Fellhauer, D., Pidchenko, I., Vitova, T., Altmaier, M., Bruno, J., *Interaction of Pu, U and Tc with iron corrosion products under hyperalkaline reducing conditions.* 15th International Conference on the Chemistry and Migration Behaviour of Actinides and Fission Products in the Geosphere, MIGRATION 2015, Abstract book, p. 329-330, 2015.
[48] Atkins, M., Glasser, F.P., *Application of Portland cement-based materials to radioactive waste immobilization.* Waste Management 12, p. 105-131, 1992.
[49] Tits, J., Wieland, E., Muller, C.J., Landesman, C., Bradbury, M.H., *Strontium binding by calcium silicate hydrates.* J Colloid Interface Sci 300, p. 78-87, 2006.
[50] Ochs, M., Mallants, D., Wang, L., *Topics in Safety, Risk, Reliability and Quality, Vol. 29. Radionuclide and Metal Sorption on Cement and Concrete*, A.V. Gheorghe, Springer International Publishing, Switzerland, 2016.
[51] Berner, U., *Evolution of pore water chemistry during degradation of cement in a radioactive waste repository environment.* Waste Manag 12, p. 201–219, 1992.

[52] Neall, F.B., *Modelling of the Near-Field Chemistry of the SMA Repository at the Wellenberg Site*, Paul Scherrer Institut, Villigen, Switzerland, 1994.
[53] Atkinson, A., Everitt, N.M., Guppy, R., *Evolution of pH in a Radwaste Repository: Experimental Simulation of Cement Leaching: Part 1*, Department of Environment, London, UK, 1989.
[54] Bradbury, M.H., Van Loon, L.R., *Cementitious near-field sorption data bases for performance assessment of a L/ILW repository in a Palfris Marl host rock*, Paul Scherrer Institute, Switzerland, 1997.
[55] Pavasars, I., Hagberg, J., Borén, H., Allard, B., *Alkaline degradation of cellulose: mechanisms and kinetics.* Journal of Polymers and the Environment 11, p. 39–47, 2003.
[56] Van Loon, L.R., Glaus, M.A., Laube, A., Stallone, S., *Degradation of cellulosic materials under the alkaline conditions of a cementitious repository for low- and intermediate-level radioactive waste: II. Degradation kinetics.* Journal of Environmental Polymer Degradation, p. 41–51, 1999.
[57] Van Loon, L.R., Glaus, M.A., *Experimental and theoretical studies on alkaline degradation of cellulose and its impact on the sorption of radionuclides*, Paul Scherrer Institute, Switzerland, 1998.
[58] Aspinall, G., Carter, M., Loss, M., *The Degradation of Xylobiose and Xylotriose by Alkali*. Journal of the Chemical Society, Chemical Communications, p. 4807-4810, 1956.
[59] Randall, M., Rigby, B., Thomson, O., Trivedi, D., *Assessment of the effects of cellulose degradation products on the behaviour of europium and thorium*, National Nuclear Laboratory, Chadwick House, Warington, UK, 2013.
[60] Pavasars, I., *Characterisation of organic substances in waste materials under alkaline conditions*, in *Department of Water and Environmental Studies*. 1999, Linköping University: Linköping, Sweden.
[61] Van Loon, L.R., Glaus, M.A., Laube, A., Stallone, S., *Degradation of cellulosic materials under the alkaline conditions of a cementitious repository for low- and intermediate-level radioactive waste. Part III. Effect of the degradation products on the sorption of radionuclides on feldspar.* Radiochimica Acta 86, p. 183–190, 1999.
[62] Keith-Roach, M., Lindgren, M., Källström, K., *Assessment of complexing agent concentrations in SFR*, Swedish Nuclear Fuel and Waste Management Co, Stockholm, Sweden, 2014.
[63] Hummel, W., Anderegg, G., Rao, L., Puigdomenech, I., Tochiyama, O., *Chemical Thermodynamics, Vol. 9. Chemical thermodynamics of compounds and complexes of U, Np, Pu, Am, Tc, Se, Ni and Zr with selected organic ligands*. OECD, NEA-TDB, Elsevier, North-Holland, Amsterdam, 2005.
[64] Rai, D., Kitamura, A., *Evaluation of equilibrium constants for deprotonation and lactonisation of α-D-isosaccharinic acid.* Journal of Nuclear Science and Technology 53, p. 459-467, 2015.
[65] Evans, N., *Studies on Metal α-Isosaccharinic Acid Complexes*. 2003, Loughborough University: Loughborough, UK.
[66] Zhang, Z., Helms, G., Clark, S.B., Tian, G., Zanonato, P., Rao, L., *Complexation of Uranium(VI) by Gluconate in Acidic Solutions: a Thermodynamic Study with Structural Analysis.* Inorg Chem, p. 3814-3824, 2009.
[67] Van Duin, M., Peters, J.A., Kieboom, A.P.G., Van Bekkum, H., *A general coordination-ionization scheme for polyhydroxy carboxylic acids in water.* Recueil des TRavaux Chimiques des Pays-Bas 108, 1989.
[68] Rai, D., Rao, L., Xia, Y., *Solubility of crystalline calcium isosaccharinate.* J. Solution Chem. 27, p. 1109-1122, 1998.

[69] Van Loon, L.R., Glaus, M.A., Vercammen, K., *Solubility products of calcium isosaccharinate and calcium gluconate.* Acta Chem. Scand. 53, p. 235-240, 1999.
[70] Vercammen, K., Glaus, M.A., Van Loon, L.R., *Complexation of calcium by α-isosaccharinic acid under alkaline conditions.* Acta Chem. Scand. 53, p. 241-246, 1999.
[71] Vercammen, K., *Complexation of Calcium, Thorium and Europium by α-Isosaccharinic Acid under Alkaline Conditions.* 2000, Swiss Federal Institute of Technology: Zurich, Switzerland.
[72] Rai, D., Hess, N.J., Xia, Y.X., Rao, L., Cho, H.M., Moore, R.C., Van Loon, L.R., *Comprehensive thermodynamic model applicable to highly acidic to basic conditions for isosaccharinate reactions with Ca(II) and Np(IV).* Journal of Solution Chemistry 32, p. 665-689, 2003.
[73] Van Loon, L.R., Glaus, M.A., Vercammen, K., *Stability of the Ion Pair Between Ca2+ and 2-(Hydroxymethyl)-3-Deoxy-D-erythro-Pentonate (α-Isosaccharinate).* Journal of Solution Chemistry 33, p. 1573-1583, 2004.
[74] Dudas, C., Kutus, B., Boszormenyi, E., Peintler, G., Kele, Z., Palinko, I., Sipos, P., *Comparison of the Ca2+ complexing properties of isosaccharinate and gluconate - is gluconate a reliable structural and functional model of isosaccharinate?* Dalton Trans 46, p. 13888–13896, 2017.
[75] Blanc, P., Bourbon, X., Lassin, A., Gaucher, E.C., *Chemical model for cement-based materials: Temperature dependence of thermodynamic functions for nanocrystalline and crystalline C–S–H phases.* Cement and Concrete Research 40, p. 851-866, 2010.
[76] Glaus, M.A., Van Loon, L.R., *Cellulose Degradation at Alkaline Conditions: Long-Term Experiments at Elevated Temperatures*, Paul Scherrer Institut, PSI, Wettingen, Switzerland, 2004.
[77] Whistler, R.L., BeMiller, J.N., *Alkaline Degradation of Guaran and Characterization of "beta"-D-Isosaccharinic Acid.* The Journal of Organic Chemistry 26, p. 2886-2892, 1961.
[78] Greenfield, B.F., Holtom, G.J., Hurdus, M.H., O'Kelly, N., Pilkington, N.J., Rosevear, A., Spindler, M.W., Williams, S.J., *The identification and degradation of isosaccharinic acid, a cellulose degradation product.* Materials Research Society Symposium Proceedings 353, p. 1151–1158, 1995.
[79] Glaus, M.A., Van Loon, L.R., *Chemical Reactivity of alpha-Isosaccharinic Acid in Heterogeneous Alkaline Systems*, Paul Scherrer Institut, CH-5232 Villigen PSI, Switzerland, 2009.
[80] Rout, S.P., Charles, C.J., Doulgeris, C., McCarthy, A.J., Rooks, D.J., Loughnane, J.P., Laws, A.P., Humphreys, P.N., *Anoxic Biodegradation of Isosaccharinic Acids at Alkaline pH by Natural Microbial Communities.* PLoS One 10, p. e0137682, 2015.
[81] Kuippers, G., Bassil, N.M., Boothman, C., Bryan, N., Lloyd, J.R., *Microbial degradation of isosaccharinic acid under conditions representative for the far field of radioactive waste disposal facilities.* Mineralogical Magazine 79, p. 1443-1454, 2015.
[82] Bassil, N.M., Bryan, N., Lloyd, J.R., *Microbial degradation of isosaccharinic acid at high pH.* ISME J 9, p. 310-20, 2015.
[83] Rizoulis, A., Steele, H.M., Morris, K., Lloyd, J.R., *The potential impact of anaerobic microbial metabolism during the geological disposal of intermediate-level waste.* Mineralogical Magazine 76, p. 3261-3270, 2012.
[84] Van Loon, L.R., Glaus, M.A., Stallone, S., Laube, A., *Sorption of Isosaccharinic Acid, a Cellulose Degradation Product, on Cement.* Environ Sci Technol 31, p. 1243-1245, 1997.

[85] Bradbury, M.H., Sarott, F.-A., *Sorption Databases for the Cementitious Near-field of a L/ILW Repository for Performance Assessment*, Paul Scherrer Institut, CH-5232, Villigen PSI, Switzerland, 1995.
[86] Pointeau, I., Hainos, D., Coreau, N., Reiller, P., *Effect of organics on selenite uptake by cementitious materials.* Waste Manag 26(7), p. 733-40, 2006.
[87] Pointeau, I., Coreau, N., Reiller, P.E., *Uptake of anionic radionuclides onto degraded cement pastes and competing effect of organic ligands.* Radiochimica Acta 96, 2008.
[88] Pointeau, I., Reiller, P., Mace, N., Landesman, C., Coreau, N., *Measurement and modeling of the surface potential evolution of hydrated cement pastes as a function of degradation.* J Colloid Interface Sci 300, p. 33-44, 2006.
[89] Dzombac, D.A., Morel, F.M.M., *Surface ComplexationModeling: Hydrous Ferric Oxide*, Wiley–Interscience, New York, 1990.
[90] Rai, D., Kitamura, A., *Thermodynamic equilibrium constants for important isosaccharinate reactions: A review.* The Journal of Chemical Thermodynamics, 2017.
[91] Moreton, A.D., *Thermodynamic modeling of the effect of hydroxycarboxylic acids on the solubility of plutonium at high pH.* Materials Research Society Symposium Proceedings 294, p. 753–758, 1993.
[92] Greenfield, B.F., Hurdus, M.H., Spindler, M.W., Thomason, H.P., *The Effect of the Products from the Anaerobic Degradation of Cellulose on the Solubility and Sorption of Radioelements in the Near Field*, Nuclear Industry Radioactive Waste Executive (Nirex), UK, 1997.
[93] Moreton, A.D., Pilkington, N.J., Tweed, C.J., *Thermodynamic Modeling of the Effect of Hydroxycarboxylic Acids on the Solubility of Plutonium at High pH*, Nuclear Industry Radioactive Waste Executive (Nirex), UK 2000.
[94] Rai, D., Rao, L., Moore, D.A., *The influence of isosaccharinic acid on the solubility of Np(IV) hydrous oxide.* Radiochimica Acta 83, p. 9–13, 1998.
[95] Rai, D., Rao, L., Moore, R.C., Bontchev, R., Holt, K., *Development of Biodegradable Isosaccharinate-Containing Foams for Decontamination of Actinides: Thermodynamic and Kinetic Reactions between Isosaccharinate and Actinides on Metal and Concrete Surfaces*, USA, 2004.
[96] Pallagi, A., Tasi, Á., Gácsi, A., Csáti, M., Pálinkó, I., Peintler, G., Sipos, P., *The solubility of Ca(OH)2 in extremely concentrated NaOH solutions at 25°C.* Central European Journal of Chemistry 10, p. 332-337, 2012.
[97] Warwick, P., Evans, N., Hall, T., Vines, S., *Stability constants of uranium(IV)-α-isosaccharinic acid and gluconic acid complexes.* Radiochimica Acta 92, p. 897-902, 2004.
[98] Rai, D., Yui, M., Moore, D.A., Rao, L., *Thermodynamic Model for ThO2(am) Solubility in Isosaccharinate Solutions.* Journal of Solution Chemistry 38, p. 1573-1587, 2009.
[99] Vercammen, K., Glaus, M.A., Van Loon, L.R., *Evidences for the existence of complexes between Th(IV) and α-isosaccharinic acid under alkaline conditions.* Radiochimica Acta 84, p. 221–224, 1999.
[100] Vercammen, K., Glaus, M.A., Van Loon, L.R., *Complexation of Th(IV) and Eu(III) by alpha-isosaccharinic acid under alkaline conditions.* Radiochimica Acta 89, p. 393-401, 2001.
[101] Allard, S., Ekberg, C., *Complexing properties of α-isosaccharinate: thorium.* Radiochimica Acta 94, p. 537-540, 2006.
[102] Allard, S., Ekberg, C., *Complexing Properties of α-Isosaccharinate: Stability Constants, Enthalpies and Entropies of Th-complexation with Uncertainty Analysis.* Journal of Solution Chemistry 35, p. 1173-1186, 2006.

[103] Tits, J., Wieland, E., Bradbury, M.H., Eckert, P., Schaible, A., *The uptake of Eu(III) and Th(IV) by calcite under hyperalkaline conditions*, Paul Scherrer Insitut, Villigen, Switzerland, 2002.
[104] Wieland, E., Tits, J., Dobler, J.P., Spieler, P., *The effect of α-isosaccharinic acid on the stability of and Th(IV) uptake by hardened cement paste.* Radiochimica Acta 90, p. 683–688, 2002.
[105] Tits, J., Wieland, E., Bradbury, M.H., *The effect of isosaccharinic acid and gluconic acid on the retention of Eu(III), Am(III) and Th(IV) by calcite.* Applied Geochemistry 20, p. 2082-2096, 2005.
[106] Altmaier, M., Neck, V., Müller, R., Fanghänel, T., *Solubility of ThO2·xH2O(am) in carbonate solution and the formation of ternary Th(IV) hydroxide-carbonate complexes.* Radiochimica Acta 93, p. 83–92, 2005.
[107] Colàs, E., *Complexation of Th(IV) and U(VI) by polyhydroxy and polyamino carboxylic acids*. 2014, Universitat Politècnica de Catalunya (UPC): Barcelona, Spain.
[108] Zhernosekov, K.P., Mauerhofer, E., Getahun, G., Warwick, P., Rösch, F., *Complex formation of Tb3+ with glycolate, D-gluconate and α-isosaccharinate in neutral aqueous perchlorate solutions.* . Radiochimica Acta 91, p. 599–602, 2003.
[109] Wang, L., Martens, E., Jacques, D., De Cannière, P., Berry, J., Mallants, D., *Review of sorption values for the cementitious near field of a near surface radioactive waste disposal facility*, Brussels, Belgium., 2009.
[110] Tits, J., Fujita, T., Harfouche, M., Dähn, R., Tsukamoto, M., Wieland, E., *Radionuclide uptake by calcium silicate hydrates: Case studies with Th(IV) and U(VI)*, Paul Scherrer Institut, CH-5232 Villigen PSI, Switzerland, 2014.
[111] Mandaliev, P., Stumpf, T., Tits, J., Dähn, R., Walther, C., Wieland, E., *Uptake of Eu(III) by 11Å tobermorite and xonotlite: A TRLFS and EXAFS study.* Geochimica et Cosmochimica Acta 75, p. 2017-2029, 2011.
[112] Gaona, X., Dahn, R., Tits, J., Scheinost, A.C., Wieland, E., *Uptake of Np(IV) by C-S-H phases and cement paste: an EXAFS study.* Environ Sci Technol 45, p. 8765-71, 2011.
[113] Wieland, E., Van Loon, L.R., *Cementitious Near-Field Sorption Data Base for Performance Assessment of an ILW Repository in Opalinus Clay*, Paul Scherrer Institut, CH-5232 Villigen PSI, Switzerland, 2002.
[114] Allard, B., Eliasson, L., Hoglund, S., Andersson, K., *Sorption of Cs, I and actinides in concrete systems*, 1984.
[115] Hoglund, S., Eliasson, L., Allard, B., Andersson, K., Torstenfelt, B., *Sorption of some fission products and actinides in concrete systems.* Materials Research Society Symposium Proceedings 50, p. 683–690, 1985.
[116] Bayliss, S., McCrohon, R., Oliver, P., Pilkington, N.J., Thomason, H.P., *Near-field sorption studies: January 1989 to June 1991*, 1996.
[117] Bayliss, S., Howse, R.M., McCrohon, R., Oliver, P., *Near-field sorption studies*, 2000.
[118] Aggarwal, S., Angus, M.J., Ketchen, J., *Sorption of radionuclides onto specific mineral phases present in repository cements*, 2000.
[119] Pointeau, I., Landesman, C., Coreau, N., Moisan, C., Reiller, P., *Etude de la rétention chimique des radionucléides Cs(I), Am(III), Zr(IV), Pu(IV), Nb(V), U(VI) et Tc(IV) par les matériaux cimentaires dégradés*, 2004.
[120] Baston, G.M.N., Berry, J.A., Brownsword, M., Heath, T.G., Tweed, C.J., Williams, S.J., *Sorption of plutonium and americium on repository, backfill and geological materials relevant to the JNFL low-level radioactive waste repository at Rokkasho-Mura.* Materials Research Society Symposium Proceedings 353, p. 957–964, 1995.

[121] Holgersson, S., Albinsson, Y., Allard, B., Borén, H., Pavasars, I., Engkvist, I., *Effects of Gluco-isosaccharinate on Cs, Ni, Pm and Th Sorption onto, and Diffusion into Cement.* Radiochimica Acta 82, p. 393-398, 1998.
[122] Ochs, M., Colàs, E., Grivé, M., Olmeda, J., Campos, I., Bruno, J., *Reduction of radionuclide uptake in hydrated cement systems by organic complexing agents: Selection of reduction factors and speciation calculations*, 2014.
[123] Felipe-Sotelo, M., Hinchliff, J., Evans, N., Warwick, P., Read, D., *Sorption of radionuclides to a cementitious backfill material under near-field conditions.* Mineralogical Magazine 76, p. 3401-3410, 2012.
[124] Altmaier, M., Metz, V., Neck, V., Müller, R., Fanghänel, T., *Solid-liquid equilibria of Mg(OH)2(cr) and Mg2(OH)3Cl·4H2O(cr) in the system Mg-Na-H-OH-Cl-H2O at 25°C.* Geochimica et Cosmochimica Acta 67, p. 3595-3601, 2003.
[125] Altmaier, M., Gaona, X., Fellhauer, D., Buckau, G., *FP7 EURATOM Collaborative Project "Redox Phenomena Controlling Systems"Intercomparison of redox determination methods on designed and near-natural aqueous systems*, KIT Scientific Reports 7572, Karlsruhe, Germany, 2010.
[126] Gamsjäger, H., Gajda, T., Sangster, J., Saxena, S.K., Voigt, W., *Chemical Thermodynamics Series, Vol. 12. Chemical Thermodynamics of Tin*, NEA-TDB, Elsevier, North Holland, Amesterdam, 2012.
[127] Kobayashi, T., Scheinost, A.C., Fellhauer, D., Gaona, X., Altmaier, M., *Redox behavior of Tc(VII)/Tc(IV) under various reducing conditions in 0.1M NaCl solutions.* Radiochimica Acta 101, p. 323–332, 2013.
[128] Yalcintas, E., Gaona, X., Scheinost, A.C., Kobayashi, T., Altmaier, M., Geckeis, H., *Redox chemistry of Tc(VII)/Tc(IV) in dilute to concentrated NaCl and MgCl2 solutions.* Radiochimica Acta 103, p. 57–72, 2015.
[129] Schepperle, J., *Untersuchungen zur Löslichkeit und Komplexierung von vierwertigem Plutonium und Neptunium in verdünnten und konzentrierten Salzlösungen (on-going)*, in *Institute for Nuclear Waste Disposal (INE)*. 2017, Karlsruhe Institute of Technology: Karlsruhe, Germany.
[130] Akatsu, J., *Separation of Plutonium-238 from Fission Products by Solvent Extraction Using HDEHP.* Journal of Nuclear Science and Technology 10, p. 696-699, 1973.
[131] Nitsche, H., Lee, S.C., Gatti, R.C., *Determination of plutonium oxidation states at trace levels pertinent to nuclear waste disposal.* Journal of Radioanalytical and Nuclear Chemistry 124, p. 171-185, 1988.
[132] Schramke, J.A., Rai, D., Fulton, R.W., Choppin, G.R., *Determination of aqueous plutonium oxidation states by solvent extraction.* Journal of Radioanalytical and Nuclear Chemistry, p. 333-346, 1989.
[133] Nitsche, H., Roberts, K., Xi, R., Prussin, T., Becraft, K., Al Mahamid, I., Silber, H., Carpenter, S.A., Gatti, R.C., Novak, C.F., *Long term plutonium solubility and speciation studies in a synthetic brine.* Radiochimica Acta, p. 3-8, 1994.
[134] Manchanda, V.K., Mohapatra, P.K., *1-Phenyl-3-methyl-4-benzoyl-pyrazolone-5: A Promising Extractant for Plutonium.* Separation Science and Technology 29, p. 1073-1086, 1994.
[135] Graser, C.H., Banik, N.L., Bender, K.A., Lagos, M., Marquardt, C.M., Marsac, R., Montoya, V., Geckeis, H., *Sensitive redox speciation of iron, neptunium, and plutonium by capillary electrophoresis hyphenated to inductively coupled plasma sector field mass spectrometry.* Anal Chem 87, p. 9786-94, 2015.
[136] Joint Commitee on Powder Diffraction Standards, *JCPDS-Powder diffraction files*, Swarthmore, USA, 2001.

[137] Seah, M.P., Gilmore, L.S., Beamson, G., *XPS: Binding energy calibration of electron spectrometers 5 - Re-evaluation of the reference energies.* . Surface and Interface Analysis 26, p. 642-649, 1998.
[138] Rothe, J., Butorin, S., Dardenne, K., Denecke, M.A., Kienzler, B., Loble, M., Metz, V., Seibert, A., Steppert, M., Vitova, T., Walther, C., Geckeis, H., *The INE-Beamline for actinide science at ANKA.* Rev Sci Instrum 83, p. 043105, 2012.
[139] Ravel, B., Newville, M., *ATHENA, ARTEMIS, HEPHAESTUS: data analysis for X-ray absorption spectroscopy using IFEFFIT.* Journal of Synchrotron Radiation 12, p. 537-541, 2005.
[140] Brendebach, B., Banik, N.L., Marquardt, C.M., Rothe, J., Denecke, M., Geckeis, H., *X-ray absorption spectroscopic study of trivalent and tetravalent actinides in solution at varying pH values.* Radiochimica Acta 97, p. 701-708, 2009.
[141] Stern, E.A., Newville, M., Ravel, B., Yacoby, Y., Haskel, D., *The UWXAFS analysis package – philosophy and details.* Physica B 209, p. 117-120, 1995.
[142] Ankudinov, A.L., Ravel, B., Rehr, J.J., Conradson, S.D., *Realspace multiple-scattering calculation and interpretation of X-ray absorption near-edge structure.* Phys. Rev. B 58, p. 7565-7576, 1998.
[143] De Nolf, W., Vanmeert, F., Janssens, K., *XRDUA: crystalline phase distribution maps by two-dimensional scanning and tomographic (micro) X-ray powder diffraction.* Journal of Applied Crystallography 47, p. 1107-1117, 2014.
[144] Smrcok, L., *Rietveld refinement of Y2O3, using the pearson VII profile shape function.* Crystal Research and Technology 24, p. 607-611, 1989.
[145] Kinniburgh, D.G., Cooper, D.M., *PhreePlot: Creating graphical output with PHREEQC*. 2009, Centre for Ecology and Hydrology: Deiniol Road, Bangor, Gwynedd, LL57 2UW, UK.
[146] Parkhurst, D.L., Appelo, C.A.J., *User's guide to PHREEQC (Version 2) – a computer program for speciation, batch reaction, one-dimensional transport and inverse geochemical calculation*, USGS, Denver, Colorado, USA, 1999.
[147] Parkhurst, D.L., Appelo, C.A.J., *U.S. Geological Survey Techniques and MethodsDescription of input and examples for PHREEQC version 3—A computer program for speciation, batch-reaction, one-dimensional transport, and inverse geochemical calculations: U.S. Geological Survey Techniques and Methods*, available only at http://pubs.usgs.gov/tm/06/a43/. 2013.
[148] Ciavatta, L., *The specific interaction theory in evaluating ionic equilibria.* Ann. Chim. (Rome) 70, p. 551–567, 1980.
[149] Hummel, W., *Ionic strength corrections and estimation of SIT ion interaction coefficients*, Paul Scherrer Institut, Villigen, Switzerland, 2009.
[150] Powell, M.J.D., *A method for minimizing a sum of squares of non-linear functions without calculating derivatives.* The Computer Journal 7, p. 303–307, 1965.
[151] Nelder, J.A., Mead, R., *A simplex method for function minimization.* Computer Journal 7, p. 308, 1965.
[152] Hohenberg, P., Kohn, W., *Inhomogeneous Electron Gas.* Physical Review 136, p. B864-B871, 1964.
[153] Kohn, W., Sham, L.J., *Self-Consistent Equations Including Exchange and Correlation Effects.* Physical Review 140, p. A1133-A1138, 1965.
[154] Ahlrichs, R., Furche, F., Hättig, C., Klopper, W.M., Sierka, M., Weigend, F., *TURBOMOLE v7.0*. 2015, University of Karlsruhe and Forschungszentrum Karlsruhe GmbH: Karlsruhe, Germany.
[155] Treutler, O., Ahlrichs, R., *Efficient molecular numerical integration schemes.* The Journal of Chemical Physics 102, p. 346-354, 1995.

[156] Eichkorn, K., Weigend, F., Treutler, O., Ahlrichs, R., *Auxiliary basis sets for main row atoms and transition metals and their use to approximate coulomb potentials.* Theor. Chem. Acc. 97, p. 119-124, 1997.
[157] Eichkorn, K., Treutler, O., Öhm, H., Ahlrichs, H.M., Ahlrichs, R., *Auxiliary basis sets to approximate Coulomb potentials.* Chem. Phys. Letters 242, p. 652-660, 1995.
[158] Deglmann, P., May, K., Furche, F., Ahlrichs, R., *Nuclear second analytical derivative calculations using auxiliary basis set expansions.* Chemical Physics Letters 384, p. 103-107, 2004.
[159] von Arnim, M., Ahlrichs, R., *Geometry optimization in generalized natural internal coordinates.* The Journal of Chemical Physics 111, p. 9183-9190, 1999.
[160] Schäfer, A., Horn, H., Ahlrichs, R., *Fully optimized contracted Gaussian basis sets for atoms Li to Kr.* The Journal of Chemical Physics 97, p. 2571-2577, 1992.
[161] Ahlrichs, R., Furche, F., Grimme, S., *Comment on "Assessment of exchange correlation functionals"*. Chem. Phys. Lett. 325(1-3), p. 317-321, 2000.
[162] Moritz, A., Cao, X., Dolg, M., *Quasirelativistic energy-consistent 5f-in-core pseudopotentials for trivalent actinide elements.* Theoretical Chemistry Accounts 117, p. 473-481, 2006.
[163] Moritz, A., Cao, X., Dolg, M., *Quasirelativistic energy-consistent 5f-in-core pseudopotentials for divalent and tetravalent actinide elements.* Theoretical Chemistry Accounts 118, p. 845-854, 2007.
[164] Klamt, A., Schuurmann, G., *Chem Soc Perkin Trans 2 1993, 5, 799;(b) Baldridge, K.; Klamt.* A. J Chem Phys 106, p. 6622, 1997.
[165] Klamt, A., *Conductor-like Screening Model for Real Solvents: A New Approach to the Quantitative Calculation of Solvation Phenomena.* J. Phys. Chem. 99, p. 2224-2235, 1995.
[166] Zachariansen, W.H., *Crystal Chemical Studies of the 5f-series of Elements. XII. New Compounds Representing known Structure Types.* Acta Crystallographica 2, p. 388-390, 1949.
[167] Gardner, E.R., Markin, T.L., Street, R.S., *The Plutonium-Oxygen phase diagram.* Journal of Inorganic Nuclear Chemistry 27, p. 541, 1965.
[168] Rothe, J., Walther, C., Brendebach, B., Büchner, S., Fuss, M., Denecke, M.A., Geckeis, H., *A combined XAFS, ESI TOF-MS and LIBD study on the formation of polynuclear Zr(IV), Th(IV) and Pu(IV) species.* Journal of Physics: Conference Series 190, p. 012188, 2009.
[169] Rothe, J., Walther, C., Denecke, M., Fanghaenel, T., *XAFS and LIBD Investigation of the Formation and Structure of Colloidal Pu(IV) Hydrolysis Products.* Inorganic Chemistry 43, p. 4708-4718, 2004.
[170] Courteix, D., Chayrouse, J., Heintz, L., Baptist, R., *XPS study of Pu oxides.* Solid State Communications 39, p. 209-213, 1981.
[171] Larson, D.T., Haschke, J.M., *XPS-AES Characterization of Plutonium Oxides and Oxide Carbide. The Existence of Plutonium Monoxide.* Inorganic Chemistry 20, p. 1945-1950, 1981.
[172] Cox, L.E., Farr, J.D., *4fbinding-energy shifts of the light-actinide dioxides and tetrafluorides.* Physical Review B 39, p. 11142-11145, 1989.
[173] Neck, V., Kim, J.I., *Solubility and hydrolysis of tetravalent actinides.* Radiochimica Acta 89, p. 1-16, 2001.
[174] Neck, V., Altmaier, M., Rabung, T., Lützenkirchen, J., Fanghänel, T., *Thermodynamics of trivalent actinides and neodymium in NaCl, MgCl2, and CaCl2 solutions: Solubility, hydrolysis, and ternary Ca-M(III)-OH complexes.* Pure and Applied Chemistry 81, p. 1555-1568, 2009.

[175] Gaona, X., Fellhauer, D., Altmaier, M., *Thermodynamic description of Np(VI) solubility, hydrolysis, and redox behavior in dilute to concentrated alkaline NaCl solutions.* Pure and Applied Chemistry 85, p. 2027–2049, 2013.
[176] Kobayashi, T., Sasaki, T., Kitamura, A. *Thermodynamic Study on the Complexation of U(IV) with Isosaccharinic Acid*. in *Actinides Conference, Book of abstracts*. 2017. Sendai.
[177] Neck, V., Altmaier, M., Fanghänel, T., *Thermodynamic data for hydrous and anhydrous PuO2+x(s).* Journal of Alloys and Compounds 444-445, p. 464-469, 2007.
[178] Cucinotta, D., De Stefano, C., Giuffrè, O., Lando, G., Milea, D., Sammartano, S., *Formation, stability and empirical relationships for the binding of Sn2+ by O-, N- and S-donor ligands.* Journal of Molecular Liquids 200, p. 329-339, 2014.
[179] Gaona, X., Tits, J., Dardenne, K., Liu, X., Rothe, J., Denecke, M.A., Wieland, E., Altmaier, M., *Spectroscopic investigations of Np(V/VI) redox speciation in hyperalkaline TMA-(OH, Cl) solutions.* Radiochimica Acta 100, p. 759-770, 2012.
[180] Shannon, R.D., *Revised effective ionic-radii and systematic studies of interatomic distances in halides and chalcogenides.* Acta Crystallogr. A 32, p. 751–767, 1976.
[181] Marcus, Y., *Thermodynamics of solvation of ions.* J. Chem. Soc. Faraday Trans. 87, p. 2995-2999, 1991.
[182] McNeilly, C.E., *The electrical properties of plutonium oxides.* Journal of Nuclear Materials 11, p. 53-58, 1964.
[183] Atlas, L.M., Schlehman, G.J., Readey, D.W., *Defects in PuO2-x: Density Measurements at High Temperature.* Journal of The American Ceramic Society 49, p. 624, 1966.
[184] Haschke, J.M., Hodges, A.E., Bixby, G.E., Lucas, R.L., *The reaction of Plutonium with water: kinetic and equilibrium behavior of binary and ternary phases in the Pu+O+H system*. G.A. Riordan, Albuquerque Operations Office, U.S. Department of Energy, Golden, Colorado, USA, 1983.
[185] Dinh, L.N., Haschke, J.M., Saw, C.K., Allen, P.G., McLean, W., *Pu2O3 and the plutonium hydriding process.* Journal of Nuclear Materials 408, p. 171-175, 2011.
[186] Haschke, J.M., Dinh, L.N., McLean, W., *The plutonium–oxygen phase diagram in the 25–900°C range: Non-existence of the PuO1.515 phase.* Journal of Nuclear Materials 458, p. 275-280, 2015.
[187] Petit, L., Svane, A., Szotek, Z., Temmerman, W.M., Stocks, G.M., *Electronic structure and ionicity of actinide oxides from first principles.* Physical Review B 81, p. 045108, 2010.
[188] Haschke, J.M., Allen, T.H., Morales, L.A., *Reaction of Plutonium Dioxide with Water: Formation and Properties of PuO2+x.* Science 287, p. 285-287, 2000.
[189] Conradson, S.D., Begg, B.D., Clark, D.L., Den Auwer, C., Espinosa-Faller, F.J., Gordon, P.L., Hess, N.J., Hess, R., Webster Keogh, D., Morales, L.A., Neu, M.P., Runde, W., Tait, C.D., Veirs, D.K., Villella, P.M., *Speciation and Unusual Reactivity in PuO2+x.* Inorganic Chemistry 42, p. 3715–3717, 2003.
[190] Petit, L., Svane, A., Szotek, Z., Temmerman, W.M., *First-principles calculations of PuO2+-x.* Science 301, p. 498-501, 2003.
[191] Banik, N.L., Brendebach, B., Marquardt, C.M., *Investigations of actinides in the context of final disposal of high-level radioactive waste: trivalent actinides in aqueous solution.* Journal of Radioanalytical and Nuclear Chemistry 300, p. 177-183, 2014.
[192] Skerencak-Frech, A., Maiwald, M., Trumm, M., Froehlich, D.R., Panak, P.J., *The complexation of Cm(III) with oxalate in aqueous solution at T = 20-90 degrees C: a combined TRLFS and quantum chemical study.* Inorg Chem 54, p. 1860-8, 2015.

[193] Frohlich, D.R., Trumm, M., Skerencak-Frech, A., Panak, P.J., *The Complexation of Cm(III) with Succinate Studied by Time-Resolved Laser Fluorescence Spectroscopy and Quantum Chemical Calculations.* Inorg Chem 55, p. 4504-11, 2016.
[194] Bouby, M., Geckeis, H., Lützenkirchen, J., Mihai, S., Schäfer, T., *Interaction of bentonite colloids with Cs, Eu, Th and U in presence of humic acid: A flow field-flow fractionation study.* Geochimica et Cosmochimica Acta 75, p. 3866-3880, 2011.
[195] Stronach, S.A., Glasser, F.P., *Modelling the impact of abundant geochemical components on the phase stability and solubility of the CaO-Si=2-H2O system at 25 C.* Adv. in Cem. Res. 9, p. 167-181, 1997.
[196] Lagerblad, B., *Leaching performance of concrete based on studies of samples from old concrete constructions,* Swedish Nuclear Fuel and Waste Management Co, Stockholm, Sweden, 2001.
[197] Cronstrand, P., *Modelling the long-time stability of the engineered barriers of SFR with respect to climate changes,* Swedish Nuclear Fuel and Waste Management Co, Stockholm, Sweden, 2007.
[198] Duro, L., Domènech, C., Grivé, M., Roman-Ross, G., Bruno, J., Källström, K., *Assessment of the evolution of the redox conditions in a low and intermediate level nuclear waste repository (SFR1, Sweden).* Applied Geochemistry 49, p. 192-205, 2014.
[199] Holman, D.A., Bennett, D.W., *A multicomponent kinetics study of the anaerobic decomposition of aqueous sodium dithionite.* J. Phys. Chem. 98, p. 13300-13307, 1994.
[200] Kilroy, W.P., *Anaerobic decomposition of dithionate in alkaline solution.* Journal of Inorganic Nuclear Chemistry 42, p. 1071-1073, 1980.
[201] Greenfield, B.F., Harrison, W.N., Robertson, G.P., Somers, P.J., Spindler, M.W., *Mechanistic Studies of the Alkaline Degradation of Cellulose in Cement,* AEA Technology Plc, Harwell, United Kingdom, 1993.
[202] Cho, H., Rai, D., Hess, N.J., Xia, Y.X., Rao, L., *Acidity and structure of isosaccharinate in aqueous solution: a nuclear magnetic resonance study.* Journal of Solution Chemistry 32, p. 69, 2003.
[203] Wong-Ng, W., McMurdie, H.F., Hubbard, C.R., A.D., M., *JCPDS-ICDD Research Associateship (Cooperative Program with NBS/NIST).* Journal of Research of the National Institute of Standards and Technology 106, p. 1013-1028, 2001.
[204] Cohen, D., *The Absorption Spectra of Plutonium Ions in Perchloric Acid Solutions.* Journal of Inorganic Nuclear Chemistry 18, p. 211-218, 1961.
[205] Scrivener, K., Snellings, R., Lothenbach, B., *A Practical Guide to Microstructural Analysis of Cementitious Materials*, CRC Press, Taylor & Francis Group, Boca Raton, FL (USA), 2016.
[206] Sha, W., O'Neill, E.A., Guo, Z., *Differential scanning calorimetry study of ordinary Portland cement.* Cement and Concrete Research 29, p. 1487-1489, 1999.

6 Appendix

6.1 Auxiliary thermodynamic data on Pu aqueous species and solid compounds

Table A1. Thermodynamic data, used for the equilibrium calculations of Pu.

Reaction	log *K*°	Reference
Redox processes		
$Pu^{3+} \leftrightarrow Pu^{4+} + e^-$	–(17.69 ±0.04)	[5, 9]
$Pu^{3+} + 2\ H_2O(l) \leftrightarrow PuO_2(am,hyd) + 4\ H^+ + e^-$	–(15.36 ± 0.52)	[5, 9]
$Pu^{4+} + 2\ H_2O(l) \leftrightarrow PuO_2^{+} + 4\ H^+ + e^-$	–(17.45 ± 0.69)	[5, 9]
$PuO_2^{+} \leftrightarrow PuO_2^{2+} + e^-$	–(15.82 ± 0.09)	[5, 9]
$PuO_2(am,hyd) \leftrightarrow PuO_2^{+} + e^-$	–(19.78 ± 0.09)	[5, 9]
Solubility and hydrolysis of Pu(III)		
$Pu(OH)_3(am) \leftrightarrow Pu^{3+} + 3\ OH^-$	–(26.2 ± 1.5)[a)]	[9]
$Pu^{3+} + OH^- \leftrightarrow Pu(OH)^{2+}$	(7.1 ± 0.3)[b)]	[5, 9]
$Pu^{3+} + 2\ OH^- \leftrightarrow Pu(OH)_2^{+}$	(12.9 ± 0.7)[b)]	[5, 9]
$Pu^{3+} + 3\ OH^- \leftrightarrow Pu(OH)_3^{0}(aq)$	(15.8 ± 0.5)[b)]	[5, 9]
Solubility and hydrolysis of Pu(IV)		
$PuO_2(am, hyd) \leftrightarrow Pu^{4+} + 4\ OH^-$	–(58.33 ± 0.52)	[5, 9]
$PuO_2(cry) \leftrightarrow Pu^{4+} + 4\ OH^-$	–(64.03 ± 0.51)	[5, 9]
$Pu^{4+} + OH^- \leftrightarrow Pu(OH)^{3+}$	(14.6 ± 0.2)	[5, 9]
$Pu^{4+} + 2\ OH^- \leftrightarrow Pu(OH)_2^{2+}$	(28.6 ± 0.3)	[5, 9]
$Pu^{4+} + 3\ OH^- \leftrightarrow Pu(OH)_3^{+}$	(39.7 ± 0.4)	[5, 9]
$Pu^{4+} + 4\ OH^- \leftrightarrow Pu(OH)_4^{0}(aq)$	(47.5 ± 0.5)	[5, 9]
Solubility and hydrolysis of Pu(V)		
$PuO_2OH(am) \leftrightarrow PuO_2^{+} + OH^-$	–(9.0 ± 0.5)	[5, 9]
$PuO_{2.5}(s,hyd) \leftrightarrow PuO_2^{+} + OH^-$	–(14.0 ± 0.5)	[5, 9]
$PuO_2^{+} + OH^- \leftrightarrow PuO_2OH^0(aq)$	(2.7 ± 0.7)[c)]	[5, 9]
$PuO_2^{+} + 2\ OH^- \leftrightarrow PuO_2(OH)_2^{-}$	(4.4 ± 0.5)[c)]	[5, 9]

Table continues on next page

Solubility and hydrolysis of Pu(VI)

$PuO_2(OH)_2 \cdot H_2O(s) \leftrightarrow PuO_2^{2+} + 2\ OH^- + H_2O(l)$	–(22.5 ± 1.0)	[5, 9]
$PuO_2^{2+} + OH^- \leftrightarrow PuO_2(OH)^+$	(8.5 ± 0.5)	[5, 9]
$PuO_2^{2+} + 2\ OH^- \leftrightarrow PuO_2(OH)_2^0(aq)$	(14.8 ± 1.5)	[5, 9]
$PuO_2^{2+} + 3\ OH^- \leftrightarrow PuO_2(OH)_3^-$	(21.7 ± 0.4)	[5, 9]
$2\ PuO_2^{2+} + 2\ OH^- \leftrightarrow (PuO_2)_2(OH)_2^{2+}$	(20.5 ± 1.0)	[5, 9]

[a] value is originally reported in [30], but with an assigned uncertainty of ± 0.8 in log-units
[b] in analogy with Am(III)
[c] in analogy with Np(V)

Table A2. SIT ion interaction coefficients for Pu aqueous species in NaCl solutions.

species i	***species j***	ε_{ij} ***[mol·kg^{-1}]***	**Reference**
H^+	Cl^-	(0.12 ± 0.01)	[9]
Na^+	Cl^-	(0.03 ± 0.01)	[9]
Na^+	OH^-	(0.04 ± 0.01)	[9]
Pu^{3+}	Cl^-	(0.23 ± 0.02)	[174]
$Pu(OH)^{2+}$	Cl^-	–(0.04 ± 0.07)	[174]
$Pu(OH)_2^+$	Cl^-	–(0.06 ± 0.08)	[174]
$Pu(OH)_3^0(aq)$	Cl^-	0.00 [a]	
$Pu(OH)_3^0(aq)$	Na^+	–(0.17 ± 0.10)	[174]
Pu^{4+}	Cl^-	(0.4 ± 0.1)	[173]
$PuOH^{3+}$	Cl^-	(0.2 ± 0.1)	[173]
$Pu(OH)_2^{2+}$	Cl^-	(0.1 ± 0.1)	[173]
$Pu(OH)_3^+$	Cl^-	(0.05 ± 0.1)	[173]
$Pu(OH)_4^0(aq)$	Na^+/Cl^-	0.00 [a]	
PuO_2^+	Cl^-	-(0.09 ± 0.05) [b]	[9]
$PuO_2OH(aq)$	Na^+/Cl^-	0.00 [a]	
$PuO_2(OH)_2^-$	Na^+	–(0.01 ± 0.07) [b]	[9]
PuO_2^{2+}	Cl^-	(0.21 ± 0.02) [c]	[9]
PuO_2OH^+	Cl^-	(0.05 ± 0.1) [c]	[149]
$PuO_2(OH)_2(aq)$	Na^+/Cl^-	0.00 [a]	
$PuO_2(OH)_3^-$	Na^+	–(0.09 ± 0.05) [d]	[175]
$(PuO_2)_2(OH)_2^{2+}$	Cl^-	(0.69 ± 0.07) [c]	[9]

[a] by definition in SIT formalism
[b] in analogy with Np(V)
[c] in analogy with U(VI)
[d] in analogy with Np(VI)

6.2 Synthesis, characterization and stability of NaISA(s)

The Na-salt of ISA was synthesized from commercial $Ca(ISA)_2$(s) using a cation exchange resin (Chelex® 100, Na-form). The complete description of the method is reported elsewhere [11, 86, 107, 201]. Briefly, 2 g of commercial $Ca(ISA)_2$(s) were suspended in 500 mL of Milli-Q water in the presence of 25 g of resin. The mixture was agitated with a magnetic stirrer for approximately 1 hour, and then filtered with filter paper (Whatman blue ribbon, < 2 μm). The filtrate was evaporated on a heating plate at T = 60 °C until a brown viscous liquid was obtained. The remaining water-content was removed using water-free diethyl-ether. The combination of repeated addition/evaporation of diethyl ether with a cooling step (9 °C, in laboratory fridge) resulted in a pale yellow NaISA(s) solid phase. The yield of the synthetis ranged between 50 and 90 n% (average yield = 68 n%). Both commercial $Ca(ISA)_2$(s) and synthesized NaISA(s) salts were thoroughly characterized using several techniques: ^{1}H and ^{13}C nuclear magnetic resonance spectroscopy (NMR, Bruker Avance III 400 spectrometer, operating at 400.18 MHz for ^{1}H and 100.63 MHz for ^{13}C), X-ray powder diffraction (XRD, D8 Advance diffractometer, Bruker AXS), quantitative and semi-quantitative chemical analysis (by inductively coupled plasma–optical emission spectroscopy: ICP–OES, Optima 8300 DV, Perkin Elmer or standard inductively coupled plasma–mass spectroscopy: ICP–MS, X-Series II, Thermo Scientific), total organic and inorganic carbon measurements (TOC and TIC, respectively, Shimadzu TOC5000) and ion chromatography (IC, ICS-3000 equipped with an AS9HC column, Thermo Scientific).

Figure A1 and Figure A2 show the ^{1}H and ^{13}C NMR spectra, respectively of commercial $Ca(ISA)_2$(s) and NaISA(s) synthesized in the present work (dissolved in D_2O). All main peaks observed in both, the ^{1}H and the ^{13}C NMR spectra can be unequivocally assigned to the H- and C- atoms in the ISA molecule [202]. XRD pattern collected for commercial $Ca(ISA)_2$(s) were found to be in good agreement with data previously reported by Rai and co-workers [68] and furthermore by the comparison with the reference patterns [203] of lactose hydrate and calcite, presence of these phases were excluded above the detection limit (DL, ~10 w%) of the technique (see Figure A3). IC results (not shown) clearly disregarded the presence (above the DL, $\sim 10^{-4} - 10^{-5}$ M of the technique) of chloride, bromide, fluoride, nitrate, phosphate and sulfate in the analyzed commercial $Ca(ISA)_2$(s) and synthetic NaISA(s). The combination of quantitative chemical analyses, TIC and TOC measurements showed an excess of Na and Ca with respect to ISA, which was associated to a large impurity of carbonate. With the aim of obtaining a carbonate-free NaISA stock solution, the synthetic NaISA(s) was dissolved in Milli–Q water and acidified to $pH_m \approx 3$ with 1 M HCl. The solution was then heated to T = 80

°C (in order to avoid the potential decomposition of the ligand [78]) for 3 hours with a continuous purge of Ar gas to facilitate the CO_2(g) degassing. The resulting solution was transferred to Ar atmosphere whilst still hot. The stock was allowed to cool down, and was titrated slowly with 1 M carbonate-free NaOH solution to obtain a weakly alkaline solution ($pH_m \approx 9$). The final stock solution was characterized as (0.16 ± 0.02) M NaISA with pH_m = 8.9. Because of the titration steps required to remove carbonate impurities, the stock solution contained an excess of Na^+ in the form of 0.18 M NaCl. Total carbonate content in the NaISA stock solution was quantified as < $3 \cdot 10^{-4}$ M (DL of TIC considering the dilution factors in the measurements). Subsequent ^{1}H and ^{13}C NMR analysis confirmed the presence of only ISA in the system. The well-characterized NaISA stock solution was stored in a sealed glass container under Ar atmosphere and used in the preparation of all samples involving the use of ISA.

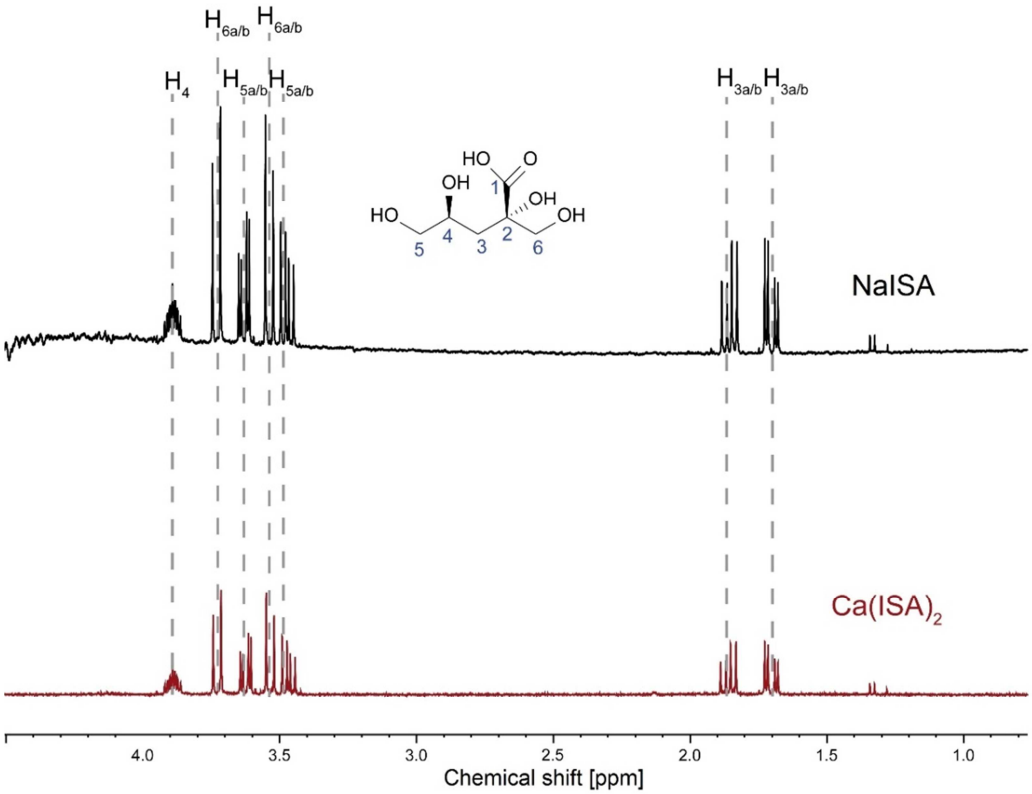

Figure A1. *^{1}H NMR spectra of commercial $Ca(ISA)_2$ (bottom, red spectrum) and NaISA synthesized in the present work (black spectrum, top), at $m(ISA)_{tot}$ = 0.01 m in D_2O.*

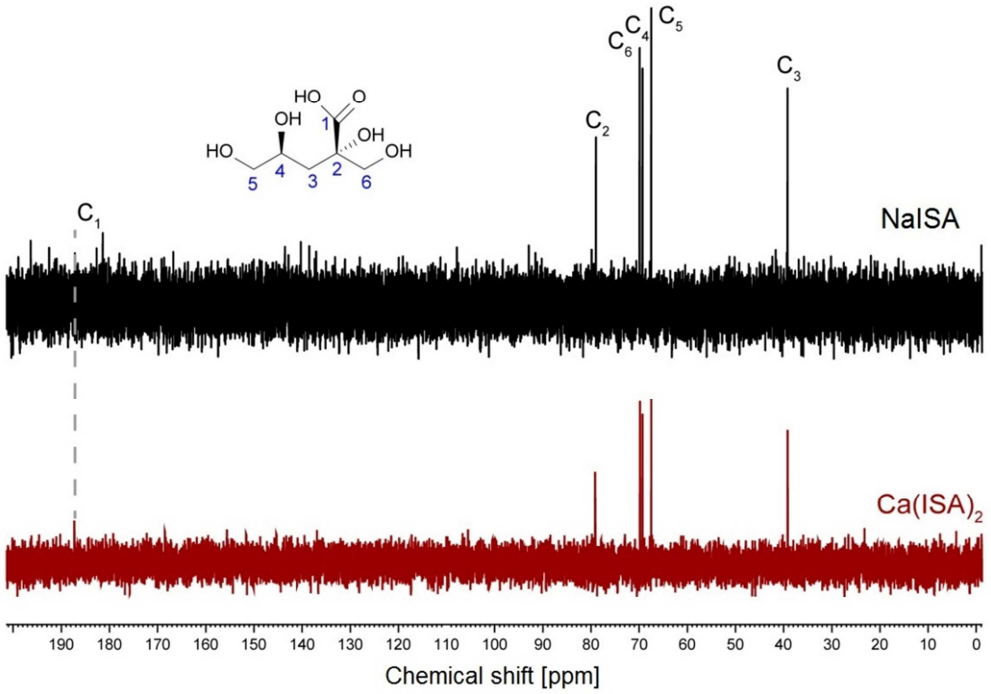

Figure A2. *Proton-decoupled ^{13}C direct excitation NMR spectra of commercial $Ca(ISA)_2$ (bottom, red spectrum) and NaISA synthesized in the present work (black spectrum, top), at $m(ISA)_{tot}$ = 0.01 m in D_2O.*

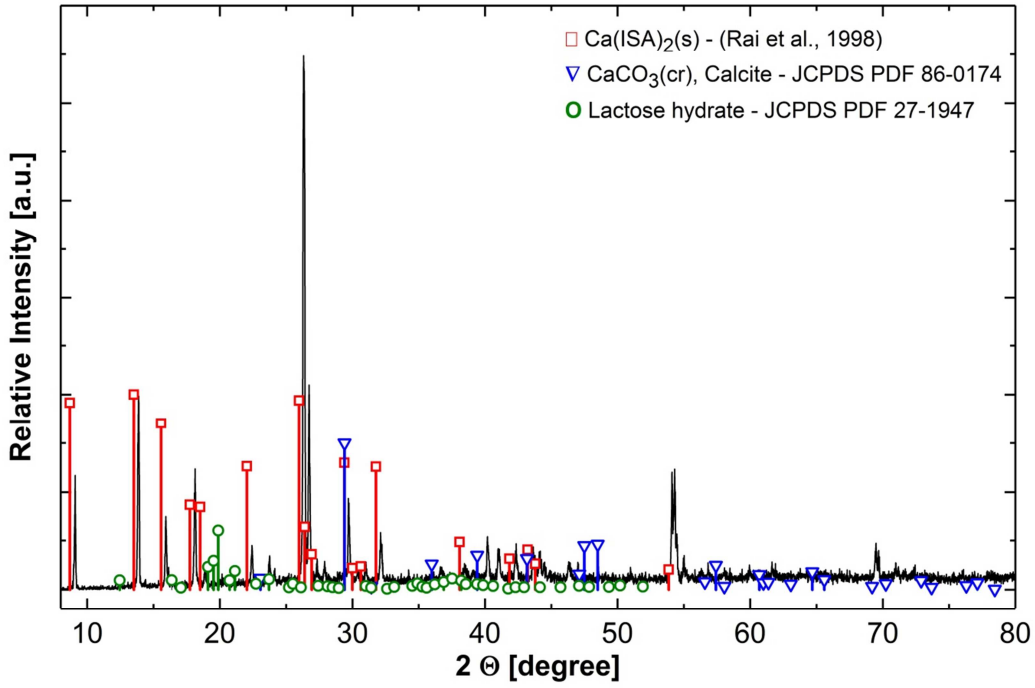

Figure A3. *XRD patterns collected in the present work for commercial $Ca(ISA)_2(s)$. Reference data reported for $Ca(ISA)_2(s)$ [68], calcite (PDF 86-0174) and lactose hydrate (PDF 27-1947) are appended for comparison.*

6.3 Stability of ISA under reducing, alkaline conditions

The stability of ISA under alkaline reducing conditions was also investigated in a series of batch experiments in the absence of Pu. A constant ISA total concentration of 0.01 M was maintined at I = 0.10 M (NaCl). Reducing conditions were fixed with 2 mM or 10 mM HQ, Sn(II) or $S_2O_4^{2-}$ at pH_m = 9 (buffered by CHES) or 12. Two additional samples were prepared with the same matrix compositions (pH_c, I, $[ISA]_{tot}$) but in the absence of reducing chemicals. Although not used as reducing agent in the solubility experiments with Pu, $Na_2S_2O_4$ was also included in this series of experiments to evaluate the possible impact of Sn(II) on the speciation and chemical behavior of ISA. The reducing capacity of Sn(II) ($pe + pH_m \approx 1 - 2$) and $Na_2S_2O_4$ ($pe + pH_m \approx 0 - 1$) are observed to be similar. In the course of 5 months, pH_m and E_h values of the solutions were monitored, and aliquots of supernatants were taken for ^1H and ^{13}C NMR measurements.

Within the investigated time-frame, all NMR spectra (not shown) remained identical (as the original ones collected for the stock solution), thus, supporting the stability of ISA under alkaline and reducing conditions. To assess the possibility of long-term degradation processes, the experiments are still on-going. Nevertheless, after appr. 2 years of allowed equilibration time, results confirm the prominent stability of ISA (even well-beyond the timeframe of the solubility experiments with Pu).

The same set of samples were also serving as subjects to assess the role of Sn(II)–ISA complexation. Visible features, such as chemical-shifts, intensities of ^1H and ^{13}C NMR signals (associated to ISA) in the spectra were obtained to be virtually the same for the cases of absence and presence of Sn(II). This observation does not disregard the presence of Sn(II)–ISA complexes (if yes, only minor), but it clearly confirms that ISA exists predominantly in the free ligand form within the conditions of the solubility study consucted in the present work.

6.4 Pu(VI) stock solution

The UV-VIS-NIR spectra of the synthetized Pu(VI) stock solution at 1 day after the complete dissolution of the original $Na_2Pu_2O_7.H_2O$(am) solid phase (before the initiation of sorption experiments) and at 14 months (after the finalization of all sorption experiments) are shown in Figure 66. Since the most intensive absorption-line corresponding to $Pu(VI)_{aq}$ species at λ = ~832 nm (with a molar extinction coefficient of ε = 555 $dm^3mol^{-1}cm^{-1}$) [204] is not fully depicted, the display-range of the spectral window has been re-adjusted for a better overview. All features of the initially collected spectra perfectly match the absorption spectra of the PuO_2^{2+}(aq) ion in $HClO_4$ solution reported by Cohen *et al.* [204], indicating the predominance of Pu(VI) in the stock solution. Applying the Lambert-Beer law on the detected absorption value at λ = ~953 nm by using ε = 24 $dm^3mol^{-1}cm^{-1}$ [204], the calculated concentration of $Pu(VI)_{aq}$ with a value of $[Pu(VI)_{aq}]$ = 0.011 M is found to be in good agreement with the quantified total Pu concentration of $[Pu]_{tot}$ = (0.0116 ± 0.0001) by SF-/ICP-MS techniques. The spectra recorded on the same stock solution after the finalization of all sorption experiments (14 months) clearly indicates the presence of $Pu(IV)_{aq}$ ions besides $Pu(VI)_{aq}$. Accounting for the presence of $Pu(IV)_{aq}$ ion on the subtracted spectra (red curve in Figure 66) using the absorption value at λ = 665 nm and the ε = 31 $dm^3mol^{-1}cm^{-1}$ [204], a Pu(IV) total concentration of $[Pu(IV)_{aq}] = 2 \cdot 10^{-3}$ M can be determined, which, in combination with the quantifiable $Pu(VI)_{aq}$-content (at λ = 953 nm with ε = 24 $dm^3mol^{-1}cm^{-1}$) results in a total concentration of Pu identical to the initial value: $[Pu]_{tot}$ = (0.0116 ± 0.0001) M. These results show the slow reduction of $Pu(VI)_{aq}$ within the time-frame, resulting in 20 mol% contribution of $Pu(IV)_{aq}$ in the stock solution after 14 months. $Pu(VI)_{aq}$ is expected to be quickly reduced to $Pu(III/IV)_{aq}$ in the presence of reducing agents such as HQ, Sn(II) or dithionate within the supernatant solution after the introduction to the system. The UV-Vis-NIR absorption spectra (not shown) of the stock solution collected during and directly after the preparation of all Pu sorption batch experiments, showed the only presence of $Pu(VI)_{aq}$ in solution, indicating the constant, well-defined composition of the stock solution during the preparation procedure.

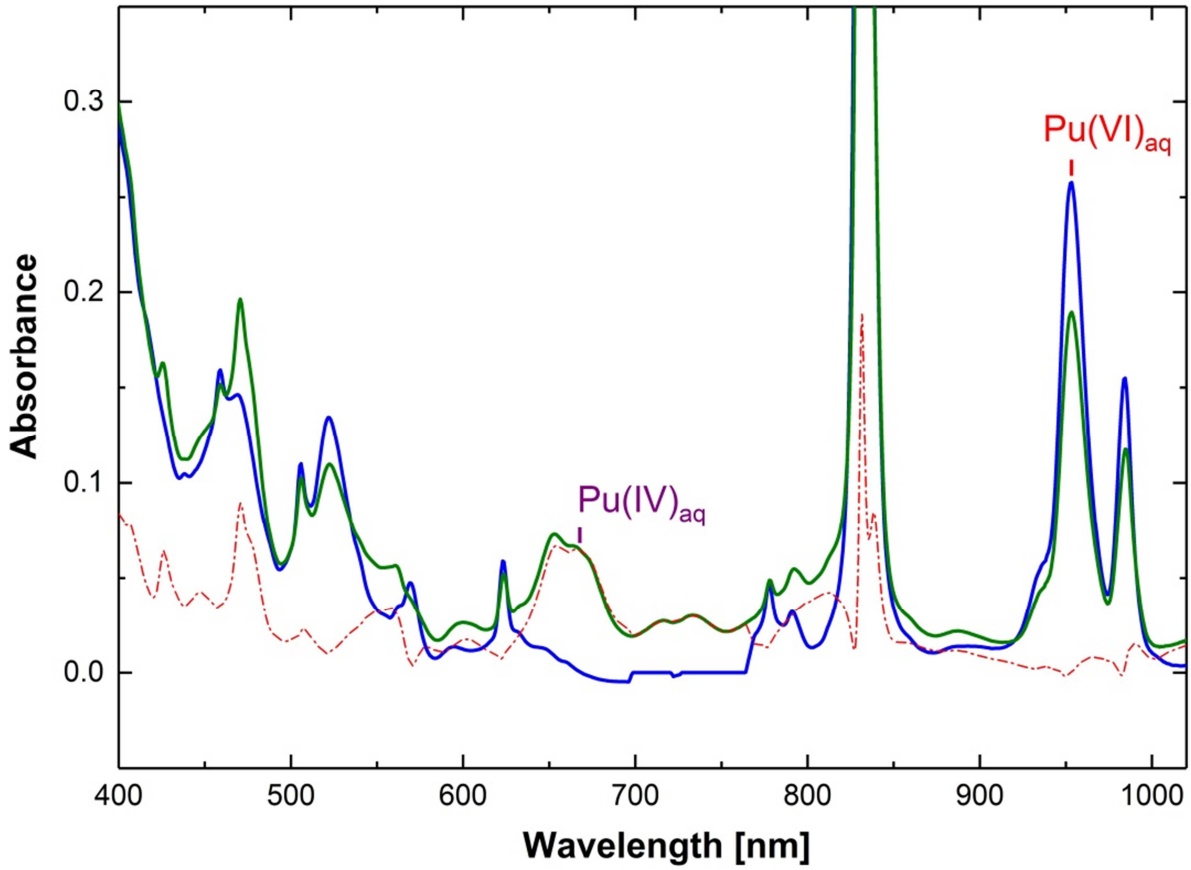

Figure 66. *Background-corrected UV-VIS-NIR spectra of the synthetized Pu(VI) stock solution (quantified by SF-/ICP-MS techniques as* $[Pu]_{tot}$ *= (0.0116 ± 0.0001) M at pH = 0.8 in 0.075 M NaCl media) collected 1 day (blue curve) and 14 months (green curve) after preparation. The red curve depicts the subtraction result of the latter two spectra normalized to the concentration of the* $Pu(VI)_{aq}$ *ion within the two sample, using the absorption values at* λ *= 953 nm with* $\varepsilon = 24\ dm^3mol^{-1}cm^{-1}$ *[204].*

6.5 Characterization of the initial cement powder

Figure 67 shows the background-subtracted XRD pattern of the initial cement powder, together with the identified major and minor phases as adapted from JCPDS database [136]. The collected diffractogram on the powdered material indicates the presence of two major phases: C-S-H phases with highly amorphous character (causing an intensity-increase in baseline level) and the crystalline Portlandite (PDF 04-0733). Calcite was found to be not highly abundant in the sample, however its presence with minor contribution (~10 %) can be unequivocally underlined. The lack of reflections associated to non-hydrated clinker components (such as Alite PDF 85-1378 and Belite PDF 09-0351) indicates the fully hydrated state of the solid specimen (and the generated powder as well). As certain low-intensity reflections may also indicate the presence of other minor phases, such as Ettringite (AFt) or calcium-aluminoferrite (Brownmillerite), an unambiguous identification of the phases was not possible due to low data quality (even within the extended data acquisition time of > 40 hours).

TG-DSC curves collected on the initial cement powder are displayed in Figure 68. The weight-loss of the material within the temperature range 0 – 300 °C can be partly attributed to the loss of surface-bound water, dehydration reactions of C-S-H phases and also the dehydration and dehydroxylation processes of Ettringite [205]. The relatively small endothermic peak at 392 °C possibly corresponds to the water-loss of a hydrated Fe_2O_3 solid solution, originally forming through the hydration process of calcium-aluminoferrite [206]. The second major peak observed at ~494 °C can be assigned to the dehydroxylation reaction of $Ca(OH)_2$(cr). Given that the decomposition reaction of Portlandite is a well-defined, distinct chemical reaction, the weight of the evaporated water can be used to calculate the amount of $Ca(OH)_2$(cr) present in the sample. As the total weight-loss until 600 °C (–26.55 w/w%) provides the anhydrous weight of the cement powder, the –5.75 w/w% weight-loss determined for the dehydroxylation reaction gives a value of 32.2 w/w% Portlandite with regard to the anhydrous weight of the original material. This value is obviously highly overestimated since it is referred to the “dry” weight of the powder, nevertheless, it can be used as a standardized value for comparison purposes.

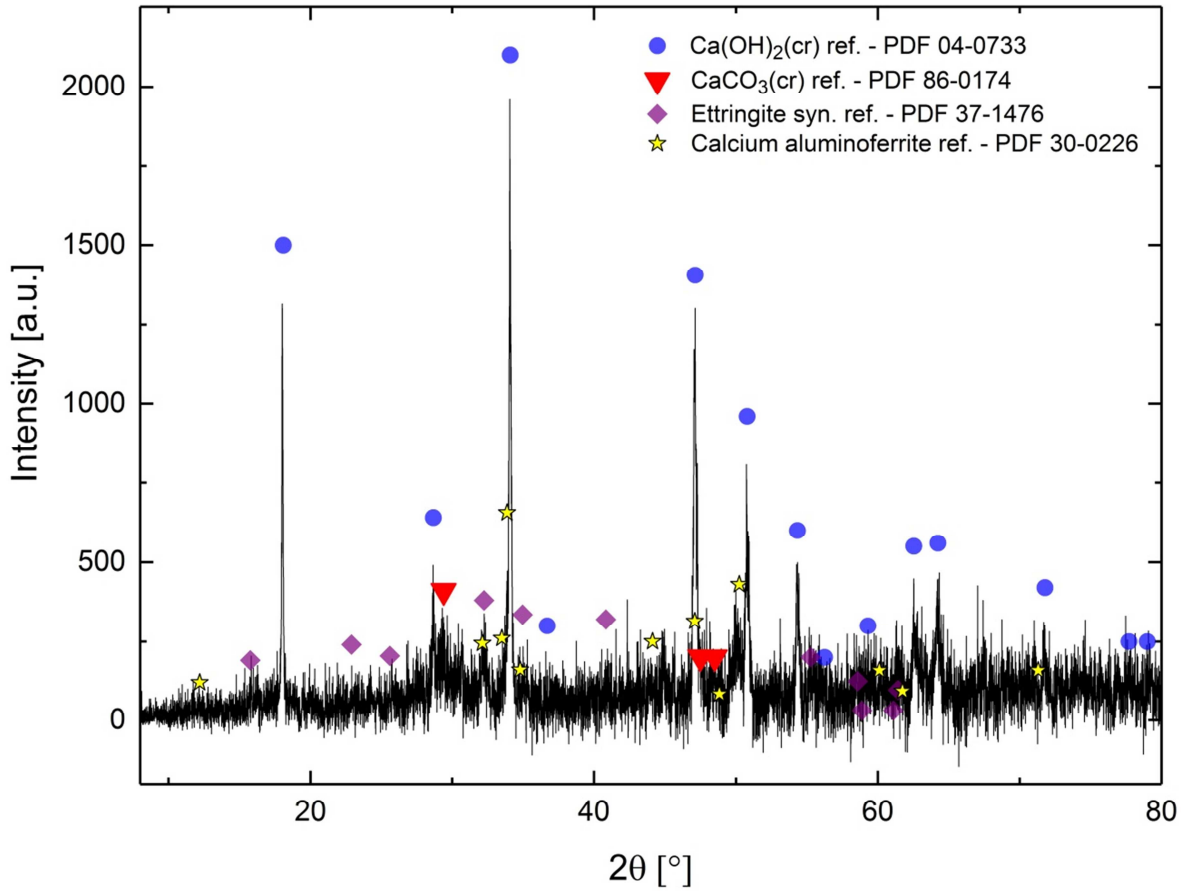

Figure 67. *XRD pattern collected for the initial cement powder generated in the present work. Reference data reported for Portlandite: $Ca(OH)_2$(cr) (PDF 04-0733), calcite: $CaCO_3$(cr) (PDF 86-0174), Ettringite (syn.): $Ca_6Al_2(SO_4)_3(OH)_{12}.26H_2O$ (PDF 37-1476) and calcium-aluminoferrite (Brownmillerite): $Ca_2(Al,Fe)_2O_5$ (PDF 30-0226) are appended for comparison.*

As the weight-loss observed at a higher temperature-range (700 – 720 °C) is strictly related to the decarbonation reaction of the calcite present in the material, the mass of $CaCO_3$(cr) can be determined via the measured generation of CO_2(g). With regard to the anhydrous weight of the cement powder, calcite was found to be present with ~3 w/w% of the initial material, indicating a slightly lower contribution to the hydrated cement phase than shown by XRD. It is of note as well, that these values have rather high uncertainties (~5 – 10 w/w%), generally associated to the heterogeneity, the small total amount of the analyte and also the deconvolution procedure of TGA curves.

The last clearly distinguishable feature (exothermic reaction) in the TGA curve at around 810 °C corresponds to the decomposition (dehydroxylation) of C-S-H phases to wollastonite ($CaSiO_3$) [205].

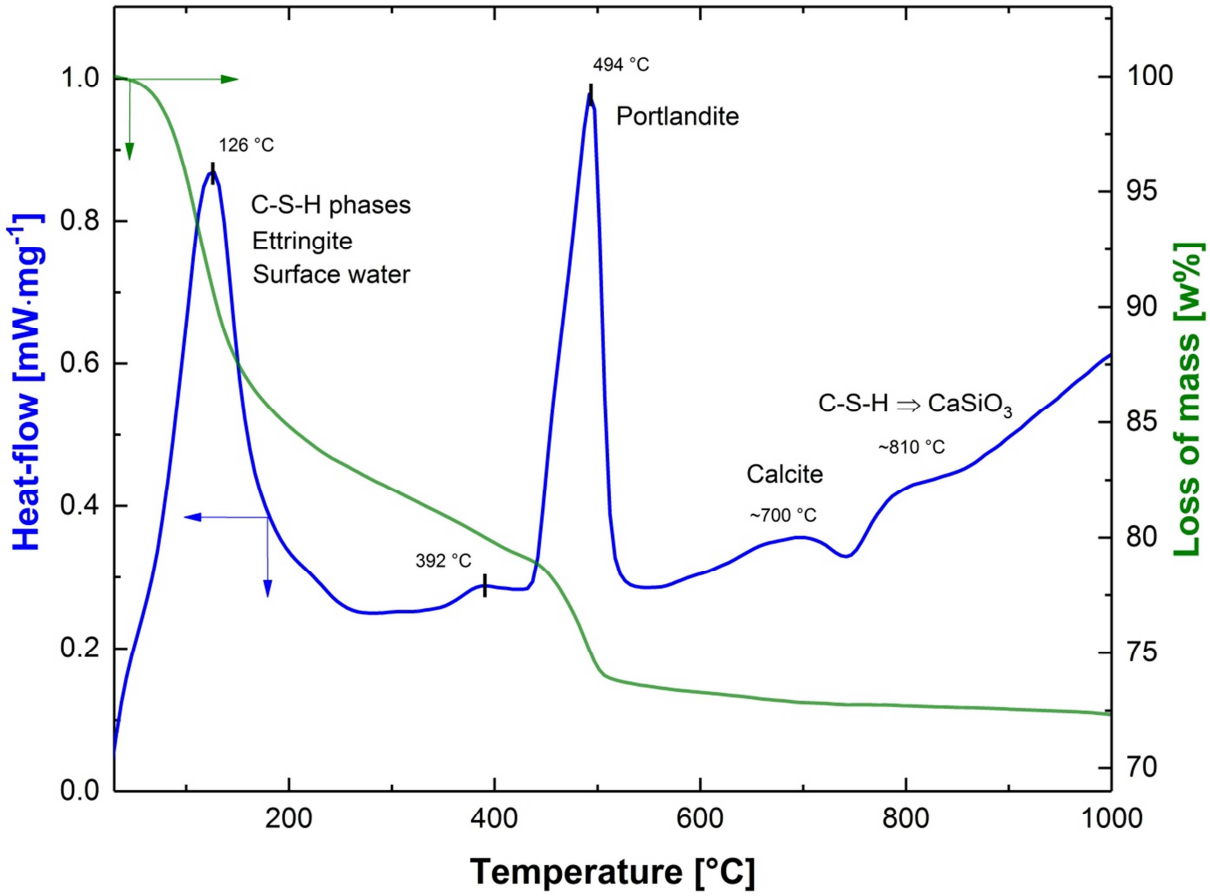

Figure 68. *TG-DSC data recorded on the initial cement powder: differential scanning calorimetry (DSC) signal (blue curve) as specific heat-flow ($mW \cdot mg^{-1}$) and loss of sample mass (green curve) in normalized weight-percentage (w%) unit.*

The calculated chemical composition of the cement powder (with regard to the oxide-contents normalized to the anhydrous weight of the material) obtained after the digestion of the sample by quantitative analysis and as measured by XPS on the dry powder are summarized in Table 22 along with the original data provided by the manufacturer.

Table 22. *Chemical composition of the cement specimens as provided by the manufacturer and the transformed data on the generated cement powder obtained from the results of the quantitative elemental analysis by ICP-OES and ICP-MS after the digestion of the sample and calculated values from the elemental atomic concentrations measured by XPS on the solid material. Values derived within the present study were normalized with regard to the anhydrous weight of the cement powder provided by TG-DSC measurements.*

Analysis method	***CaO w%***	***SiO_2 w%***	***Al_2O_3 w%***	***Fe_2O_3 w%***	***MgO w%***	***Na_2O w%***	***K_2O w%***	***SO_3 w%***
Original mat.	64.00	22.20	3.60	4.40	0.94	0.07	0.72	2.20
ICP-OES/-MS	60.6	20.0	3.6	3.6	0.9	0.1	-	1.7
XPS	61.3	24.3	6.7	2.8	2.4	-	-	1.4

The quantitative analysis of the chemically digested material provides more of a bulk information, *i.e.* representative values for the overall chemical composition of the material, whilst XPS is a surface-specific technique. Thus, the relatively good agreement between the latter two results attests the obtained high homogeneity within the generated powder. As discussed before, the digestion of the sample could not provide any information on the K-content of the material and as for the XPS both, the Na- and the K-atom concentrations were found to be below the detection limit of the technique. The grinding and sieving procedures affected the Ca-content of the material only to a limited extent as a deviation of –3 w/w% is witnessed between the manufacturer information and the result of digestive quantification by ICP-OES (but it is beyond associated uncertainties). This however, indicates the slight loss of Ca in the course of the powdering process. Atomic concentrations determined by XPS are also found to be in good agreement with the latter values, except for the minimal increase for Si, Al and Mg. Since the uncertainties associated to the quantification results by XPS method exceed the magnitude of these deviations, further conclusion cannot be drawn from the observations. Despite the good agreement between the oxide composition of the original and the powdered material, additional, minor alteration effects caused by the exposure to air and by the mechanical heat generated during the milling and sieving process cannot be excluded.

Figure 69 shows an exemplary narrow scan of C 1s XPS spectrum collected for the freshly grinded and sieved cement powder. The displayed curve fit accounts for the contribution of

the carbonate, potentially present as calcite: $CaCO_3$(cr) and of the 'C-O' and the adventitious, 'C_xH_y' (hydrocarbon) functional groups related to organic impurities.

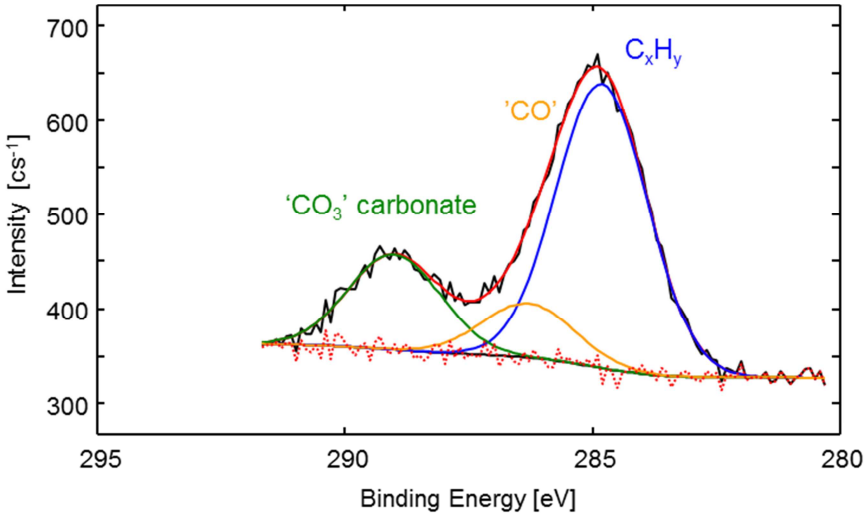

Figure 69. *C 1s XPS spectrum collected for the freshly grinded and sieved cement powder, together with the fit performed accounting for the contribution of carbonate-, potentially present as calcite: $CaCO_3$(cr) and of 'C-O' and the adventitious, 'C_xH_y' (hydrocarbon) functional groups (corresponding to organic impurities).*

The distribution of the chemical groups related to the C 1s elemental line in combination with the atomic concentration of carbon provided by the survey scan indicates the presence of 7.0 w/w% $CaCO_3$(cr) on the surface of the generated powder (the converted value with regard to the anhydrous weight of the cement powder is ~9.0 w/w%). This slight carbonation on the surface of the sample may originate from the powdering procedure as well as from the sample preparation procedure undertaken before XPS data collection.

BET-N_2 measurements provided a high specific surface area with a value of 79.2 m^2g^{-1} for the well-homogenized, initial cement powder. Since the majority of the expected hydrated solid phases present in OPC have relatively low specific surface areas (1 – 10 m^2g^{-1}), except for C-S-H phases (148 m^2/g at Ca:Si ratio of ~1.7, provided by Tits *et al.* [49]), the determined value unambiguously indicates the presence of the latter phases.

In summary, combining all solid phase characterization results for the cement material it can be stated that the chemical composition of the powdered material has not been modified by the preparation procedure and the main, hydrated solid phases present in the OPC powder are the amorphous C-S-H phases and Portlandite. Considering the plausible assumption that in the course of the hydration process all Ca-content of the material are either consumed by the

forming Portlandite or the C-S-H phases, and all the Si-content will be solely taken up by the C-S-H phases, an estimate of 1.7 – 1.9 can be calculated for Ca:Si atom-concentration ratio for the present C-S-H phases based on the ICP-OES/-MS, TG-DSC and XPS results. This value is in close agreement with the reported data of 1.8 resulting from model calculations on OPC pastes with similar chemical characteristics [195-197]. The cement powder used in the sorption experiments can be taken as a representative material for the original cement specimens. Small deviations such as surface carbonation (~3 – 10 w/w%) and the potential dehydration of minor phases originating from the powdering process and from the storage of the sample is considered to have negligible effect on the sorption properties of the material.

6.6 Chemical compositions of equilibrated cement pastes and porewater solutions

Figure 70 shows the background-subtracted XRD patterns of equilibrated cement paste samples (treated with propan-2-ol) retrieved from: (1) the solid phase in equilibrium with the generated porewater (used for all sorption studies simulating Stage II of the cement degradation process) and from (2) a batch sample of the Cement-ISA sorption experiment series (at $[ISA]_{tot}$ = 0.01 M and S:L ratio = 2 gdm^{-3}). Data on the Sample 1 (named as "porewater cement") was collected after the preparation of all sorption experiments (~1 year of contact time), whilst the diffractogram on the 2nd sample (denoted as "ISA-cement") was recorded after an equilibration time of 14 days (final t_{eq} of Cement-ISA sorption investigations). XRD patterns are shown together with the identified major and minor phases as adapted from JCPDS database [136].

Both raw XRD patterns originally depicted a highly increased baseline-level, confirming the predominance of amorphous C-S-H phases in the retrieved pastes. The collected diffractogram on porewater cement indicates the presence of crystalline Portlandite (PDF 04-0733) in the paste, however the decreased intensities show that the phase has been partly washed out through the procedure. The liquid phase used for the preparation of all sorption experiments is saturated with regard to Portlandite solubility equilibrium. More intensive reflections for $Ca(OH)_2$(cr) were detected in the sample equilibrated with porewater solution with $[ISA]_{tot}$ = 0.01 M, demonstrating that the dissolution of the phase was not substantial at the highest total concentration of the ligand. As for the initial cement material, calcite was found to be present in both of the analyzed samples with a minor contribution above the detection limit of the technique (~10 w/w%). The latter identification is however purely qualitative, as certain XRD reflections of $Ca(OH)_2$(cr) are highly sensitive to preferred orientation effects. Furhter, minor hydrated phases were not possible to be detected.

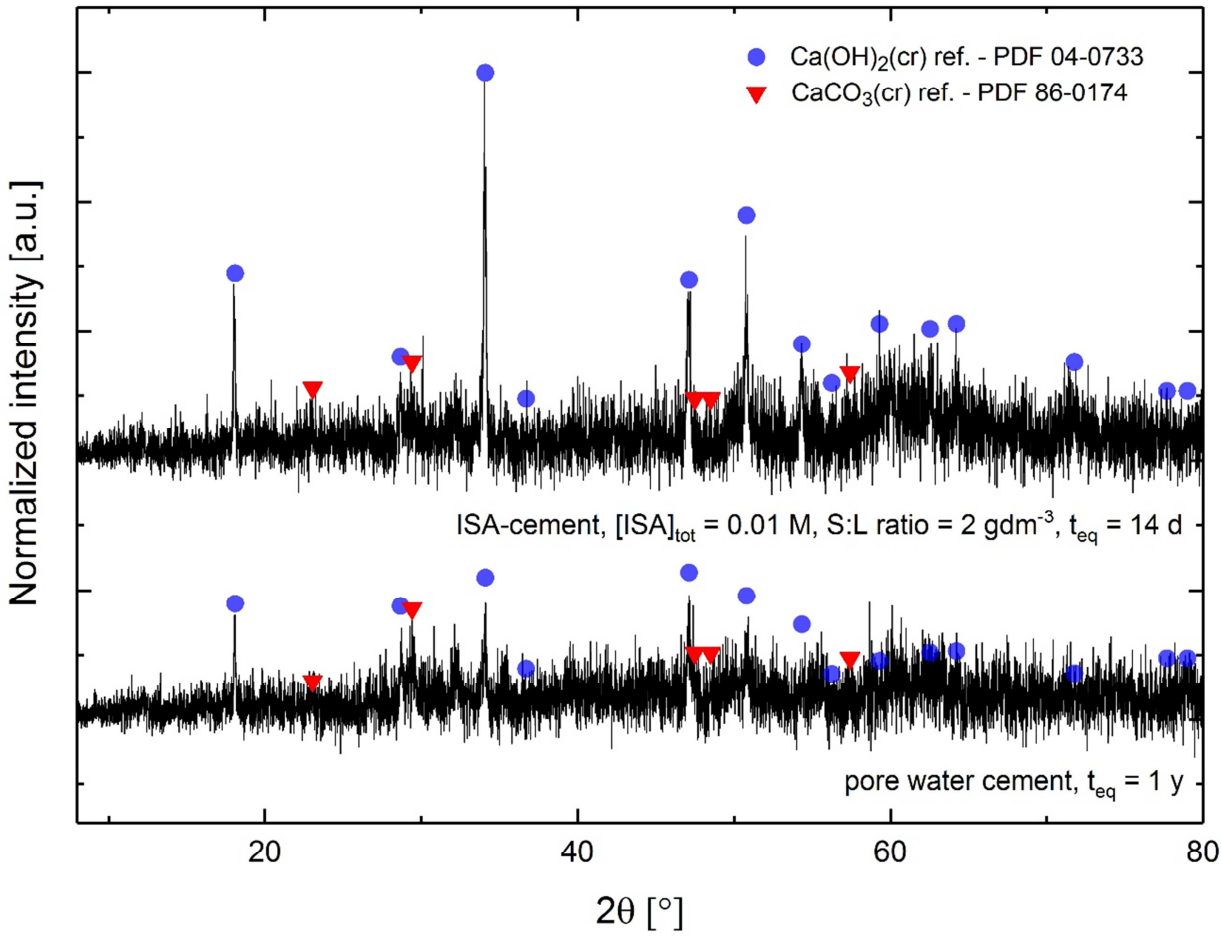

Figure 70. *XRD patterns collected in the present work for cement pastes: "porewater cement" indicates the retrieved cement paste, at t_{eq} = 1 year used for the generation of the porewater for sorption investigations, "ISA-cement" is a cement solid phase equilibrated in porewater with $[ISA]_{tot}$ = 0.01 M at S:L ratio = 2 gdm^{-3} for 14 days. Hydration stoppage on the samples was achieved by the use of propan-2-ol. Reference data reported for Portlandite: $Ca(OH)_2$(cr) (PDF 04-0733), Calcite: $CaCO_3$(cr) (PDF 86-0174) are appended for comparison.*

TG-DSC curves collected on the above described two cement samples are displayed in Figure 71. All identified features are matching the TG-DSC data recorded for the initial cement powder. The concurring weight-losses of the two specimens in the temperature-range of 0 – 300 °C (porewater cement: –15.35 w/w%, ISA-cement: –16.51 w/w%) and the almost identical anhydrous weight (calculated from the total weight-loss till 600 °C) are indicating the reliability of the applied hydration stoppage method. Using the anhydrous weight of the sample and the weight-losses attributed to the dehydroxylation reaction of $Ca(OH)_2$(cr) phase provide values of 26.91 w/w% and 25.19 w/w% for the contributions of Portlandite in the

porewater cement and ISA-cement samples. Compared to the analogous value of the initial cement material, both values depict a small loss (with relative values of 5.3 w/w% and 7 w/w%, respectively) of Portlandite from the samples.

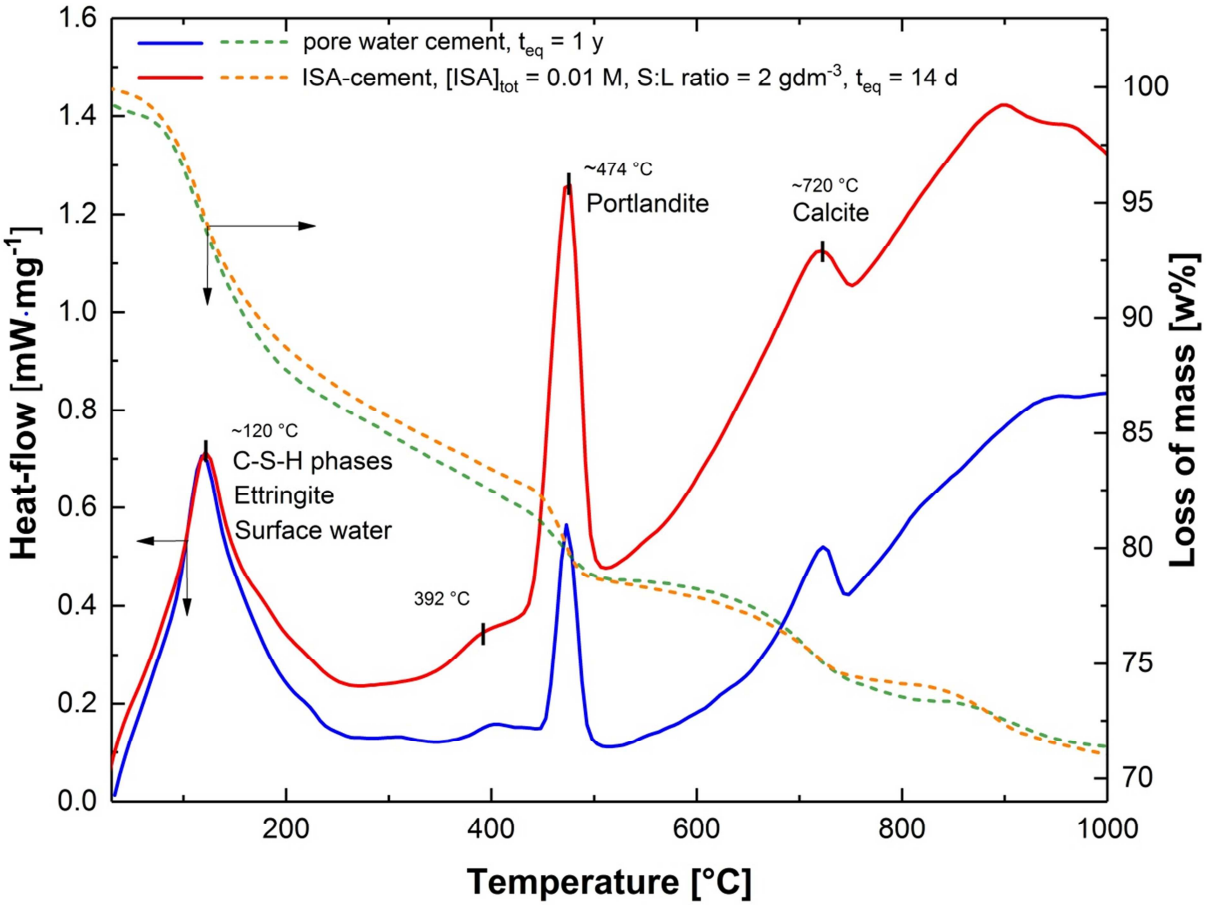

Figure 71. *TG-DSC data recorded on equilibrated cement pastes: "porewater cement" indicates the cement paste, at t_{eq} = 1 y, used for the generation of the porewater for sorption investigations (blue and green curves), "ISA-cement" is a cement solid phase equilibrated in porewater with $[ISA]_{tot}$ = 0.01 M at S:L ratio = 2 gdm^{-3} for 14 days (red and orange curves). Hydration stoppage on the samples was achieved by the use of propan-2-ol. Differential scanning calorimetry (DSC) signal (continuous curve) is displayed as specific heat-flow (mWmg^{-1}) and loss of sample mass (dashed curve) is in weight-percentage (w/w%) unit.*

Accounting for the presence of calcite, using the weight-loss observed at the temperature-range of 700 – 720 °C, relative weight-percentages of $CaCO_3$(cr) with regard to the anhydrous weight of the cement powder was calculated to be ~15.1 w/w% for the porewater cement and ~12.34 w/w% for the ISA-cement sample, indicating a higher contribution than for the initial material. These values are in good agreement with the qualitative experimental findings of the

XRD method as well. The relative differences between the values of the equilibrated samples and of the initial material show only a negligible carbonation effect, which is considered to have almost no influence on the chemical composition of the porewater or on the sorption properties of the material under the given conditions.

Table 23 shows the calculated chemical characteristics of the cement powder (with regard to the oxide compositions normalized to the anhydrous weight of the material) as measured by XPS method on the equilibrated cement phases described above and on the initial cement powder as well.

Table 23. *Chemical characteristics of the cement specimens with regard to oxide compositions determined by XPS on the initial cement powder, the "porewater cement" sample (indicating the cement paste, at t_{eq} = 1 y, used for the generation of the porewater for sorption investigations) and on the "ISA-cement" (depicting a cement solid phase equilibrated in porewater with $[ISA]_{tot}$ = 0.01 M at S:L ratio = 2 gdm^{-3} for 14 days). Hydration stoppage on the samples was achieved by the use of propan-2-ol. All values are normalized with regard to the anhydrous weight of the cement powder provided by TG-DSC measurements.*

Analysis method	***CaO w%***	***SiO_2 w%***	***Al_2O_3 w%***	***Fe_2O_3 w%***	***MgO w%***	***Na_2O w%***	***K_2O w%***	***SO_3 w%***
Original mat.	61.3	24.3	6.7	2.8	2.4	-	-	1.4
Porewater cement	52.2	24.8	8.0	0.9	1.3	-	-	7.6
ISA-cement	47.9	19.8	6.8	4.9	0.7	-	-	1.5

Compared to the initial material, the chemical compositions of both retrieved specimen show a pronounced decrease in Ca-content, indicating the loss of Portlandite from the system, in accordance with the findings of TG-DSC analysis.

Accounting for the carbonate-group contribution from the deconvolution results on the narrow scan of C 1s XPS spectrum collected for the "porewater cement" (Figure 72) in combination with the atomic concentration of carbon provided by the survey scan on the sample indicates the presence of 11.8 w/w% $CaCO_3$(cr) on the surface (calculated using the hydrated weight of

the cement powder). This slightly enhanced calcite-content, compared to the analogous data on the initial material is in agreement with the observations made by TG-DSC measurements. Figure 73 shows the exemplary narrow scan by C 1s XPS spectrum collected for the ISA-cement sample. For the purpose of quantification, binding energies of the elemental lines were charge referenced to Si 2p3/2 at 101.5 eV and the binding energy of Si 2p3/2 was determined by charge referencing to the C 1s elemental line of adventitious hydrocarbon at 284.8 eV using the XP spectra of an analogously prepared sample without ISA in solution (not shown).

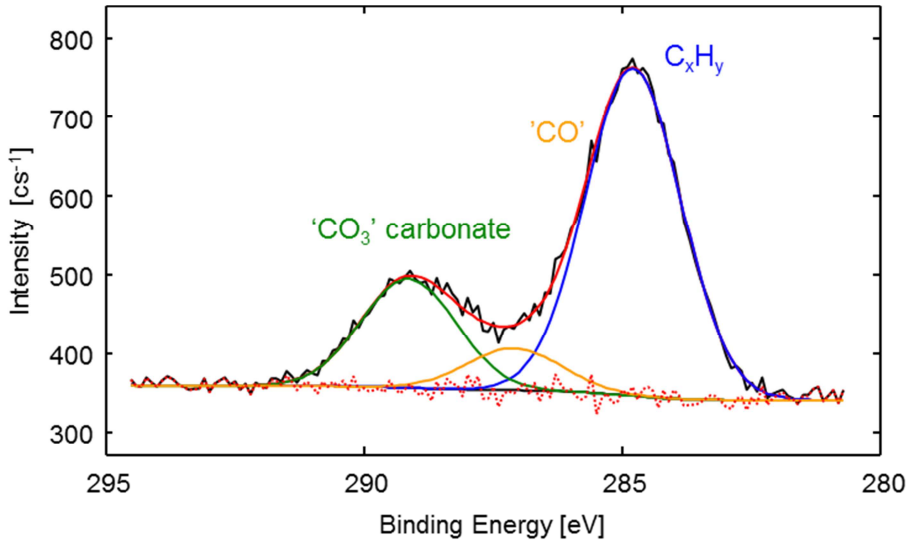

Figure 72. *C 1s XPS spectrum collected for the "porewater cement" sample (indicating the cement paste, at t_{eq} = 1 y, used for the generation of the porewater for sorption investigations), together with the fit performed accounting for the contribution of carbonate-, potentially present as calcite: $CaCO_3$(cr) and the adventitious, CxHy (hydrocarbon) functional groups.*

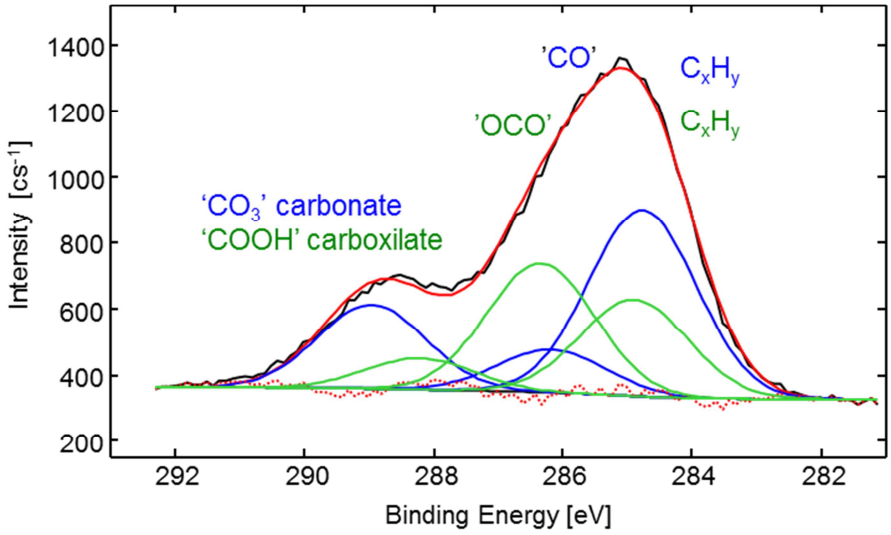

Figure 73. *C 1s XPS spectrum collected for "ISA-cement" (depicting a cement solid phase equilibrated in porewater with* $[ISA]_{tot}$ *= 0.01 M at S:L ratio = 2* gdm^{-3} *for 14 days), together with the fit performed accounting for the contribution of carbonate-, potentially present as calcite:* $CaCO_3$*(cr), adventitious, CxHy (hydrocarbon) and ISA-related functional groups.*

The presence of ISA on the cement surface is clearly confirmed upon the displayed curve fit as the contributions of the carbonate-, the 'C-O' and the adventitious, 'C_xH_y' (hydrocarbon) functional groups alone cannot represent all the features of the given elemental line.

Based upon the stoichiometric contributions of the different carbon functional groups present in the ISA molecule together with the latter two signals and the atomic concentration of carbon provided by XPS indicates the presence of 18.0 w/w% $CaCO_3$(cr) and 12.3 w/w% "HISA" on the surface of the retrieved cement phase (with regard to original weight analyzed by XPS method). Calculated values depict an extensive carbonation on the surface, compared to the results provided by TG-DSC measurements. However, due to the loss of Ca-content from the analyzed material these contributions can only be compared in relative terms, since they are normalized to the elemental composition on the surface of the hydrated sample. Hence, considering the surface-sensitivity of the technique and the preparation procedure of the sample for measurement, carbonate-contents derived by XPS method are highly overestimated with regard to the real bulk information provided by TG-DSC method. Yet, it can be stated, that a formation of calcite on the surface is definitely occurring. The performed hydration stoppage did not remove ISA bound to the potential sorbing sites on the cement phase and hence, it was detectable and quantified to be present with 1:3 molar ratio to the surface concentration of carbonate ion on the surface of the analyzed sample.

Table 18 (provided in Section 3.2.1.2) summarizes the concentrations of the major and minor elements in the equilibrium solutions of the abovementioned two samples: (i) porewater cement sample and (2) the ISA-cement sample as quantified by ICP-OES and ICP-MS measurements.

The initial composition of the porewater together with the determined $pH_c = (12.55 \pm 0.08)$ (averaged value of multiple measurements on the porewater) are in good agreement with the calculated and the previously reported porewater conditions ($pH_c = 12.50$) representing Stage II of the cement degradation process [4, 198]. A slightly lower value has been quantified for the Na concentration, whereas concentration of K was found to be in good agreement with reference data, both indicating the successful pre-washing step aiming to remove the alkali-content of the initial cement powder. Reference values for Mg and Fe) are not provided in the literature, whilst the concentration of Si is below the detection limit of ICP-MS, in agreement with the low level reported.

The measured pH value of the ISA-cement porewater sample ($pH_c = 12.60 \pm 0.03$) was observed to be within the uncertainty-range of the values collected in the absence of ISA (the calculated theoretical value under identical conditions is $pH_c = 12.57$). The chemical composition of the equilibrated porewater with $[ISA]_{tot} = 0.01$ M at S:L ratio of 2 gdm^{-3} show distinct changes in the depicted elemental concentrations especially with regard to Na ion concentration. These discrepancies are originating from the introduction of ISA-stock solution to the system, which was later confirmed by the characterization of identical solutions prepared in the absence of cement solid phases. Ca ion concentration was found to be negligibly affected by the high ligand concentration in solution, which is in agreement with thermodynamic calculations, assuming that the concentration of Ca^{2+} is governed by the dissolution of Portlandite and by its complex formation reactions with ISA in solution (when $[ISA]_{tot}$ does not exceed ~0.1 M, *i.e.* precipitation of $Ca(ISA)_2(s)$ does not occur). Accounting for the latter chemical equilibria, the calculated theoretical increase (without taking into account the sorption of the ligand) in $[Ca]_{tot}$ with the level of $2.7 \cdot 10^{-3}$ M is close to absolute value of the uncertainty-range ($\pm$ 3 10^{-3} M) associated to the quantification of $[Ca]_{tot}$ by the applied ICP-OES technique.

In summary, it can be clearly stated that the generated porewater to be used as the liquid phase in the later Pu sorption experiments is a chemically representative solution of cement pore fluids expected at the second stage of the cement degradation process. Solid phase characterization results on the retrieved cement solid phase coincide with the latter observation. Moreover, the ISA concentration of 0.01 M in the supernatant with S:L ratio = 2

gdm^{-3} was neither affecting the main chemical parameters of interest (pH_c, $[Ca]_{tot}$) in solution and nor the main chemical composition (presence of Portlandite and C-S-H phases) of the HCP. The main changes determined can be modelled by assuming Portlandite dissolution equilibria in combination with Ca(II)-OH-ISA complex formation reactions in solution, which is in agreement with the observation of previous studies [104].